The role of sea ice in mediating atmosphere-ice-ocean momentum transfer

Samuel Brenner

A dissertation
submitted in partial fulfillment of the
requirements for the degree of

Doctor of Philosophy

University of Washington

2022

Reading Committee:

Luc Rainville, Chair

Jim Thomson, Chair

Georgy Manucharyan

Program Authorized to Offer Degree:
School of Oceanography

University of Washington

Abstract

The role of sea ice in mediating atmosphere-ice-ocean momentum transfer

Samuel Brenner

Co-Chairs of the Supervisory Committee:
Principal Oceanographer Luc Rainville
Applied Physics Laboratory

Senior Principal Oceanographer Jim Thomson
Applied Physics Laboratory

The ongoing loss of Arctic sea ice prompts questions about changes in momentum transfer across the atmosphere-ice-ocean system and potential climate feedback mechanisms, but the role of the ice in mediating that process is not fully understood. To address knowledge gaps about atmosphere-ice-ocean momentum transfer, this study makes use of *in situ* measurements collected during two recent observational campaigns in the Beaufort Sea: the Marginal Ice Zone (MIZ) program and the Stratified Ocean Dynamics of the Arctic (SODA) program. The research is presented in two parts. Part I develops data processing methods for instrumentation deployed as part of the SODA program while part II uses data from both programs to evaluate controls of sea ice on the ocean surface stress and the associated response in the ocean surface mixed layer (ML).

Measurements of upper ocean properties can be challenging in the Arctic Ocean due to environmental conditions, including the need for moored instruments to avoid contact with sea ice. Part I of this work describes methods for developing usable data products from upward-looking Acoustic Doppler Current Profiler (ADCP) measurements on the SODA moorings. This encompasses methods for creating combined data records from vertically-offset ADCPs on the same mooring chain and methods for using ADCPs to estimate surface ML depth and temperature. As ML depth and temperature measurements are not typically possible from subsurface moorings in the Arctic, the approach developed here provides considerable value and could be applied to other extant mooring records to recover information about ML property variability or trends.

Building on these measurements, part II considers how sea ice properties, such as concentration and morphology, affect the transfer of momentum from the sea ice to the ocean and the associated upper-ocean dynamics. Ice-ocean drag coefficients, a measure of momentum transfer efficiency, calculated using a force-balance approach from the SODA mooring data show seasonal variations consistent with past observations, but at odds with previous model results. Tests of model parameterizations of drag based on direct observations of under-ice morphology reveal that the model-observation mismatch can be attributed to inaccuracies in empirical translations from bulk geometric properties to detailed geometry statistics, especially under-representation of floe sizes. The mooring measurements further show a seasonal upper-ocean response to surface stress, with minimal energy in ML inertial oscillations under sea ice cover. A simplified momentum budget for the coupled ice-ocean system shows that the seasonality stems from a combination of internal stress in the ice damping the oscillations and seasonal variability in the ocean ML depth. Finally, shipboard measurements from the MIZ program show the evolution of ice-edge-located freshwater front as it reacted to changes in the surface wind stress, raising questions about how sea ice might impact spatial heterogeneity of stress and how that might interact with frontal dynamics.

This research shows that boundary layer dynamics and internal ice mechanics both play a role in mediating atmosphere-ice-ocean momentum transfer. The results suggest future trends of more “slippery” ice-ocean boundary layer, and decreasing internal sea ice stress, which could lead to increased sea ice drift speeds and more direct atmosphere-ocean coupling.

TABLE OF CONTENTS

Appendices

Appendices

LIST OF FIGURES

LIST OF TABLES

ACKNOWLEDGMENTS

Throughout the writing of this dissertation and performing the research it describes, I have lived and worked on the territories of the Coast Salish peoples, including the tribes and bands of the Duwamish, Puyallup, Suquamish, Tulalip and Muckleshoot nations. Additionally, for this work I have passed through the lands and waters of the Unangan, Yup'ik, and Inupiaq peoples.

This work was supported by the Office of Naval Research (ONR) as part of the Stratified Ocean Dynamics of the Arctic (SODA) and Marginal Ice Zone (MIZ) research projects. I thank Captain Greg Tlapa and Captain MaryEllen Durley, along with the rest of the command team and crew of USCGC Healy for operational support of the SODA program in 2018 and 2019. I also thank the captain and crew of R/V Norseman II for support of the MIZ program in 2014. This research could not have been done without engineering and technical support from Joe Talbert, Jason Gobat, Ben Jokinen, and Eric Boget.

RADARSAT-2 Data and Products ©MDA Geospatial Services Inc. (2014) – All Rights Reserved. RADARSAT is an official mark of the Canadian Space Agency.

This work has benefited from ideas, feedback, and mentorship from many members of the SODA project team. I also appreciate the helpful views and conversations shared over the years with a wide number or friends and collaborators, including members of the oceanography community and the Environmental Fluid Mechanics group at University of Washington. My committee, Alison Gray, Jodi Young, Georgy Manucharyan, and Bonnie Light, have all been excellent support and encouragement throughout this journey.

Chiefly, I would like to acknowledge and thank my supervisors, Luc Rainville and

Jim Thomson. This work would not have been possible without their guidance, support, and mentorship. I appreciate most their trust in my ideas and direction and in my ability as a scientist.

Chapter 1

INTRODUCTION

The polar regions are losing ice, and their oceans are changing rapidly. The consequences of this polar transition extend to the whole planet, and are affecting people in multiple ways IPCC, 2019

1.1 Motivation and background

1.1.1 Arctic sea ice loss

Arctic sea ice is undergoing an unprecedented and dramatic reduction in both extent and volume (e.g., *Kwok*, 2018; *Stroeve and Notz*, 2018) in response to anthropogenic climate change (*Stroeve and Notz*, 2015; *Notz and Stroeve*, 2016). This reduction is enhanced during the September sea ice minimum (average of 13.0% extent decrease per decade) compared to the March sea ice maximum (2.7% per decade; *Meier and Stroeve*, 2022), leading to a much more seasonal Arctic ice pack (e.g., *Thomson et al.*, 2016b; *Onarheim et al.*, 2018; *Peng et al.*, 2018; *Meier and Stroeve*, 2022). Accompanying this decrease in ice extent is a loss of multiyear sea ice (*Maslanik et al.*, 2011; *Kwok*, 2018; *Meier and Stroeve*, 2022), an increase in the relative extent of marginal ice zones (MIZs; *Strong and Rigor*, 2013; *Rolph et al.*, 2020), and an acceleration of ice drift speeds (*Rampal et al.*, 2009; *Spreen et al.*, 2011; *Kwok et al.*, 2013). Additionally, the wider areas of open water are associated with an increase in surface wave activity in the Arctic (*Thomson and Rogers*, 2014; *Thomson et al.*, 2016b; *Liu et al.*, 2016). Modern climate models predict that even under a low-emission scenario (RCP2.6 or SSP126), summer Arctic sea ice extent will continue to decline for a number of decades (*Stroeve and Notz*, 2015; *Årthun et al.*, 2021).

Much of the observed sea ice loss to date is either a direct (through surface melting) or indirect (e.g., through ice-albedo feedback; *Perovich et al.*, 2007) response to increased atmospheric temperatures. However, recent studies have highlighted the potential increasing importance of subsurface oceanic heat as a driver of melt (e.g., *Carmack et al.*, 2015, and references therein). The Arctic Ocean is classified as a "β-ocean" (*Carmack*, 2007), on the basis that it exists in a temperature-salinity range in which stratification is set primarily by salinity (the name β-ocean is in reference to haline contraction coefficient, β). Together with strong freshwater inputs, the haline density control results in a relatively cold and fresh surface layer across the Arctic that insulates sea ice from warmer waters beneath (*Carmack et al.*, 2016). Throughout the Arctic, Atlantic-origin water is a reservoir of heat at depth (with the core at ∼150–500 m); in the Western Arctic, Pacific-origin water provides an additional shallower (∼50–100 m depth) source of subsurface heat (e.g., *Timmermans and Marshall*, 2020, and references therein). The heat contained in both of these subsurface reservoirs has been increasing (*Timmermans et al.*, 2018; *Polyakov et al.*, 2017; *Barton et al.*, 2018), and it is thought that as sea ice coverage decreases, a number of different drivers may enable the upward mixing of that heat (e.g., *Rainville et al.*, 2011). The ultimate fate of waters in both of these subsurface reservoirs and their ability to contribute to further sea ice loss will depend on surface momentum transfer and potential feedback mechanisms across a range of scales.

The Beaufort Sea in the Western Arctic in one of the regions that is undergoing the most substantial changes in sea ice loss and increased seasonality of ice conditions (*Thomson et al.*, 2016b; *Onarheim et al.*, 2018). As such, it has been the site of a number of recent Office of Naval Research (ONR) observational campaigns (*Lee et al.*, 2017), including the Marginal Ice Zone project (MIZ; *Lee et al.*, 2012, and `www.apl.uw.edu/miz`) and the Stratified Ocean Dynamics of the Arctic project (SODA; *Lee et al.*, 2016, and `www.apl.uw.edu/soda`).

1.1.2 Basin-scale feedbacks in the Western Arctic

Basin-scale circulation in the Beaufort's Canada Basin is dominated by the Beaufort Gyre: an anti-cyclonic circulation pattern that can act to store both heat and freshwater (*Carmack et al.*, 2016). Recent work has identified that the reduction of atmosphere-ocean momentum transfer by sea ice (section 1.2.1) has the potential to act as a major control on basin-scale circulation in the Beaufort Sea by minimizing or reversing Ekman pumping relative to open-water conditions (*Meneghello et al.*, 2018a,b; *Dewey et al.*, 2018; *Doddridge et al.*, 2019; *Meneghello et al.*, 2020a). The heat content of subsurface waters in the Beaufort Gyre has been increasing in recent years, as a result of increasing surface temperature of the major inflow pathways and the Chukchi Sea (where the gyre is ventilated) (*Timmermans et al.*, 2018). The degree to which this stored heat is available for increased surface-driven mixing and sea ice melt depends partly on accompanying changes in freshwater storage in the surface of the gyre (freshwater accumulation deepens the winter mixed layer and reduces access to the stored subsurface heat; e.g., *Cole and Stadler*, 2019). As such, quantifying the gyre's freshwater content has been a subject of numerous studies (e.g., *Giles et al.*, 2012; *Krishfield et al.*, 2014; *Regan et al.*, 2019; *Proshutinsky et al.*, 2019), which show both seasonal and inter-annual variability.

The freshwater storage of the gyre is maintained by a balance between eddy fluxes and Ekman pumping (which is a function of surface stress) (e.g., *Manucharyan and Spall*, 2016). The stress transfer from the atmosphere to the ocean is modified by sea ice (see section 1.2.1), so an effect referred to as the "ice-ocean governor" (*Meneghello et al.*, 2018a) adds an additional term when considering the tendency and equilibrium of the gyre, leading to a three-way balance (*Doddridge et al.*, 2019; *Meneghello et al.*, 2020a). The effect of the ice-ocean governor within the balance is a negative feedback mechanism between internal ice stress and geostrophic velocity in the gyre that tends to promote gyre equilibrium (*Dewey et al.*, 2018; *Meneghello et al.*, 2018a, 2020a). While there is some expectation that ongoing sea ice loss would reduce the impact of the ice-ocean governor and thus require higher eddy fluxes to maintain balance (*Armitage et al.*, 2020), the details of such a mechanism and our ability to predict future changes depends on a more complete understanding of how momentum is transferred across the atmosphere-sea ice-ocean system (*Meneghello et al.*, 2020a).

1.1.3 Momentum transfer and vertical mixing

In addition to surface stress feedbacks on basin-scale circulation patterns, there are also thought to be more direct links between surface stress and sea ice loss. Specifically, it is thought that Arctic sea ice loss leads to increased wind energy input to the ocean and thus more vertical mixing (e.g., *Rainville et al.*, 2011). As a result, there may be an increase in ocean heat flux (i.e., heat flux from the ocean to the ice) (*Ivanov et al.*, 2016; *Polyakov et al.*, 2017, 2020b), promoting further ice melt in a positive feedback loop.

Shear-driven mixing

Ocean surface currents energized by surface stress can lead to shear at the mixed-layer base. Associated shear-driven mixing can entrain subsurface heat into the mixed layer, where it is available for ice-ocean heat transfer and melting. Indeed, storm events have been shown to enhance the upward mixing of subsurface heat (*Meyer et al.*, 2017; *Peterson et al.*, 2017) and lead to sea ice melt or delayed freeze-up (*Jackson et al.*, 2012; *Peterson et al.*, 2017; *Smith et al.*, 2018; *Graham et al.*, 2019b). The ability for surface stress to mix up subsurface heat depends on a competition between shear and stratification. *Barton et al.* (2018) suggest that in the Arctic's Eurasian basin, the future of this interplay may be complex with different behaviours predicted over different timeframes. Though, in a hindcast simulation, *Hordoir et al.* (2022) showed that vertical mixing has increased over much of the Arctic relative to a period from 1970–1999 (with the Beaufort Sea's Canada Basin being an exception).

Internal-wave-driven mixing

The low interior mixing environment of the Arctic Ocean relative to lower latitudes (*Rainville and Winsor*, 2008; *Fer*, 2009; *Guthrie et al.*, 2013; *Shaw and Stanton*, 2014; *Scheifele et al.*, 2020; *Dosser et al.*, 2021) has been partly attributed to the lack of internal wave energy present in the Arctic (*D'Asaro and Morison*, 1992), with wave fields that have been measured as having 3–7 % of the energy of mid-latitude oceans (*Levine et al.*, 1987). Through a range of mechanisms, the presence of sea ice impacts the internal waves in the near-inertial frequency band (*Rainville et al.*, 2011, and references therein), potentially suppressing near-inertial wave (NIW) generation (*Rainville and Woodgate*, 2009; *Martini et al.*, 2014; *Dosser et al.*, 2014; *Dosser and Rainville*, 2016; *Kawaguchi et al.*, 2019) and causing wave dissipation in the ice-ocean boundary layer (*Morison et al.*, 1985; *Pinkel*, 2005). Changing sea ice conditions are expected to lead to an increase of internal wave-driven vertical mixing in the Arctic; though even with sea ice loss to date, this hasn't yet been observed (*Guthrie et al.*, 2013).

1.1.4 *Challenges and open questions*

Despite the fundamental importance of ocean surface stress in ice-ocean feedback processes, we still don't fully understand the controls of momentum transfer across the atmosphere-sea ice-ocean system. Ongoing sea ice loss may suggest a positive trend of increasing surface stress to the ocean, but modelling indicates that even the sign of the trend (let alone its magnitude) is sensitive to details of the dynamic coupling between the ocean and the ice (*Martin et al.*, 2016). While the thick, multi-year ice of the past has been seen as inhibiting atmosphere-ocean momentum transfer, marginal sea ice may actually enhance surface stress (*Guest et al.*, 1995; *Martin et al.*, 2014, 2016), which could shift the seasonality and strength of surface forcing. A number of historical studies have provided insight into details of the boundary layers both above (e.g. *Arya*, 1975; *Overland*, 1985; *Guest et al.*, 1995; *Grachev et al.*, 2007; *Wenta and Herman*, 2018) and below (e.g. *McPhee* *and Smith*, 1976; *McPhee*, 1982; *Morison et al.*, 1987; *Shirasawa et al.*, 1989; *Svensson and Omstedt*, 1990; *McPhee*, 1999; *Fer et al.*, 2004) the sea ice, which act as controls on the momentum flux (see section 1.2), but making measurements of these boundary layers is logistically challenging. In general, measurements of the ice-ocean boundary have been made from drifting ice floes, and so most of our understanding of these systems is from a Lagrangian perspective based on thicker multiyear floes (which are typically used as measurement platforms for logistical reasons). For these reasons, we don't know how representative these measurements are, especially of processes in the MIZ or a more seasonal first-year-ice pack. Recent work has shown that the efficiency of momentum transfer across the atmosphere-sea ice-ocean system is highly seasonal (*Tsamados et al.*, 2014; *Martin et al.*, 2016; *Cole et al.*, 2017; *Dewey*, 2019), but models and observations don't agree on the sense of that seasonality, making future predictions particularly challenging. Given the increase in seasonality of Arctic sea ice and widening of marginal ice zones, it is necessary to resolve these discrepancies and build a deeper understanding of coupling across the atmosphere-sea ice-ocean system in order to understand the potential impacts of the ongoing loss of Arctic sea ice.

1.2 *Theoretical framework*

1.2.1 *Surface stress*

The over-arching questions and common framework for this work revolve around the momentum transfer across the atmosphere-sea ice-ocean system. That momentum transfer (a.k.a., surface stress: $\boldsymbol{\tau}_s$) is mediated by turbulence in the boundary layers at each of the interfaces (atmosphere-ice, atmosphere-ocean, and ice-ocean), which is described in the Reynold's-averaged Navier Stokes (RANS) equations by turbulent fluctuations, $\boldsymbol{u'}$ and w' (horizontal and vertical, respectively), i.e., the "Reynold's stress", evaluated at the boundary ($z = z_0$) (e.g., *Thorpe*, 2007):

$$\frac{\boldsymbol{\tau}_s}{\rho} = \langle \boldsymbol{u'} w' \rangle \Big|_{z=z_0}. \tag{1.1}$$

This is also frequently written in terms of a friction velocity: $\boldsymbol{\tau}_s\rho^{-1} = \boldsymbol{u}_*\|\boldsymbol{u}_*\|$.

As turbulence is unresolved in most modelling or observational frameworks, surface momentum fluxes are frequently described based on bulk parameters using the "quadratic drag law". The quadratic drag law relates the friction velocity to a bulk velocity through a turbulent transfer coefficient, a.k.a., a drag coefficient, C_d:

$$\boldsymbol{\tau}_s = \rho C_d \boldsymbol{U}\|\boldsymbol{U}\|, \tag{1.2}$$

where and $\boldsymbol{U}$ in an appropriate bulk velocity, and ρ is the density of the associated fluid. Drag coefficients are essentially a measure of the efficiency of the turbulent momentum flux, and vary based on the surface roughness (as described in section 1.2.2).

In open water conditions the total surface stress on the ocean is directly transferred from the wind, and is mediated by surface gravity waves. Gravity waves impact the stress transfer through both changes in the surface roughness (i.e., variations in C_d; see section 1.2.2), and as a sink of momentum during wave growth and radiation (*Gemmrich et al.*, 1994; *Zippel et al.*, 2022). Despite the complexity of these processes, the leading-order effects of surface waves on atmosphere-ocean stress transfer is reasonably well understood, and it is even possible to make approximations of the atmosphere-ocean drag coefficient, C_{ao} (and thus the total surface stress to the ocean) using only the wind speed (*Large and Pond*, 1981, and see section 1.2.2).

Conversely, in fully ice covered conditions, there are separate stresses on both the atmosphere-ice and ice-ocean interfaces: $\boldsymbol{\tau}_{ai}$ and $\boldsymbol{\tau}_{io}$, respectively. These can be similarly calculated with eq. (1.2) using appropriate densities (ρ_a and ρ_o) and drag coefficients (C_{ai}, C_{io}). In each case, the bulk velocity $\boldsymbol{U}$ used in eq. (1.2) is relative to the sea ice motion. As wind speeds are typically one to two orders of magnitude greater than ice drift speeds, the sea ice velocity is frequently neglected when calculating $\boldsymbol{\tau}_{ai}$ (i.e., the bulk velocity is taken as the wind velocity only). For calculating $\boldsymbol{\tau}_{io}$, the bulk velocity $\boldsymbol{U}$ is the relative ice-ocean velocity $\boldsymbol{u}_{rel} = \boldsymbol{u}_i - \boldsymbol{u}_o$.

Different frameworks exist for calculating surface momentum fluxes in mixed surface conditions (e.g., sea ice and open water). *Lüpkes and Birnbaum* (2005) summarizes the two main approaches used for calculating the net momentum flux out of the atmosphere ($\boldsymbol{\tau}_{atm}$) in mixed ice/open water conditions, these being the "parameter-averaging method", and the "flux-averaging method" (also called the "mosaic method"). In the parameter-averaging method, the momentum flux is calculated based on a "mean surface"; i.e., using grid-cell averaged values of roughness length. In the flux-averaging method, the total momentum flux is calculated based on the concentration-weighted average of the separate fluxes over the sea ice and open water:

$$\boldsymbol{\tau}_{atm} = A\boldsymbol{\tau}_{ai} + (1 - A)\boldsymbol{\tau}_{ao}, \tag{1.3}$$

where A is fractional sea ice concentration, and $\boldsymbol{\tau}_{ai}$ and $\boldsymbol{\tau}_{ao}$ represent the stress components at each of the interfaces ("ai": atmosphere-ice; "ao": atmosphere-ocean). An implicit assumption of the flux-averaging method is that there is some vertical level, the blending height l_b, at which the wind velocity is independent of the surface type (*Claussen*, 1991, 1995).

When calculating $\boldsymbol{\tau}_{ai}$ and $\boldsymbol{\tau}_{ao}$ with eq. (1.2), the bulk velocity scale, $\boldsymbol{U}$, is taken as the wind velocity, $\boldsymbol{u}_a$ (typically at a 10-m reference height). As a result, the total surface stress on the atmosphere can also be calculated as $\boldsymbol{\tau}_{atm} = \rho_a C_e \boldsymbol{u}_a \|\boldsymbol{u}_a\|$, where ρ_a is the atmospheric density, and C_e is an effective drag coefficient, which could be determined using either the parameter-averaging or flux-averaging methods. In the flux averaging approach, $C_e = AC_{ai} + (1 - A)C_{ao}$, where C_{ai} and C_{ao} are separate drag coefficient on the atmosphere-ice and atmosphere-ocean interfaces (this is found by combining eq. 1.2 and eq. 1.3).

The total momentum flux into the ocean, $\boldsymbol{\tau}_{ocn}$, in partially ice-covered conditions is commonly represented as (e.g., *Steele et al.*, 1989; *Yang*, 2006; *Meneghello et al.*, 2017; *Dewey et al.*, 2018, and others):

$$\boldsymbol{\tau}_{ocn} = A\boldsymbol{\tau}_{io} + (1 - A)\boldsymbol{\tau}_{ao}. \tag{1.4}$$

This representation mirrors eq. (1.3), and so represents a flux-averaging approach for calculating the stress. This describes a combination of the direct transfer of momentum between the atmosphere and the ocean, and an indirect transfer mediated by sea ice. In contrast to the calculations for $\boldsymbol{\tau}_{atm}$, different densities and bulk velocity scales are used with eq. (1.2) for calculating $\boldsymbol{\tau}_{io}$ and $\boldsymbol{\tau}_{ao}$, so a single effective drag coefficient cannot be constructed. For the same reason, the parameter-averaging approach may not be tenable for calculating $\boldsymbol{\tau}_{ocn}$.

It is not entirely clear over which horizontal scales the flux-averaging assumptions are valid. The use of sea ice concentration, A, in eqs. (1.3) and (1.4) necessitates that the averaging is performed over some areal extent. A wide range of satellite observation products of A are available, with a resolution of $25\,\mathrm{km} \times 25\,\mathrm{km}$ being common (e.g., *Fetterer et al.*, 2017), but not ubiquitous. Within some observation extent, sea ice can exist across a range of floe scales. A given fractional ice concentration of $0 \leq A \leq 1$ can be potentially achieved with a single large floe surrounded by an of area open water, or by a range of smaller floes (fig. 1.1). While both geometries would be equivalent in eqs. (1.3) and (1.4) , in reality the total surface stresses may differ between the scenarios. As momentum flux is controlled by boundary layer turbulence, it is likely that there minimum scale over which different surface types (ice or open water) can be considered to be distinct, and that scale will be controlled by scales of the associated turbulent eddies in the boundary layer. Moreover, surface types can have downstream effects: turbulent wakes in the lee of sea ice floes likely impact momentum flux over adjacent open water areas (e.g., *Lüpkes and Birnbaum*, 2005), and differences in fetch mean that locally-generated surface gravity waves will be smaller in the lee of floes. Both surface-type distinction and downstream effects will impact the total surface stress differently for different floe size distributions even in areal extents that have the same ice concentration (e.g., see different proportion of hypothetical downstream area in each panel of fig. 1.1). The effects likely differ for ocean and atmosphere stresses ($\boldsymbol{\tau}_{atm}$ and $\boldsymbol{\tau}_{ocn}$) because of differences in the boundary layer structures above and below the sea ice. For this reason, the flux-averaging approach may break down in aggregations of "small" sea ice floes in locally high ice

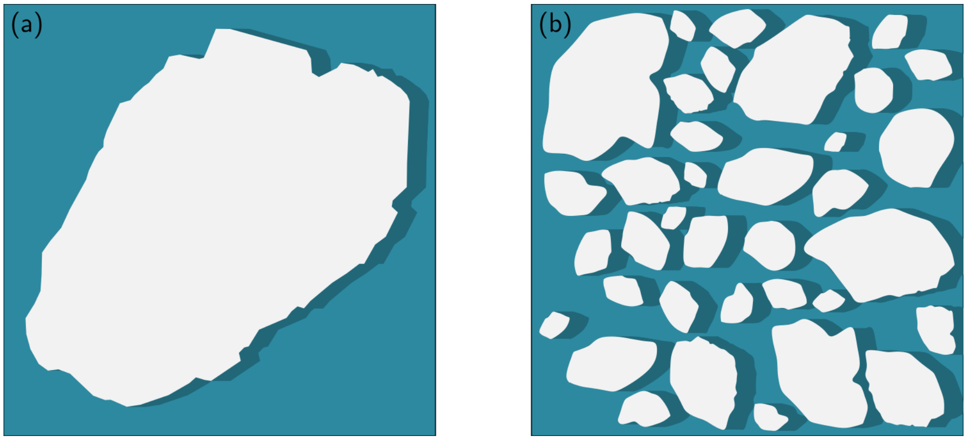

Figure 1.1: Schematic representations of the same fractional sea ice concentration of $A = 0.5$ for (a) a single large floe, and (b) a range of smaller floes. Darker shading in the water represents the hypothetical downstream area effected by wind from the left of each panel (set as a fixed offset from the sea ice that is equal for both panels).

concentration conditions (as are frequently seen in bands in marginal ice zones), and for thin leads in compact sea ice.

Determining the relevant horizontal scales associated with flux-averaging assumptions is complicated by the fact that direct *in situ* measurements of turbulent Reynold's stresses have some measurement footprint that they aggregate over. For example, a fixed measurement platform in the atmospheric boundary layer (e.g., on an ice floe or a research vessel) may need to make averages over 10-min windows in order to separate turbulent fluctuations from the mean flow. Even in a light wind speed of $\sim 5\,\mathrm{m\,s^{-1}}$, that 10-min window represents an advective length scale of 3 km over which the fluxes are integrated – too large to resolve different boundary layer characteristics of individual sea ice floes in the marginal ice zone. In this work, chapter 4 makes estimates of the ice-ocean stress in week-long windows (necessary to statistically account for potential impacts of internal stress on the force balance approach used there); for the observed sea ice velocities, these windows correspond to a measurement footprint of ∼50–100 km (though that chapter primarily considers the direct ice-ocean stress instead of the total ocean surface stress, eq. (1.4)).

Despite these complications, the flux-averaging approach is widely used and considered appropriate for grid-scale averaged surface stresses. Following from that, the impact of sea ice on ocean surface stress and atmosphere-ocean momentum flux can be investigated by combining eq. (1.3) and eq. (1.4) using the sea ice momentum balance (*Martin et al.*, 2016). Doing so gives $\boldsymbol{\tau}_{ocn} = \boldsymbol{\tau}_{atm} + \sum \boldsymbol{F}_{ice}$, where $\sum \boldsymbol{F}_{ice}$ represents the sum of forces acting on and within the sea ice (e.g., ice acceleration, internal stresses). It is through the inclusion of $\sum \boldsymbol{F}_{ice}$ that sea ice mediates the atmosphere-ocean momentum transfer; however, these forces are not easy to resolve. Accounting for internal ice stress requires understanding of sea ice rheology, which is an area of active research (see *Feltham*, 2008, for a review). Even in free-drift conditions, when internal stresses are negligible, Coriolis and accelerative forces still lead to non-zero $\sum \boldsymbol{F}_{ice}$ (discussed in chapter 4). Because of the inclusion of $\sum \boldsymbol{F}_{ice}$, atmosphere-ocean momentum transfer is highly dependant on sea ice dynamics. However, as those dynamics are influenced by both atmosphere and ocean velocities, the atmosphere-sea ice-ocean system is strongly coupled.

1.2.2 *Variability of drag coefficients*

In absence of buoyancy fluxes, the value of the surface drag coefficient C_d depends on a surface roughness length, z_0. In the open ocean, surface gravity waves act as roughness elements for momentum transfer, as described by the Charnock relation ($z_0 = \alpha u_*^2 g^{-1}$; *Charnock*, 1955) and included in bulk parameterizations (e.g., in the COARE bulk algorithm; *Fairall et al.*, 2003; *Edson et al.*, 2013). Because of strong relationships between wind speed, wind stress, and equilibrium sea state, simple wind-speed-based parameterizations of the atmosphere-ocean drag coefficient, C_{ao}, provide a good first estimate; for example:

$$C_{ao} = 10^{-3} \times \left[\frac{2.7}{\|\boldsymbol{u}_a\|} + 0.142 + \frac{\|\boldsymbol{u}_a\|}{13.09} \right], \tag{1.5}$$

where $\|\boldsymbol{u}_a\|$ is the wind speed in $\mathrm{m\,s^{-1}}$ measured at a height of $10\,\mathrm{m}$ (*Large and Yeager*, 2004, which is an update to the classic *Large and Pond*, 1981 formulation).

In the boundary layer above or below the ice, the roughness length is expected to be based on the physical roughness of the ice, which must be determined with in-situ measurements. However, since the geometry is characterized by discrete roughness elements (i.e., ice sails and keels and floe and melt-pond edges), the drag coefficient represents a combination of skin drag and form drag; for example, the ice-ocean drag coefficient, C_{io}, can be written as (*Lu et al.*, 2011; *Tsamados et al.*, 2014):

$$C_{io} = C_f + C_k + C_s, \tag{1.6}$$

where C_f is the form drag on floe edges, C_k is the form drag on keels, and C_s is the skin drag. Because of this combination of form and skin drag, determining a characteristic roughness length for sea ice is challenging. Quoted values of z_0 on the underside of the ice vary over a wide range (e.g., over 4 order of magnitude, from 10^{-3}–10^{1} cm; *Cole et al.*, 2017), and suggest that multiyear ice has higher values of z_0 than first year ice (*McPhee*, 2012, and references therein). However, in most cases these are an "effective roughness length", that combines the effects of form and skin drag together. There has been limited work in trying to identify a roughness length associated with level ice (*McPhee*, 2002, provides one example).

Drag coefficients at the atmosphere-ice interface (C_{ai}) have received considerable attention in literature (e.g., *Overland*, 1985; *Guest et al.*, 1995; *Andreas et al.*, 2010a; *Lüpkes and Birnbaum*, 2005; *Lüpkes et al.*, 2012; *Lüpkes and Gryanik*, 2015), due in part to their importance for weather modelling (*Lüpkes et al.*, 2012; *Elvidge et al.*, 2016). Observations have shown that C_{ai} varies with the ice concentration, A, (with a maximum at some intermediate concentration) leading to a number of concentration-based parameterizations (e.g., *Birnbaum and Lüpkes*, 2002; *Andreas et al.*, 2010a; *Lüpkes et al.*, 2013). *Lüpkes et al.* (2012) suggested a partitioning of C_{ai} (analogous to eq. 1.6), with the component parts each themselves being functions of ice concentration based on empirical relations. Some atmospheric forecasting models (e.g., *ECMWF*, 2019a) have instituted ice concentration-based parameterizations of atmosphere-ice drag.

In contrast, the ice-ocean drag coefficient (C_{io}) is often taken as a constant in models of sea ice dynamics (*Köberle and Gerdes*, 2003; *Timmermann et al.*, 2009; *Losch et al.*, 2010; *Rousset et al.*, 2015; *Rampal et al.*, 2016) and calculations of ocean surface stress (e.g., *Yang*, 2006; *Meneghello et al.*, 2017; *Dewey et al.*, 2018; *Regan et al.*, 2019; *Armitage et al.*, 2020). The traditionally accepted value of 5.5×10^{-3} is based on work by *McPhee* (1980), and determined using a force-balance approach from a drifting ice camp during the AIDJEX field campaign. The force-balance approach (using observed sea ice motion and wind stress, and inverting the free-drift sea ice momentum equation) is less widely used for determining drag coefficients than by directly measuring turbulent fluxes and applying eq. (1.2) (though see *McPhee*, 1980; *Madsen and Bruno*, 1987; *Randelhoff et al.*, 2014; *Kim et al.*, 2017; *Dewey*, 2019; *Heorton et al.*, 2019, for examples of the force balance approach). Nonetheless, the value of 5.5×10^{-3} is roughly consistent with mean values of the ice-ocean drag coefficient determined across a range of studies (including those done use direct turbulent measurements; e.g, *Morison et al.*, 1987; *Shirasawa et al.*, 1989; *Shirasawa and Ingram*, 1997; *Randelhoff et al.*, 2014; *Cole et al.*, 2014, 2017; *Gallaher*, 2019). However, there is still significant variability of measured drag coefficient values in the literature (e.g., see table 1 in *Lu et al.*, 2011).

Some of the observed variation of C_{io} between studies may be partly due to difference in measurement depth (explained below) or technique (e.g., force-balance versus direct turbulent measurements). Nevertheless, it is likely that much of the diversity in measured drag coefficients can be attributed to differences in sea ice geometry (i.e., through changes in bulk roughness due to ice keels and floe edges). Some ice dynamics models have instituted parameterizations for variable ice-ocean drag coefficients that reflect changes in sea ice roughness (indirectly, based on "deformation energy", *Steiner*, 2001, or directly, based on sea ice geometry, *Lu et al.*, 2011; *Tsamados et al.*, 2014), but these approaches still require validation and are not widespread.

Because of vertical variations in bulk velocity profiles ($\boldsymbol{U}$ in eq. 1.2), a consistent framework needs to be adopted for meaningful use and comparison of drag coefficients. In the atmosphere, a measurement elevation of 10 m is standardized. The height of the "law-of-the-wall" logarithmic boundary layer (in which the stress is approximately constant) in the atmosphere is on the order of hundreds of meters (*Holton*, 2004, chapter 5), so the 10-m measurement height is well within that layer. However, there is no consistent reference depth for the ice-ocean drag coefficient (e.g., see table 1 in *Lu et al.*, 2011). Choices in ice ocean drag coefficient values to use in models or analysis reflect different reference depth choices, and thus may either implicitly or explicitly make assumptions about the underlying sea ice-ocean boundary layer (IOBL) structure (see section 1.2.3).

1.2.3 *Ice-ocean boundary layer structure*

The momentum transferred into the ocean depends on the coupling of sea ice and ocean velocities (e.g., through the use of $\boldsymbol{u}_{rel}$ in eq. 1.2).

At steady state, the ocean surface velocity relative to an underlying "far field" geostrophic velocity ($\boldsymbol{u}_g$) is often described by the one-dimensional balance:

$$f\hat{\boldsymbol{k}} \times \left(\boldsymbol{u} - \boldsymbol{u}_g\right) = \frac{1}{\rho_0}\frac{\partial \boldsymbol{\tau}}{\partial z}, \tag{1.7}$$

where f is the Coriolis parameter and $\hat{\boldsymbol{k}}$ the vertical unit vector. The classic Ekman-spiral solution (*Ekman*, 1905) is then obtained by solving eq. (1.7) with boundary conditions $\boldsymbol{\tau}(0) = \boldsymbol{\tau}_s$ (see section 1.2.1) and $\lim_{z\to-\infty} \boldsymbol{\tau} = 0$, and using a turbulent closure model of the form $\boldsymbol{\tau}(z) = \rho_0 K \frac{\partial \boldsymbol{u}}{\partial z}$ assuming a constant eddy viscosity, K. The solution features a surface velocity that is directed at an angle that is 45° to the right of the surface stress direction, a velocity structure that spirals and decays with depth, and an integrated transport ($\boldsymbol{M}_E = \int \left[\boldsymbol{u} - \boldsymbol{u}_g\right] dz$) directed 90° to the right of the surface stress. However, *Ekman* (1906, as cited in *Ekman*, 1928) recognized that observations where better described using a vertically-varying K that is reduced in a shallow "skin-layer" near the surface. *Ekman* (1928) showed that this can result in significant modification of the spiral, with additional velocity turning within the skin-layer so that the deflection angle of the surface velocity can be much less than 45° (though, within the skin layer there is minimal turning or variation of the actual stress, $\boldsymbol{\tau}$).

A profile resembling this "modified Ekman spiral" was observed under drifting sea ice by *Hunkins* (1966). Since then, descriptions of the vertical structure of the ocean boundary layer under sea ice have been the subject of a wide number of works (e.g., *McPhee and Smith*, 1976; *McPhee*, 1982; *Mcphee*, 1994; *McPhee*, 2012, and others), and which are summarized in *McPhee* (2008). Generally, these describe the IOBL using some version of Rossby Similarity Theory (RST; e.g., *Rossby and Montgomery*, 1935; *Blackadar and Tennekes*, 1968), which is an asymptotic matching of an "inner boundary layer", and an "outer boundary layer" (fig. 1.2; where the outer layer is described by eq. 1.7). This method is analogous to that by *Ekman* (1906, 1928), with the strongly sheared inner boundary layer being equivalent to what *Ekman* (1928) described as the skin-layer. *McPhee* (2008, and others) builds upon this by using mixing-length theory to describe the variations of K under different buoyancy flux conditions.

Under neutral conditions (when the surface buoyancy flux $\mathcal{B} \equiv \langle w'b' \rangle|_{z=z_0} = 0$), the inner boundary layer is roughly described by the "law-of-the-wall", where the eddy viscosity varies linearly with the distance from the boundary: $K = \kappa z \|\boldsymbol{u}_*\|$, with κ the von Kármán constant ($\kappa = 0.41$). In the outer boundary layer, K is constant, and the layer is consistent with classical (*Ekman*, 1905) theory. On the basis of dimensional analysis and similarity scaling, *McPhee* (2008) shows that in the outer layer $K = K_* \|\boldsymbol{u}_*\|^2 f^{-1}$, for K_* a non-dimensional eddy viscosity that he suggests should be constant. This implies that the the full boundary layer has a depth $\|\boldsymbol{u}_*\| f^{-1}$ (*McPhee*, 2008), and that the depth of the surface/inner layer $z_{sl} = (K_* \kappa^{-1})(\|\boldsymbol{u}_*\| f^{-1})$.The ratio $K_* \kappa^{-1}$ is ~ 0.05 (*Shaw et al.*, 2008), so the inner boundary layer is roughly 5% of the total boundary layer depth. Note that the classical Ekman layer solution (*Ekman*, 1905) is described as having an "Ekman depth" of $\delta_{Ek} = \sqrt{2Kf^{-1}}$, which is the *e*-folding scale of the vertical velocity decay. Substituting McPhee's outer-layer K gives $\delta_{Ek} = \sqrt{2K_*}(\|\boldsymbol{u}_*\| f^{-1})$. So the boundary layer

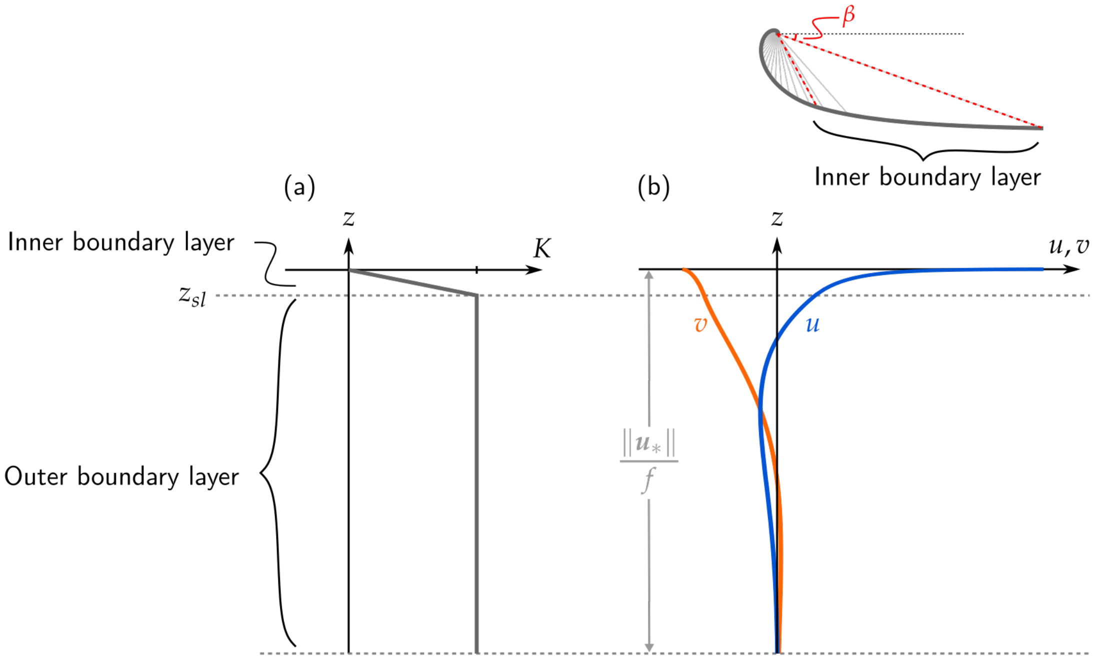

Figure 1.2: Schematic of the Rossby Similarity Theory description of the IOBL for neutral conditions, as described by *McPhee* (2008): (a) vertical profile of eddy viscosity, and (b) vertical profiles of velocity components relative to the geostrophic velocity (bottom), and associated hodograph (top).

depth $\|\boldsymbol{u}_*\| f^{-1}$ is not equivalent to the e-folding scale, and differs by a factor $\sqrt{2K_*} \sim 0.25$. As the language used to describe these surface layers is the same, this subtlety can be easily missed.

Asymptotic matching across the inner and outer regions produces an equation for the non-dimensional geostrophic ice-ocean relative velocity, Γ (*McPhee*, 2008):

$$\Gamma = \frac{1}{\kappa} \left[\ln\left(\mathrm{Ro}_*\right) - (A + iB) \right], \tag{1.8}$$

where Ro_* is the surface friction Rossby number, and A and B are similarity constants. Γ is the ice velocity, $\boldsymbol{u}_i$, relative to the geostrophic ocean velocity, $\boldsymbol{u}_g$, normalized by the friction velocity ($[\boldsymbol{u}_i - \boldsymbol{u}_g]\boldsymbol{u}_*^{-1}$), and expressed in complex notation (i.e., velocities $\boldsymbol{u} = u, v$ are written as $u + iv$). The surface friction Rossby number is defined in terms of the friction velocity and surface roughness length: $\mathrm{Ro}_* = \|\boldsymbol{u}_*\|(fz_0)^{-1}$. The similarity constants A, B

are found empirically, and the sign of B switches in the southern hemisphere (across a number of studies, empirical estimates of A and B are both ~ 2). In non-neutral conditions (stabilizing or destabilizing buoyancy flux $\mathcal{B} \neq 0$), the classic RST is combined with Monin-Obukhov similarity theory (*Monin and Obukhov*, 1954) and the similarity constants A, B are replaced with empirically derived functions of buoyancy flux (*McPhee*, 1982).

Application and generalization

McPhee (2012, and others; see table 1 in *Lu et al.*, 2011) suggest that when calculating the ice-ocean stress (with eq. 1.2) the geostrophic velocity should be used for the ocean reference velocity used for defining $\boldsymbol{u}_{rel}$. Then, RST gives that the ice-ocean drag coefficient $C_{io} = |\Gamma|^{-2}$. In this framework it is necessary to include a "turning angle", β (fig. 1.2b), to account for unresolved Ekman turning in the boundary layer when predicting the ice-ocean stress: $\boldsymbol{\tau}_{io} = \rho_0 C_{io} e^{i\beta} \boldsymbol{u}_{rel} \|\boldsymbol{u}_{rel}\|$.

One challenge with RST is that the surface friction Rossby number in eq. (1.8), Ro_*, is a function of the friction velocity, so the ice-ocean drag coefficient C_{io} and turning angle β are both functions of velocity, thus the relationship between relative ice-ocean velocity and ice-ocean stress is no longer quadratic. *McPhee* (1979, 2012) instead suggest an alternate power-law relationship: $\|\boldsymbol{\tau}_{io}\| \propto \|\boldsymbol{u}_{rel}\|^n$ where $n \neq 2$ and is found empirically (though that relation isn't derived from RST).

Park and Stewart (2016) present an alternative approach for RST with the goal of extending the theory for mixed ice and open-water conditions. Instead of using the geostrophic velocity as the ocean reference velocity in applying the quadratic drag law, they use the velocity at the interface between the inner and outer boundary layer (i.e., at z_{sl}). This velocity is found by applying classical Ekman theory (e.g., eq. 1.7) within the outer boundary. Then the quadratic drag law explicitly describes only the inner "law-of-the-wall" boundary layer. This has the advantage that (to a good approximation) it is not necessary to include a turning angle β in the quadratic drag law (a turning angle between the sea ice and the geostrophic velocity can be determined analytically), and that C_{io} is independent of sea ice velocity and that solutions are more analytically tractable.

Limitations

While RST forms the basis for much of the modern understanding of the IOBL, a number of limitations exist, providing questions about ice-ocean momentum transfer which have been the subject of a variety of further studies.

Aside from the inclusion of non-neutral conditions ($\mathcal{B} \neq 0$), RST neglects the influence of stratification. In open ocean conditions with near-surface constant stratification, N, *Pollard et al.* (1973) suggested that an Ekman-like boundary layer develops to a depth of $\|\boldsymbol{u}_*\|(Nf)^{-1/2}$. As an Ekman-like layer describes the dynamics of the outer boundary layer in RST, this implies a modification to the RST from the effects of stratification (note the similarity of the form the boundary layer depth from *Pollard et al.* 1973 to the RST form, $\|\boldsymbol{u}_*\| f^{-1}$). Furthermore, in homogeneous surface mixed layers, Ekman spirals can be constrained by the mixed-layer depth (*Price et al.*, 1987; *Schudlich and Price*, 1998). Under sea ice, *Randelhoff et al.* (2014) shows that this effect leads to an increase in the effective turning angle, β from RST (also see *McPhee*, 2012). Building on RST, an iterative numerical method, the local turbulence closure (LTC) model (*McPhee*, 1999; *McPhee et al.*, 1999), has been used to describe the IOBL while accounting for shallow stratification (e.g., *McPhee et al.*, 1999; *McPhee*, 2002; *Shaw et al.*, 2008; *Gallaher*, 2019).

An additional challenge of RST is the scaling up of in situ point measurements of Reynold's stresses (and derived drag coefficients) to floe-scale or regional-scale representative values remains an open problem (*McPhee*, 2002). Discrete roughness elements (i.e., sea ice keels) are represented through an effective roughness length scale z_0 in Ro_*. However, it is not clear what the relationship is between sea ice geometry and roughness length, and there are order-of-magnitude differences across inferred roughness lengths from *in situ* measurements (e.g., *McPhee*, 1990; *Cole et al.*, 2017). Moreover, it unlikely that the assumptions built into the development of RST hold when roughness elements extend many times the depth of the inner boundary layer: keels can extend ≥ 20 m (e.g., *Wadhams and Toberg*, 2012), while the inner boundary layer is typically reported being only a few meters thick (*Cole et al.*, 2017). In a numerical model, *Skyllingstad* (2003) showed that wake turbulence from ice keels produces spatially heterogeneous boundary layer structures (with a strong impact on the variability of ice-ocean heat fluxes). *In situ* turbulence measurements made downstream of ice keels show that the keels have a significant influence on locally measured turbulent dissipation and ice-ocean momentum flux (*McPhee*, 2002; *Fer and Sundfjord*, 2007; *Shaw et al.*, 2008; *Randelhoff et al.*, 2014).

The motion of sea ice integrates the effects of spatial heterogeneity in the IOBL across the ice floes. In order to predict that motion, methods for calculating ice-ocean momentum flux in sea ice models must represent appropriate floe-scale averages (i.e., through appropriate values of C_{io}). Force-balance approaches of determining the ice-ocean stress or ice-ocean drag coefficients (*McPhee*, 1980; *Randelhoff et al.*, 2014; *Kim et al.*, 2017; *Dewey*, 2019; *Heorton et al.*, 2019) implicitly account for the integrating effects of the sea ice and represent floe- or region-averaged results. *Randelhoff et al.* (2014) explicitly compared values of $\boldsymbol{\tau}_{io}$ determined using both the force-balance approach and direct turbulent measurements from a ~1-week ice drift. Their results showed that $\boldsymbol{\tau}_{io}$ found with the force-balance approach was roughly 3× greater than the direct point measurements at the same time and place. Similarly, using data from *Cole et al.* (2017) in a force-balanced based optimization procedure, *Heorton et al.* (2019) predicted ice-ocean drag coefficients greater than those found using direct turbulent measurements in the original study. These results suggest either (a) a systematic error in the force balance approach; or (b) that point measurements of turbulence are not representative of floe-integrated results. While the former option cannot be ruled out, the previously observed sensitivity of turbulent measurements to the presence of ice keel wakes suggests the latter option is a major factor.

That IOBL heterogeneity due to sea ice keels plays such a strong role in controlling the net ice-ocean momentum flux adds additional challenges for the use of RST. The RST framework assumes that stress input is a boundary condition at the surface (specifically at $z = z_0$), and then characterizes the flow structure in a shallow layer immediately below that. In contrast, wake effects from sea ice keels would require that the stress input occurs throughout a layer whose thickness is comparable to the keel depth. Without some prescription of vertical structure of stress input over that layer, it is unlikely that RST descriptions of the IOBL could be accurate except in the absence of ice keels. That RST has fit some past observations may be a function of the logistical challenges associated with making under-ice turbulent measurements, which are typically done in relatively level ice, away from keels. Indeed, in the presence of notably ice topography, RST does not fit measured profiles and the LTC model (which iteratively adjusts turbulent diffusivity profiles to fit observed stress values) or other semi-empirical approaches have been used instead to interpret observations (*McPhee*, 2002).

1.2.4 Free-drift sea ice dynamics

Sea ice is considered to be in free drift if internal stress terms are negligible. At steady state and ignoring Coriolis and sea surface tilt terms, the free-drift sea ice momentum equation reduces to a balance between the atmosphere-ice stress and the ice-ocean stress: $\boldsymbol{\tau}_{ai} \sim \boldsymbol{\tau}_{io}$ (e.g., *Steele et al.*, 1997, who also show that Coriolis and tilt terms are often small). This balance suggests a direct transfer of momentum from the atmosphere to the ocean.

Identifying free drift conditions in observations is challenging, and has been based on "rule-of-thumb" approaches. It has been suggested that sea ice will be in free drift if the ice concentration is sufficiently low (e.g., $\leq 85\%$ *Hunke and Dukowicz*, 2003; *Heorton et al.*, 2019), or if the wind factor (which is the ratio of ice speed to wind speed: $\|\boldsymbol{u}_i(\boldsymbol{u}_a^{-1})\|$) is sufficiently high (e.g., $\geq 2\%$ *McPhee*, 1980). The wind factor has previously been found to be a good indicator for atmosphere-ice-ocean momentum transfer (*Lepparanta and Omstedt*, 1990; *Martini et al.*, 2014; *Dosser and Rainville*, 2016).

Employing the quadratic drag law (eq. 1.2), and ignoring ocean velocity, the stress balance $\boldsymbol{\tau}_{ai} \sim \boldsymbol{\tau}_{io}$ can be rearranged to express the wind factor as a function of atmosphere-ice and ice-ocean drag coefficients, i.e., the Nansen number, Na (e.g., *Weiss and Marsan*, 2004, chapter 2):

$$\frac{\|\boldsymbol{u}_i\|}{\|\boldsymbol{u}_a\|} \sim \mathrm{Na} \quad \text{for} \quad \mathrm{Na} \equiv \sqrt{\frac{\rho_a C_{ai}}{\rho_o C_{io}}}. \tag{1.9}$$

Using typical values ($\rho_a \sim 1.3\,\mathrm{kg\,m^{-3}}$, $\rho_o \sim 1025\,\mathrm{kg\,m^{-3}}$, $C_{ai} \sim 1.5 \times 10^{-3}$, and $C_{io} \sim 5.5 \times 10^{-3}$), Na $\sim 1.85\%$, which is roughly consistent with the "2%-rule" for the wind factor of sea ice in free drift, despite the excluded terms. Observed seasonal and inter-annual variations in the wind factor (*Maeda et al.*, 2020) suggest trends in drag coefficient values and total atmosphere-ocean momentum coupling.

1.2.5 Mixed-layer models

In much of the Arctic Ocean, a fairly homogeneous (weakly stratified) fresh surface mixed layer overlies a strong halocline stratification (*Peralta-Ferriz and Woodgate*, 2015). Surface momentum flux drives currents and mixing within the surface mixed layer, which acts as the dynamical link between the surface and the ocean interior. Because of the strongly coupled nature of atmosphere-sea ice-ocean momentum transfer (section 1.2.1), mixed-layer dynamics have a strong impact for sea ice-ocean feedback processes.

Vertical 1D models are frequently used to investigate the ocean mixed layer evolution in response to wind forcing. A number of these models have been employed in the Arctic (e.g., *Lemke and Manley*, 1984; *Toole et al.*, 2010; *Davis et al.*, 2016; *Dewey et al.*, 2017; *Smith et al.*, 2018), typically for the purpose of evaluating ice-ocean heat flux and shear-driven mixing. While a range of model complexities are possible, wind-forced 1D models typical solve some version of the unsteady form of eq. (1.7) (i.e., the horizontal equations of motion, ignoring advective terms and lateral gradients):

$$\frac{\partial \boldsymbol{u}}{\partial t} + f\hat{\boldsymbol{k}} \times \boldsymbol{u} = \frac{1}{\rho_0}\frac{\partial \boldsymbol{\tau}}{\partial z} \tag{1.10}$$

usually accompanied by equivalent vertical evolution equations for temperature and salinity. Different modelling frameworks for eq. (1.10) represent a range of complexities and approaches through their treatment of turbulent fluxes ($\boldsymbol{\tau}$ for momentum, and $\langle w'T' \rangle$, $\langle w'S' \rangle$, for heat and salt). One class of vertical 1D models are *bulk mixed-layer models* which assume that momentum is homogenized within the mixed layer. These include the Price-Weller-Pinkel (PWP; *Price et al.*, 1986) model and linearly-damped slab-ocean model (e.g. *Pollard and Millard*, 1970; *D'Asaro*, 1985). Relative to other turbulence closure schemes (i.e., the range of eddy-viscosity models), bulk models are simpler and may be much less realistic or unable to simulate some of the relevant physical processes (e.g., the damped slab model does not simulate entrainment or mixing at the based of the mixed-layer). Nonetheless, they provide useful tools for understanding certain physical processes.

While the 1D description may be appropriate to describe mixed-layer dynamics in much of the Arctic, strong horizontal gradients at the ice edge may lead to other dynamic processes. In particular, changes in air temperature and surface roughness across the ice edge are thought to cause local atmospheric variations (*Heorton et al.*, 2014; *Guest et al.*, 2018), and convergent ocean flow (leading to localized ice-edge upwelling; e.g., *Niebauer*, 1982; *Fennel and Johannessen*, 1998). Additionally, strong ice-edge located freshwater fronts (*Wulff et al.*, 2016) may lead to the generation of baroclinic instabilities (*Lu et al.*, 2015; *Manucharyan and Thompson*, 2017). However, it is challenging to make observations of those systems.

1.3 Outline

1.3.1 Scientific objectives

The overriding objective of this thesis work is to advance our understanding of momentum transfer across the atmosphere-sea ice-ocean system. In particular, I will seek to better understand how sea ice impacts the total input stress ($\boldsymbol{\tau}_{ocn}$) at the ocean surface and address two key scientific questions:

Question #1 How do sea ice properties, such as concentration and ice bottom morphology, impact the transfer of momentum from the sea ice to the ocean ($\boldsymbol{\tau}_{io}$), and how well represented are these processes in models?

Question #2 How are upper ocean dynamics impacted by the total atmosphere-ice-ocean momentum transfer ($\boldsymbol{\tau}_{ocn}$), and what role does sea ice have in imparting/dissipating momentum and energy in the surface layer.

In tackling these questions, emphasis must be placed on the effects of the shift to a thinner, seasonal ice cover which is now a significant feature of the Arctic sea ice system. While these questions are motivated by potential feedback processes in the Western Arctic, the physical processes are relevant to all sea ice-covered polar regions.

1.3.2 *Organization*

The remainder of this thesis is organized into two parts. Part I provides a methodological overview of the processing and novel uses of moored Acoustic Doppler Current Profiler (ADCP) measurements taken during the SODA campaign. Part II makes use of the measurements described in part I in concert with other measurements from the MIZ program to provide insight into the two scientific questions posed above. Part I is presented in two chapters:

- Chapter 2 describes the procedures used to process the ADCP measurements on the SODA moorings, with a focus on (1) creating merged velocity profiles from multiple instruments; and (2) extracting data from altimeter distance measurements.
- Chapter 3 demonstrates that ADCPs installed on subsurface moorings are capable of inferring otherwise unresolved details about the surface mixed layer. This chapter has been submitted to the *Journal of Atmospheric and Oceanic Technology* as:

> Brenner, S., J. Thomson, L. Rainville, D. Torres, M. Doble, J. Wilkinson, and C. Lee, Acoustic sensing of ocean mixed layer depth and temperature from uplooking ADCPs

Part II includes three chapters that describe different aspects of atmosphere-ice-ocean momentum transfer and upper ocean dynamics:

- Chapter 4 addresses ***Question #1*** by considering variations in the ice-ocean drag coefficient as they compare to ice-geometry based parameterizations. This chapter is reproduced from:

  > Brenner, S., L. Rainville, J. Thomson, S. Cole, and C. Lee, Comparing Observations and Parameterizations of Ice-Ocean Drag Through an Annual Cycle Across the Beaufort Sea, *J. Geophys. Res. Oceans*, 126(4), 29, doi:10.1029/2020JC016977, 2021.

- Chapter 5 addresses ***Question #2*** by interpreting upper ocean observations using a simplified, one-dimensional, ice-ocean coupled model. This chapter has been submitted to the *Journal of Physical Oceanography* as:

  > Brenner, S., L. Rainville, J. Thomson, L. Crews, and C. Lee, Wind-driven motions of the ocean surface mixed layer in the Western Arctic

- Chapter 6 builds on ***Question #2*** to consider lateral processes. This chapter presents novel observations of an ice-edge localized front, and shows frontal evolution in response to wind stress over a short timescale. This chapter is reproduced from:

  > Brenner, S., L. Rainville, J. Thomson, and C. Lee, The evolution of a shallow front in the Arctic marginal ice zone, *Elem. Sci. Anth.*, 8(17), 17, doi:10.1525/elementa.413, 2020.

Finally, chapter 7 summarizes the major conclusions of this study and provides a prospective of possible future research directions.

Part I

Chapter 2

PROCESSING AND COMBINING ADCP RECORDS FROM THE SODA MOORINGS

2.1 *Introduction*

A major component of the Office of Naval Research (ONR) Stratified Ocean Dynamics of the Arctic (SODA) research program (*Lee et al.*, 2016) was the installation of a series of three heavily instrumented moorings across a north-south range that is aligned along the axis of the Canada Basin (fig. 2.1a). The goal of the moorings was to provide high temporal resolution measurements of sea ice and upper ocean velocities, sea ice geometry, surface gravity waves, and upper ocean temperature and salinity. By measuring at fixed locations in the basin, the moorings can sample across a wide range of different sea ice conditions (e.g., fig. 2.1b) as well as measuring different parts of the larger Beaufort Gyre circulation (e.g., fig. 2.1c), so that these measurement complement those made by drifting platforms.

Chapters 3 to 5 of this thesis make extensive use of measurements from Acoustic Dooper Current Profilers (ADCPs) installed on each of the moorings (section 2.2). However, creating usable data products from these measurements has been non-trivial. This chapter describes the procedures used to process the ADCP measurements on the SODA moorings, with a particular focus on (1) creating merged velocity profiles from multiple instruments in order to provide a continuous velocity record of the upper ~80 m of the ocean (section 2.3); and (2) extracting useful data from altimeter distance measurements, including classification of measurements as either sea ice or open water (section 2.4).

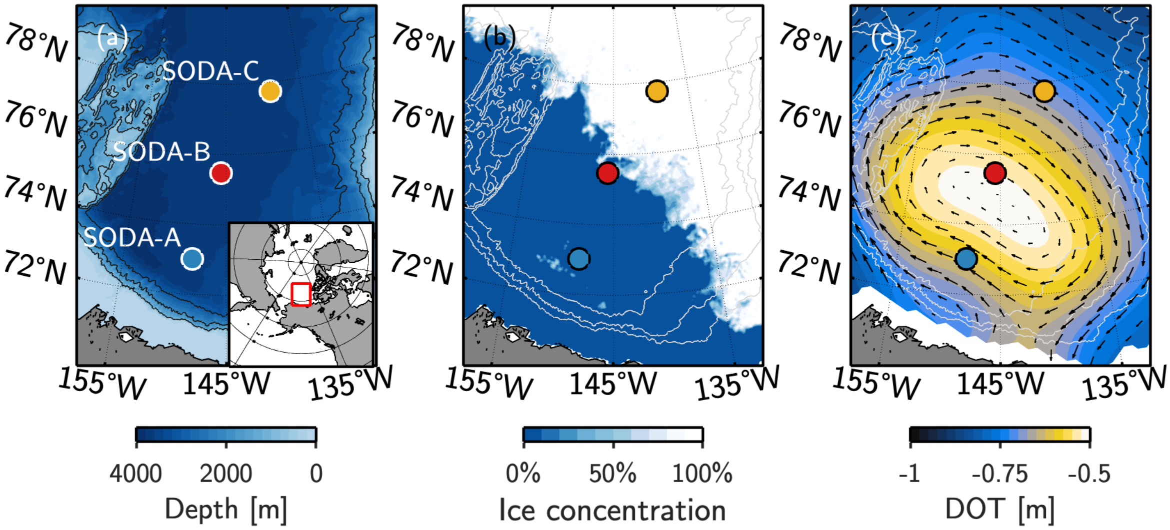

Figure 2.1: Maps showing the locations of the moorings in the context of (a) the bathymetry of the Beaufort Sea (with the inset showing the map location); (b) the sea ice concentration from September 18, 2018 (the 2018 sea ice minimum); and (c) the smoothed Dynamic Ocean Topography (DOT; colour) and corresponding geostrophic velocity (black arrows) showing the gyre circulation averaged over the mooring deployment period (Sept. 2018–Oct. 2019). Dark grey contours in (a) and light grey contours in (b,c) show 1000-m isobaths. Sea ice concentration in (b) is from the Sea Ice Remote Sensing database at the University of Bremen (*Spreen et al.*, 2008). Arctic dynamic topography and geostrophic currents data in (c) were provided by the Centre for Polar Observation and Modelling, University College London (`www.cpom.ucl.ac.uk/dynamic_topography`; *Armitage et al.*, 2016, 2017, extended to full CryoSat-2 time period).

2.2 *Mooring descriptions*

Each of the moorings included three separate ADCPs installed at different depths and configurations (fig. 2.2). This chapter primarily focuses on measurements made by the two upward looking ADCPs on each mooring: a Nortek Signature-500 (hereafter SIG500) 5-beam ADCP on the topmost subsurface float (at depths 27–45 m depending on mooring), and a Teledyne Workhorse-300 (hereafter WH300) ADCP on a second float roughly 45 m deeper than the SIG500s. A downlooking Teledyne Longranger ADCP was installed

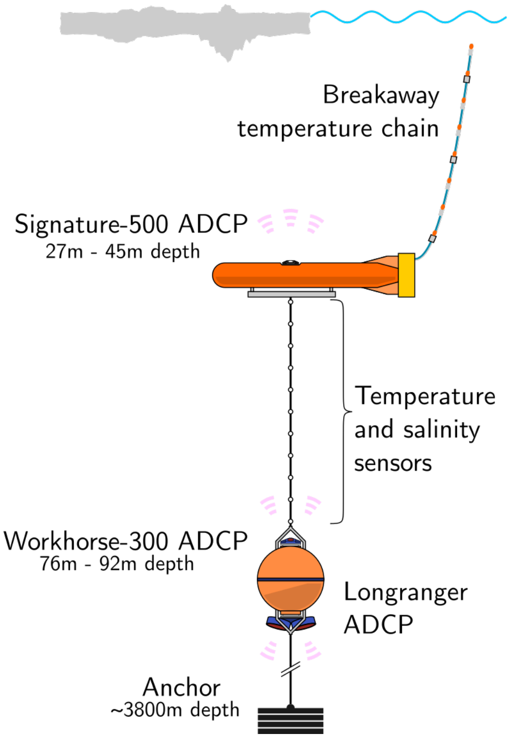

Figure 2.2: Schematic of mooring instrument configuration.

on the same floats as the WH300. Together, the SIG500 and WH300 ADCPs provide a velocity record of the top ∼80 m of the water column at each mooring; the Longrangers extend this record to a depth of ∼400 m.

In addition to traditional velocity measurements, the vertical beam on the SIG500s allowed for simultaneous altimeter measurements, which can be used to measure sea ice geometry or surface gravity waves. The SIG500 ADCPs were programmed to collect data in a concurrent sampling scheme using two separate plans:

1. *Average with ice drift and ice draft (keel)*: 60 s long ensembles were collected every 10 min. During the ensemble, the sampling frequency was 1 Hz. Individual samples were quality controlled (similar to procedures from *Gordon*, 2015), and ensemble-averaged to generate 10 min resolution data. This mode provided standard ADCP current measurements in 2 m bins, ice drift, and altimeter distance.

2. *Waves height and direction*: Ensembles are collected every 2 h, each containing 2048 sample points at a frequency of 2 Hz (so the ensemble duration is approximately 17 min). This mode provided both high temporal resolution altimeter measurements and standard ADCP current measurements in 1.8 m bins.

For both sampling plans, the ADCPs operated in narrowband mode to increase performance in a low-scattering environment.

The WH300s measured velocity in 4 m bins with a temporal resolution of 2 min. Even after quality control of the raw data (filtering of low echo intensity and low correlation data), there was some conspicuous banding in the WH300 ADCPs velocity timeseries, with some bins having relatively slower velocities than adjacent bins. The banding was due to acoustic returns that were reflecting from other mooring components (notably the Stablemoor floats) which are stationary relative to the WH300s. The reflections have high echo intensity and correlation, and were thus not filtered out based on those quality metrics. The erroneous data are evident in profiles of the annual-averaged error velocity: $\langle u_{error} \rangle$ (fig. 2.3); however, the individual ping error velocities proved insufficient in filtering out these data. Instead all WH300 data in bins which have a magnitude of $|\langle u_{error} \rangle| > 1.5 \times 10^{-3}\,\mathrm{m\,s^{-1}}$ were discarded.

The downlooking Longranger ADCPs measured velocity in 8 m bins with a temporal resolution of 10 min. These data are not analysed here, but cursory investigation showed significant noise within the data, and a number of horizontal and vertical bands. Nonetheless, some features are still evident.

In addition to the ADCPs, the moorings also hosted a number of temperature and salinity sensors, including shallow "breakaway" temperature chains extending from the top float of each mooring, and a set of Seabird SBE-37 ("MicroCAT") conductivity, temperature, depth (CTD) and SBE-56 temperature sensors at roughly 5 m spacing in the ∼45 m distance between the SIG500s and WH300s (see fig. 2.2 and chapter 3). The topmost MicroCAT CTD sensor, immediately below the top float of each mooring, was

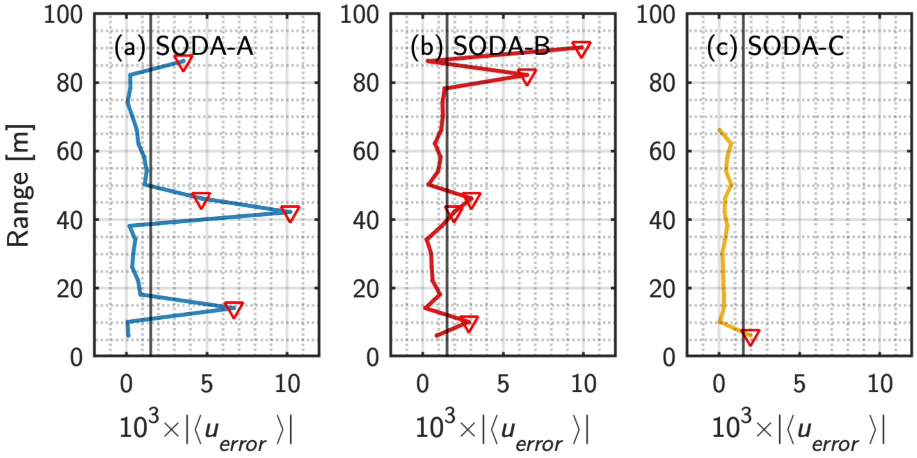

Figure 2.3: Magnitudes of the annual-averaged error velocity, $|\langle u_{error} \rangle|$, for each of the three moorings (panels a–c, as labelled). The vertical black lines in each panel identify the $1.5 \times 10^{-3}\,\mathrm{m\,s^{-1}}$ threshold for discarding data bins. Red triangles show bins in which this threshold is exceeded.

used to help calibrate measurements from SIG500s (section 2.4).

2.3 *Combining velocity profiles*

The SIG500s and WH300s recorded velocity from near the ocean surface to a depth of ∼70–85 m (depending on mooring). This sections describes how those separate records were combined into a continuos velocity profile timeseries for each mooring.

2.3.1 *Compass calibration*

One challenge in merging the two velocity records on each mooring is that pre-cruise calibrations of the internal magnetic compasses of the WH300s were not performed together with the SIG500s, so each instrument type has a separate compass offset, impacting the reported instrument headings.

Heading measurements are used to rotate the velocity vectors from an instrument-centred coordinate system (“xyz”) to an Earth coordinate system (“ENU”). After accounting for roll and pitch (which can be done separately), the transformation to convert from xyz to ENU coordinates is:

$$\boldsymbol{u}_{ENU} = \begin{bmatrix} \cos(\phi) & \sin(\phi) & 0 \\ -\sin(\phi) & \cos(\phi) & 0 \\ 0 & 0 & 1 \end{bmatrix} \boldsymbol{u}_{xyz}, \tag{2.1}$$

where ϕ is the instrument heading. Discrepancies in ϕ from separate compass calibrations between the two instruments will lead to artificial (rotational) shear in the combined velocity profiles.

For both ADCPs, the instrument heading is calculated internally from magnetometer measurements. These measurements, $\boldsymbol{M}$, are a three-component vector. The instrument heading is calculated from the horizontal projection of of that vector: $\boldsymbol{M}_H = (M_{xH}, M_{yH})$, which forms a circle as the instrument spins and samples the magnetic field (e.g., fig. 2.4a). The instrument heading is $\phi = \angle \boldsymbol{M}_H = \text{atan2}(M_{yH}, M_{xH})$, where atan2 is the quadrant-preserving arctangent function.

An uncalibrated compass results in the an offset of the centre of the $\boldsymbol{M}_H$ circle. In that case, the reported compass heading on the instrument is $\phi_r = \text{atan2}(M_{yr}, M_{xr})$ where $\boldsymbol{M}_r$ is the horizontal projection of the recorded, stored magnetometer data, while the true (corrected) compass heading should be $\phi_c = \text{atan2}(M_{yc}, M_{xc})$ and $\boldsymbol{M}_r = \boldsymbol{M}_c + \boldsymbol{M}_o$ for constant offset vector $\boldsymbol{M}_o$. This leads to a heading correction angle $\mathcal{E} = \phi_c - \phi_r$, which varies as a function of the recorded heading (fig. 2.4b).

Post-deployment compass calibration of SIG500 ADCPs

The SIG500s store raw three-component magnetometer data, enabling post-deployment recalibration/reprocessing based on the in situ magnetic field (e.g., *Gordon*, 2015). The horizontal projection of the recorded magnetometer data is (Dan Torres, personal commu-

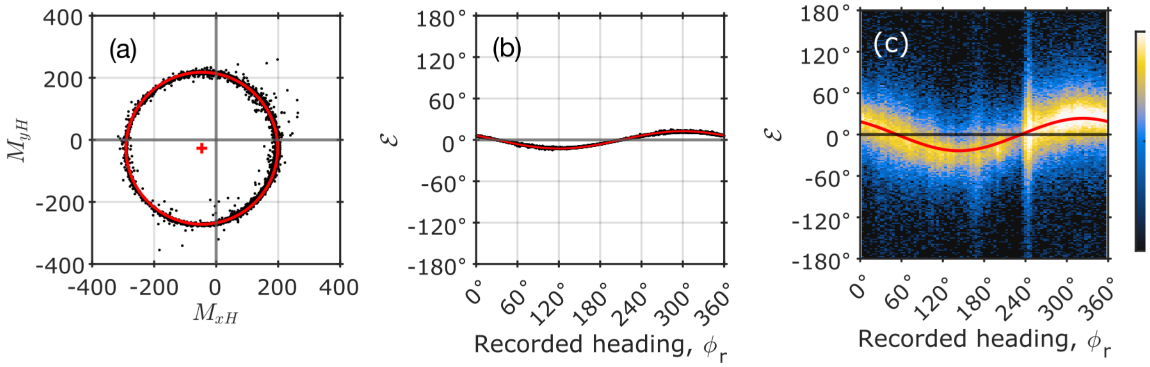

Figure 2.4: Example of compass calibration fitting from the SODA-B mooring: (a) Projected SIG500 magnetometer data $\boldsymbol{M}_r$ (black points), with fitted circle (red) showing the offset $\boldsymbol{M}_o$ (red cross); (b) heading correction $\mathcal{E}$ as a function of recorded heading ϕ_r associated with panel a (black points), and curve from eq. (2.4) calculated with the fitted $\boldsymbol{M}_o$ (red line); and (c) two-dimensional histogram ("bin-scatter") showing the density of $\mathcal{E}$ as a function of recorded heading ϕ_r in 4° × 4° bins for the WH300 based on velocity direction differences, with eq. (2.4) fit to those data (red line).

nication):

$$\begin{bmatrix} M_{xH} \\ M_{yH} \end{bmatrix} = \begin{bmatrix} \cos\theta & -\sin\theta\sin\psi & -\sin\theta\cos\psi \\ 0 & \cos\psi & -\sin\psi \end{bmatrix} \begin{bmatrix} M_x \\ M_y \\ M_z \end{bmatrix}, \tag{2.2}$$

where ψ and θ are, respectively, the roll and pitch of the instrument and all values are functions of time. Note that this is the same transformation as in *Menn et al.* (2014) except that the roll is defined with the opposite sign (possibly because of differences in instrument orientation definitions).

After horizontally projecting the SIG500 magnetometer data, offsets $\boldsymbol{M}_o^{\text{SIG500}}$ were found for each instrument by fitting circles to the ensemble-averaged magnetometer values $\boldsymbol{M}_r^{\text{SIG500}}$ from the "Average" sampling plan data (red cross and circle in fig. 2.4a). Those offsets were applied to raw sample data for all sampling modes to generate $\boldsymbol{M}_c^{\text{SIG500}}$. Corrected headings for the SIG500s were then found directly from the corrected magnetometer circles: $\phi_c^{\text{SIG500}} = \angle \boldsymbol{M}_c^{\text{SIG500}}$. This process resulted in corrections of up to approximately 15° from the reported heading values (e.g., fig. 2.4b). Note that for the SIG500s, it was not necessary to calculate $\mathcal{E}$ explicitly in order to make the correction.

Applying compass corrections to WH300 ADCPs

For WH300 ADCPs, the magnetometer data $\boldsymbol{M}$ is not stored, so the procedure above could not be directly applied. Instead the overlap in the sampling regions of the SIG500s and WH300s together with the corrected SIG500 compass headings allowed for fitting the correction function $\mathcal{E}$. The corrected WH300 headings are $\phi_c^{\text{WH300}} = \phi_r^{\text{WH300}} + \mathcal{E}$.

The SIG500s and WH300s were on separate floats on the moorings, and were able to rotate independently from each other. Differences between the corrected SIG500 headings and the uncorrected WH300 headings are thus a combination of both heading corrections and heading differences. That is, $\phi_c^{\text{SIG500}} - \phi_r^{\text{WH300}} = \mathcal{E} + \Delta\phi$, where $\Delta\phi$ corresponds to the physical offset in the headings of the two instruments (which varies in time and is unknown), so differences in their headings alone are not meaningful for calculating $\mathcal{E}$. However, headings measurements are used to rotate the velocity vectors from an instrument-centred coordinate system to an Earth coordinate system, and so the reported velocities from each instrument can be used to find $\mathcal{E}$. This is most easily seen by considering only the horizontal components of the velocities ("xy" and "EN"), and expressing them in complex notation ($\boldsymbol{u} = u + iv$); then the coordinate transformation (eq. 2.1) is $\boldsymbol{u}_{EN} = \boldsymbol{u}_{xy}e^{-i\phi}$. If the instrument-coordinate velocity $\boldsymbol{u}_{xy} = Ue^{i\alpha}$, then $\boldsymbol{u}_{EN} = Ue^{i(\alpha-\phi)}$ and the flow direction $\angle\boldsymbol{u}_{EN} = \alpha - \phi$. Differences in the measured direction of flow in the Earth-centred coordinate system between a corrected and uncorrected instrument correspond to the heading correction: $\angle\boldsymbol{u}_{EN}^{c} - \angle\boldsymbol{u}_{EN}^{r} = (\alpha - \phi_c) - (\alpha - \phi_r) = -\mathcal{E}$. Ideally, the corrected flow directions, $\angle\boldsymbol{u}_{EN}^{c}$, reflect the true physical system irrespective the instrument that they are measured with, and independent of $\Delta\phi$ (in reality there is some measurement noise and uncertainty).

Having corrected the SIG500 compass headings, the Earth-coordinate $\boldsymbol{u}_{EN}^{\text{SIG500}}$ are taken as true. With that, overlapping sampling regions between the two instruments were used to calculate heading correction points $\mathcal{E} = \angle \boldsymbol{u}_{EN}^{\text{SIG500}} - \angle \boldsymbol{u}_{EN}^{\text{WH300}}$ (WH300 data were first temporally averaged and vertically interpolated to be on a consistent grid with the SIG500 data, and post-calibration SIG500 velocities were used). Measurement noise in the velocities from both instruments and errors due to the averaging/interpolation become imprinted on this calculation, so there is a high amount of scatter in the estimates of $\mathcal{E}$ (see fig. 2.4c). To reduce the effect of noise, any corrections calculated when there is a disagreement in the velocity magnitude between the two instruments of more than $0.25\,\mathrm{m\,s^{-1}}$ or when the velocity magnitude from either instrument is below $0.01\,\mathrm{m\,s^{-1}}$ were rejected.

In order to apply the heading correction non-overlapping data, the calculated $\mathcal{E}$ points were used to fit a curve of $\mathcal{E}$, and find heading corrections as a function of the reported heading, ϕ_r. To fit $\mathcal{E}$ to the measurements first requires writing it as a function only of ϕ_r and a set of constant fitting parameters. This can be done by expressing $\boldsymbol{M}_c$ in terms of $\boldsymbol{M}_r$, $\boldsymbol{M}_o$ ($\boldsymbol{M}_c = \boldsymbol{M}_r - \boldsymbol{M}_o$), with each of their component values rewritten in a polar coordinate system centred on the corrected magnetometer circle (e.g., $(M_{xo}, M_{yo}) \to (r_o, \phi_o)$). Thus, $M_{xc} = \mathcal{R}\cos\phi_r - r_o\cos\phi_o$ and $M_{xc} = \mathcal{R}\sin\phi_r - r_o\sin\phi_o$, where

$$\mathcal{R}^* = \frac{\mathcal{R}}{R} = r_o^* \cos(\phi_r - \phi_o) + \sqrt{1 - r_o^{*2}\sin^2(\phi_r - \phi_o)}, \tag{2.3}$$

with $r_o^* = r_o/R$ a constant, and R the radius of the circle defined by $\boldsymbol{M}_c$. Equation (2.3) is the polar coordinate representation for a circle that is not centred at the origin. Then,

$$\mathcal{E} = \operatorname{atan2}\left(\mathcal{R}^* \sin\phi_r - r_o^* \sin\phi_o, \mathcal{R}^* \cos\phi_r - r_o^* \cos\phi_o\right) - \phi_r, \tag{2.4}$$

which is a function of the measured ϕ_r, and constant fitting parameters r_o^*, ϕ_o. As the function atan2 is based on a ratio of the input values, the constant R has been factored out and cancelled.

Note that while $\mathcal{E}$ visually appears sinusoidal in figs. 2.4b and c, that is not strictly the case as seen by eqs. (2.3) and (2.4). However, following some algebraic manipulation, a

Taylor series expansion can be used to show that for small $\mathcal{E}$ (which occur for small r_o^*), the correction (expressed in radians) is

$$\mathcal{E} \sim r_o^* \sin(\phi_r - \phi_o), \tag{2.5}$$

which explains the similarity to a sinusoid. For these data, the approximation is likely sufficient for fitting r_o^*, ϕ_o, but the full expression for $\mathcal{E}$ (eq. 2.4) was used nonetheless.

Following calculation of $\mathcal{E}$ points from the overlapping velocity measurements, I used a least-squares method to fit eq. (2.4) and find the parameters r_o^*, ϕ_o (red line in fig. 2.4c). Corrected headings for the WH300s were then computed based on the reported headings and the heading correction curve: $\phi_c^{\text{WH300}} = \phi_r^{\text{WH300}} + \mathcal{E}$. This process resulted in corrections of up to approximately 25° from the reported heading values (e.g., fig. 2.4c). Note that with this procedure, it is not necessary to recover the magnetometer data $\boldsymbol{M}_c$ for the WH300s.

Applying compass corrections to Longranger ADCPs

As the Longranger data were not analysed in detail, compass corrections were not applied to the those ADCPs.

In theory, the approach described above for the WH300 ADCPs could be applied for the Longranger ADCPs; however, there is no overlap between the velocity profiles of the Longranger and those of the other instruments so finding offset values to fit the $\mathcal{E}$ curve could be difficult and may involve making assumptions about rotational shear in the flow. Instead, recognizing that on each of the moorings the Longrangers and WH300s were mounted together on the same float and could not rotate independently from each other, differences in the headings between the two instruments could be used to generate offsets that can be used to fit $\mathcal{E}$. That is, similar to above, $\phi_c^{\text{WH300}} - \phi_r^{\text{Longranger}} = \mathcal{E} + \Delta\phi$, where $\Delta\phi$ corresponds to the physical offset in the headings of the two instruments; however, here the offset $\Delta\phi$ is static and can be treated as an additional fitting parameter.

2.3.2 *Merging profiles*

Following compass calibration/correction, timeseries of horizontal velocity profiles combining both SIG500 and WH300 data were created. Data from both instruments were extracted in 1-h windows. Within each time window, outlier points were removed based on moving-mean criteria in 10 m vertical windows (outliers were identified as points with velocity more than 3 standard deviations from the mean in each window). For each window, remaining u and v velocity points and associated time-varying measurement depths were averaged in 2 m vertical bins. Because of mooring movement, the measurement cell depths on each ADCP varied slightly with time. The vertically bin-averaged u and v velocities were then interpolated to a set of constant 2 m depth bins using a smoothing spline with smoothing parameter 0.05. The shallowest depth bin was at a depth of 6 m, and the maximum corresponded to the annual median depth of WH300 at each mooring. The spline fit allows for some slight curvature in the velocity over the sections of the profiles that were discarded due to reflections from other mooring components (section 2.2), and also provided a consistent vertical shear scale throughout the profile despite differences in vertical bin sizes between the two instruments. Figure 2.5 provides an example of profile fit.

2.4 ***Altimeter data***

Altimeter distances from the vertical beam of the SIG500s are used for calculating ice draft/geometry and surface gravity wave statistics (e.g., *Magnell et al.*, 2010). The SIG500s report altimeter distances using two different edge detection algorithms designed for the separate acoustic return characteristics of the water-air and water-ice interfaces: the "acoustic surface tracking" (AST) algorithm is designed for the water-air interface, while the "leading edge" (LE) algorithm is designed for the water-ice interface (*Magnell et al.*, 2010). In practice, the LE algorithm produced poor data quality (significant noise, data dropouts, and unphysical values) so AST measurements were used for all conditions (ice

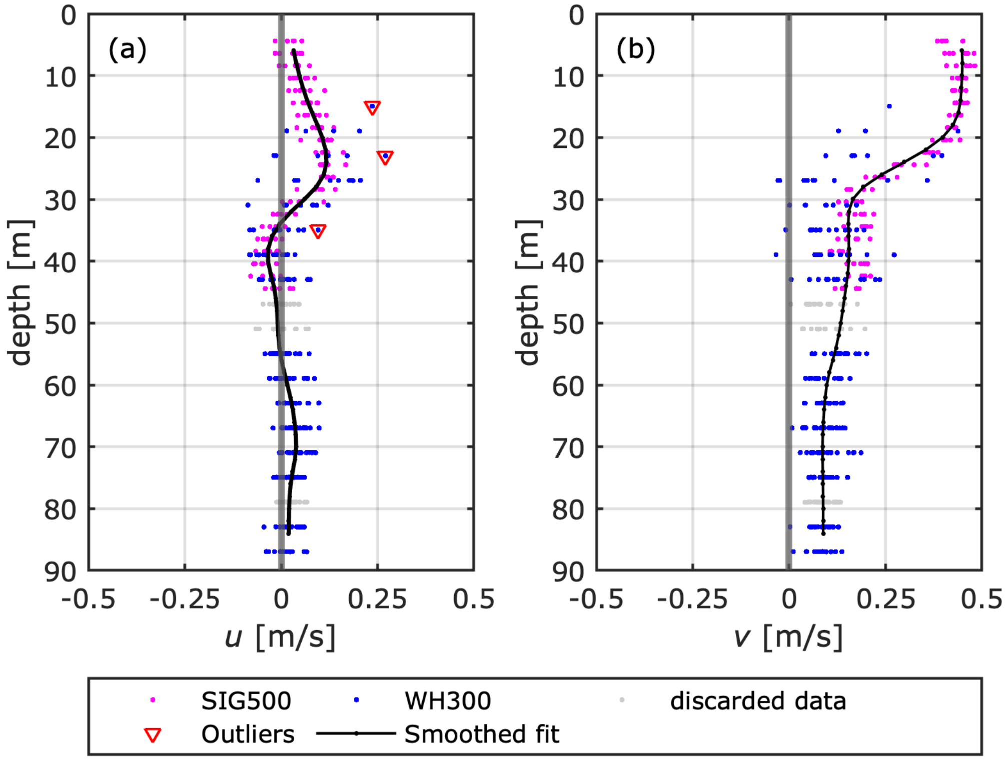

Figure 2.5: Example of merging SIG500 and WH300 velocity profiles for (a) the zonal velocity, u and (b) the meridional velocity, v. Points are coloured based on instrument, per the legend. The "discarded data" refer to velocities from depth-bins that were discarded due to reflections from other mooring components (section 2.2).

or open water).

2.4.1 *Distance corrections*

Altimeter distances reported by the SIG500 ADCPs need to be corrected for ADCP tilt and sound speed variations (e.g., *Krishfield et al.*, 2014; *Magnell et al.*, 2010).

The altimeter distances should be reported vertically from the instrument to the water/ice surface; however, they are actually recorded along the line-of-view of the instrument. While the instruments were nearly vertical facing throughout the deployment, the small tilt values experienced still have a non-zero effect on distances.

When determining altimeter distances, the ADCP is actually measuring acoustic signal time t_s, and converting that into distance using the speed of sound of seawater. The instruments calculate c_s based on measured water temperature and pressure, and an assumed (constant) salinity. As described below, differences between the recorded and actual water temperatures, and between the assumed and actual salinity measurements lead to differences in sound speed that impact the reported altimeter distances.

Combining the tilt and sound speed effects, the corrected altimeter distance, D_c can be written as:

$$D_c = [\cos\psi\cos\theta]\left[\frac{(c_s)_c}{(c_s)_r}\right] D_r, \tag{2.6}$$

where ψ and θ are the instrument roll and pitch; $(c_s)_r$ and $(c_s)_c$ are the raw and corrected speed of sound; and D_r are the raw altimeter distances. Corrections from instrument tilt, and from sound speed variations both give corrections of ~1%–2% of the raw distance, and thus differences of $\mathcal{O}(0.1\,\mathrm{m})$.

Temperature, salinity, and sound speed corrections

Comparisons between the instrument-reported water temperatures and those from the MicroCAT CTD installed directly beneath the float (a vertical offset of ~1 m) showed that the SIG500 temperatures were 0.5–1.75 °C higher than expected. Furthermore, this offset varied depending on the sampling mode active on the instrument (average or burst), suggesting that it may have been due to instrument-generated heat during sampling. To account for the temperature offset, regressions were determined between MicroCAT measured water temperatures (when those data were available) and those by the SIG500s, separately for each mooring and for each of the different sampling regimes (fig. 2.6). These regressions were then applied to create a corrected temperature record for the full SIG500 data record.

The sound speed is less sensitive to salinity than it is to temperature, so a fixed salinity value is generally appropriate provided that is roughly consistent with the in-situ

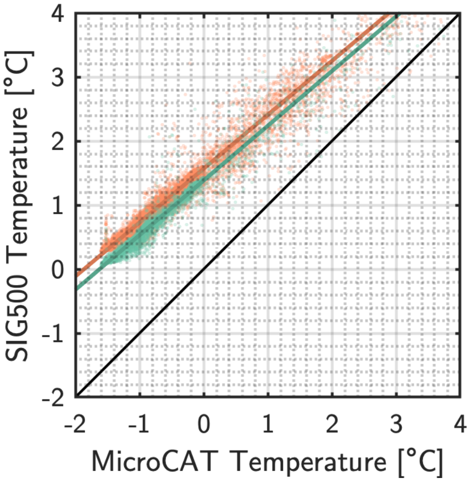

Figure 2.6: Example of regression between MicroCAT and SIG500 measured temperatures; points show individual measurements, and lines show corresponding linear fits. Different colours correspond to whether or not the burst measurement mode ("Waves height and direction") was concurrently running. The black line shows the one-to-one slope. Data are from SODA-A and are all from "Average with ice drift and draft" measurement mode.

salinity. When programming the ADCPs, the fixed salinity used for calculating sound speed was left as 35 psu, which is the default value in the deployment software. The actual salinity (measured by the MicroCAT) was ∼28–30 psu, so a salinity correction must also be applied to the sound speed calculation. This was done by interpolating the MicroCAT-measured salinity values to the SIG500 measurement timestamps when those data were available. Following failure of the uppermost MicroCAT, salinity measurements from deeper in the water column were extrapolated to the SIG550 depth; as sound speed only depends only weakly on salinity, the errors associated with this extrapolation are unimportant.

Following water temperature and salinity corrections, the corrected sound speed at the instrument, $(c_s)_c$, was calculated using functions provided in the Gibbs Seawater Oceanographic toolbox (*IOC et al.*, 2010).

2.4.2 *Burst classification*

Altimeter data from the the SIG500s' "Waves height and direction" (burst) mode can be used both for making measurements of surface gravity waves, and of sea ice geometry [including resolving individual keels and leads](*Magnell et al.*, 2010). However, in order to use those data, it is first necessary to determine whether each burst is measuring sea ice or open water.

Burst measurements from the altimeter were classified as being either sea ice or open water based primarily on spectral properties. One dimensional spectra of sea ice geometry are expected to be predominantly "red", with most of the energy contained lower wavenumber (or equivalently, lower frequencies as sampling occurs in time; see figs. 2.7a and b and *Rothrock and Thorndike*, 1980). In contrast, surface gravity waves have distinct and well known spectral shapes, with energy primarily contained in higher frequencies (figs. 2.7c and d). As such, bursts were classified as being either sea ice or open water based on a ratio of high and low spectral energy, following *Shcherbina et al.* (2016) and *Kirillov et al.* (2020) (and see fig. 2.8). Bursts classified as open water were further screened based on peak frequency, noise, and skewness criteria before bulk wave statistics were calculated using the MATLAB *UVZWaves* function in the SWIFT-codes database (`https://github.com/jthomson-apluw/SWIFT-codes`; updated 05/2018); these wave statistics were used by *Cooper et al.* (2021).

This classification is binary: each burst either represents surface gravity waves or sea ice. In reality, the two can coexist in an individual burst as surface gravity waves can transmit through partial sea ice cover and exist in leads and gaps between ice floes. Individual spectra reveal occasional bursts classified as sea ice, but with small surface gravity wave spectral peaks superimposed (e.g., figs. 2.7e and f). However, manual inspection of all spectra reveal very few unambiguous occurrences of bursts measuring a combination of sea ice and surface gravity waves.

In theory, additional wave classification can be performed based on pressure mea-

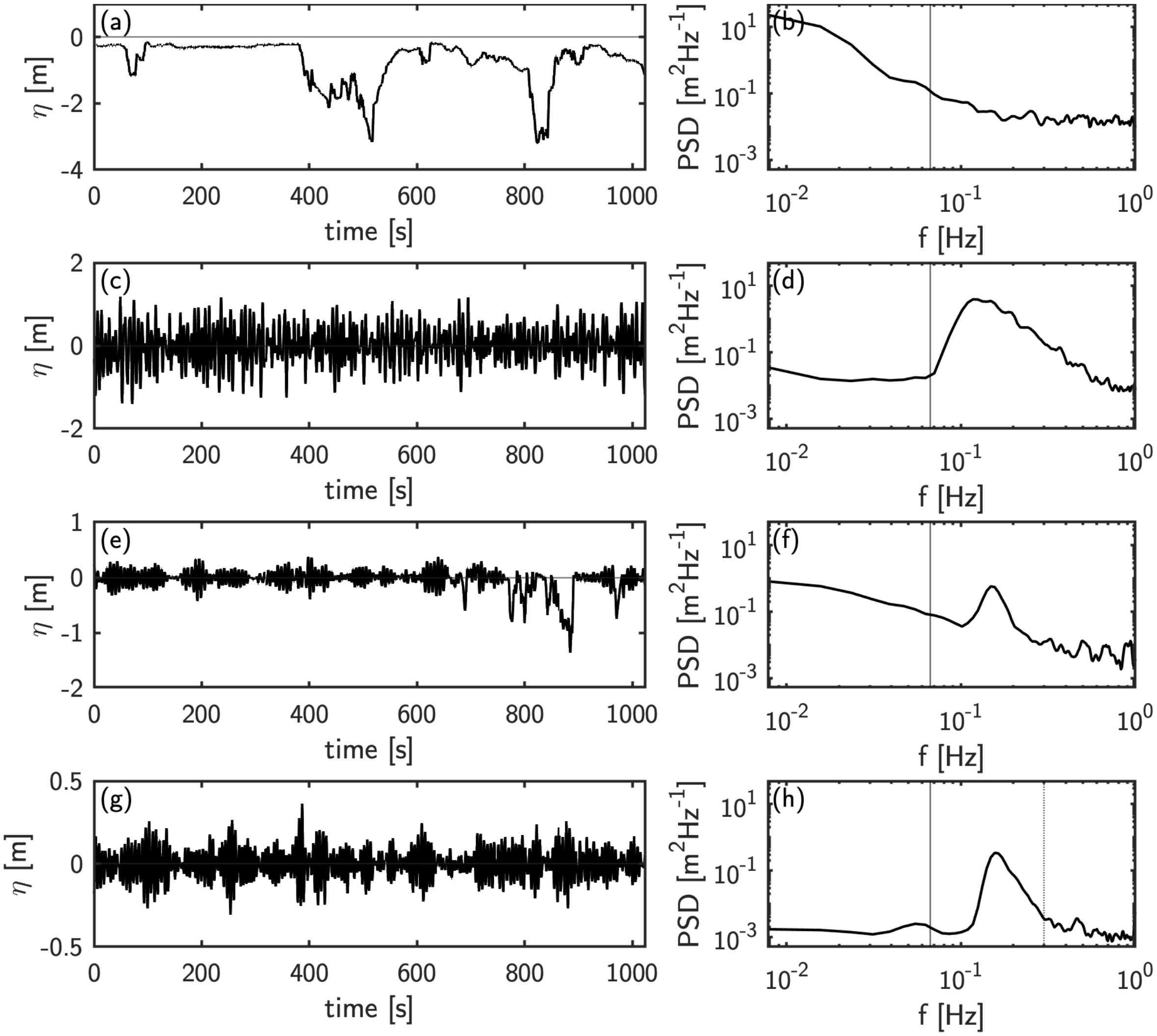

Figure 2.7: Examples of individual burst altimeter data: each row shows a timeseries of surface deflection (η), and its corresponding power spectra (PSD) for different measurement types: (a,b) sea ice cover; (c,d) surface gravity waves; (e,f) mixed sea ice and open water with waves; (g,h) surface gravity waves with high frequency energy damped by sea ice. The solid vertical lines in (b,d,f,h) shows the cut-off frequency used to define "high" and "low" frequencies. The vertical dotted line in (f) corresponds to the 0.3 Hz frequency cut-off used by *Thomson* (2020) for fitting spectral slopes.

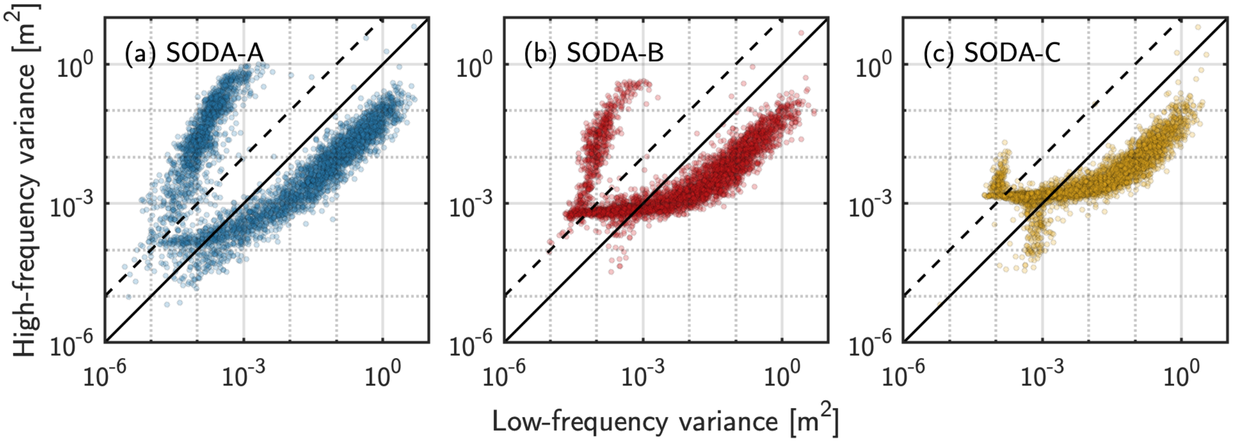

Figure 2.8: Separation of burst data based on low- and high-frequency variance for each of the moorings (a–c, as labelled); each point corresponds to one burst measurement. Solid black lines show the 1:1 slope, while dashed black lines show the 10:1 cut-off ratio used for classification (points above this line are open water, and below the line are sea ice).

surements from the ADCPs after appropriate corrections for dynamic pressure decay with depth. In practice, these moorings were too deep for any meaningful wave data to be recovered from the pressure records (beyond frequencies of $\sim$0.1 Hz, the pressure decay correction amplified only noise). However, inspection of the pressure spectra revealed that the mooring platforms had a natural resonant response with a period of $\sim$17 s, which could easily be confused with surface gravity waves. Fortunately, only velocities associated with intermittent passing eddies were strong enough to excite motions with measurable pressure signals, and these were generally absent from the altimeter measurements (which had a higher noise floor).

We note that *Thomson* (2020) also use spectral properties for similar burst classification, but with a different procedure. In those data, spectra are classified based on power-law fits of the high frequency spectral range. The spectral tail of surface gravity waves are expected to follow $E \propto f^q$, with $q \leq -4$ in open water or mixed sea ice conditions , so *Thomson* (2020) only calculate wave statistics for bursts where fitted $q \leq -2$ for frequencies

$f > 0.3\,\mathrm{Hz}$. Application of that method to these measurements showed a number of false-negative classifications of surface gravity wave spectra. In particular this occurred for spectral slopes steeper than $q = -4$ (e.g, when higher frequency energy was likely damped by sea ice; *Rogers et al.*, 2016) so that above $f > 0.3\,\mathrm{Hz}$ the signal dropped below the noise floor (figs. 2.7g and h).

2.5 *Summary*

This chapter describes some of the challenging aspects associated with creating useful data products from measurements made by two separate ADCPs on each of the SODA moorings. This focused on combining velocity data from two ADCPs into a continuos record of the upper ~80 m of the water column, and on correcting and classifying altimeter data.

Creating merged velocity profiles from the two ADCPs required data filtering to account for acoustic reflections from other mooring instruments, and post-deployment compass corrections to ensure that there was no introduction of extraneous rotational shear. The compass correction was straightforward for the SIG500s, which record internal magnetometer data for the purpose of making such corrections. For the deeper WH300s, novel use of the overlapping velocity fields between instruments allowed for compass corrections even in the absence of magnetometer measurements. Finally, spline interpolation of windowed data allowed for the creation of merged velocity profiles with a consistent vertical scale.

The altimeter data from the vertical beam of the SIG500s is a powerful tool for understanding both the sea ice (e.g., *Brenner et al.*, 2021) and surface gravity waves (e.g., *Cooper et al.*, 2021). Altimeter distances were corrected to account for instrument tilt and sound speed errors. The sound speed errors stemmed largely from inaccuracies in the measured SIG500 temperatures (which may have been a result of instrument-generated heat), and were corrected by regression with an independent MicroCAT temperature sensor. Corrected altimeter bursts measurements were then classified as either sea ice or open water based on their spectral properties.

These procedures have lead to the creation of data products that are used through the remainder of this thesis.

Chapter 3

ACOUSTIC SENSING OF THE ARCTIC OCEAN MIXED-LAYER FROM MOORED SUBSURFACE ADCPS

3.1 Introduction

Arctic Ocean interactions with either the sea ice or the atmosphere are modulated by the ocean mixed layer (ML), where surface heat and momentum exchanges are linked to deeper waters (e.g., *Toole et al.*, 2010). ML properties such as depth and temperature are critical variables for understanding and predicting the changing Arctic. Making sustained measurements of these variables in the region near the sea surface is challenging, primarily because of the presence of sea ice.

A variety of platforms provide measurements of ML properties, though these are both spatially and temporally scattered (*Peralta-Ferriz and Woodgate*, 2015). Traditional shipboard sampling of water column properties are seasonally biased towards open water periods, and regions where navigation is easier; i.e., thinner ice regions. Ice Tethered Profilers (ITPs; *Krishfield et al.*, 2008; *Toole et al.*, 2010) provide a growing resource of year-round upper-ocean measurements under sea ice in the Arctic, helping alleviate some issues with shipboard sampling. ITPs are deployed on drifting multi-year ice floes and not fixed in space, so they allow for an understanding of the seasonal evolution of the ML in the sea ice reference frame. Characterizing ML development over the sea ice-to-open water transition or looking at interannual variability would benefit from additional Eulerian sampling. Moorings are useful platforms for providing long term records of oceanographic conditions at fixed locations in the Arctic (e.g., *Lin et al.*, 2019; *Polyakov et al.*, 2020a; *Fine and Cole*, 2022); however, measurements of the ML in the Arctic Ocean from moorings can be particularly challenging. Due to the presence of sea ice, moorings deployed in the Arctic have no surface expression and the uppermost subsurface floats on these moorings must be sufficiently deep to avoid sea ice keels (e.g, *Krishfield et al.*, 2014), and are thus unable to measure the shallow MLs characteristic of the spring and summer season (e.g., *Peralta-Ferriz and Woodgate*, 2015; *Gallaher et al.*, 2016; *Cole et al.*, 2017).

This study demonstrates that upward looking Acoustic Doppler Current Profilers (ADCPs) installed on subsurface floats are capable of estimating both the depth and temperature of the Arctic Ocean ML. As ADCPs are commonly included on moorings, this methodology may allow for additional data recovery and value from preexisting mooring arrays.

Observations from the Beaufort Sea, including moorings measurements, autonomous assets, and remote sensing, and are described in section 3.2. Signatures of the ML manifest in the ADCP measurements from each of the moorings as peaks in acoustic backscatter and inertial velocity shear; section 3.3 presents an approach for finding these peaks and merging them into an annual timeseries of ML depth, and compares the results with observations of the vertical temperature structure at the moorings. ADCP measurements of ice draft (from a vertical altimeter beam) can be used to infer the surface ML temperature during summer. In open water, non-zero measurements of sea ice draft reflect variations in acoustic travel time due to differences in the speed of sound in the warmer surface layer. Using the results from section 3.3 together with these erroneous ice draft measurements, section 3.4 describes the construction of a two-layer inverse sound speed model that can be used to predict the ML temperature.

3.2 *Measurements*

The Office of Naval Research (ONR) Stratified Ocean Dynamics of the Arctic (SODA) research program (*Lee et al.*, 2016) included the installation of three subsurface moorings in the Beaufort Sea from fall 2018 to 2019 (fig. 3.1, and see *Brenner et al.*, 2021). The moorings are designated, from south to north, as SODA-A, -B, and -C (fig. 3.1a). They were highly instrumented in the top ∼90 m of the water column (fig. 3.1b) to measure upper ocean

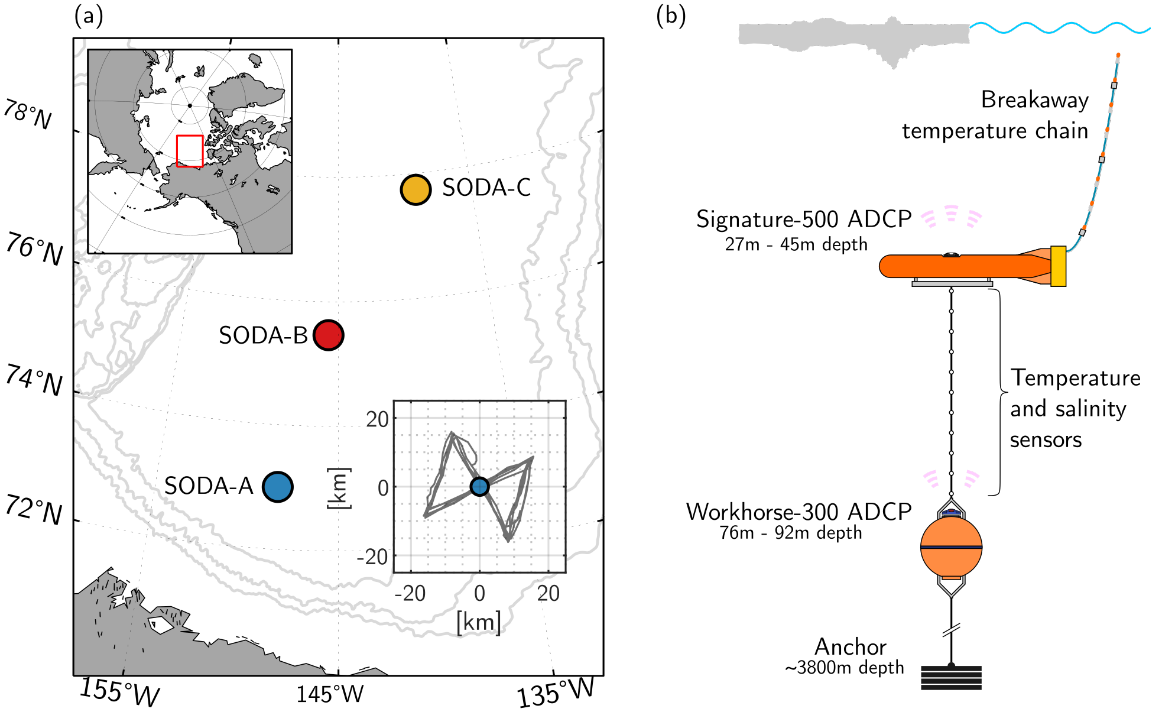

Figure 3.1: (a) Maps showing the locations of the moorings, with insets showing the map location and the Seaglider track in the vicinity of SODA-A. Grey contours show 1000-m isobaths. (b) Schematic of mooring instrument configuration.

temperature, salinity, and velocity, along with sea ice drift speed and geometry. Estimates of ML depth and ML temperature were made using ADCP measurements from these moorings and compared to upper ocean temperatures collected both by the moorings and by an autonomous instrument and remote sensing.

3.2.1 *ADCP measurements*

Each of the three moorings included two upward-looking ADCPs installed on floats at different depths. The top float of each mooring, a DeepWater Buoyancy StableMoor (see *Harding et al.*, 2017), housed a Nortek Signature-500 (hereafter SIG500) 5-beam ADCP . A syntactic foam float ~45–50 m deeper contained a Teledyne Workhorse-300 (hereafter

WH300) ADCP (fig. 3.1b). The depths of each of the top floats varied from 27–45 m between moorings, while the distance between the upper and lower instruments was roughly fixed (the water depth in the region is ∼3800 m). Data from the SIG500 ADCPs were previously presented by *Brenner et al.* (2021), and the concurrent sampling schemes used with those instruments are described in that paper. Velocity measurements from both ADCPs were merged together to create a continuous product within the top ∼80 m of the water column, with a 2 m vertical bin spacing and a temporal resolution of 1 h.

Horizontal velocities (u, v) were filtered to retain the clockwise-rotating near-inertial frequency band (section 3.3) using complex demodulation with a fourth-order low-pass Butterworth filter applied with a frequency with a cutoff of $0.1f$. The inertial shear magnitude is $S_I = [(\frac{\partial u_I}{\partial z})^2 + (\frac{\partial v_I}{\partial z})^2]^{1/2}$, where subscript I refers to the inertially-filtered velocities.

The echo intensity/amplitude recorded from each of the ADCPs were treated separately (i.e., the Signature500 and WH300 echo data on each mooring were not merged). For each record, the relative acoustic backscatter (SV) was found from the recorded echo data by accounting for acoustic transmission loss and beam spreading following *Gostiaux and van Haren* (2010), which is based on *Deines* (1999) but with empirical fits of the scale factor k_c and a more careful accounting for signal-to-noise ratios near the noise floor. The relative backscatter is calculated as

$$SV = I_{dB} - A + 20 \log R + 2\alpha R, \tag{3.1}$$

where R is a distance from the instrument, A is an empirical constant value that incorporates transmit power and geometric factors, α is a frequency-dependant attenuation coefficient (taken as 0.069 for the WH300s, *Deines*, 1999; and 0.146 for the SIG500s, calculated from *Francois and Garrison*, 1982), and I_{dB} is a relative acoustic intensity (in dB) derived from the recorded echo intensity, E after scaling and subtracting noise:

$$I_{dB} = 10 \log \left(10^{\frac{k_c E}{10}} - 10^{\frac{k_c E_{\text{noise}}}{10}} \right) \tag{3.2}$$

Acoustic reflections of other mooring components were frequently seen in the echo data from the deeper WH300 ADCPs, so contaminated bins were removed, identified based on the magnitude of the annually-averaged error velocity (using a threshold of $1.5 \times 10^{-3}\,\mathrm{m\,s^{-1}}$). In addition to reflections from the pycnocline that are used to determine ML depth (section 3.3), the acoustic backscatter also recorded signals of biological activity in the water column including both the diel vertical migration of zooplankton (e.g. *Dmitrenko et al.*, 2020, 2021), and seasonal differences that might be associated with the phytoplankton bloom (e.g., *Ardyna et al.*, 2014). The signal associated with diel vertical migration produced peaks in backscatter that competed with the pycnocline reflection, so to minimize this impact we averaged the acoustic backscatter in daily time bins. This smears out the signal of the diel migration while leaving the peak associated with the ML depth relatively intact.

Altimeter distances from the vertical beam of the SIG500 were corrected for ADCP tilt, speed of sound (measured at the instrument), and atmospheric pressure variations (*Brenner et al.*, 2021). Sea ice draft was calculated as the difference between the instrument depth, H, (based on pressure measurements) and the altimeter distance, D. Altimeter burst measurements were categorized as being either sea ice or open water based on their spectral properties, following *Shcherbina et al.* (2016; also see *Kirillov et al.*, 2020; *Brenner et al.*, 2021). In sea ice cover, the difference between the instrument depth, H, (based on pressure measurements) and the altimeter distance, D, was used to calculate sea ice draft: $d = H - D$. For bursts identified as being in open water (based on spectral characteristics), erroneous non-zero values of d (i.e., non-zero values of ice draft) indicate water column sound speed variations due to shallow stratification (section 3.4).

3.2.2 *Temperature and salinity measurements*

On each of the moorings, the ~45 m distance between the two ADCPs was instrumented with a set of Seabird SBE37 MicroCAT conductivity, temperature, depth (CTD) sensors and SBE56 temperature (T) sensors (fig. 3.1b). A total of 10 of sensors (6 SBE37 and 4 SBE56) were installed with a spacing of ∼4–5 m between instruments, and instrument types alternating. At all three of the moorings, the uppermost SBE37 (positioned directly underneath the topmost float) failed sometime during the summer season (between late May and early July), but pressure and temperature measurements made by the SIG500 ADCP itself continued to provide a record at that float throughout the full data record, albeit with a decreased temporal resolution and accuracy (prior to failure, the uppermost SBE37 was used to correct and calibrate the SIG500 temperature measurements).

In addition, a 40 m long, buoyant "breakaway chain" of high spatial resolution (0.25 m spacing) temperature sensors was attached to the tail of the StableMoor (the topmost float) in order to measure temperatures shallower than the float depth. The sensors measured with a 3-h sampling period. The chain was built up of 8 sections that were each 5 m long (a total length of 40 m) and connected with a set of weak links of progressively increasing strength. All data collected by the sensors along the chain was recorded by a data logger housed in the StableMoor float. This allowed for sections of the chain to break off without the loss of data as they were raked by passing sea ice keels. The breakaway chains were successfully deployed for SODA-A and SODA-C. At SODA-B, a rough sea state during (anchor-last) mooring deployment resulted in the chain fouling with the main mooring line and no data above the StableMoor. At SODA-C, which was located in perennial sea ice cover, the shallower top float depth (∼27 m) resulted in some chain sections being initially against the ice at the surface, so most of the chain broke away shortly after deployment. Of the 8 chain sections, 5 of them (the top 25 m) had broken off by 12-Oct-2018 (less than one week after deployment). An additional 5-m section broke off on 11-Mar-2019, leaving only 2 sections (10 m) for the remainder of the deployment. At SODA-A, one section broke away on 18-Dec-2018, and a second section was lost 19-Feb-2019; the other 6 sections (30 m) of the chain remained intact. Pressure sensors located at distances of 5 m, 20 m, and 35 m along each of the chains allowed for reconstruction of their positions in the water column and the depths of each of the temperature sensors. This was done using a quadratic model fit to the available pod distances and pressures (which decreased in number as chain sections broke away) including the pressure measured by the Signature500 ADCPs at distance 0. The pressure measurements show that the strong ocean currents at SODA-A (up to $0.5\,\mathrm{m\,s^{-1}}$) resulted in significant movement and frequent "blow down" of the chain (in extreme cases, the vertical extent measured by the chain was ¡5 m even when the chain was 30 m long). At SODA-C, which was more quiescent, the chain was usually fairly vertical. There were occasional data spikes or dropouts along some sections of the breakaway chain. These were more prominent at SODA-A (possibly due to chain movement which may have disrupted internal cabling), with sections #1 and #3 missing data for most of the year. Though less frequent at SODA-C, similar spikes and dropouts still occurred. Data spikes were most apparent as unphysically high temperatures. To account for these issues, all temperatures above 6.5 °C were removed from the record of both moorings, and temperatures were interpolated across data gaps and dropouts. Measurements were then bin-averaged in 2-m along-chain (8 sensor) bins. Some noise and horizontal banding remaining in the final data record shows some calibration offsets/errors associated with individual sensors that could not be resolved.

Temperatures measurements made by the Seabird sensors on the mooring line and by the breakaway chains were both temporally averaged into 1-day bins.

In addition to the mooring measurements, a autonomous Seaglider (SG229) sampled temperature and salinity from 16-Aug-2019 to 30-Sep-2019 in a 20-km "bow-tie" pattern around SODA-A, with a mean distance from the mooring of ~12 km (fig. 3.1a). Seaglider is a small, reusable, long-range autonomous underwater vehicles designed to glide from the ocean surface to 1000 m and back while collecting profiles of temperature, salinity, and other oceanic variables. Gliders steer through the water by controlling attitude (pitch and roll) and can thus navigate between waypoints to execute survey patterns, in this case with successive dives separated by ~4 km, and ~6.5 h. Temperature and salinity were measured by SG229 were averaged into 1 m vertical bins and temporally averaged into 1-day bins for consistency with the other data sources.

In situ measurements were supplemented with satellite-derived sea ice concentrations (A) and sea surface temperatures (SSTs) provided by the Operational Sea Surface Temperature and Sea Ice Analysis (OSTIA) data product (*Donlon et al.*, 2012). These are provided at daily intervals at 0.05° resolution. Data were interpolated to provide timeseries of A and SST at each mooring.

3.3 ML depth

3.3.1 Approach

Sharp temperature and salinity gradients cause reflections of acoustic signals due to changes in acoustic impedance (e.g., *Ross and Lavery*, 2012), so peaks in measured acoustic reflectance (backscatter) can be related to stratification (e.g., *Shibley et al.*, 2020). This principle has been used to identify oceanic structures from acoustic echosounder or seismic data (e.g., *Penrose and Beer*, 1981; *Holbrook and Fer*, 2005; *Stranne et al.*, 2017, and others; including of the Arctic ML, *Stranne et al.*, 2018).

Peaks in stratification are also often a location of strong vertical shear of horizontal velocity. The ocean ML responds directly to wind forcing (e.g., *Price et al.*, 1987; *Randelhoff et al.*, 2014; *Chaudhuri et al.*, 2021). Particularly for inertial oscillations, which are rotational motions of the ML at the local Coriolis frequency, the velocity profile is generally more or less uniform in the ML (the "slab" models of *Pollard and Millard*, 1970; *D'Asaro*, 1985), with strong inertial shear at the ML base. Because of the slab-like structure of inertial oscillations, inertial shear will be relatively weak within the ML and have a strong signal at the ML base. As such, inertial-band shear is likely a better indicator of the ML depth than broad-band shear (which would likely include other signals within the ML; e.g., due to mixing-layer development).

Macrander et al. (2007) previously showed that a seafloor mounted ADCP could be used to identify the interface depth of a deep exchange flow: the Denmark Strait Overflow.

Those authors considered both echo intensity (a measure of acoustic backscatter) and shear separately to construct and compare different timeseries of Denmark Strait Overflow interfacial depth. As both shear and backscatter in the surface ML can be impacted by a variety of processes absent in deeper overflow water, we adapt and build on the ideas presented by *Macrander et al.* (2007) in order to develop a methodology for identify the ML depth from moored (uplooking) subsurface ADCPs.

Here, the ML depth is identified using ADCP measurements of inertial shear and acoustic backscatter together. An overview of procedure is as follows:

1. For each of the data sources (WH300 backscatter, SIG500 backscatter, inertial shear), identify ML depth at each timestep from local maxima, subject to constraints on "peak prominence" and the depth range considered (see below).

2. Combine individual ML depth measurements for separate sources into a single timeseries for each season.

3. Perform a weighted-moving average.

Steps are described below in more detail. These steps were performed separately for "winter" and "summer" seasons to account for different ML characteristics: deeper MLs throughout the ice-covered period of the year, with a shift to shallow MLs with the injection of freshwater from melting sea ice (*Peralta-Ferriz and Woodgate*, 2015). Different constraints on the depth range considered were used for each season. The delineation between these seasons was chosen manually based on visual inspection of backscatter and shear. Winter/summer boundaries were identified as 12-Jun-2019, 04-Jul-2019, and 18-July-2019 for SODA-A, -B, and -C, respectively; before these dates was considered "winter", and afterwards was considered "summer". At all three moorings these dates correspond to sea ice concentrations of $A \sim 68\%$. It is likely that summer freshwater layers were present earlier than these dates, but were too shallow to be identified (the

Table 3.1: ML depth algorithm parameters for each of the data sources: Threshold identifies the minimum peak prominence used for identifying local maxima. Depth range identifies the vertical bounds of the search algorithm for each of the two seasons. Date range shows when data from each instrument were considered.

		WH300 backscatter	SIG500 backscatter	Inertial shear
Threshold		0.5 dB	1.5 dB	$1.5 \times 10^{-3}\,\mathrm{s}^{-1}$
Depth Range	Winter	25–70 m	–	6–70 m
	Summer	–	6–40 m	6–40 m
Date Range	SODA-A	14-Nov-2019 – 12-Jun-2019	12-Jun-2019 – R.E.	F.R.
	SODA-B	R.S. – 15-Jun-2019	04-Jul-2019 – R.E.	F.R.
	SODA-C	R.S. – 15-Jun-2019	18-Jul-2019 – R.E.	F.R.

R.S.: record start; R.E.: record end; F.R.: full record

shallowest resolvable ADCP measurements were $\sim$6 m deep due to surface sidelobe reflection).

Step 1. Rather than identifying the ML as the absolute maximum values of shear or backscatter for a given timestep (as in *Macrander et al.*, 2007), we searched for local maxima. At each timestep, we associated the ML with the shallowest local maxima whose peak extends above background values by some minimum threshold, and is within a specified depth range (with different depth bounds for the search algorithm for winter and summer seasons, and for different data sources; table 3.1). This was done separately for each of the three data sources, using the MATLAB *findpeaks* function with a "minimum peak prominence". Peak thresholds were chosen ad hoc after inspecting the data fields (table 3.1). ML depths were only identified for times when there were peaks that met the threshold value. For each of the identified peaks, a three-point quadratic stencil was applied to points centred on the peak, with the ML depth taken as depth of the maximum of the quadratic fit (fig. 3.2).

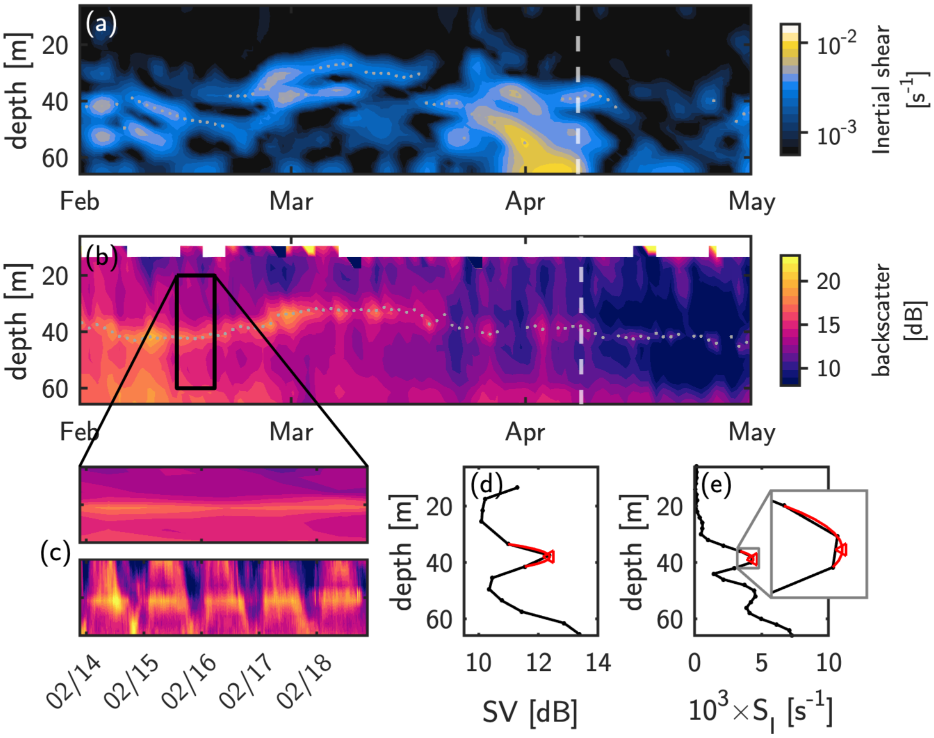

Figure 3.2: Example of ML depth identification from a 3-month period in winter/spring 2019 at SODA-C, showing timeseries of (a) inertial shear magnitude, S_I, and (b) daily-averaged relative acoustic backscatter, SV. Points in (a) and (b) show identified ML depths. (c) shows an inset from (b) demonstrating the effects of diel migration on backscatter; the top panel in (c) shows the daily-averaged backscatter used for identifying the ML, and the bottom panel shows the same data before averaging. Panels (d,e) show the peak identification for individual profiles of backscatter (d), and shear (e), including the sub-grid 3-point stencil (inset in e) for the times identified by vertical dashed lines in (a) and (b).

Step 2. For each season, individual ML depth points from the different sources (backscatter and shear) were combined into a single timeseries. Due to instrument limitations (depth and range) and environmental differences, the blended data included different data from different data sources during different times of the year. In particular, elevated mid-water column backscatter during sea ice breakup and open water (possibly due to seasonal phytoplankton bloom) partly obfuscated WH300 backscatter measurements, and lead to the divergence of peaks found in backscatter and inertial shear. As inertial shear is more representative of ML dynamics, we took this divergence as an indication that those backscatter data were not reflective of ML depth. For this reason, backscatter-derived ML depth points from the WH300 were included during winter only. Depths from the SIG500 were included during summer only, when MLs would be consistently above those instruments, while inertial shear data were included throughout the full year, as summarized in table 3.1.

Step 3. A smoothed daily ML depth timeseries was constructed by taking the weighted averages of depths in centred moving 7-day windows. Weights were calculated as the prominence of each peak (from the peak detection algorithm) normalized by the minimum threshold for each data type; this gives higher weights to peaks associated with strong acoustic reflection or shear. For windows containing 3 or fewer measurements, no calculation was performed. Finally, days in which no averages were reported due to lack of data were filled in with linear interpolation.

Figure 3.2 provides an example of the ML depth identification procedure from a 3-month period in winter at SODA-C (including a view of the diel variations of acoustic backscatter). The figure demonstrates the variability in both of the backscatter and shear signals.

3.3.2 Results

Figure 3.3 shows timeseries of the ML depths found for each mooring. At all moorings, the method produced ML depths similar to recent measurements in the same region (*Cole et al.*, 2017), with winter mean ML depths of 42.7 m, 40.0 m, and 39.7 m, for SODA-A to -C, respectively, and mean summer depths of 20.2 m, 16.2 m, and 14.4 m. *Cole et al.* (2017) found ML depths of 40 m in winter and depths 10–15 m at the beginning of summer, which deepened through September.

The ML depths determined from ADCP shear and backscatter (black line in fig. 3.3) followed variations in the measured upper ocean temperature from the moorings and Seaglider. Wintertime variability in ADCP-derived ML depth corresponded to vertical displacement of isotherms, and tracked the depth a strong vertical temperature gradient. To quantify the fit, the $-1\,^{\circ}\mathrm{C}$ isotherm was taken as representative of the winter ML depth from SODA-A and -C mooring sections (since the surface water was at the freezing temperature during winter ice cover, this corresponds to a ΔT threshold of $\sim 0.8\,^{\circ}\mathrm{C}$). From Aug.–Sep at SODA-A, a ML depth was defined based on the depth of the maximum buoyancy frequency, N, from the Seaglider measurements. These ML depths are shown as white contours in fig. 3.3.

There is good correspondence between the ADCP-estimated ML and that determined from the mooring/Seaglider sections (fig. 3.4). Correlation coefficients and root-mean-square-errors were $r = 0.60$, $RMSE = 8.28$ m for SODA-A, and $r = 0.88$, $RMSE = 2.67$ m for SODA-C. The approach used to identify ML depths from the ADCP measurements is entirely independent of the temperature-salinity data, so the ML depths determined using those measurements corroborate this method.

At SODA-B, where shallower temperature data were less available, direct comparisons or validation of the estimated ML depths was not possible. Nonetheless, some of the temporal variations in the ML depth during winter at that mooring match with the heaving of isotherms deeper in the water column.

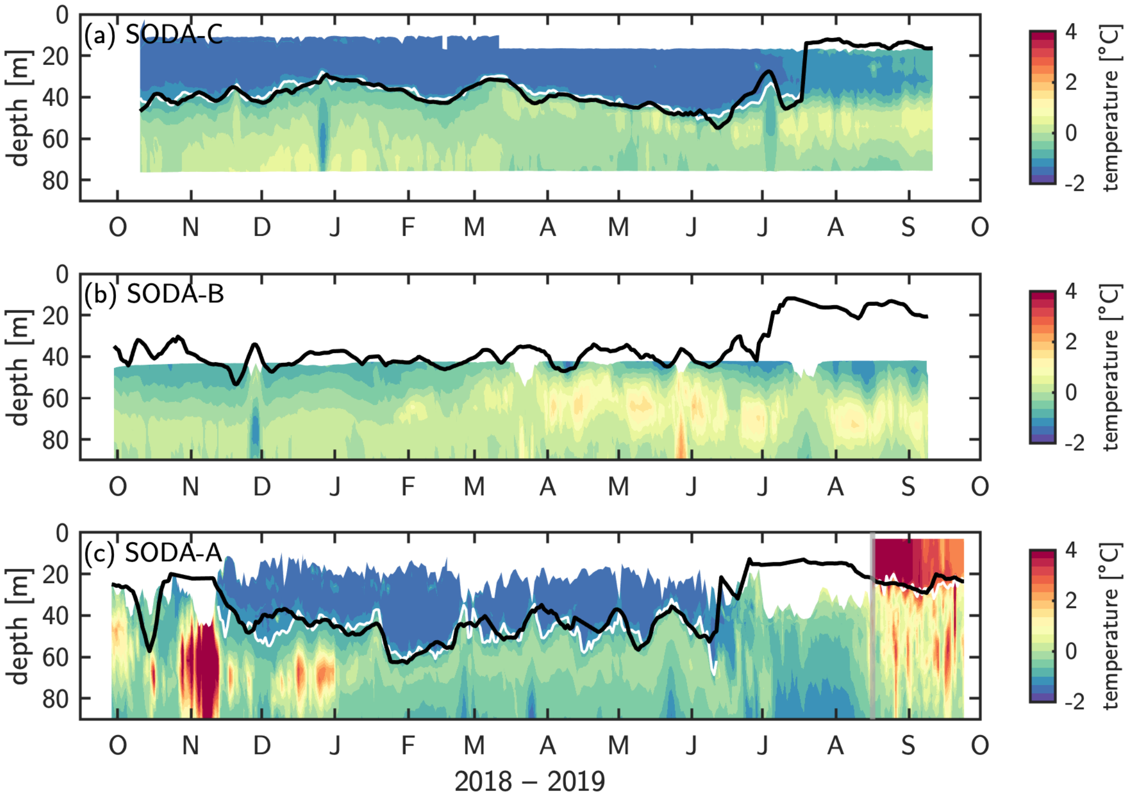

Figure 3.3: Timeseries of upper ocean temperatures at each of the three moorings (as labelled). For SODA-A, temperatures shown are from mooring measurements prior to 16-Aug-2019, and from the Seaglider after that date (delineated by a vertical grey line in panel c); for SODA-B and -C, temperature measurements are only from the mooring. Black lines in each panel show the final ML depth timeseries identified through shear and backscatter (i.e., independent of temperature measurements). White contours in (a) and (c) show the ML depth based on the $-1\,^{\circ}\mathrm{C}$ isotherm (through winter), or from the peak N from Seaglider measurements (panel c; summer).

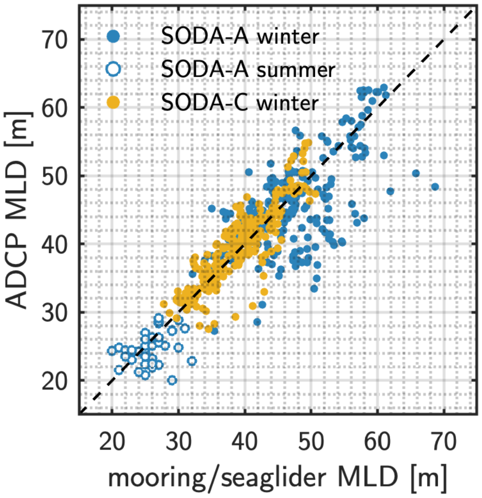

Figure 3.4: ML depths based on on the $-1\,^{\circ}$C isotherm (SODA-A and -C winter) or from the peak N in Seaglider measurements (SODA-A summer) versus ML depths estimated from ADCP-measured shear and backscatter. The black dashed line shows the 1:1 slope.

Aside from when the Seaglider measurements were available, temperature data were too deep in the water column to compare ML depth measurements during the summer shallow ML period. This highlights the limitations of using those data to investigate summer MLs, and the value of being able to derive those measurements from ADCPs.

3.4 *ML temperature*

3.4.1 *Approach*

The advent of vertical altimeter beams on some ADCP models allows for measurements of sea ice draft or surface gravity waves (e.g., *Magnell et al.*, 2010; *Thomson and Rogers*, 2014; *Kirillov et al.*, 2020; *Brenner et al.*, 2021; *Cooper et al.*, 2021). However, stratification shallower than the ADCPs leads to small offsets in these altimeter measurements, primarily due to changes in acoustic travel time due to a vertically varying sound-speed profiles. As such, offsets between the pressure-derived instrument depth, H, and the altimeter-derived instrument depth, D, measured in open water have been used to make empirical sound speed corrections to these measurements (e.g, *Kirillov et al.*, 2020; *Brenner et al.*, 2021). Here, we instead make use of those erroneous measurements from a SIG500 ADCP to infer the summertime ML temperature using an inverse sound speed model.

We focus only on summer measurements from SODA-A as a demonstrative example. At SODA-A, measurements of $H - D$ in open water reached as high as ~ 0.5 m (fig. 3.5). Shallow stratification can cause errors in these measurements due to both sound speed changes (which impact the altimeter distance, D) and density changes (which impact the conversion from pressure to instrument depth, H). Thus, open-water depth offsets $d = H - D$ can be expressed as $d = \varepsilon_H + \varepsilon_D$, where ε_H and ε_D are the separate errors associated with H and D. While in general these effects cannot be separated, Arctic waters exist in a temperature-salinity regime in which density, and hence ε_H, is set almost entirely by salinity. So ε_H can be estimated separately given an appropriate model of salinity. For the environmental conditions expected here, ε_H is likely small and most of the error can be attributed to ε_D.

The speed of sound in water is a strong function of temperature. Inverse sound speed models provide a measure of integrated ocean heat content based on observed travel times of acoustic signals (*Watts and Rossby*, 1977). Together with a model for the water column structure, these measurements have been leveraged to determine details of the vertical temperature distribution. For example, *Sanchez et al.* (2021) use acoustic travel times measured by pressure-sensor-equipped inverted echo sounders (PIES; *Meinen and Watts*, 1998) to investigate temperature and thickness of Atlantic Water inflow to a glacial fjord. Knowing upper and lower layer temperatures, *Macrander et al.* (2007) also makes use of travel time measurements from PIES to estimate the depth interface of the Denmark Strait Overflow (for comparison to the backscatter and shear methods; section 3.3).

Prior to the onset of the shallow summer stratification, the ML was at the local freezing temperature (fig. 3.3). As sea ice concentration decreases and shallow summer stratification sets in, the ML is expected to rapidly warm (e.g., *Peralta-Ferriz and Woodgate*,

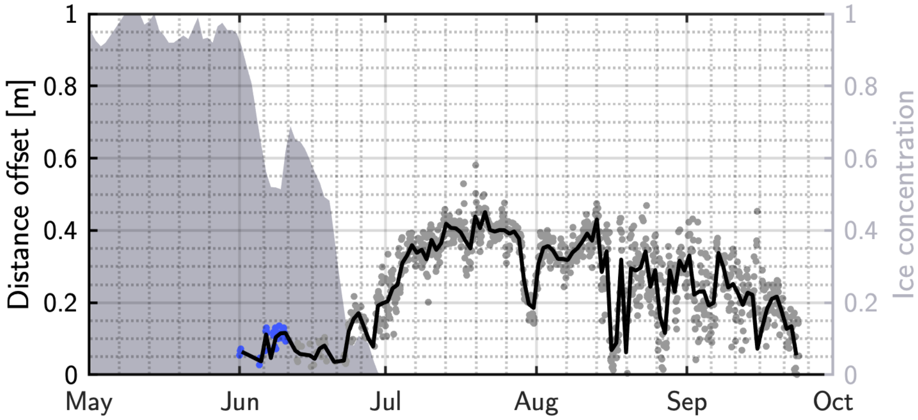

Figure 3.5: Distance offset ($H - D$) measurements for burst data at SODA-A identified as open water (left axis), and sea ice concentration (left axis). Points show individual measurements, while the solid line show daily averages. Note that open water bursts occur for non-zero ice concentration due to measurements between sea ice floes. Blue points at the beginning of the record show times when the ML depth was below the depth of the instrument.

2015) while the ocean below the ML remains approximately the same temperature. As a first-order approximation, we model the upper ocean as a two-layer system with a homogeneous surface ML of depth h_1 overlying a lower layer of depth h_2 with constant linear temperature and salinity gradients (fig. 3.6). The lower-layer gradients dT/dz and dS/dz are assumed constant, and found by making linear fits to measurements from the mooring line between July–August 2019 (i.e., only using measurements deeper than the ADCP). So $T_2(z) = T(H) + (dT/dz)(H - z)$, where $T(H)$ is the temperature at the ADCP, taken from the mooring measurements, and equivalently $S_2(z) = S(H) + (dS/dz)(H - z)$.

For a two-layer system, the vertical two-way travel time of an acoustic signal is:

$$t_{2w} = 2 \left[\frac{h_1}{\langle c_1 \rangle} + \frac{h_2}{\langle c_2 \rangle} \right], \tag{3.3}$$

where $\langle c_n \rangle$ is the harmonic mean of the depth varying sound speed in layer n: $\langle c_n \rangle = h_n \left[\int_{h_n} \frac{dz}{c(z)} \right]^{-1}$. As the ML is assumed to be homogeneous, $\langle c_1 \rangle$ is approximately constant; sound speed does vary slightly with pressure, but the effects are negligible in this depth

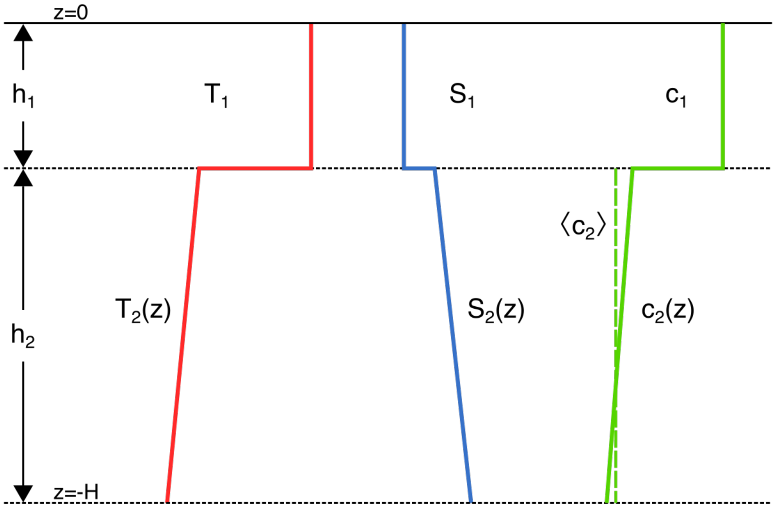

Figure 3.6: Schematic of the two-layer model showing profiles of temperature (T), salinity (S), and sound speed (c) with depth.

range. Equating eq. (3.3) with the acoustic travel time inferred from the mooring altimeter distance ($t_{2w} = 2Dc(H)^{-1}$, where $c(H)$ is the speed of sound measured at the instrument at depth $H = h_1 + h_2$) gives an expression for the ML sound speed:

$$c_1 = c(H)\left[\left(1 - \frac{\varepsilon_D}{h_1}\right) + \left(1 - \frac{c(H)}{\langle c_2 \rangle}\right)\left(\frac{h_2}{h_1}\right)\right]^{-1}, \tag{3.4}$$

where ε_D is the portion of the distance offset measurements that can be attributed to sound speed variation within the water column.

Inversion of c_1 to find the ML temperature requires some prescription of the ML salinity, S_1. As the input of freshwater to the ML is a result of sea ice melt, an approximation for ML salinity is based on a conservation of salt mass within the sea ice and the water column:

$$h_1 S_1 + \int_{-H}^{-h_1} S_2(z)dz = d_e S_i + \int_{-H}^{-d_e} S_2(z)dz, \tag{3.5}$$

where d_e is an effective ice draft $d_e = (1 - A)d_i$ for A the fractional sea ice concentration (from satellite measurements) and d_i the average sea ice draft prior to the onset of melt (taken as 1.2 m), and S_i the sea ice salinity (taken as $6\,\mathrm{kg\,m^{-3}}$) In this formulation, an assumed hydrostatic balance for sea ice was used to replace ice thickness with draft and eliminate density terms. This is equivalent to the "salt deficit" model used by *Wilson et al.* (2019) and to the sea ice meltlayer thickness model used by *Peralta-Ferriz and Woodgate* (2015, see their Appendix A). Using the density profile associated with the modelled salinity, we also calculate ε_H. Values of ε_H were $\sim$0.02 m during partial sea ice cover, and increased to $\sim$0.04 m in open water; there was very little variation in calculated ε_H. Distance offset measurements ($H - D$) made in non-zero ice concentration (in gaps between ice floes; *Cooper et al.*, 2021) when the ML was deeper than the instrument (so $\varepsilon_D = 0$; blue points in fig. 3.5, $\sim$3% of measurements) cannot be fully explained by the calculated values of ε_H, so an additional empirical offset of 0.05 m was added to ε_H. Using these, $\varepsilon_D = d - \varepsilon_H$ from the distance offsets, d (from fig. 3.5).

Equation (3.4) was applied to calculate c_1 with daily-averaged values of ε_D, using h_1 from section 3.3 (and $h_2 = H - h_1$), and sound speeds $c(H)$ and $\langle c_2 \rangle$ calculated from the modelled lower-layer profiles $T_2(z)$, $S_2(z)$ using functions provided in the Gibbs Seawater Oceanographic toolbox (*IOC et al.*, 2010). Then, c_1 values were numerically inverted using the estimated ML salinity, S_1, to find the ML temperature, T_1. As sound speed is only weakly dependant on salinity, estimates of T_1 were insensitive to the modelled ML salinity (differences of $\leq$0.1 °C compared to simply extending the S_2 profile to the surface). To account for uncertainty, T_1 were re-calculated with ±3 m differences in the ML depth (the summertime *RMSE* in h_1 in section 3.3) and ±0.05 m differences in d (roughly the uncertainty associated with the pressure sensor).

3.4.2 *Results*

The sound speed model produces realistic ML temperatures (fig. 3.7). Uncertainties in h_1 and d translated to relatively large uncertainty range of +5 °C/-3 °C in ML temperature

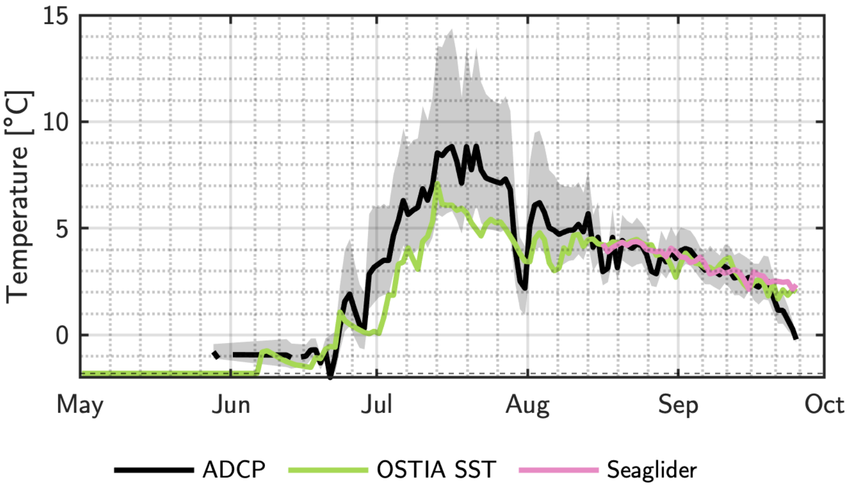

Figure 3.7: ML temperatures as determined using the ADCP with the sound speed model (black line with shading showing uncertainty), and from satellite SST (from OSTIA) and the Seaglider measurements.

when h_1 was shallow (in mid-July; fig. 3.3), but had minimal impact on T_1 estimates for deeper MLs ($\pm 1\,^{\circ}\mathrm{C}$ in mid-August–October). Modelled temperatures exceeded satellite SSTs by up to $\sim 3\,^{\circ}\mathrm{C}$ when temperatures peaked in mid-July, though satellite SSTs roughly overlapped with the lower uncertainty bound on temperature. From mid-August onwards, the modelled ML temperature matched with both satellite SST and the ML temperature observed by Seagliders (fig. 3.7). Correlation coefficients and root-mean-square-errors between the ADCP-derived ML temperatures and the satellite SST product were $r = 0.89$ and $RMSE = 1.46\,^{\circ}\mathrm{C}$. For the Seaglider, they were $r = 0.79$ and $RMSE = 0.85\,^{\circ}\mathrm{C}$.

The mismatch between satellite SST and ADCP-derived estimates of the ML temperature in July might be partly attributed to the simplicity of the two-layer model being applied here (fig. 3.6), and partly to larger-scale (smoother) satellite SST estimates underestimating values relative to point measurements. Heat within some transition layer underneath the homogeneous ML (e.g., *Price et al.*, 1986) would be misattributed here to higher ML temperatures. In applying a sound speed model to find the temperatures in Sermilik Fjord, *Sanchez et al.* (2021), fits hyperbolic-tangent profiles for temperature and salinity with some constant known interfacial thickness. A similar model might improve these results, though it is unlikely that the interfacial thickness would remain constant through the summer. There are also a variety of other reasons why *in situ* ML temperature measurements with satellite SST might disagree. There are challenges in determining SST from satellite measurements in the Beaufort Sea, and variability between different data products (*Castro et al.*, 2016). Additionally, skin effects lead to temperature offsets between SST and the underlying ocean temperature (*Minnett et al.*, 2019). *Crews et al.* (2022) found differences between *in situ* observations of surface temperature and satellite SST of ∼1 °C in the same study region (though of the opposite sign than suggested here, and using a different SST product). While further work is needed to address potential mismatches, the strong correlation between the satellite SST and ADCP-derived ML temperatures ($r = 0.89$) indicates the viability for prediction of ML temperatures from ADCP altimeter measurements.

3.5 *Discussion*

This study demonstrates that viable estimates of the surface ML depth and ML temperature can be made from upward-looking ADCPs installed on subsurface moorings. ML depths were estimated from a combination of maxima in both acoustic backscatter and inertial shear. Results were consistent with previous studies in the area, with winter depths of ∼40 m and summer of ∼15–20 m, and followed mooring and Seaglider measurements of the thermocline depth. Summertime ML temperatures at the southernmost mooring were estimated using an inverse sound speed model and produced results similar to to satellite SST measurements, and matching those measured by an autonomous Seaglider.

Additional measurements could be used to improve and further validate the results from this study. This could include optimization of the algorithmic approaches for identifying the ML depth on shorter time scales, especially during the initial onset of the ice melt and the establishment of the summer shallow ML. It would be beneficial to further investigate approaches for identifying the timing of the shift to summer ML conditions;

here that was done manually based on observed backscatter and shear properties, but it is possible that the timing could be linked to changes in sea ice conditions that would be detectable from remote sensing products. Improvements to ML temperature estimates could be made by using more realistic models of temperature/salinity stratification in the sound speed model.

As moorings in the sea ice covered Arctic Ocean lack surface expressions, these methods can be used to fill in observational gaps above the topmost float of subsurface moorings, and infer measurements of the surface ML that could be critical for better understanding ice-ocean interactions in this region. There are a number of long-term mooring records in the Arctic that include upward looking ADCPs (e.g. *Armitage et al.*, 2017; *Lin et al.*, 2019; *Polyakov et al.*, 2020a) for which the ML depth detection methods could be applied. While ADCPs with altimeters are less commonly deployed, the methods for temperature inversion from altimeter data could be similarly applied to stand-alone upward-looking sonars installed on some moorings (such as those in *Krishfield et al.*, 2014).

Future mooring deployments can be designed to take advantage of these methods. For example, the newer *echosounder* mode available on some Nortek Signature ADCPs (e.g., *Velasco et al.*, 2018) can provide acoustic backscatter measurements at much higher fidelity and sensitivity and may facilitate easier identification of ML depth. These measurements can be available down to centimeter scales, greatly improving the accuracy and resolution of potential ML depth estimates. With some additional study, it may even be possible to link acoustic reflection measurements from these instruments to stratification strength (*Shibley et al.*, 2020).

The ML properties derived here provide additional understanding and context for other observations from these moorings. For example, ML inertial oscillations, which have been shown to be highly seasonal in the Arctic (e.g., *Plueddemann et al.*, 1998; *Rainville and Woodgate*, 2009; *Polyakov et al.*, 2020b) are also sensitive to the ML depth (*D'Asaro*, 1985). Using this timeseries of ML depths together with mooring measurements of ML and sea ice velocities allows us to parse out different drivers of that seasonality.

Part II

Chapter 4

COMPARING OBSERVATIONS AND PARAMETERIZATIONS OF ICE-OCEAN DRAG THROUGH AN ANNUAL CYCLE ACROSS THE BEAUFORT SEA

4.1 Introduction

Ongoing and dramatic changes in Arctic sea ice (e.g., *Stroeve and Notz*, 2018) and the underlying ocean (*Jackson et al.*, 2011; *Timmermans et al.*, 2018; *Armitage et al.*, 2020) highlight the need to understand Arctic system feedback processes. Sea ice dynamics are thought to play an important role in both localized (e.g., *Ivanov et al.*, 2016) and large-scale ice-ocean feedbacks (*Dewey et al.*, 2018; *Meneghello et al.*, 2018a; *Armitage et al.*, 2020). However, there are still fundamental gaps in our knowledge of the role of sea ice in mediating momentum transfer across the atmosphere-ice-ocean system, especially in understanding spatial and seasonal variability in ice-ocean drag.

Turbulent processes in the ocean and in the atmosphere drive surface momentum flux (a.k.a., stress, $\boldsymbol{\tau}$) across the ice-ocean and ice-atmosphere interfaces. These turbulent fluxes are commonly described by the quadratic drag law:

$$\boldsymbol{\tau} = \rho C_d \boldsymbol{u} \left| \boldsymbol{u} \right| , \tag{4.1}$$

which uses a turbulent transfer coefficient (or drag coefficient), C_d, to describe the momentum flux, $\boldsymbol{\tau}$, in terms of an appropriate bulk, velocity $\boldsymbol{u}$. Thus, the ice-ocean stress, $\boldsymbol{\tau}_{io}$, and atmosphere-ice stress, $\boldsymbol{\tau}_{ai}$ depend on ice-ocean and atmosphere-ice drag coefficients: C_{io} and C_{ai}, respectively. While there has been considerable work in relating observed values of the atmosphere-ice drag coefficient, C_{ai}, to sea ice properties (*Arya*, 1975; *Guest and Davidson*, 1987; *Garbrecht et al.*, 2002; *Lüpkes and Birnbaum*, 2005; *Andreas et al.*, 2010a; *Andreas*, 2011; *Lüpkes et al.*, 2012; *Castellani et al.*, 2014; *Elvidge et al.*, 2016; *Petty* *et al.*, 2017, and others), there is relatively little analogous work on the ice-ocean drag coefficient, C_{io}. Indeed, despite a wide range of observed values of C_{io} spanning across an order of magnitude (e.g., *McPhee*, 1980; *Morison et al.*, 1987; *McPhee*, 2002; *Shaw et al.*, 2008; *Randelhoff et al.*, 2014; *Cole et al.*, 2014, 2017), by default many sea ice models use a constant value for the drag coefficient (e.g., *Köberle and Gerdes*, 2003; *Timmermann et al.*, 2009; *Losch et al.*, 2010; *Rousset et al.*, 2015; *Rampal et al.*, 2016), such as the "canonical" value of $C_{io} = 5.5 \times 10^{-3}$ determined by *McPhee* (1980). Moreover, studies show that modelled sea ice thickness is sensitive to the chosen value of C_{io} (*Kim et al.*, 2006; *Hunke*, 2010).

Recent observations show both spatial and seasonal variations in the ice-ocean drag coefficient (*Cole et al.*, 2017), suggesting the importance of ice morphology on the values of C_{io} (e.g., due to form drag; *Steele et al.*, 1989; *Lu et al.*, 2011; *Tsamados et al.*, 2014). Model studies that incorporate a variable ice-ocean drag via parameterization of form drag (directly, *Tsamados et al.*, 2014; or indirectly, *Steiner*, 2001) show first-order impacts both on the sea ice (*Castellani et al.*, 2018) and the underlying ocean (*Martin et al.*, 2016; *Castellani et al.*, 2015, 2018). Although form drag parameterizations of the ice-ocean drag provide a nice theoretical description for the relationship between sea ice morphology and the ice-ocean drag coefficient(*Lu et al.*, 2011; *Tsamados et al.*, 2014), until now there has been no detailed observational study comparing morphological features with observed values of C_{io} across a range of sea ice conditions.

In this study, we present observations made over an annual cycle from an array of moorings in the Beaufort Sea. Using a force-balance approach, mooring measurements and atmospheric re-analysis data are used to infer ice-ocean drag coefficients. Uplooking sonar on the moorings provide snapshots of under-ice topography and statistics related to ice keels and floe edges. Together, these results 1) provide insight into the morphological drivers underlying variations of the ice-ocean drag coefficient, 2) are used for evaluation of model parameterization schemes, and 3) provide context for a broader understanding of momentum transfer into the upper ocean in the changing Arctic. The remainder of this

Table 4.1: Notation

a_i	ice covered area	S_c	sheltering function
a_{rdg}	area covered in ridged ice	s_l	attenuation parameter
b_1, b_2, A_*	geometry parameters	$\boldsymbol{u}$	generic bulk velocity
A	ice concentration	$\boldsymbol{u}_*$	friction velocity
c_f	floe-edge drag coefficient of resistance	$\boldsymbol{u}_a$	wind velocity at 10 m
c_k	keel drag coefficient of resistance	$\boldsymbol{u}_i$	ice drift velocity
c_s	skin drag coefficient of resistance	$\boldsymbol{u}_o$	ocean velocity at a reference depth
C_d	generic drag coefficient	$\boldsymbol{u}_g$	geostrophic ocean velocity
C_f	form drag from floe edges	$\boldsymbol{u}_{rel}$	ice-ocean relative velocity
C_k	form drag from keels	v_{rdg}	volume of ridged ice
C_s	skin drag	z_0	roughness length
C_{ao}	atmosphere-ocean drag coefficient	z_{0i}	level ice bottom roughness length
C_{ai}	atmosphere-ice drag coefficient	z_{0w}	roughness length water
C_{io}	ice-ocean drag coefficient	z_{ref}	reference depth
C_{equiv}	atmosphere-ocean equivalent drag	α_k	keel slope
d_i	ice draft	β	turning angle
d_{lvl}	level ice draft	η	sea surface displacement
f	Coriolis parameter	κ	von Kármán constant (= 0.41)
$\boldsymbol{F}_a$	ice acceleration force	ρ	fluid density
$\boldsymbol{F}_i$	ice interaction force	ρ_a	air density
g	gravitational acceleration	ρ_i	ice density
h_i	ice thickness	ρ_o	ocean density
h_k	keel depth (generic)	$\boldsymbol{\sigma}$	internal ice stress tensor
$h_{k\mathrm{rel}}$	relative keel depth	$\boldsymbol{\tau}$	surface stress
$h_{k\mathrm{tot}}$	total keel depth	$\boldsymbol{\tau}_{ai}$	atmosphere-ice stress
ℓ_f	floe length	$\boldsymbol{\tau}_{ao}$	atmosphere-ocean stress
ℓ_k	keel spacing	$\boldsymbol{\tau}_{io}$	ice-ocean stress
ℓ_l	lead length	$\boldsymbol{\tau}_{oi}$	ocean-ice stress
m_e	effective ice mass per unit area	$\boldsymbol{\tau}_{ocn}$	total ocean stress
m_w	skin drag attenuation parameter	$\boldsymbol{\tau}_{atm}$	total atmosphere stress
P_0	boundary-layer integration function	ϕ_k	keel porosity

chapter is organized as follows: sections 4.1.1 and 4.1.2 provide additional background about momentum fluxes across the atmosphere-ice-ocean interface (with focus on the sea ice momentum equation and the total atmosphere-ocean momentum flux). Section 4.2 provides a review of the geometry-based parameterization schemes developed by *Lu et al.* (2011) and *Tsamados et al.* (2014), thus giving important context for interpreting the study results. In section 4.3 we describe the field study and measurements, along with the force-balance and geometry-based descriptions of the ice-ocean drag coefficient. Descriptions of variations in C_{io}, along with evaluation of the parameterization schemes, and a description of the morphological drivers of ice-ocean drag are presented in section 4.4. Then, in section 4.5, these results are placed in the context of previous observations of ice-ocean drag and total momentum flux. The main contributions of the study are summarized in section 4.6.

4.1.1 *The sea ice momentum equation*

The conservation of momentum of sea ice can be written as (e.g., *Heorton et al.*, 2014):

$$m_e\left[\underbrace{\frac{\partial \boldsymbol{u}_i}{\partial t}}_{\text{I}} + \underbrace{\boldsymbol{u}_i \cdot \nabla \boldsymbol{u}_i}_{\text{II}} + \underbrace{f\hat{\boldsymbol{k}} \times \boldsymbol{u}_i}_{\text{III}}\right] = \underbrace{A\boldsymbol{\tau}_{ai}}_{\text{IV}} + \underbrace{A\boldsymbol{\tau}_{oi}}_{\text{V}} + \underbrace{\boldsymbol{\nabla} \cdot \boldsymbol{\sigma}}_{\text{VI}} + \underbrace{m_e g \boldsymbol{\nabla} \eta}_{\text{VII}}, \tag{4.2}$$

for m_e the "effective" ice mass per unit area, $m_e = A\rho_i h_i$, and other variables as defined in table 4.1, with ∇ the horizontal gradient operator. This form of the sea ice momentum equation is consistent with that presented by *Leppäranta* (2011), but modified to ensure consistent scaling for mixed ice-open water conditions (per *Hunke and Dukowicz*, 2003; *Connolley et al.*, 2004). The terms of the equation are as follows: (I) local ice acceleration; (II) advective ice acceleration; (III) Coriolis acceleration; (IV) stress of the atmosphere acting on the ice; (V) stress of the ocean acting on the ice; (VI) internal stress ("ice-ice" stress); and (VII) gravitational force from sea surface tilt. Advective acceleration (term II) is generally considered negligible and excluded. The final term (VII) in eq. (4.2) can be expressed in terms of the geostrophic balance $f\hat{\boldsymbol{k}} \times \boldsymbol{u}_g = g\nabla\eta$ and then combined with the Coriolis term, so that term III becomes $f\hat{\boldsymbol{k}} \times (\boldsymbol{u}_i - \boldsymbol{u}_g)$ (*Leppäranta*, 2011). An additional term representing wave radiation stress in the marginal ice zone has been shown to be locally important at the ice edge (e.g., *Perrie and Hu*, 1997; *Steele et al.*, 1989; *Thomson et al.*, 2021), but overall is small, so it is neglected. *Leppäranta* (2011) also includes an atmospheric pressure gradient term which is not included here. In mixed ice-open water conditions, the ocean-ice and atmosphere-ice stresses ($\boldsymbol{\tau}_{ai}$ and $\boldsymbol{\tau}_{oi}$) represent the stress acting only on the ice-covered area and are distinct from the total stress out of the ocean/atmosphere (*Hunke and Dukowicz*, 2003).

Sea ice is considered to be in "free drift" if the internal ice stress (term VI) is negligible (e.g., *McPhee*, 1980; *Hunke and Dukowicz*, 2003; *Connolley et al.*, 2004; *Leppäranta*, 2011). This is often assumed to be the case if the ratio of ice speed to wind speed ($|\boldsymbol{u}_i|/|\boldsymbol{u}_a|$, the "wind factor") is sufficiently high (typically $\geq$2%; e.g., *McPhee*, 1980), or if ice concentration is sufficiently low (e.g., $\leq$85%; *Hunke and Dukowicz*, 2003; *Heorton et al.*, 2019). For freely drifting sea ice, the ice-ocean stress ($\boldsymbol{\tau}_{io} = -\boldsymbol{\tau}_{oi}$) can be expressed as:

$$\boldsymbol{\tau}_{io} = \boldsymbol{\tau}_{ai} - \rho_o d_i \left[\frac{\partial \boldsymbol{u}_i}{\partial t} + f\hat{\boldsymbol{k}} \times (\boldsymbol{u}_i - \boldsymbol{u}_g) \right], \tag{4.3}$$

where the sea ice mass per unit area $\rho_i h_i$ (for ice density ρ_i and total ice thickness h_i) has been replaced with $\rho_o d_i$ (for ocean density ρ_o and ice draft d_i) assuming hydrostatic balance. *McPhee* (1980) and *Dewey* (2019) use this balance, assuming steady-state ($\frac{\partial \boldsymbol{u}_i}{\partial t} = 0$), in order to calculate ice-ocean stress and infer the ice-ocean drag coefficient, while *Randelhoff et al.* (2014) employ this equation retaining the local acceleration. The ice-ocean stress is also frequently presented in terms of friction velocity, u_*, defined by $\boldsymbol{\tau}_{io} = \rho_o \boldsymbol{u}_* |\boldsymbol{u}_*|$.

4.1.2 Total momentum flux into the ocean

Using the quadratic drag law (eq. 4.1), the ice-ocean stress, $\boldsymbol{\tau}_{io}$, and atmosphere-ice stress, $\boldsymbol{\tau}_{ai}$, are written as:

$$\boldsymbol{\tau}_{io} = \rho_o C_{io} \boldsymbol{u}_{rel} \left| \boldsymbol{u}_{rel} \right| , \tag{4.4a}$$

$$\boldsymbol{\tau}_{ai} = \rho_a C_{ai} \boldsymbol{u}_a \left| \boldsymbol{u}_a \right| , \tag{4.4b}$$

where the ice-ocean stress uses the relative ice-ocean horizontal velocity, $\boldsymbol{u}_{rel} = \boldsymbol{u}_i - \boldsymbol{u}_o$, as a bulk velocity, while the atmosphere-ice stress uses the wind speed, $\boldsymbol{u}_a$ (for other variable definitions, see table 4.1). The atmosphere-ice stress is also sometimes written with an atmosphere-ice relative velocity $\boldsymbol{u}_a - \boldsymbol{u}_i$ as the bulk velocity (mirroring the use of relative velocity in the ice-ocean stress), but since typically $\boldsymbol{u}_a \gg \boldsymbol{u}_i$, the ice velocity is frequently neglected from eq. (4.4b). It is also common to include a rotation matrix in eq. (4.4a) to account for unresolved Ekman turning in the boundary layer (if the velocity is expressed as a complex exponential, $\boldsymbol{u} = u + iv$, then this is achieved by multiplying eq. 4.4a by $e^{i\beta}$ for turning angle β). While also occasionally included in eq. (4.4b), the much greater boundary layer heights in the atmosphere compared to the ocean means that there typically is not unresolved Ekman turning there, so it is not necessary to include an equivalent rotation matrix for calculating the atmosphere-ice stress (note that even with no atmospheric turning, there can still be an offset in wind direction and ice drift direction due to other forces in the sea ice momentum equation, and this offset is also occasionally referred to as a turning angle). Under-ice Ekman layers are not a subject of the present study, so rotation matrix is not included in eq. (4.4a), but we will accept values of $\boldsymbol{\tau}_{io}$ that are not aligned with $\boldsymbol{u}_{rel}$ that result from the presence of Ekman turning.

In mixed ice and open-water conditions, there is both a direct transfer of momentum between the atmosphere and the ocean, and an indirect transfer mediated by sea ice. It is common to represent these fluxes as combinations of the corresponding atmosphere-ice-ocean stresses weighted by sea ice concentration (e.g., *Martin et al.*, 2014, 2016). Then, the total momentum flux into the ocean, $\boldsymbol{\tau}_{ocn}$, and the total momentum flux out of the atmosphere $\boldsymbol{\tau}_{atm}$ can be represented as:

$$\boldsymbol{\tau}_{ocn} = A\boldsymbol{\tau}_{io} + (1 - A)\boldsymbol{\tau}_{ao}, \quad \text{and} \tag{4.5a}$$

$$\boldsymbol{\tau}_{atm} = A\boldsymbol{\tau}_{ai} + (1 - A)\boldsymbol{\tau}_{ao}, \tag{4.5b}$$

where A is sea ice concentration, and each of the stress components (ice-ocean: $\boldsymbol{\tau}_{io}$; atmosphere-ice: $\boldsymbol{\tau}_{ai}$; atmosphere-ocean: $\boldsymbol{\tau}_{ao}$) is described by the quadratic drag law with corresponding drag coefficients: $\boldsymbol{\tau}_{ao} = \rho_a C_{ao} \boldsymbol{u_a} |\boldsymbol{u_a}|$, and $\boldsymbol{\tau}_{io}$, $\boldsymbol{\tau}_{ai}$ from eqs. (4.4a) and (4.4b). As a first approximation, the atmosphere-ocean drag coefficient, C_{ao}, can be described as a function of wind speed (e.g., *Large and Yeager*, 2004). The atmosphere-ice drag coefficient, C_{ai}, is expected to depend on sea ice geometry in a similar way to the ice-ocean drag (*Andreas*, 2011; *Lüpkes et al.*, 2012; *Tsamados et al.*, 2014); however, it is sometimes parameterized simply as a function of ice concentration, A (see appendix 4.C), or taken as a constant (then the equivalent total atmospheric drag coefficient is still a function of ice concentration per eq. 4.5b; see *Elvidge et al.*, 2016 for additional details and a comparison of atmospheric drag coefficient relationships with sea ice concentration for a variety of models).

Combining eqs. (4.2), (4.5a) and (4.5b) leads to the expression:

$$\boldsymbol{\tau}_{ocn} = \boldsymbol{\tau}_{atm} + \boldsymbol{F}_i + \boldsymbol{F}_a, \tag{4.6}$$

where $\boldsymbol{F}_i$ is the ice interaction force (derived from the inclusion of term VI in eq. 4.2), and $\boldsymbol{F}_a$ is the equivalent force from the acceleration and tilt terms (terms I, III, VII in eq. 4.2; i.e., the term in brackets in eq. 4.3). Equation (4.6) mirrors the expression from *Martin et al.* (2014, their equation 2), except for the inclusion of the equivalent forces from ice acceleration, $\boldsymbol{F}_a$, which they neglect.

In the scenario where the transfer of momentum is an overall flux from the atmosphere into the ocean, this equation can be interpreted to state that all of the momentum flux out of the atmosphere ($\boldsymbol{\tau}_{atm}$) goes into either the ice ($\boldsymbol{F}_i + \boldsymbol{F}_a$), or into the ocean ($\boldsymbol{\tau}_{ocn}$). Although, because of the vector summation in eq. (4.6), both of $\boldsymbol{F}_i$ and $\boldsymbol{F}_a$ can either enhance or subtract from $\boldsymbol{\tau}_{atm}$. Ice interaction is usually thought as a momentum sink that opposes $\boldsymbol{\tau}_{atm}$ (*Steele et al.*, 1997; *Martin et al.*, 2014), but ice acceleration terms could potentially be an additional source of ocean momentum.

To examine the effect of sea ice in mediating the total momentum flux from the atmosphere to the ocean, consider an "equivalent drag coefficient", C_{equiv}, based on the construction of a quadratic drag law between the wind speed and the total ocean stress; i.e.,

$$C_{equiv} = \frac{|\boldsymbol{\tau}_{ocn}|}{\rho_a |\boldsymbol{u}_a|^2}. \tag{4.7}$$

C_{equiv} does not have a clean analytic form, nor is it a useful prognostic variable: its value will depend on $\boldsymbol{u}_i$ and $\boldsymbol{u}_o$, which are themselves functions of the total atmosphere-ice-ocean momentum transfer. Instead, C_{equiv} is a diagnostic of momentum transfer efficiency, where higher values indicate that a greater proportion of atmospheric momentum is ultimately transferred to the ocean. This is similar to the use of a normalized effective stress in *Martin et al.* (2014, 2016).

4.2 *Drag from geometry-based parameterizations*

This study compares estimates of the observed ice-ocean drag to two schemes that parameterize the ice-ocean drag as a function of the observable ice geometry. Both *Lu et al.* (2011) and *Tsamados et al.* (2014) present similar ice geometry-based parameterizations of the ice-ocean drag coefficient based on a combination of skin and form drag components, with the scheme by *Tsamados et al.* (2014) available in the CICE sea ice model (*Hunke et al.*, 2020). *Steiner* (2001) presents an alternative scheme using a "deformation energy" approach. That method has been used in the sea ice component of the MITgcm model (*Losch et al.*, 2010) to investigate the impact of variable ice-ocean drag (*Castellani et al.*, 2018); however, we cannot track deformation energy with our measurements, so the deformation energy scheme is not considered here. Strictly, ice geometry-based parameterizations in the forms presented below only model the neutral ice-ocean drag coefficients and do not account for the impacts of stabilizing or destabilizing buoyancy fluxes. Buoyancy fluxes modify the total drag, and are included in atmospheric models as correction term to the neutral drag coefficient, based on Monin-Obukhov similarity theory (*Monin and Obukhov*, 1954)(which could be included in sea ice models using a parameterization by *Lüpkes and Gryanik*, 2015). We are unable to account for stability effects in the present study, which may modify some interpretations of the results.

4.2.1 *Details of parameterization schemes*

Ice-geometry based parameterizations of the ice-ocean drag coefficient write the total drag as a sum of form drag from floe edges, form drag from keels, and skin drag (*Lu et al.*, 2011; *Tsamados et al.*, 2014):

$$C_{io} = C_f + C_k + C_s. \tag{4.8}$$

For both schemes, these three drag components can be written as:

$$\text{floe edge drag:} \quad C_f = \frac{1}{2} c_f A \frac{d_{lvl}}{\ell_f} \left[S_c \left(\frac{d_{lvl}}{\ell_l} \right) \right]^2 P_0(d_{lvl}, z_{0w}), \tag{4.9a}$$

$$\text{keel drag:} \quad C_k = \frac{1}{2} c_k A \frac{h_k}{\ell_k} \left[S_c \left(\frac{h_k}{\ell_k} \right) \right]^2 P_0(h_k, z_{0i}), \tag{4.9b}$$

$$\text{skin drag:} \quad C_s = c_s A \left(1 - m_w \frac{h_k}{\ell_k} \right), \quad \text{if } \frac{h_k}{\ell_k} \leq \frac{1}{m_w} \tag{4.9c}$$

with variables defined in table 4.1. So the ice geometry appears in the parameterizations as the floe "aspect ratio", d_{lvl}/ℓ_f, and the "ridging intensity", h_k/ℓ_k. The scheme by *Tsamados et al.* (2014) is an adaptation of an atmospheric drag parameterization by *Lüpkes et al.* (2012). Note that in *Tsamados et al.* (2014), the inequality in the valid range for the skin drag, C_s ($h_k/\ell_k \leq 1/m_w$), is mistakenly reversed (compare their eq. 19 with the work of *Arya*, 1975 on which skin drag is based); eq. (4.9c) presents the correct inequality for both of the parameterization schemes.

The two schemes are functionally similar. The differences between them are due to the following factors: (1) different values of the coefficients of resistance, c_f, c_k, and c_s

(which account for the drag on individual elements); (2) different forms of the "sheltering functions" S_c; and (3) the inclusion (or not) of the functions P_0 (which are included in the *Tsamados et al.*, 2014 scheme but not in the *Lu et al.*, 2011 scheme). Additionally, the two schemes use slightly different definitions for keel depth (relative versus total; see fig. 4.1).

The sheltering function S_c accounts for the reduction in drag of downstream obstacles due to the wake effect of upstream obstacles (*Steele et al.*, 1989). Both parameterization schemes employ different, empirically-derived, sheltering functions:

$$\text{Tsamados et al. (2014):} \qquad S_c\left(x\right) = \left[1 - \exp\left(-\frac{s_l}{x}\right)\right]^{1/2} \tag{4.10a}$$

$$\text{Lu et al. (2011):} \qquad S_c\left(x\right) = \left[1 - \left(x\right)^{1/2}\right] \tag{4.10b}$$

For keel sheltering, the input argument, x, is the the ridging intensity, h_k/ℓ_k, which mirrors its other use eq. (4.9b). For floe sheltering, the argument for the sheltering function is d_{lvl}/ℓ_l (the denominator is the distance between floes), instead of the aspect ratio d_{lvl}/ℓ_f that appears earlier in eq. (4.9a).

Tsamados et al. (2014) include a term in C_f and C_k which arises due to integration of a depth-varying velocity profile over the height of an obstacle, here called P_0 (it differs from the definition of P_0 in *Lüpkes et al.*, 2012). In the atmospheric drag parameterization, *Lüpkes et al.* (2012) assume a "law-of-the-wall" velocity profile: $u(z) = (u_*/\kappa)\ln(z/z_0)$, which *Tsamados et al.* (2014) maintains in adapting the scheme to the ice-ocean boundary layer. This gives

$$P_0(h, z_0) = \left[\frac{\ln(h/z_0)}{\ln(z_{\text{ref}}/z_0)}\right]^2, \tag{4.11}$$

where the input variable h is either the level ice draft, d_{lvl} or keel depth, h_k for floe edge drag or keel drag, respectively, and an appropriate choice of roughness length is used (see eqs. 4.9a, 4.9b). Inclusion of P_0 allows the ice-ocean drag coefficient to be an explicit function of the reference depth z_{ref}. The form of P_0 depends on the assumed law-of-the-wall boundary-layer structure, which is suitable for the atmosphere where the height of logarithmic boundary layer typically much greater than the reference height

z_{ref} (e.g., *Holton*, 2004, chapter 5). However, it is not clear that this is appropriate in the ice-ocean boundary layer. The P_0 functions are not included in the scheme by *Lu et al.* (2011).

The coefficient of resistance, c_s used in the skin drag parameterization (C_s, eq. 4.9c) represents the baseline skin drag associated with level ice in the absence of ridges. Both *Tsamados et al.* (2014) and *Lu et al.* (2011) treat this term as a free parameter. Keeping with the law-of-the-wall velocity assumption used to develop P_0, the baseline skin drag could instead be represented by

$$c_s = \left[\frac{\kappa}{\ln(z_{\mathrm{ref}}/z_{0i})}\right]^2, \tag{4.12}$$

where the von Kármán constant $\kappa = 0.41$. This reduces the number of free parameters in the model, and allowing c_s to be an explicit function of the reference depth z_{ref}. As with P_0, the actual form will depend strongly on boundary layer structure.

In applying their parameterization scheme (eqs. 4.9, 4.10a, and 4.11), *Tsamados et al.* (2014) use total keel depth, $h_{k\mathrm{tot}}$, which is measured from the waterline (fig. 4.1) as the definition of h_k. However, in full ice cover, it should be the keel depth relative to the level ice draft, $h_{k\mathrm{rel}}$, that contributes to form drag (as in *Lu et al.*, 2011) (note: $h_{k\mathrm{tot}} = h_{k\mathrm{rel}} + d_{lvl}$). Similarly, the reference depth z_{ref} in eqs. (4.11) and (4.12) should also be relative to the level ice draft (e.g., $z_{\mathrm{ref}} - d_{lvl}$), because that is the range over which the boundary layer develops. In mixed ice-open water conditions, the use of $h_{k\mathrm{rel}}$ is still consistent with the parameterization scheme as floe-edge drag (eq. 4.9a) is accounted for separately.

4.2.2 Translating model outputs to ice geometry

The details of sea ice geometry necessary for calculating the ice-ocean drag coefficient with eq. (4.9) are not generally resolved by models, which do not simulate individual ice floes or keels. *Tsamados et al.* (2014) developed a scheme for estimating average keel properties based on outputs in the CICE model using assumptions about the keel geometry that are guided by observations (see their supplementary information). Namely, the scheme

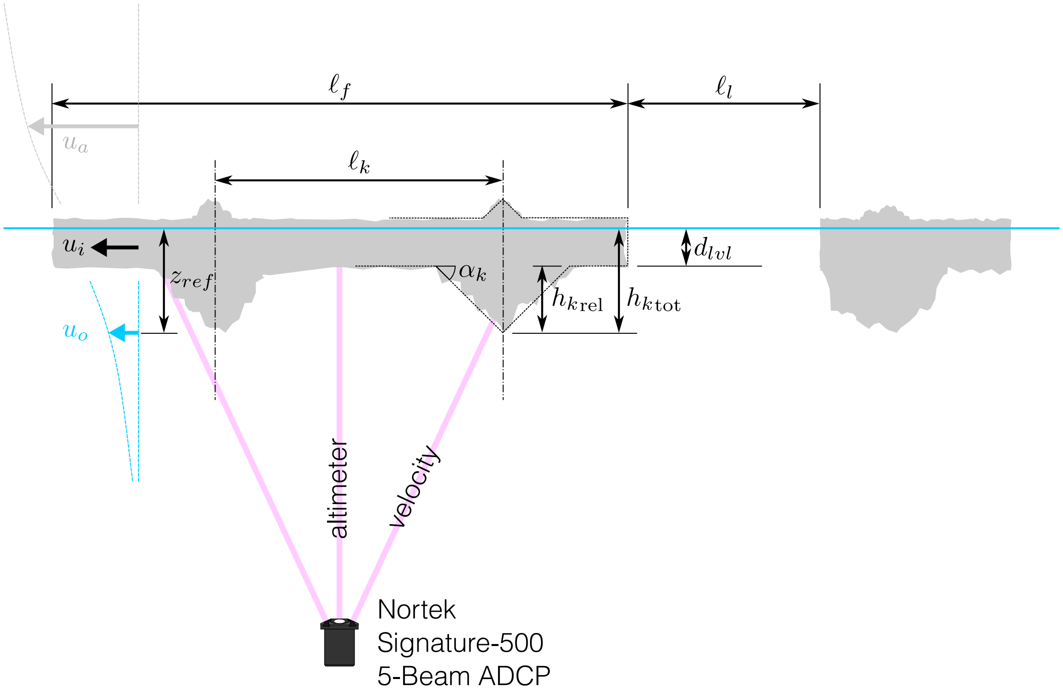

Figure 4.1: Schematic representation of an ice floe showing sea ice geometry with idealized triangular representation of ice keels, and the in-situ ADCP measurements. Dimension labels of ice geometry correspond to table 4.1.

uses area extent and volume of ridged ice in a model grid cell (a_{rdg} and v_{rdg}, respectively), along with the ice area in a grid cell (a_i, which is the ice concentration A multiplied by the grid-cell area).

For subsurface measurements (as presented below), keel depth and keel spacing are given by taking the limit as $R_h \rightarrow \infty$ in equations 24 and 25 from *Tsamados et al.* (2014) (where R_h is the ratio of keel depth to sail height, so the limit states that all ridged ice in the measurements is attributed to keels). This gives the expressions:

$$h_k = 2\frac{v_{rdg}}{a_{rdg}}\frac{b_1}{\phi_k}, \tag{4.13a}$$

$$\ell_k = 2h_k\frac{a_i}{a_{rdg}}\frac{b_1}{\tan(\alpha_k)}, \tag{4.13b}$$

where b_1 is a weight function accounting for the overlap of keels with level ice (taken as 0.75), ϕ_k is the keel porosity (taken as 1), and α_k is the keel slope (see fig. 4.1).

The floe and lead lengths (ℓ_f, ℓ_l) used in eq. (4.9a) are also parameterized. Using measurements derived from aerial photographs of the marginal ice zone of Fram Strait, *Lüpkes et al.* (2012) developed an empirical model for estimating floe size based on ice concentration:

$$\ell_f = \ell_{f,min}\left(\frac{A_*}{A_* - A}\right)^{b_2}, \tag{4.14}$$

with b_2 a tunable parameter (ranging from 0.3 to 1.4), and A_* a value calculated such that the limits of ℓ_f range from $\ell_{f,min}$ to $\ell_{f,max}$ (for $A \rightarrow 0, 1$), the minimum and maximum floe lengths, respectively (see eq. 27 in *Lüpkes et al.*, 2012). Using default parameters, this gives average floe lengths that are limited to range from a minimum of 8 m to a maximum of 300 m. *Tsamados et al.* (2014) implement this floe size model in their parameterization scheme, though they acknowledge that observations have shown that floe size follows a power-law distribution with a much wider range of scales than is possible with that scheme (e.g., *Weiss and Marsan*, 2004; see also *Stern et al.*, 2018 and references therein). They further acknowledge that this scheme may breakdown in the winter when ice concentration is near 100%, given that the parameterization was developed for the marginal ice zone; but it is employed through the full year nonetheless.

4.3 *Drag from field measurements*

4.3.1 *Field measurements*

Data were collected during the Stratified Ocean Dynamics of the Arctic (SODA) experiment: an Office of Naval Research (ONR) project to better understand the controls of heat and momentum transfer in the Arctic's upper ocean. A program component included the installation of three subsurface moorings in a line stretching from the south to the north of the Beaufort Sea, which are designated as SODA-A, SODA-B, and SODA-C (figs. 4.2a and b). The moorings recorded a full annual cycle of sea ice growth and melt from their installation in fall 2018 to their recovery in fall 2019. The spatial distribution of the moorings allowed for sampling of different ice regimes: the southernmost mooring (SODA-A) was in the seasonal ice zone and experienced prolonged open-water periods in summer (fig. 4.2e); SODA-B was near the edge of the seasonal ice zone and has a minimal open-water period but a longer period of time in marginal ice (fig. 4.2d); whereas SODA-C was still ice-covered all year long (fig. 4.2c; the mooring at that location was both deployed and recovered through the ice).

This study utilizes measurements made with uplooking Nortek Signature-500 5-beam acoustic Doppler current profilers (ADCPs) installed on the top float of each mooring (fig. 4.1). The instrument depths were approximately 45 m for SODA-A, 42 m for SODA-B, and 27 m for SODA-C. To minimize the effects of mooring knock-down, the top float of each mooring was a DeepWater Buoyancy Stablemoor500, which are designed to remain level even during knockdown events (*Harding et al.*, 2017). The maximum tilt deviation measured by any of the ADCPs was $\leq 2^\circ$ from their resting position. A Seabird SBE-37 conductivity-temperature-depth sensor installed underneath the float ($\sim$1 m vertical offset from the ADCP) collected temperature and salinity measurements to compliment the temperature measurements made by the ADCP to calculate and correct the speed of

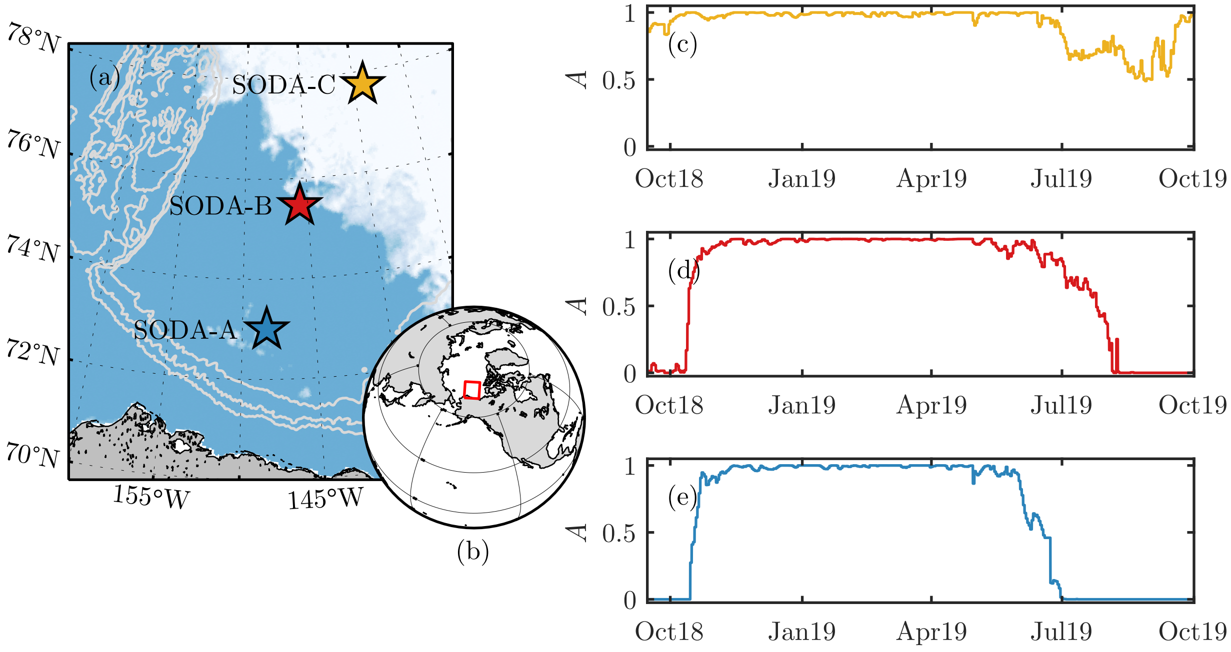

Figure 4.2: (a,b) Maps of (a) the Beaufort Sea showing the locations of the three moorings overlaid on sea ice concentration map from Sept. 18, 2018 (the 2018 sea ice minimum), with baythymetry shown by grey contours (contours are 1000-m isobaths); and (b) the location of (a). The ice concentration in (a) is from the Sea Ice Remote Sensing database at the University of Bremen (*Spreen et al.*, 2008). (c–e) The annual cycle of sea ice concentration averaged over the mooring locations during the measurement period: (c) SODA-C, (d) SODA-B, and (e) SODA-A.

sound (which is used to calculate altimeter distance).

The four slant beams of the ADCP measured velocity profiles, while the fifth vertical beam acted as an altimeter (fig. 4.1) and measured the distance to the surface (either the water surface or ice bottom). The vertical beam has a beam width of 2.9°, so for the deployment depths here, the width of the ensonified area was roughly 2.3 m for SODA-A, 2.1 m for SODA-B, and 1.4 m for SODA-C. The ADCPs operated with two concurrent sampling plans: "Average+Ice", and "Burst+Waves". For both modes, the ice draft was derived from the difference between the water depth (determined by instrument pressure) and altimeter distance, after making corrections for ADCP tilt, speed of sound, and atmospheric pressure variations (e.g., *Magnell et al.*, 2010; *Krishfield et al.*, 2014).

During the Average+Ice sampling mode, the ADCP measured altimeter distance, water column velocity, and ice drift velocity. Ice drift velocities were measured using the instrument's built-in ice-tracking mode, which functions similarly to traditional ADCP "bottom-tracking": a ping is emitted separate to the water velocity-measuring pings with longer pulse-length that fully ensonifies the ice area for the full beam width and provides velocity measurements that are typically more accurate than in the water column (e.g., *Belliveau et al.*, 1989). Measurements of each of the variables were provided every 10 min based on raw data collected in 1-min long ensembles at a sampling rate of 1 Hz (reported measurements are ensemble-medians after quality control processing of the raw data). The water velocities were measured in 2-m vertical range bins. Due to sidelobe interference, the upper $\sim$ 10% of each vertical velocity profile (2.7–4.5 m) was discarded, so near-ice logarithmic boundary layers could not be directly observed. At each time step the velocity profiles were interpolated to find the horizontal velocity, $\boldsymbol{u}_o$, at a fixed reference depth, z_{ref}; here, $z_{ref} = 10$ m to conform to the *Tsamados et al.* (2014) parameterization scheme. The 10-min sampled Average+Ice measurements of $\boldsymbol{u}_i$, $\boldsymbol{u}_o$, and d_i were bin-averaged in 1-h bins to match the atmospheric re-analysis measurements used (see below). The fig. 4.13 shows examples of the timeseries of each of the velocity components at SODA-B.

As indicated by its name, the Burst+Waves plan is designed for the measurement of surface gravity waves using altimeter measurements from the vertical beam. However, those altimeter measurements can also be used for measuring under-ice geometry (e.g., ice keels; *Magnell et al.*, 2010). In Burst+Waves mode, the ADCPs measured "bursts" of data containing 2048 samples at a rate of 2 Hz, so each burst length was 1024 s ($\sim$ 17 min). These bursts were collected once every two hours. Because the Burst+Waves and Average+Ice measurement plans were concurrent, the ADCPs recorded two values of the ice drift speed during each burst. Using the mean of those two ice drift measurements, the sampling time for each burst was converted to an along-burst distance. Within each burst, ice draft data were despiked using a moving-median outlier criteria in 127-point windows (outliers are identified as points more than three scaled median absolute deviations from the median, and replaced with linearly interpolated values). Then, the ice draft from Burst+Waves sampling were used to characterize the ice geometry (see section 4.3.3).

We used atmospheric forcing from the European Center for Medium-Range Weather Forecasts (ECMWF) Reanalysis version 5 (ERA5; *Hersbach et al.*, 2020). ERA5 provides hourly measurements at a 0.25° × 0.25° grid resolution. A recent comparison with in situ measurements in the Eastern Arctic showed that of the six re-analysis products assessed, ERA5 provided the best representation of wind speed (which is the primary variable of interest here) during winter and spring, and second best (by a small margin) during summer (*Graham et al.*, 2019a). To generate a timeseries of atmospheric forcing at each mooring, grid points were averaged within a 30 km radius centred at each of the mooring locations (14–16 gridpoints per mooring). There is a degree of uncertainty in re-analysis wind measurements in the Arctic (particularly in the marginal ice zone; e.g., *Brenner et al.*, 2020). Nonetheless, there is strong coherence between the re-analysis wind velocities and the in situ measured ice drift velocities (not shown) and associated high correlations between the two (correlation coefficients of $r = 0.69$, 0.75, and 0.63 for SODA-A, -B, and -C, respectively). To test sensitivity, wind velocities at the mooring locations were also found using two alternative re-analysis products: Modern-Era Retrospective analysis for Research and Applications version 2 (MERRA-2; *Gelaro et al.*, 2017) and Japanese 55-year Reanalysis (JRA-55; *Kobayashi et al.*, 2015, which is on a slightly coarser grid in both space and time). Across these different products, wind velocities at the mooring locations were very similar; MERRA-2 wind velocities were correlated with ERA5 winds with $r = 0.97$ across all three moorings, and JRA-55 were correlated with ERA5 with $r = 0.96$ (after subsetting ERA5 to the same timestamps). Resulting drag coefficient measurements (calculated per section 4.3.2) were correlated with $r = 0.94$ between MERRA-2 and ERA5, and $r = 0.84$ between JRA-55 and ERA5. Thus, the results presented in this study are not overly sensitive to the choice of re-analysis product used.

4.3.2 *Application of the force-balance approach*

Following *McPhee* (1980; see also *Randelhoff et al.*, 2014; *Dewey*, 2019), we use a force-balance approach (eq. 4.3) to calculate the ice-ocean stress, $\boldsymbol{\tau}_{io}$. Then the ice-ocean drag coefficient, C_{io}, is inferred from the quadratic drag law (eq. 4.4a).

The ice-ocean stress ($\boldsymbol{\tau}_{io}$) is calculated hourly with eq. (4.3) using data from the ADCP measurements and ERA5 re-analysis. The ice draft (d_i) and ice velocity ($\boldsymbol{u}_i$) are from the 1-hour-averaged ADCP measurements. The local acceleration ($\frac{\partial \boldsymbol{u}_i}{\partial t}$) is the numerical derivative of the 1-hour-averaged $\boldsymbol{u}_i$ values. The geostrophic velocity ($\boldsymbol{u}_g$) is estimated as the depth-averaged velocity between $5\,\mathrm{m}$ and $20\,\mathrm{m}$ (based on results by *Armitage et al.*, 2017), and low-pass filtered with a 2-day cutoff (the result is insensitive to these choices for $\boldsymbol{u}_g$; see appendix 4.B). The atmosphere-ice stress ($\boldsymbol{\tau}_{ai}$) is determined using the quadratic drag law (eq. 4.4b), with 10-m wind velocity and surface air density taken from ERA5 re-analysis and C_{ai} parameterized as a function of ice concentration (following *ECMWF*, 2019a; see appendix 4.C). In mixed ice-open water conditions, the atmosphere-ice stress, $\boldsymbol{\tau}_{ai}$, used in eq. (4.3) is distinct from the total atmospheric stress (eq. 4.5b). Because eq. (4.3) assumes that ice is in free drift, values for which the wind factor ($|\boldsymbol{u}_i|/|\boldsymbol{u}_a|$; determined hourly) was less than 2% were rejected (the so-called "2%-rule"). The use of wind factor as a filtering criteria implies an intermittency of internal ice stresses, which is consistent with *Steele et al.* (1997), who found that on short timescales the atmospheric stress input to the ice ($\boldsymbol{\tau}_{ai}$) was primarily balanced by only one of either the ocean-ice stress ($\boldsymbol{\tau}_{oi}$) or the internal ice stress. ($\nabla \cdot \boldsymbol{\sigma}$). The friction velocity ($\boldsymbol{u}_*$) is determined from $\boldsymbol{\tau}_{io}$ assuming a constant $\rho_o = 1025\,\mathrm{kg\,m^{-3}}$ (with the definition $\boldsymbol{\tau}_{io} = \rho_o \boldsymbol{u}_* |\boldsymbol{u}_*|$).

To calculate the ice-ocean drag coefficient, the record is split into windows. Within each window the quadratic drag law (eq. 4.4a) is applied by regressing hourly calculated values of $|\boldsymbol{u}_*|^2$ (as described above) with hourly measured $|\boldsymbol{u}_{rel}|^2$ (with $\boldsymbol{u}_o$ defined at a

10-m reference depth). Then the value of C_{io} is the slope of the regression line (fig. 4.3). Windows are chosen to be 7 days in length, which provides an average of 80 points in each window (after using the 2%-rule to exclude non-free-drift points). Based on average ice drift speeds, each window covers roughly 75 km of ice (though there is both spatial and temporal variability in the actual window size). While shorter window lengths can resolve some higher frequency variability at the expense of larger uncertainties, the overall seasonal patterns found here are not sensitive to the window length chosen. Regression is performed with a bisquare robust linear fitting algorithm and forced through the origin (*Huber*, 1981). This method iteratively reduces the weighting on outliers, which may occur, for example, from intermittent violation of the free-drift assumption. Performing regression within windows instead of calculating C_{io} on a point-by-point basis (as in *Dewey*, 2019) minimizes the effects of noise and uncertainty (particularly for low values of $\boldsymbol{u}_{rel}$), which may have resulted from a combination of measurement noise, higher frequency temporal variations, or unaccounted stresses (e.g., internal ice stress). Calculated values of the drag coefficient were rejected if the uncertainty in C_{io} was $\geq 2.5 \times 10^{-3}$ (based on a t-test with 95% confidence interval; *Bendat and Piersol*, 1971). High uncertainties in C_{io} occurred most frequently in winter when many of the data were rejected due to free drift conditions not being met. Tests using non-linear fits of the form $|\boldsymbol{\tau}_{io}| \propto |\boldsymbol{u}_{rel}|^n$ (see section 4.5.1) did not produce better fits than the quadratic drag law with $n = 2$ (r^2 values from $n \neq 2$ fits were approximately equal to those with $n = 2$). Given the direct concurrent and collocated measurements of the ice and ocean velocities here, it is not necessary to exclude periods of small ice-ocean relative velocity, a condition often necessary when using satellite remote sensing to estimate ocean velocities (e.g., in *McPhee*, 1980).

This method of drag calculation essentially asks what value of C_{io} would be required to reproduce the observed sea ice motion. In doing so, the method effectively integrates over both the temporal intermittency and the spatial heterogeneity of turbulent momentum fluxes across ice floes and thus provides bulk-average drag coefficient values. These

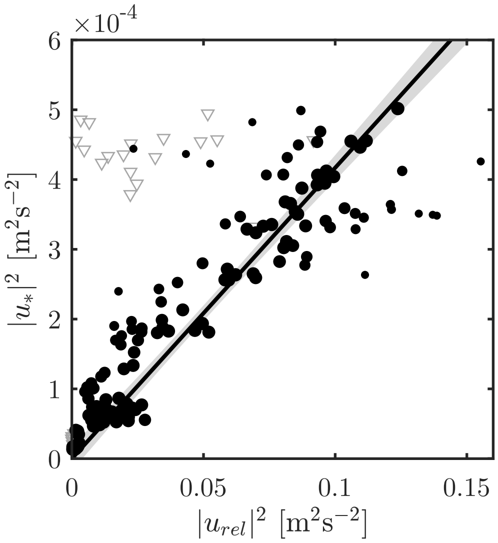

Figure 4.3: Example of quadratic-drag-law fit between hourly values of observed relative velocity ($|\boldsymbol{u}_{rel}|^2 = |\boldsymbol{u}_i - \boldsymbol{u}_o|^2$), and calculated friction velocity ($|\boldsymbol{u}_*|^2 = |\boldsymbol{\tau}_{io}|/\rho_o$) from the force-balance approach (eq. 4.3). Black points show values used in the fitting procedure, with point sizes an indicator of the relative weighting determined by the robust fitting method. Grey triangles show points rejected from the fit by the 2%-rule and demonstrate the utility of the wind factor to filter points that are not in free drift. The black line shows the regression line with 95% confidence interval shaded in grey. Data correspond to 1 week of measurements in November 2018 at SODA-A.

resulting drag coefficients are appropriate for comparison to model parameterizations as the goal of those parameterizations is to provide a bulk coefficient for use within a model grid cell.

There is no physical basis to expect that the relationship between total ocean stress, $\boldsymbol{\tau}_{ocn}$, and wind speed should follow the quadratic drag law, so the linear fitting procedure used to calculate C_{io} cannot be similarly applied to find C_{equiv}. Instead, C_{equiv} is computed on a point-by-point (hourly) basis using eq. (4.7), with $\boldsymbol{\tau}_{ocn}$ given by eq. (4.5a) and with A from ERA5. For points defined as being in free-drift (based on the 2%-rule), the ice-ocean stress, $\boldsymbol{\tau}_{io}$ used in eq. (4.5a) is the same as described above (eq. 4.3). The analysis was extended beyond free-drift periods by calculating $\boldsymbol{\tau}_{io}$ for those times using eq. (4.4a) and values of C_{io} from the regression procedure, interpolated to points with a wind factor $< 2\%$.

4.3.3 *Ice geometry*

During periods of ice cover, the ADCP Burst+Waves sampling provides one dimensional (along-drift) tracking of the under-ice geometry (fig. 4.4a). We use these to quantify the geometric characteristics used in the parameterization schemes in section 4.2. Importantly, the fixed mooring platforms allow for sampling across a broad range of different ice conditions as they evolve over the annual cycle.

Spectral analysis is used as part of a filtering criteria to separate ice-covered conditions from open water conditions; this ensures that surface gravity waves are not erroneously misidentified as ice keels. For each burst, frequency spectra of measured altimeter distances are constructed. Surface gravity waves have distinct and well known spectral shapes (e.g., *Phillips*, 1985), with peaks at relatively high frequencies ($\gtrsim$0.04 Hz), while sea ice has broadly distributed spectral energy with energy concentrated at lower horizontal wavenumbers (which translate to low frequencies) (e.g., *McPhee and Kantha*, 1989). Following *Shcherbina et al.* (2016) and *Kirillov et al.* (2020), ice-covered conditions are identified using the ratio of integrated spectral energy in low- and high-frequency bands (using a cutoff frequency of 0.1 Hz, based on observed conditions): burst are deemed to be ice-covered when the ratio of high-to-low frequency spectral energy is less than 5. Then, bursts identified as being open-water but with measured non-zero level ice draft, d_{lvl}, provide a secondary empirical correction to ice draft measurements to account for water-column sound-speed variations (e.g., due to shallow stratification; *Kirillov et al.*, 2020). These corrections were small, and primarily applied to marginal ice covered periods.

For each ice-covered burst we quantify the draft of level ice, the extent and number of leads, and the number and size of keels (fig. 4.4b). Prior to classification, bursts

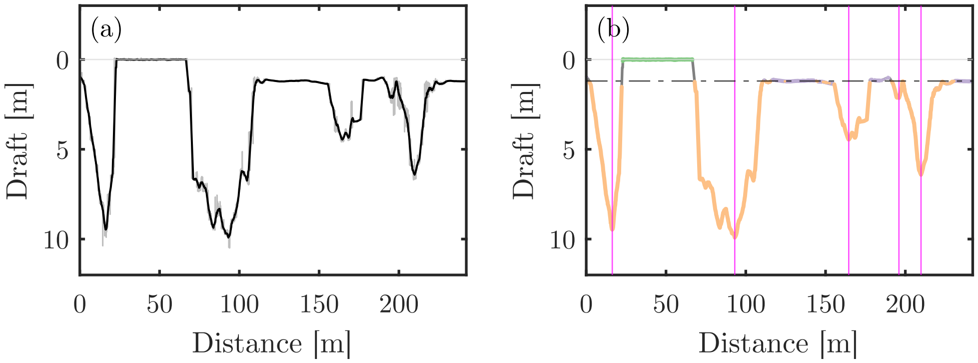

Figure 4.4: Example of ice draft from burst measurements: (a) Raw (thin grey line) and smoothed (black line) ice draft during a single burst (∼17 min) in April 2019 at SODA-A. (b) The burst from (a) classified to show leads (green line), level ice (purple), and ridged ice (orange), with vertical magenta lines showing unique keels (based on Rayleigh criterion), and black dashed-dotted line showing the level ice draft classified for that burst.

are smoothed with a moving-average filter using a centered window with a width of 2 m (because of variability in ice drift speed, the number of points in each window varies from burst to burst). Bursts frequently contained apparent leads, identified as all points in a burst with a measured draft below a tolerance level (taken as 0.15 m to account for instrument noise and uncertainty associated with both atmospheric pressure variations and sound speed). Strictly, this procedure is unable to differentiate between open-water leads and refrozen leads containing thin ice, but from the perspective of the drag parameterizations (section 4.2), both scenarios are dynamically equivalent in that they both contribute to the floe edge form drag. Within each burst, level ice is defined by a local gradient less than 0.025 (equivalent to the process in *Wadhams and Horne*, 1980) and a draft of less than 3 m (roughly the limit of thermodynamic growth; *Maykut and Untersteiner*, 1971). The level ice draft for each burst is then taken as the median draft of all ice identified as level within the burst. In cases where no level ice was identified (i.e., the entire burst measured ridged ice), the level ice draft is found by interpolating across adjacent bursts. Keels identification follows *Martin* (2007), using a

Rayleigh criterion to define unique keels (see also *Williams et al.*, 1975; *Wadhams and Horne*, 1980; *Wadhams and Davy*, 1986) with a minimum keel depth cutoff of 0.5 m relative to the level ice draft for that burst. Relative keel depths at each of the moorings closely followed exponential probability distributions (not shown), which is in line with previous literature (e.g., *Wadhams and Horne*, 1980; *Wadhams and Davy*, 1986), and a total of 14 694 individual keels are identified throughout the full study period (6282, 4305, and 4107 at SODA-A, -B, and -C, respectively). The maximum relative keel depth measured at any of the moorings through the full deployment was 11.4 m at SODA-B. Keel sizes across the three moorings were fairly similar.

The parameterized ice-ocean drag is based on statistical descriptions of the ice geometry (see section 4.2). Statistics are accumulated over one-week periods to be consistent with the windowing procedure for the ice-ocean drag (section 4.3.2). The keel depth (h_k) and level ice draft (d_{lvl}) are simply averages of individual measurements taken for all bursts in each window. The average keel spacing (ℓ_k) is taken as the total distance measured by all bursts in a given window (both ice and open water) divided by the total number of keels counted during that window. Except for some bursts in the marginal ice zone, floe lengths are typically longer than the distance measured by an individual burst. To estimate an average floe length (ℓ_f) the total measured ice-covered distance for a given window is divided by the number of leads counted in that window. Similarly, the average lead length (ℓ_l) was the total open water distance divided by the number of leads. These definitions for ℓ_k and ℓ_f are consistent with their inclusion in parameterizations (*Lu et al.*, 2011; *Tsamados et al.*, 2014). A local average daily ice concentration, (A) was also calculated using burst data as a ratio of the total measured ice-covered distance to the total distance measured by all bursts (ice and open water). Using A, the average lead length can be written as $\ell_l = \ell_f(1 - A)/A$ for one-dimensional measurements (*Lu et al.*, 2011). The values ℓ_f and ℓ_l are only defined for ice concentration less than 100%. The measurements show seasonal signals in all of the measured geometry statistics at all moorings (fig. 4.5). Despite both d_{lvl} and ℓ_f decreasing in the summer/fall (figs. 4.5a and c), the much wider range of variation of ℓ_f (over roughly 3 order of magnitude) compared to d_{lvl} results in floe aspect ratios (d_{lvl}/ℓ_f) that are elevated in the fall (fig. 4.5e). The relative keel depths and spacing ($h_{k\mathrm{rel}}$ and ℓ_k) appear to have some negative correlation (cf., figs. 4.5b and d), so that both signals contribute to the minimum ridging intensity (h_k/ℓ_k) in the summer/fall (fig. 4.5f).

4.3.4 *Implementing model parameterization schemes*

Four different variations of ice-ocean drag parameterizations were tested. These are summarized in table 4.2. In the first two variations (labelled L11 and T14(I), respectively), direct measurements of the sea ice geometry (section 4.3.3) were used to test the parameterization schemes proposed by *Lu et al.* (2011) and *Tsamados et al.* (2014) (section 4.2.1) using default parameter values in each scheme. We introduce an alternative version of the *Tsamados et al.* (2014) scheme, labelled T14(II), which uses slightly modified geometry definitions and coefficient values, and still uses direct ice geometry measurements. Finally, the T14(III) variation tested a combination of both physics and ice geometry parameterization from *Tsamados et al.* (2014), and thus is most comparable to modelling efforts where geometry measurements are not available.

The T14(II) scheme is a modification of the T14(I) scheme, introduced for this study. It still uses the direct measurements of sea ice geometry, but uses the relative definitions of keel depth and reference depth (see section 4.2.1). Additionally, in T14(II), some of the parameters have been changed from their default values. The skin drag coefficient of resistance (c_s) is replaced with eq. (4.12) and the roughness length associated with level ice bottom, z_{0i} is replaced with a value of 1×10^{-3} m, which is reflective of observations of ice with no significant morphology (*McPhee et al.*, 1999; *McPhee*, 2002). With this z_{0i} and a 10-m reference depth, the value of c_s calculated for a 1-m ice draft is 2×10^{-3}, which is the same as in T14(I); however, the use of eq. (4.12) allows c_s to vary slightly through the year as the ice draft changes seasonally, and gives it an explicit dependence on z_{ref}.

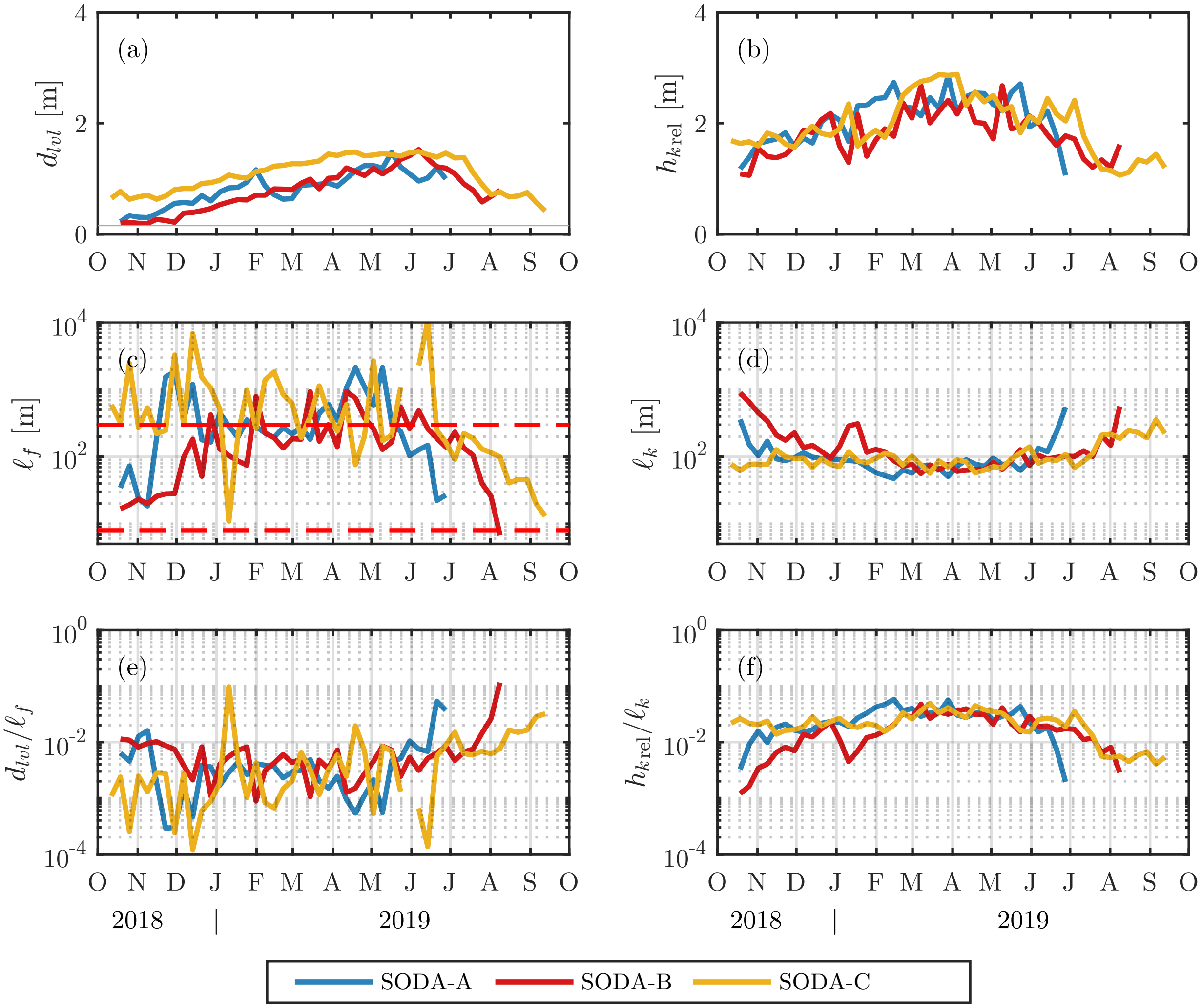

Figure 4.5: Weekly statistics of sea ice geometry for each mooring: (a) mean level ice draft; (b) mean relative keel depth; (c) mean floe length; (d) mean keel spacing (e) aspect ratio (d_{lvl}/ℓ_f); and (f) ridging intensity (h_k/ℓ_k). Horizontal dashed red lines in (c) show the maximum and minimum extents of the parameterized floe length (eq. 4.14).

Table 4.2: Summary of parameters and functions used in the parameterization schemes tested.

	L11	T14(I)	T14(II)	T14(III)
c_f	1	1	0.3†	1
c_k	$1/\pi$	0.2	0.4†	0.2
c_s	2×10^{-3}	2×10^{-3}	eq. (4.12)‡	2×10^{-3}
z_{0i}	n/a	5×10^{-4} m	1×10^{-3} m	5×10^{-4} m
z_{0w}	n/a	3.27×10^{-4} m	3.27×10^{-4} m	3.27×10^{-4} m
m_w	10	10	10	10
s_l	n/a	0.18	0.18	0.18
S_c	eq. (4.10b)	eq. (4.10a)	eq. (4.10a)	eq. (4.10a)
P_0	n/a	eq. (4.11)	eq. (4.11)‡	eq. (4.11)
h_k	meas. $h_{k\mathrm{rel}}$	meas. $h_{k\mathrm{tot}}$	meas. $h_{k\mathrm{rel}}$	eq. (4.13a)
ℓ_k	meas.	meas.	meas.	eq. (4.13b)
ℓ_f	meas.	meas.	meas.	eq. (4.14)

†parameters adjusted based on best fit to observations in this study;
‡using a relative reference depth ($z_{\mathrm{ref}} - d_{lvl}$);
n/a: not applicable;
meas.: measured (see section 4.3.3)

By using this formulation c_s is no longer a free parameter. Finally, the coefficients of resistance c_f and c_k have been replaced with values that provide the closest fit between parameterized and observed drag coefficient values when considered across all moorings. These values were found with multiple linear regression: first the values c_f and c_k in eqs. (4.9a) and (4.9b) were set to 1, then resulting C_f and C_k from all moorings were regressed against the residual observed drag after subtracting the skin drag component, $C_{io} - C_s$; the regression coefficients then gave the new values of c_f and c_k which were used in T14(II). While used as fitting parameters here, c_f and c_k should be reflective of the individual geometries of the floe edges and keels. For example, the value of $c_k = 0.4$ found with this method corresponds to a keel slope angle of 19.6° based on the fit to experimental results by *Zu et al.* (2020) (noting that their definition of C_k introduces a factor of $\pi/2$ difference in values of c_k compared to this study), which is close to the mean keel slope of first year ridges of $\alpha_k = 26.6°$ found by *Timco and Burden* (1997), and the value of $\alpha_k = 22°$ used in the parameterization by *Tsamados et al.* (2014). Note that the T14(II) scheme does not reflect a full optimization tuning of all of the available parameters, nor is it a rigorous fitting approach for c_f, c_k (as discussed in section 4.5.2).

As the ADCP measurements provide direct observations of ice geometry (section 4.3.3), the parameterization of ice geometry (section 4.2.2) is not necessary in order to implement eq. (4.9) in L11, T14(I), and T14(II). Instead, this allows us to separately test the physics parameterization (section 4.2.1) and the geometry parameterization (section 4.2.2). To do so, a final variation (T14(III)) is tested that uses the default parameter values from *Tsamados et al.* (2014) but instead of using the direct measurements of sea ice geometry, geometry statistics are estimated using bulk measurements and eqs. (4.13) and (4.14).

Application of eq. (4.13) using ADCP measurements provides some challenges. The ice volume (v_{rdg}) and areas (a_{rdg}, a_i) in eq. (4.13) are fundamentally defined over a two dimensional area (i.e., within a model gridcell), but the ADCP draft measurements are one dimensional (along-drift). To adapt our measurements to apply eq. (4.13), we calculate v_{rdg}, a_{rdg}, and a_i on a per-unit-width basis. However, the relative angles between the keel orientations and the direction of sampling (which is unknown) will cause an overestimate of the area or volume of the feature unless measurements are made perpendicular to the keels. Fortunately, this mismatch creates an equal bias for both volume and area calculations, so the ratio v_{rdg}/a_{rdg} in eq. (4.13a) is not impacted. However, due to crossing angle mismatch, extra care must be taken when calculating and interpreting ℓ_k from eq. (4.13b). If both keels and leads are linear features whose orientations follow the same statistical distributions then the ratio a_i/a_{rdg} measured with along-drift data will approximate the true (two-dimensional) value if averaged over a sufficiently large sample of keels and leads. However, in full ice cover leads are relatively scarce while in the marginal ice zone it may not be appropriate to consider leads to be linear features. It is unclear whether one-dimensional sampling of a_i will introduce any mean bias. For a uniformly distributed keel orientation, one-dimensional sampling will lead to a mean over-estimate of a_{rdg} by a factor of $\pi/2$. On that basis a_{rdg} are multiplied by a $2/\pi$ correction factor when applying eq. (4.13b).

4.4 Results

4.4.1 Seasonal and spatial variation of ice-ocean drag

For all three moorings, the force-balance approach provided estimates for the ice-ocean drag coefficient, C_{io}, throughout the full annual cycle (fig. 4.6) even despite some winter data gaps (due to higher internal stresses). These estimated values of the ice-ocean drag coefficient exhibit both spatial and seasonal variations.

Drag coefficients measured at SODA-A and SODA-B (the two southern moorings; fig. 4.2a) show a similar seasonal behaviour. For both, the drag coefficients start at low values ($C_{io} \sim 2 \times 10^{-3}$–$3 \times 10^{-3}$), and steadily increase through the winter to a maximum in spring (Apr.–May) before declining (figs. 4.6b and c). The decrease of C_{io} is more gradual at SODA-B than SODA-A, and summertime minimum values at SODA-A are lower than at SODA-B (cf., figs. 4.6b and c). The timing of the shift from increasing to decreasing C_{io} at these two moorings is roughly coincident with the change from net surface cooling to net surface heating in the atmospheric re-analysis data, which occurred in Apr.–May.

In contrast, the record at SODA-C begins with an elevated drag coefficient ($C_{io} \sim 6 \times 10^{-3}$) which remains roughly constant from fall through spring (fig. 4.6a). After the shift to net atmospheric surface heating in Apr.–May, there may be a slight decline in C_{io}, but values are still elevated for some months, until there is a sharp drop in early to mid-July. This sudden drop in ice-ocean drag is associated with a similar sharp decline in both floe sizes (fig. 4.5c) and ridging intensity (fig. 4.5f), suggesting a dramatic ice breakup and melting event occurred.

At all three moorings, drag coefficient values from mid-winter to spring are similar to each other, and fluctuate near or above the canonical value of $C_{io} = 5.5 \times 10^{-3}$. However, differences between the moorings in fall and summer imply large-scale spatial gradients in the ice-ocean drag coefficient across the Beaufort Sea. Section 4.4.3 discusses morphological drivers of the observed seasonality in greater depth.

4.4.2 *Evaluation of parameterization schemes*

Ice-ocean drag coefficients calculated with all of the tested parameterization schemes (table 4.2) show values and temporal variability that broadly match the values observed with the force-balance approach (fig. 4.6). This agreement indicates that variability of ice-ocean drag can be primarily explained by seasonal changes in the ice morphology and the associated skin/form drag contributions. Despite general success, some versions of the parameterization schemes are better performing. In particular, while the T14(III) scheme provides a reasonable match at all moorings in the early part of the record, it diverges significantly from the observations in the latter half of the record, and even reaches a maximum C_{io} in summer/fall when the observations show a minimum. Figure 4.7 shows direct comparisons of the observed and parameterized values for each of the four test

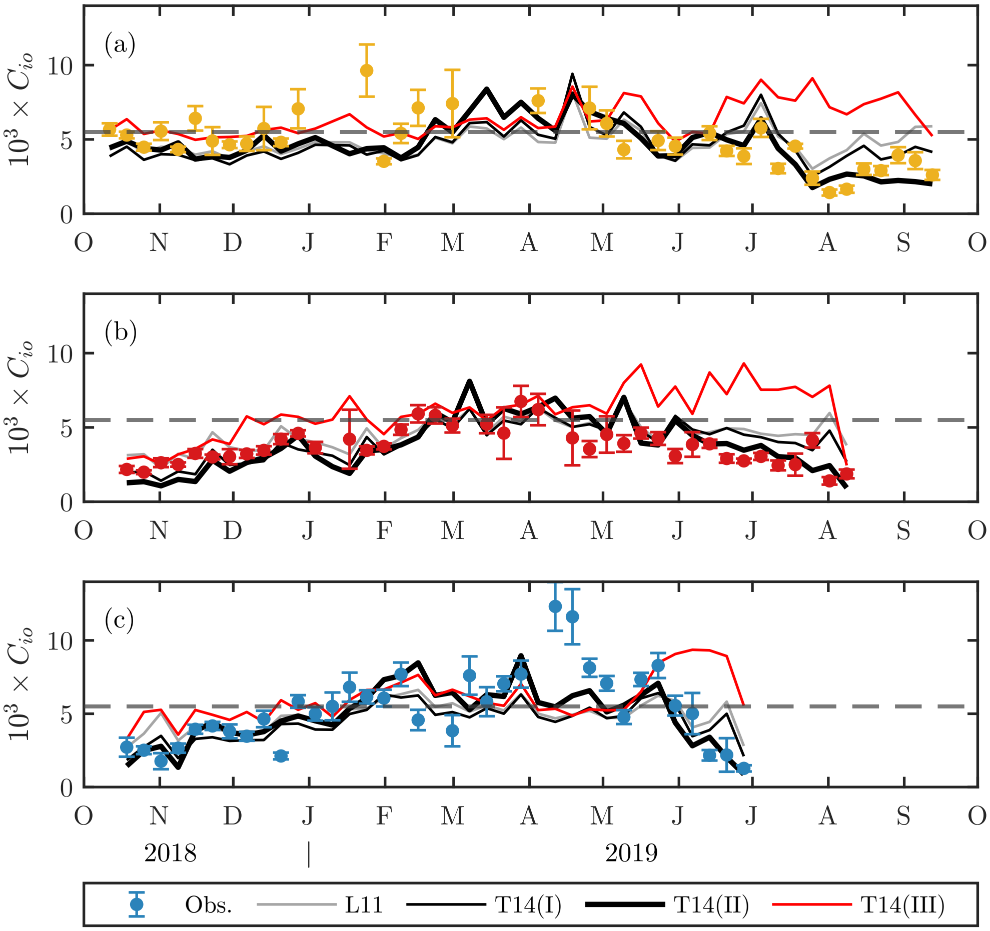

Figure 4.6: Timeseries of ice-ocean drag coefficients from north-to-south: (a) SODA-C, (b) SODA-B, and (c) SODA-A. In each panel, points with error-bars (coloured by moorings per fig. 4.2a) show the values of C_{io} calculated with the force-balance approach (labelled "Obs."), while lines correspond to the different variations of parameterization schemes (table 4.2), as indicated by the legend. Error bars show 95%-confidence interval bounds from the linear fitting procedure. The horizontal grey dashed line shows the value of $C_{io} = 5.5 \times 10^{-3}$ for comparison.

schemes. There is good agreement between the observed drag coefficients and those predicted by both L11 and T14(I) when C_{io} are low ($\lesssim 5 \times 10^{-3}$); for higher values of C_{io} ($\gtrsim 5 \times 10^{-3}$), there is a roll-off of the modelled values (figs. 4.7a and b). Values from T14(II) follow the one-to-one line across the full range of C_{io} (fig. 4.7c), while those from T14(III) are mostly above the one-to-one line and do not present any recognizable correlation with force-balance observations. A few notable outliers exist that are not described by any of the model schemes (e.g., high observed values of drag in mid-April at SODA-A; fig. 4.6a), potentially suggesting other sources of drag (e.g., internal wave drag) that cannot be explained by ice geometry variations alone; however, these points are fairly limited.

These statements are corroborated by quantitative assessments of model performance across all moorings (table 4.3). Values from both L11 and T14(I) have weak correlations with observations ($r^2 = 0.13$ and 0.22, respectively). T14(I) has a slightly negative normalized bias (NBI; -012), while L11 is approximately unbiased. The T14(II) scheme has the best correlation of the four tests ($r^2 = 0.46$), the lowest normalized root-mean-squared error (NRMSE; 0.31), though it also has a slightly negative normalized bias (-0.09). When considered over the full year, the T14(III) scheme is biased high (NBI of 0.31), has high NRMSE (0.57), and is uncorrelated with observations; however, if only the early part of the record (before May 2019) is considered, the fit is better ($r^2 = 0.17$, NRMSE=0.35). Tests in which the observed drag coefficients and geometry statistics were determined using different window lengths (ranging between 1 d and 14 d) all produce similar correlations as the 7-d windows presented (not shown), giving confidence that the parameterization schemes are appropriate over a wide range of scales.

4.4.3 *Partitioning of drag components and predictions of ice geometry*

Parameterized ice-ocean drag coefficients are built up from three components: form drag on floe edges (eq. 4.9a), form drag on keels (eq. 4.9b), and skin drag (eq. 4.9c).

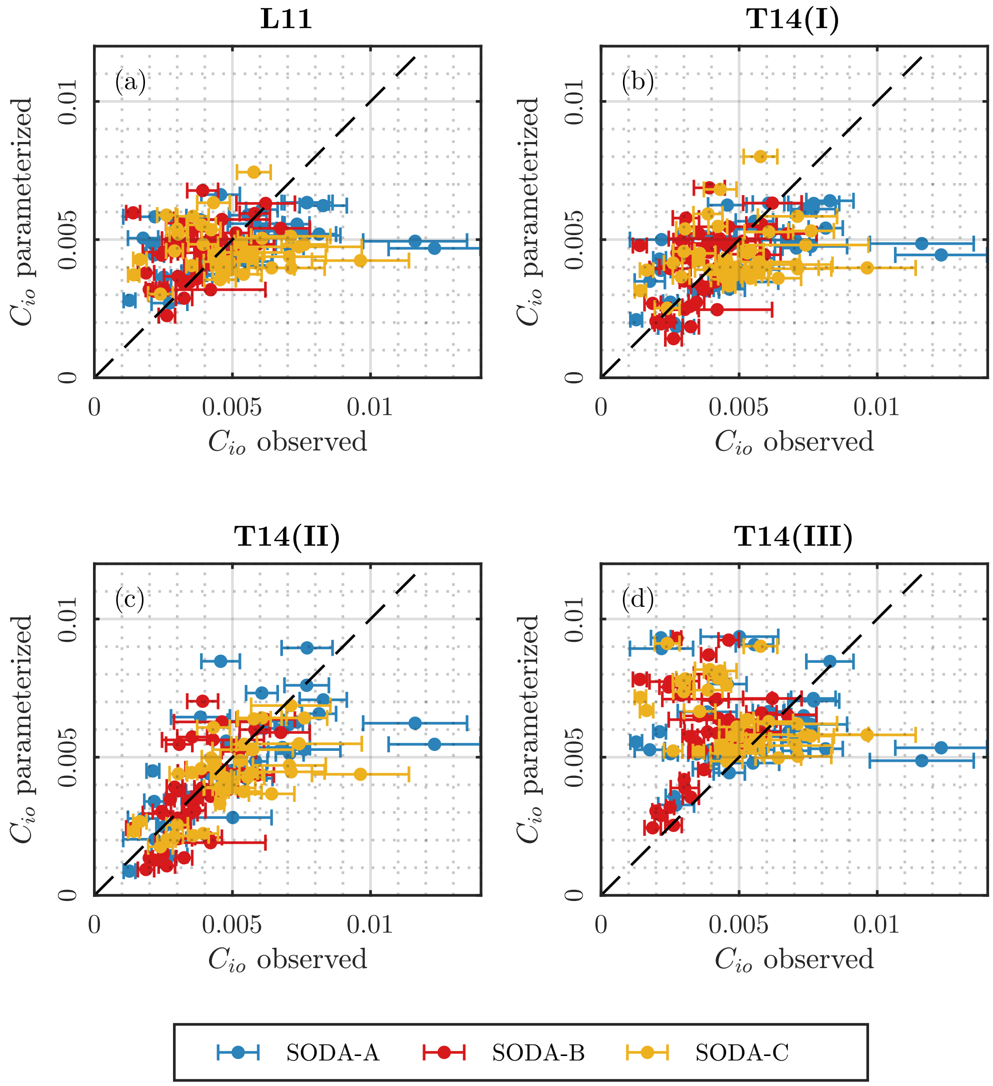

Figure 4.7: A comparison between the ice-ocean drag coefficients determined using the force-balance approach ("observed"), and using the different variations of geometry-based parameterization: (a) L11, (b) T14(I), (c) T14(II), and (d) T14(III). In each panel, the black dashed line shows the one-to-one slope, and the points are coloured by mooring according the legend.

Table 4.3: Summary of fit statistics of ice-ocean drag coefficients determined using the force-balance approach and using the different variations of geometry-based parameterization. (NRSME = normalized root mean square error; NBI = normalized bias)

Scheme	r^2	NRMSE	NBI
L11	0.13	0.37	-0.00
T14(I)	0.22	0.36	-0.08
T14(II)	0.46	0.31	-0.09
T14(III)	0.00	0.57	0.31

Insofar as the ice-ocean drag coefficient is driven by ice morphology, examination of the partitioning of drag components allows us to better understand the impact of those morphological variations. In all four of the parameterization schemes tested, the ice-ocean drag coefficient in the winter is largely driven by form drag on ice keels (C_k). Skin drag (C_s) is generally much smaller, and does not show significant seasonal variation, and floe edge drag (C_f) becomes more important in the summer as the ice begins to melt and break apart into smaller floes. This general pattern qualitatively matches results from sea ice models (*Tsamados et al.*, 2014; *Martin et al.*, 2016), but details vary from those model results.

For the three schemes that use direct measurements of the geometry (L11, T14(I), and T14(II)), the seasonality of C_{io} observed in fig. 4.6 is driven by seasonal growth and melt of ice keels, as seen by variation in C_k (T14(I) and T14(II) are shown in figs. 4.8a to 4.8f; L11 is very similar to T14(I) so it is not shown). The exact partition between C_f and C_k in these schemes depends on the values of the coefficients of resistance c_f and c_k (see table 4.2), but the overall behaviour is similar for the different schemes (c.f. figs. 4.8a to 4.8c and figs. 4.8d to 4.8f). At the southern moorings (SODA-A, -B), which start the timeseries in open water, there is initially only small contribution from C_k and most of the drag is due to a combination of C_f and C_s. As the number and size of keels grow through the year (fig. 4.5), so too does the contribution from C_k (figs. 4.8b, c, e, and f). At SODA-C, the timeseries begins in ice cover with established ridging, and C_k is the main component of C_{io} from the onset (figs. 4.8a and d). All three moorings have some small contributions to floe edge drag throughout the full year due to the presence of (potentially refrozen) leads. Following the onset of melting conditions, an increase in floe edge drag accompanies the decline of keel drag at all locations; however, the increased floe edge drag is not enough to compensate for the lack of keels at any of the moorings (figs. 4.8a to 4.8f). This contrasts the modelling results from *Tsamados et al.* (2014) and *Martin et al.* (2016), which show that floe edge drag is substantial during summer/fall. While not the main focus here, it is also noteworthy that keel decline varied between the three moorings: at both the southernmost mooring (SODA-A) and northernmost mooring (SODA-C), there was a fairly rapid drop in C_k over the period of approximately 2 weeks in late June and early July, respectively, due to both decreased size and number of keels (figs. 4.5b and d); at SODA-B, the decrease in C_k was more gradual. Note that at SODA-A and -B, where there was a strong seasonality in keel drag, growth of C_k proceeded at a much slower rate than ice cover growth; at both moorings, ice concentration was close to 100% by early November (figs. 4.2c to 4.2e), while C_k remained relatively low through January. As such, it is unlikely that ice concentration based drag parameterizations (such as are suggested for atmospheric drag; e.g., *Andreas et al.*, 2010a) would ever be able to sufficiently capture observed seasonal variations in C_{io}.

The drag partition from the T14(III) scheme (figs. 4.8g to 4.8i) differs from the results of the T14(II) scheme. While keel drag (C_k) is still the dominant contribution during winter, its seasonality is somewhat muted compared to T14(II) (compare C_k in figs. 4.8d to 4.8f with figs. 4.8g to 4.8i). More striking are the differences in floe edge drag: C_f is much higher in the T14(III) scheme at all moorings and times of the year, and in summer/fall the increase in C_f outpaces the associated decrease in C_k. As a result, the T14(III) scheme has the largest value of C_{io} in summer/fall, which conforms to previous model results

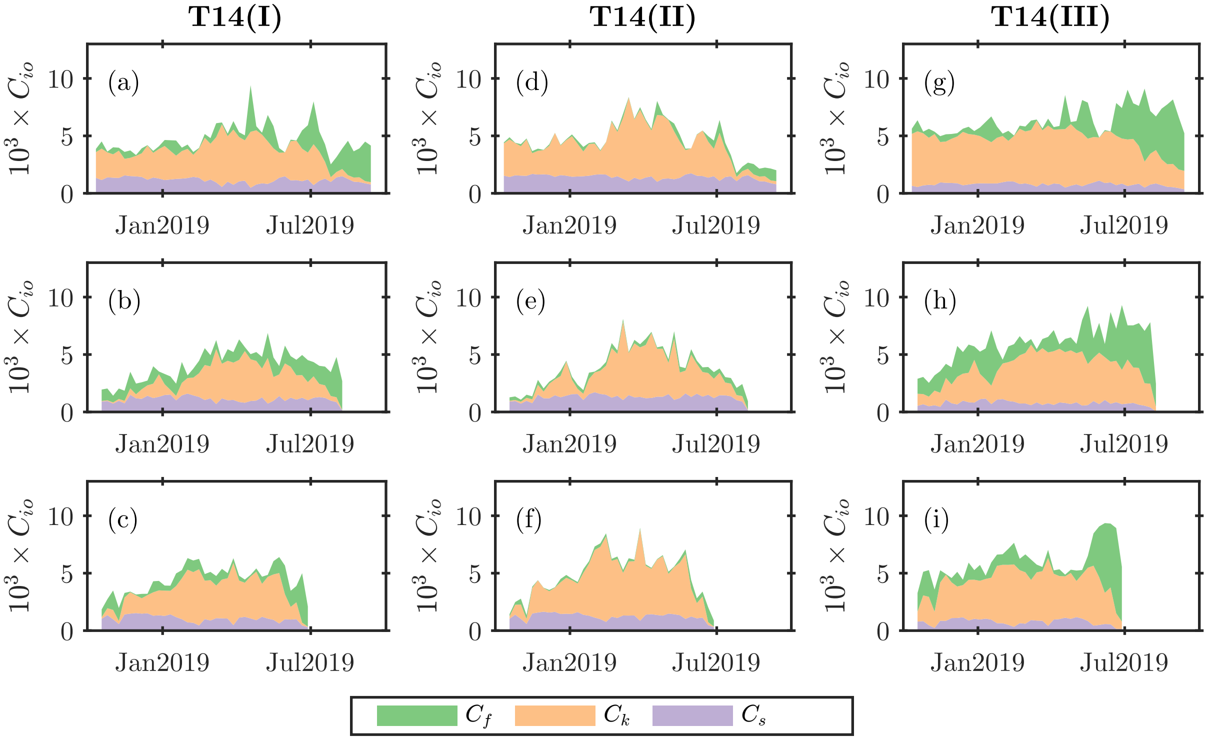

Figure 4.8: Stacked contributions to the ice-ocean drag coefficient C_{io} from form drag on floe edges (C_f), form drag on keels (C_k), and skin drag (C_s) calculated using (a-c) the T14(I) scheme, (d-f) the T14(II) scheme, and (g-i) the T14(III) scheme (see table 4.2) for (a,d,g) SODA-C, (b,e,h) SODA-B, and (c,f,i) SODA-A.

(*Tsamados et al.*, 2014; *Martin et al.*, 2016). While these differences can be partly attributed to the differences in coefficients of resistance between the two schemes (c_f and c_k, see table 4.2), the main difference arises from the fact that the T14(III) scheme does not use direct measurements of the sea ice geometry, and instead relies on parameterized geometry statistics (section 4.2.2). In the early part of the record, before C_f becomes large, the T14(III) scheme is comparable to the other parameterization schemes.

Differences in C_f between T14(II) and T14(III) depend mainly on the floe aspect ratio, d_{lvl}/ℓ_f, while differences in C_k depend on the ridging intensity, h_k/ℓ_k. As shown in figs. 4.9a and d, neither of these ratios is well predicted by the parameterizations of ice geometry eqs. (4.13) and (4.14), with parameterizations overestimating the results in both cases. For the highest values of ridging intensity ($h_k/\ell_k \gtrsim 5 \times 10^{-2}$) predicted values fall near the one-to-one line but deviate substantially as observed values decrease (fig. 4.9a). As such, the overall magnitude of C_k values is not strongly modified by the over-prediction of ridging intensity, but the decreased range of variability of modelled values is responsible for the muted seasonality of C_k seen in the T14(III) scheme. Considering the separate roles of h_k and ℓ_k in setting this ratio, the predictions of each individual variable have as much (or more) variability as observations (fig. 4.9b), but there is an apparent compensating effect between the two quantities. Predicted values of h_k and ℓ_k vary roughly along lines of constant h_k/ℓ_k, while observations vary primarily across lines of h_k/ℓ_k.

The elevated levels of C_f seen in the T14(III) test result from parameterized values of the aspect ratio, d_{lvl}/ℓ_f, being much greater than observations across nearly the full range of values (fig. 4.9d, black points), with a median factor of $\sim$4 times higher than the observed values. Differences between the observed and predicted aspect ratio are driven solely by differences in ℓ_f (d_{lvl} is not parameterized), which is generally underestimated by eq. (4.14) (fig. 4.9c). The relationship between floe lengths and ice concentration used in eq. (4.14) to predict ℓ_f is an empirical result derived from a set of aerial photos of ice in the marginal ice zone in the Fram Strait (*Lüpkes et al.*, 2012).

However, a wide variety of factors set the size and density of floes (*Roach et al.*, 2018) and so it is unlikely that such empirical relationships would be valid in different Arctic regions and all times of year. The mismatch in the seasonality of C_{io} between observations and values predicted with the T14(III) parameterization arise mainly from this overestimate of aspect ratio. A modification to the parameters used in eq. (4.14) (to $\ell_{f,min} = 18.4\,\mathrm{m}$, $\ell_{f,max} = 1730\,\mathrm{m}$, $b_2 = 0.9$) provided a much better to fit the floe length observations (fig. 4.9c, and fig. 4.9d, grey points). However, the applications of the T14(III) scheme using the modified parameters in eq. (4.14) still retained the seasonal mismatch in C_{io} (not shown), albeit to a lesser degree (possibly due to the very wide variability around the fitted curve in fig. 4.9c, noting that the comparisons in fig. 4.9d are plotted on logarithmic axes).

4.5 *Discussion*

4.5.1 *Comparison with previous drag observations*

The range of values reported for the ice-ocean drag coefficient are consistent with previous observations. *Shirasawa and Ingram* (1991) and *Lu et al.* (2011) collated observations of the ice-ocean drag coefficient from a wide set of historical studies (publication dates from 1970 to 1997). These studies indicate a broad range of measured values with extremes from as low as 0.13×10^{-3} (under land-fast ice in Hudson's bay; *Shirasawa et al.*, 1989) to the highest value of 47×10^{-3} (*Johannessen*, 1970, indirectly estimated based on fitting log-layer profiles to velocity measurements;). The bulk of the studies summarized suggest drag coefficient values range from roughly 1×10^{-3}–20×10^{-3}. More modern studies based either on direct measurements (*Shaw et al.*, 2008; *Randelhoff et al.*, 2014; *Cole et al.*, 2014, 2017) or force-balance approaches (*Randelhoff et al.*, 2014; *Kim et al.*, 2017; *Dewey*, 2019; *Heorton et al.*, 2019) provide similar limits. This study finds drag coefficient values from 1.3×10^{-3}–12.3×10^{-3}, which fall well within the conventional bounds, and the mean and median values are close to, but slightly below, the canonical drag coefficient

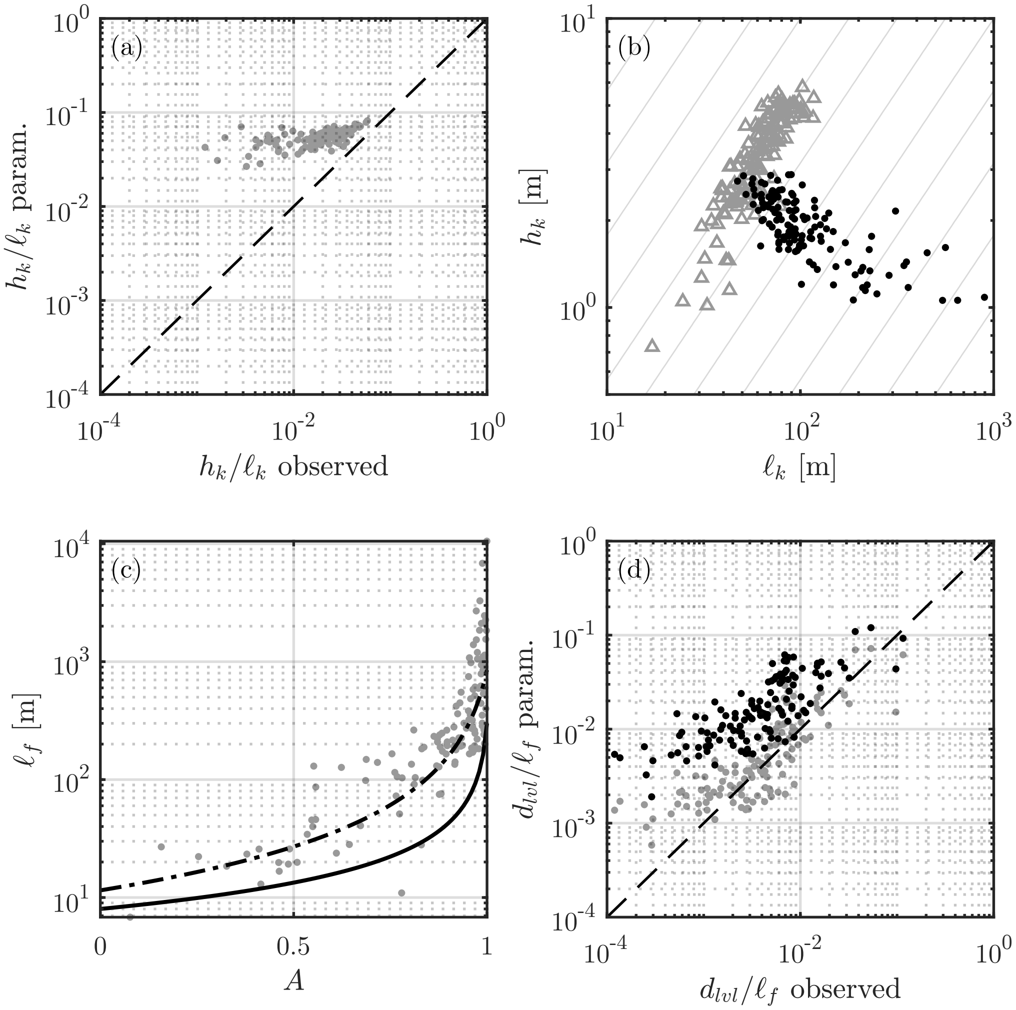

Figure 4.9: A comparison of observed and parameterized sea ice geometry statistics: (a) Observed versus parameterized ridging intensity (h_k/ℓ_k) with weekly values measured at all moorings; the black dashed line shows the one-to-one slope. (b) Weekly values of ridge spacing (ℓ_k) versus keep depth (h_k) from observations (black points) and parameterizations (grey triangles). Grey contours correspond to lines of constant h_k/ℓ_k. Observed values of h_k in (a) and (b) are relative keel depth ($h_{k\mathrm{rel}}$). (c) Observed floe length ℓ_f as a function of ice concentration A (grey points) showing the fit of eq. (4.14) when using the default parameter set (solid black line), and with modified set of parameters (dashed-dotted line). (d) As per (a) but for aspect ratio (d_{lvl}/ℓ_f); black points show the aspect ratio when ℓ_f is calculated using the default parameters in eq. (4.14), and grey points show the aspect ratio when a modified set of parameters are used in eq. (4.14).

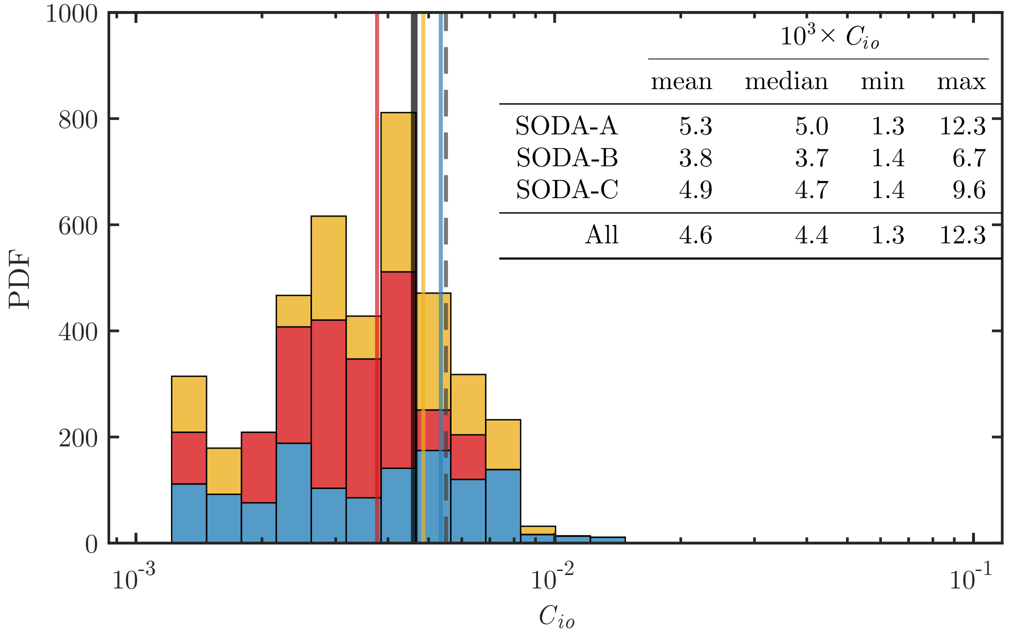

	$10^3\times C_{io}$			
	mean	median	min	max
SODA-A	5.3	5.0	1.3	12.3
SODA-B	3.8	3.7	1.4	6.7
SODA-C	4.9	4.7	1.4	9.6
All	4.6	4.4	1.3	12.3

Figure 4.10: Stacked histograms showing the probability distribution function (PDF) of the ice-ocean drag coefficient values calculated at each of the three moorings (coloured by mooring according to fig. 4.2a). Coloured vertical lines show the annual mean value of C_{io} for each mooring, and the vertical black line shows the overall mean. The vertical grey dashed line shows the value of $C_{io} = 5.5 \times 10^{-3}$ for comparison.

value of 5.5×10^{-3} (fig. 4.10). The overall mean value of 4.6×10^{-3} in these observations is very similar to the average ice-ocean drag coefficient of 4.7×10^{-3} found by *Dewey* (2019) for the Beaufort Sea.

Cole et al. (2017) present detailed analysis of surface momentum flux from four ice drift stations in the Beaufort Sea, each containing a cluster of autonomous instruments. The four clusters provide measurements spanning March to December 2014, nearly a full annual cycle. Their results show weekly median ice-ocean drag coefficients ranging from approximately 0.2×10^{-3}–10×10^{-3}, with significant spatial and temporal variability (see their figure 12). Their measured values of C_{io} span a broader range than reported here, with minimum values an order-of-magnitude lower than ours (but similar maximum values). Nonetheless, there is good agreement with some of the qualitative behaviour exhibited by the ice cluster measurements. Namely, despite strong spatial variation in the values of C_{io}, all of the ice clusters showed consistent seasonal variations in ice-ocean drag, with minimum values at the time of ice minimum (Aug.–Sep.) and maximum values in spring (Apr.–Jun.). *Dewey* (2019) find a similar seasonal cycle based on a force-balance approach to calculate C_{io} from remote measurements in the Beaufort Sea over a 5-year period from 2011–2016: basin-wide average C_{io} show minimum values from Jul.–Oct. of each year. These patterns are in agreement with our observations which show minimum ice-ocean drag coefficient values in fall (fig. 4.6). In contrast, pan-Arctic averages of C_{io} from models incorporating a variable drag coefficient scheme (section 4.2.1) show the opposite behaviour (*Tsamados et al.*, 2014; *Martin et al.*, 2016). In those models, the maximum value of C_{io} occurs during the summer/fall season, driven by form drag on floe edges (eq. 4.9a). As described above (section 4.4.3), seasonality in modelled values of C_{io} may be a result of over predicted values of the floe aspect ratio, d_{lvl}/ℓ_f.

With a few exceptions, direct observational estimates of the ice-ocean drag coefficient are made using point measurements of turbulent fluxes. In comparison to the force-balance approach used here, C_{io} values derived from point measurements require far fewer assumptions about the ice dynamics (e.g., they are valid whether or not the ice is in free drift). However, these measurements are also inherently local and as such it is not clear how they scale to application across entire ice floes. For logistical reasons, measurements are typically made away from ice keels, so reported values of C_{io} may under-represent floe- or regional-average values (*McPhee*, 2012). *Randelhoff et al.* (2014) provide a direct comparison between a force-balance approach to calculate ice-ocean drag (the procedure used here) and in-situ measurements of turbulent fluxes. Their results showed that the force-balance approach produced ice-ocean stress estimates that were, on average, 3 times larger than direct measurements. They attribute the mismatch to unmeasured sources of drag (e.g., due to internal wave radiation; *McPhee and Kantha*, 1989), but it may also be due to horizontally varying and thus non-local turbulence.

Similarly, application of the force-balance approach to the ice cluster data from *Cole et al.* (2017) shows higher values of C_{io} and decreased temporal variability compared to local measurements (*Heorton et al.*, 2019). While this may explain why the values of C_{io} observed here have a much higher minimum value than those by *Cole et al.* (2017), more work is needed to understand the inherent differences in between direct point measurements and force-balance measurements of ice-ocean drag.

In comparing values of C_{io} between different studies, it is important to consider the choice of reference depth used, which will impact the drag coefficient through depth variations of $\boldsymbol{u}_o$. For example, repeating our analysis with a shallower reference depth of $z_{ref} = 6\,\mathrm{m}$ yields slightly higher values of C_{io}, with an overall average of 5.2×10^{-3} (compared to 4.6×10^{-3} for $z_{ref} = 10\,\mathrm{m}$). Typically, values of C_{io} are reported corresponding to either fixed reference depths near the ice bottom, thus in or near the logarithmic boundary layer, or they are reported using the underlying geostrophic current, $\boldsymbol{u}_g$, as a reference velocity (table 1 in *Lu et al.*, 2011, lists reference depths used for a number of studies). Within the log-layer, $\boldsymbol{u}_o \propto \boldsymbol{u}_*$, so the application of the quadratic drag law is appropriate. However, beyond the logarithmic layer, the relationship between stress and velocity in the ice-ocean boundary layer is not expected to be quadratic (e.g., *McPhee*, 2008, and references therein). If $\boldsymbol{u}_g$ is used as a reference velocity, drag may be better described by Rossby Similarity Theory (*Blackadar and Tennekes*, 1968; *McPhee*, 2008), which accounts for the existence of an outer Ekman-like layer matched to an inner logarithmic layer (as has been observed in the ice-ocean boundary layer, e.g., *Hunkins*, 1966; *McPhee*, 1979). In this more general case, *McPhee* (1979, and others) find reasonable empirical agreement from an alternative power law form: $|\boldsymbol{\tau}_{io}| \propto |\boldsymbol{u}_i - \boldsymbol{u}_g|^n$ where $n < 2$ (e.g., *Cole et al.*, 2017, find values of n ranging from 0.51 to 1.76). The use of a fixed reference depth of $z_{ref} = 10\,\mathrm{m}$ in the present study likely extends beyond the surface log-layer so the quadratic drag law is not strictly applicable. Nonetheless, tested parameterizations that assume a law-of-the-wall velocity profile (T14(I), T14(II)) produce reasonable results (figs. 4.6 and 7). Furthermore, the relationship between stress and relative velocity seems to be well described by the quadratic drag law (fig. 4.3). This suggests a “fuzzy” transition between the inner logarithmic boundary layer and the outer Ekman-like layer such that the law-of-the-wall still provides a useful approximation for determining C_{io}. Likely, the use of a smaller reference depth that is closer to the base of the logarithmic boundary layer may increase the accuracy of the quadratic drag assumption (e.g., *Park and Stewart*, 2016, suggest a hybrid Rossby Similarity Theory using the quadratic drag law to model the inner boundary layer coupled to classic Ekman-layer dynamics for the outer layer).

4.5.2 Recommendations for model development

This study identifies some possible directions that future modelling work could focus on. The parameterizations here can be described as having two parts: one part that models the underlying physics (eqs. 4.9; tested by schemes L11, T14(I), T14(II)), and a second part for the geometry (eqs. 4.13 and 4.14; tested by scheme T14(III)). There are some opportunities for improvements in both of these parts; however, based on the results in section 4.4.3, it is apparent that there is a more urgent need to improve descriptions of the sea ice geometry.

Translating bulk sea ice model outputs to the detailed geometry needed to apply eqs. (4.9a–c) appears to be a particular challenge. Both the ridging intensity, h_k/ℓ_k, and the floe aspect ratio, d_{lvl}/ℓ_f, are overpredicted by the parameterization schemes from section 4.2.2 (see fig. 4.9). Some efforts are being made to directly model different aspects of the sea ice geometry (e.g., floe sizes, *Roach et al.*, 2018; or keel statistics, *Roberts et al.*, 2019), thus alleviating the need for geometry parameterizations. However, until such modelling schemes are widely implemented, there will be some value in improvements to existing geometry parameterizations.

The keel depth and spacing predicted from model outputs by *Tsamados et al.* (2014) (eqs. 4.13a and 4.13b) are based on geometric arguments that are informed by measurements of sea ice sails and keels. In formulating those equations, the authors assume a uniform field of equally sized, shaped, and spaced non-overlapping ridges in each grid cell box. However, past measurements have shown that keel depth, width, and spacing are better described by statistical distributions (e.g., *Hibler et al.*, 1972; *Wadhams and Davy*, 1986; *Davis and Wadhams*, 1995; *Timco and Burden*, 1997; *Martin*, 2007). Some improvement in the parameterizations could likely be made simply by considering the shape of these distributions. For example, using an exponential distribution to describe relative keel depths (per *Wadhams and Davy*, 1986), the total ice volume associated with keels will differ from that calculated with a uniform distribution by a factor of 2 when both distributions have the same mean keel depth. Figure 4.9b suggests that some of these geometry variables may be jointly distributed.

The mismatch between modelled and observed seasonal variations in ice-ocean drag coefficients is largely due to discrepancies in modelled floe lengths, ℓ_f (section 4.4.3). The floe length parameterization (eq. 4.14) is an empirical result relating ℓ_f to A from aerial photographs of ice in the Fram Strait in the 1990s (*Lüpkes et al.*, 2012). While *Lüpkes et al.* (2012) developed this relationship for the marginal ice zone, its implementation by *Tsamados et al.* (2014) does not distinguish between marginal and pack ice (though the authors acknowledge a possible breakdown in winter conditions). Additionally, *Lüpkes et al.* (2012) highlight that variability in the relationship between ℓ_f and A points to other variable dependencies on floe sizes. Employed here, we are able to adjust the input parameters to eq. (4.14) to provide a better fit to the observed floe lengths (fig. 4.9c), suggesting that some general variability in the behaviour of floe length may be modelled by some form of that equation. However, there remains a significant amount of scatter in the observations (over orders of magnitude), and so even with the adjusted parameters the model floe edge drag is still too high during the ice melt season. Future development of empirically derived floe length parameterizations should, at minimum, include observations from across different Arctic regions based in modern ice conditions. Moreover, deterministic models for the evolution of floe size distributions (*Horvat and Tziperman*, 2017; *Roach et al.*, 2018) highlight which other variables could be included in empirical fits. For example, rather than casting ℓ_f as a function just of A, it may be more appropriate to develop two-parameter empirical fits that also include the ice thickness. Further multi-parameter fits might consider the inclusion of wind speed, $|\boldsymbol{u}_a|$ (which would have impacts both on sea ice welding and breakup by driving ice motion, and on surface wave conditions which can lead to fracture), and sea surface temperature (which is important for lateral growth and melt).

While better geometry schemes should be a focus, the improvement of the T14(II) scheme over the L11 and T14(I) schemes also show that minor modifications to the physics part of the parameterization scheme have the potential to increase the predictive skill. There are a number of changes between the schemes (see table 4.2), however, most of the improvement is made by simply choosing more appropriate values of the coefficients of resistance c_f and c_k. While those are chosen here with a slightly ad hoc fitting method (using multiple linear regression; see section 4.3.4), determining appropriate ranges for these values is a subject of ongoing research (e.g., *Zu et al.*, 2020). In addition to these coefficients, the parameterization schemes tested include a number of other constants whose values are not fully constrained that could be used to tune the modelled drag coefficients: c_s, s_l, z_{0w}, z_{0i}, m_w.

Detailed optimization accounting for all free parameters or more rigorously fitting the values of c_f and c_k is deliberately not performed here. This choice is primarily driven by the fact that the tests here do not account for all of the physical processes that modify the ice-ocean drag coefficient. In particular, the parameterization schemes only model the neutral drag coefficient and do not account for variations due to buoyancy (which should be included as a correction term; e.g., *Lüpkes and Gryanik*, 2015), whereas the observed values of C_{io} reflect the total drag, including non-neutral effects. Similarly, shallow surface stratification may act to partly decouple the sea ice motion from subsurface velocity measurements, especially during the melt season. Additionally, drag due to internal wave radiation is thought to be important in some oceanographic conditions (*McPhee and Kantha*, 1989; *Pite et al.*, 1995) but is not included. Finally, the forms of the functions

P_0 (eq. 4.11) and c_s (eq. 4.12) are based on an assumed velocity profile that may not be suitable through the full reference depth; the logarithmic boundary layer at the ice-ocean interface is thought to be only ∼2 m thick (e.g., *McPhee*, 2002; *Shaw et al.*, 2008; *Randelhoff et al.*, 2014; *Cole et al.*, 2017), which is much shallower than the 10-m reference depth used. The generally close match between parameterized values of C_{io} (with T14(II)) and those determined through the force balance suggest that these effects may be small, but a thorough optimization of free parameters should be performed that considers these effects.

In addition to improvements in existing parameterizations, there has been some interest in simplified parameterization schemes for drag coefficients based solely on ice concentration (which have been applied for atmospheric drag; e.g., *Andreas et al.*, 2010a,b; *Lüpkes et al.*, 2013). While there is some value in such an approach, we recommend caution in the development of such schemes for the ice-ocean drag coefficient. The atmospheric drag schemes such as those by *Andreas et al.* (2010a) focus on the effects of floe edges, and thus might work well when the sea ice concentration dominates form drag but less well when drag is dominated by ice ridges. Because of the different scales of both the boundary layer and the ridges at the ice-ocean boundary compared to the atmosphere-ice boundary, the influence of keels on ice-ocean drag may be much more important than the influence of ice sails on atmospheric drag. Thus, approaches for simplified modelling employed in atmospheric literature may not be appropriate to adopt for ice-ocean drag. The differing timescales for ridge intensity growth (relatively slow; fig. 4.5e) compared to ice concentration growth (relatively rapid; figs. 4.2d and e), along with the strong control of ridging intensity on the total ice-ocean drag (section 4.4.3) means that concentration-based schemes are unlikely to be capable of representing ice-ocean drag. From the results of this study, we speculate that a simplified ice-ocean drag parameterization might be better described with a two-parameter scheme that includes both ice concentration and ice thickness.

4.5.3 Implications for momentum transfer into the ocean

We have focused on the efficiency of momentum transfer between the sea ice and the upper ocean; however, these questions exist in a broader context of the impact of sea ice on mediating total momentum flux between the ocean and the atmosphere. Conventional wisdom has been that sea ice damps atmosphere-ocean momentum flux (*Plueddemann et al.*, 1998; *Rainville and Woodgate*, 2009), and so an increase in open water will lead to an increase in momentum flux into the ocean (*Rainville et al.*, 2011). However, other recent studies have suggested a more complex view (*Martin et al.*, 2014, 2016; *Dosser and Rainville*, 2016). *Martin et al.* (2014, 2016) show that sea ice can either enhance or diminish momentum flux into the ocean depending on the interplay between internal ice stress and wind stress (which is amplified over the sea ice; e.g., *Guest et al.*, 1995, and many others). A detailed accounting of the upper ocean response to the combined sea ice and atmospheric forcing is outside the scope of the current study; here we consider the potential for amplification or damping of momentum flux into the ocean by sea ice.

The equivalent drag coefficient, C_{equiv} (eq. 4.7) provides a measure of the total momentum transfer efficiency between the atmosphere and the ocean as it is mediated by sea ice. To provide additional context for the observations, consider two limits for the value of C_{equiv}: (1) a "free-drift limit", where $\boldsymbol{F}_a = \boldsymbol{F}_i = 0$ in eq. (4.6), so $\boldsymbol{\tau}_{ocn} = \boldsymbol{\tau}_{atm}$; (2) the atmosphere-ice stress, $\boldsymbol{\tau}_{ai}$, is balanced by internal ice stress, $\nabla \cdot \boldsymbol{\sigma}$, and $\boldsymbol{F}_a$ is negligible, so $\boldsymbol{\tau}_{io} = 0$. Then for each case the equivalent drag coefficient is given by:

$$\text{case 1:} \qquad C_{equiv} = AC_{ai} + (1-A)C_{ao}, \tag{4.15a}$$

$$\text{case 2:} \qquad C_{equiv} = (1-A)C_{ao}. \tag{4.15b}$$

Taking C_{ao} as constant (an appropriate approximation for typical wind speeds), the two cases above provide formula for C_{equiv} that are functions solely of ice concentration (noting application of an ice-concentration based parameterization scheme for C_{ai}). While these two cases are referred to as limits, they are not strict limits as both the role of acceleration terms ($\boldsymbol{F}_a$) and the vector addition of terms in eq. (4.6) can either increase or decrease C_{equiv} beyond these bounds.

Values of C_{equiv} span a wide range, and the variability of observed values increases with increasing sea ice concentration (fig. 4.11). This increase in variability of C_{equiv} with A reflects the divergence of the two limits of C_{equiv} introduced above, which both approach C_{ao} as $A \to 0$ but either increase (eq. 4.15a) or decrease (eq. 4.15b) as A increases. Results also show a separation of C_{equiv} based on the wind factor ($|\boldsymbol{u}_i|/|\boldsymbol{u}_a|$). Points with a wind factor $\geq 2\%$ (defined as being in free drift) generally fall near the upper "free-drift limit" (as expected). This limit shows that in the absence of acceleration terms ($\boldsymbol{F}_a$), ice in free drift will amplify the efficiency of stress transfer compared to open water; however, as $\boldsymbol{F}_a$ also includes the Coriolis acceleration, $\boldsymbol{F}_a$ is non-zero even at steady-state. Points with wind factor below 2% cover a more broad range of values, but for low values (wind factor $\leq 1\%$), C_{equiv} are generally bounded by eq. (4.15b). This shows that, as expected, the ice interaction force $\boldsymbol{F}_i$ causes a reduction in momentum transfer relative to open-water conditions. Whether the net effect of the ice is to amplify or damp momentum transfer ultimately depends on the strength of this force.

Annual median values of C_{equiv} were similar for each of the three mooring locations with a slight north-south trend: 1.69×10^{-3}, 1.44×10^{-3}, 1.34×10^{-3} for SODA-A, -B, and -C, respectively. This similarity reflects that increased open-water areas (which have a lower efficiency of momentum transfer) at the southern moorings may partly offset expected increases in winter C_{equiv} due to free-drift conditions. However, because wind forcing also has strong seasonal variations with a winter maximum (e.g., *Dosser and Rainville*, 2016), long-term trends in the total momentum flux into the ocean ($\boldsymbol{\tau}_{ocn}$) will depend both on a balance of increasing open-water conditions and changing internal stress conditions in the winter.

Based on the 2%-rule, the wind factor ($|\boldsymbol{u}_i|/|\boldsymbol{u}_a|$) provides a first-order estimate of the extent of free drift conditions at each mooring. While only a rule-of-thumb, measured values of the wind factor showed asymptotic behaviour supporting use of this rule: as

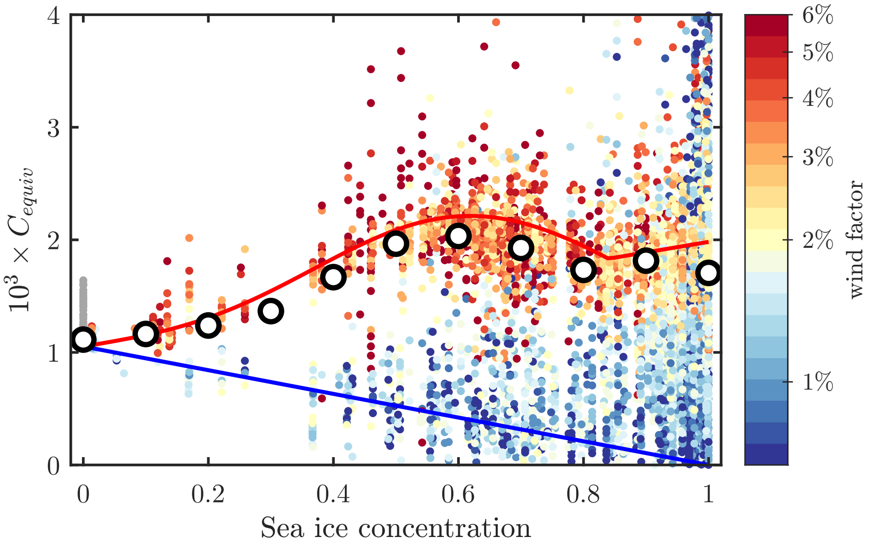

Figure 4.11: Equivalent drag coefficient C_{equiv} (eq. 4.7) as a function of sea ice concentration (from ERA5). Points shows all hourly values from all moorings, coloured by wind factor (log-scale; grey points had no measurable $\boldsymbol{u}_i$), while black circles show bin-median values by sea ice concentration. The red and blue lines shows the limit cases discussed in the text: red is eq. (4.15a); blue is eq. (4.15b).

the wind speed increased (i.e., as $\boldsymbol{\tau}_{ai}$ becomes a dominant term in the force balance), wind factor values converged around 2%; bin-average values of the wind factor stay approximately near 2% across a wide range of wind speeds (fig. 4.12a). There was also a relationship between wind factor and sea ice concentration: for concentrations below ∼80%–85%, the wind factor was elevated and generally greater than 2% (fig. 4.12b). This suggests that an 80%–85% ice-concentration-based limit for defining free drift is an approximation of the 2%-rule, but it may be the case that free drift conditions also occur intermittently for higher ice concentrations (e.g., on short timescales, atmospheric stress may be balanced primarily by only one of either the ice-ocean or ice-ice stresses, as in *Steele et al.*, 1997). The prevalence of wind factor values greater than 2% have a north-south trend, with roughly 66% of measurements designated as being free drift at SODA-A, 54% at SODA-B, and 37% at SODA-C. *Dosser and Rainville* (2016) previously showed that the wind factor is a useful indicator for atmosphere-ice-ocean momentum transfer. If the differences between SODA-A and SODA-C are indicative of future trends of sea ice (in which more and more of the Arctic is similar to SODA-A) then this suggests the potential for increasing amplification of stress transfer from the atmosphere to the ocean in the Beaufort Sea during winter.

Martin et al. (2014, 2016) suggests that interplay between wind stress enhancement over sea ice and internal ice stresses (i.e., the relative sizes of $\boldsymbol{\tau}_{atm}$ and $\boldsymbol{F}_i$ in eq. 4.6) lead to a local maximum in the normalized $\boldsymbol{\tau}_{ocn}$ at some optimal sea ice concentration (their results suggest ∼80–90 %). We see similar evidence for an optimal sea ice concentration in C_{equiv}; binned-median values of C_{equiv} have a peak near 60% ice concentration (fig. 4.11). However, our observations show that binned-median C_{equiv} roughly follow the free-drift limit (case 1), and there is not an appreciable decrease below that limit in median C_{equiv} at 100% ice concentration (which is in contrast to the pan-Arctic average results presented by *Martin et al.*, 2014). This suggests that the optimal ice concentration for momentum transfer seen in our results is driven by the maximum of eq. (4.15a), and is minimally affected the ice interaction force ($\boldsymbol{F}_i$). As such, results for optimal ice concentration will

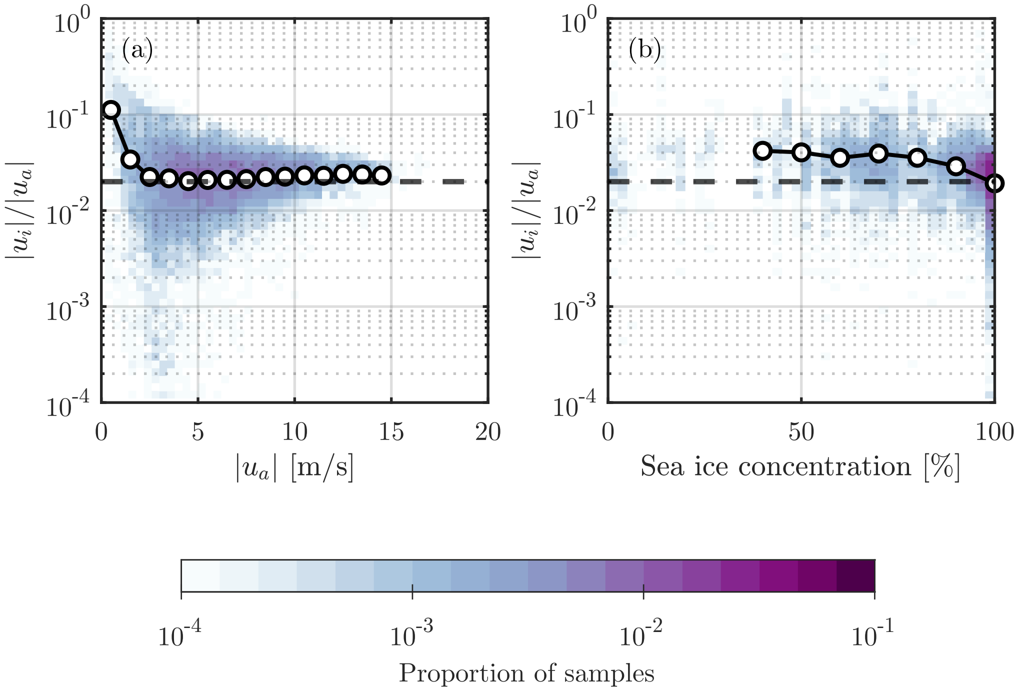

Figure 4.12: Wind factor ($|\boldsymbol{u}_i|/|\boldsymbol{u}_a|$) as a function of (a) wind speed, and (b) sea ice concentration (from ERA5). In both panels, shading shows a 2-dimensional histogram of the proportion of total samples (on a log-scale), while black lines with circles show the values of wind factor bin-averaged by (a) wind speed, and (b) sea ice concentration. Bin-averages in (b) were only produced for sea ice concentration $\geq$40% due to data scarcity for lower ice concentrations. The horizontal dashed black line in both panels corresponds to a wind factor of 2%.

be highly sensitive to the parameterization of C_{ia}. Furthermore, these results indicate that, on average, at all three moorings the presences of sea ice causes an amplification of stress transfer compared to open-water conditions for a given wind speed. This is consistent with *Martin et al.* (2016), who found that sea ice in the Beaufort Sea causes a mean amplification of stress into the ocean for all seasons regardless of whether a constant or variable ice-ocean drag coefficient was used in the model (see their figure 12).

4.6 Conclusions

Using a force-balance approach to estimate the ice ocean drag coefficient, C_{io}, the annual cycle of the efficiency of ice-ocean momentum transfer is inferred from mooring observations. These estimates compare favorably with drag coefficients using parameterization schemes, based on measured statistics of ice geometry, as well as with previous observations of ice-ocean drag. We summarize the main contributions of the study as follows:

1. The ice ocean drag coefficient, C_{io}, varied seasonally. Variations were more pronounced for the moorings in the seasonal ice zone compared to the mooring that was ice-covered through the full year (fig. 4.6), suggesting that the enhanced seasonality of the Arctic ice pack is directly influencing seasonality in C_{io}. This manifested as a decrease in C_{io} in the summer and fall, driven by changes in intensity of ridged ice (fig. 4.8). Wintertime mean values of C_{io} were similar to, or higher than, the canonical value of 5.5×10^{-3} (up to a maximum of 12.3×10^{-3}), but summer and fall values at SODA-A and -B (which may be more representative of future conditions) were as low as $\sim 1.3 \times 10^{-3}$ (fig. 4.10). The observed seasonality agrees with previous observational studies in the Western Arctic (*Cole et al.*, 2017; *Dewey*, 2019), but contrast with pan-Arctic model results (*Tsamados et al.*, 2014; *Martin et al.*, 2016).

2. Geometry-based drag parameterizations reproduce many of the spatial and temporal variations of ice-ocean drag, provided that the ice geometry is known (figs. 4.6 and 7).

Slight modifications to the existing parameterization schemes produces the most favourable results (T14(II); fig. 4.7c), but a full optimization of all free parameters has yet to be performed (and should account for non-neutral conditions and differences in boundary layer structure). Parameterization of the ice geometry (T14(III)) appears more challenging (fig. 4.7d), particularly predicting the correct floe sizes (impacting the total floe edge drag, figs. 4.8g to 4.8i). The mismatch in seasonality of ice-ocean drag between observations (*Cole et al.*, 2017; *Dewey*, 2019, and the present study) and models (*Tsamados et al.*, 2014; *Martin et al.*, 2016) is likely a direct result of the difficulties in predicting floe aspect ratios using bulk parameters. Despite these challenges, the scheme that included ice geometry parameterization (T14(III)) still provided reasonably predictions of the ice-ocean drag prior to ice breakup in the spring/summer (fig. 4.6, red lines).

3. In the seasonal ice zone, ridging intensity grows relatively slowly compared to the growth of ice concentration (compare figs. 4.2d and e with fig. 4.5f). As a result, approaches for simplified ice concentration-based parameterization schemes that have been successful for calculating atmospheric drag (e.g., *Andreas et al.*, 2010a,b) may not be the correct approach for drag at the ice-ocean interface. It is unlikely that schemes based solely on ice concentration will be able to adequately capture variations in ice-ocean drag during the ice growth season.

4. The presence of sea ice causes a net amplification of the efficiency of stress input to the ocean compared to open water (section 4.5.3) which we attribute to the prevalence of free drift conditions (including intermittently during full ice cover). Our measurements support the notion of an "optimal ice concentration" for momentum transfer (*Martin et al.*, 2014, 2016), but suggest the value of the optimal concentration has high sensitivity to the parameterization of the atmosphere-ice drag coefficient, C_{ai} (fig. 4.11). A comparison between moorings indicates that free drift conditions are more common to the south, and thus may become more common throughout

the Beaufort Sea in the future, with a net trend of amplified coupling between the atmosphere and the ocean.

The capability of models to represent the coupled atmosphere-ice-ocean system continues to evolve. Despite mismatches in predictions of ice geometry statistics which are used as inputs, the general success of the parameterization schemes described here gives greater confidence in our ability to use modelled results to learn about the "new Arctic", provided that methods can be developed to account for those mismatches. New sea-ice modelling schemes may be able to directly represent floe size distributions (*Roach et al.*, 2018) or keel statistics (*Roberts et al.*, 2019), reducing the need to redefine parameterizations of sea ice geometry. As model parameterizations of ice-ocean drag evolve, it will become important for users who apply those schemes to choose a framework that matches the model application, including an appropriate choice of reference depth, z_{ref}. For example, for an upper-ocean mixing study that uses $\boldsymbol{\tau}_{io}$ as a surface boundary condition it may be most appropriate to use a value of C_{io} consistent with drag at the base of the surface log-layer, or to choose z_{ref} in eq. (4.9) corresponding to the shallowest resolved ocean model level. Drag in a large-scale ice drift model driven by geostrophic ocean currents may be better described by Rossby Similarity Theory (*Blackadar and Tennekes*, 1968; *McPhee*, 2008) than by a quadratic drag law; though linking the "effective" roughness length used in that theory to statistics of large scale geometric features remains an open problem. Finally, differences between drag values measured at the different mooring sites indicates that variations in ice morphology may lead to large-scale spatial gradients in the ice-ocean drag, and consequently the surface momentum flux into the ocean, which may have important consequences for studies of large-scale Beaufort Sea circulation (e.g., gyre equilibrium and freshwater storage; *Meneghello et al.*, 2018a; *Timmermans et al.*, 2018; *Armitage et al.*, 2020).

APPENDICES

Appendix 4.A Timeseries example

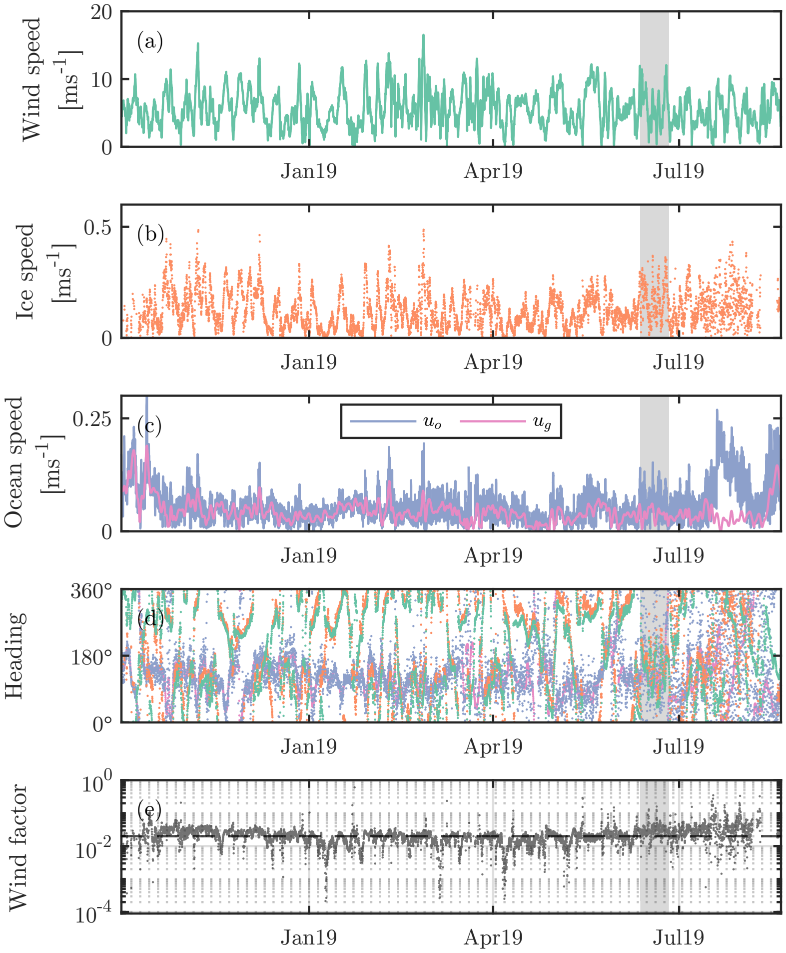

Figure 4.13: Hourly timeseries at SODA-B of (a) wind speed; (b) ice speed; (c) speed of ocean current at 10-m reference depth ($\boldsymbol{u}_o$) and geostrophic current ($\boldsymbol{u}_g$); (d) directions for each of the speeds in (a-c), coloured correspondingly (using a conventions of the direction each velocity vector is pointing towards measured clockwise from North); (e) wind factor ($|\boldsymbol{u}_i|/|\boldsymbol{u}_a|$). The shaded grey background shows the time period used in fig. 4.14.

Appendix 4.B Sensitivity of results: geostrophic velocity

The inclusion of the geostrophic velocity, $\boldsymbol{u}_g$ in eq. (4.3) arises from sea surface tilt in the sea ice momentum equation, and the assumption of geostrophic balance: $f\hat{k} \times \boldsymbol{u}_g = g\nabla\eta$. However, there is some ambiguity involved in defining a geostrophic velocity from ADCP-measured ocean velocity profiles. For the present study, $\boldsymbol{u}_g$ is based on the measured velocity averaged over some depth range, which has previously been found to be in good agreement with estimates of sea surface height from satellite altimetry on monthly timescales (*Armitage et al.*, 2017). Over a 12-year record in the Beaufort Sea, *Armitage et al.* (2017) found that the 5–20 m depth range produced the best match between monthly averaged velocities and satellite altimetry estimates of geostrophic velocity. Other studies have used different depth ranges. For example, *Randelhoff et al.* (2014) used an average velocity in the 17–22 m depth range to represent the undisturbed ocean beneath sea ice and *Cole et al.* (2017) define a geostrophic reference velocity in reference to the depth of the mixed-layer. For consistency with *Armitage et al.* (2017), we define $\boldsymbol{u}_g$ as the average velocity from 5–20 m depth low-pass filtered with a 2-day cut-off (to reflect that the geostrophic balance adjustment occurs over inertial timescales).

The values of $\boldsymbol{\tau}_{io}$ and C_{io} are fairly insensitive to the choice of averaging depth used to define the geostrophic velocity. Averaged through the full record, ice-ocean and atmosphere-ice stresses almost perfectly balance (table 4.4 and fig. 4.14). The Coriolis acceleration term is $\sim$3–4% of $\boldsymbol{\tau}_{io}$, but it largely cancelled by local acceleration and sea surface tilt. These results are generally consistent with those by *Steele et al.* (1997), who also find a minimal contribution from Coriolis and tilt terms (their model neglected local acceleration). While different choices of the depth range used for averaging in the definition of $\boldsymbol{u}_g$ result in different relative contributions to the ice-ocean stress (table 4.4), these amount to differences in $\boldsymbol{\tau}_{io}$ on the order of $\sim$1–2% and aren't substantial enough to impact the calculated values of C_{io}.

Table 4.4: Annual median values of the stress components of each of the terms in the sea ice momentum balance (eq. 4.3) projected onto the direction of $\boldsymbol{\tau}_{io}$. Different rows for the sea surface tilt component, $\rho_o d_i f \hat{k} \times \boldsymbol{u}_g$, (labelled 1–4) correspond to different depth-ranges used for averaging in the definition of $\boldsymbol{u}_g$: (1) 5–20 m, used for the main text; (2) 17–22 m; (3) the full depth profile measured by the ADCP; and (4) rather an a depth-averaged velocity, $\boldsymbol{u}_g$ is defined by the velocity in the deepest ADCP bin.

	Projected stress [mPa]		
	SODA-A	SODA-B	SODA-C
$\boldsymbol{\tau}_{io}$	116.7	96.8	69.3
$\boldsymbol{\tau}_{ai}$	116.5	97.7	71.4
$-\rho_o d_i \frac{\partial \boldsymbol{u}_i}{\partial t}$	0.1	0.4	0.3
$-\rho_o d_i f \hat{k} \times \boldsymbol{u}_i$	-5.4	-2.7	-4.4
$^{(1)}$ $\rho_o d_i f \hat{k} \times \boldsymbol{u}_g$	5.0	1.5	1.5
$^{(2)}$ $\rho_o d_i f \hat{k} \times \boldsymbol{u}_g$	4.1	1.1	0.8
$^{(3)}$ $\rho_o d_i f \hat{k} \times \boldsymbol{u}_g$	3.6	0.9	1.3
$^{(4)}$ $\rho_o d_i f \hat{k} \times \boldsymbol{u}_g$	2.3	0.4	0.3

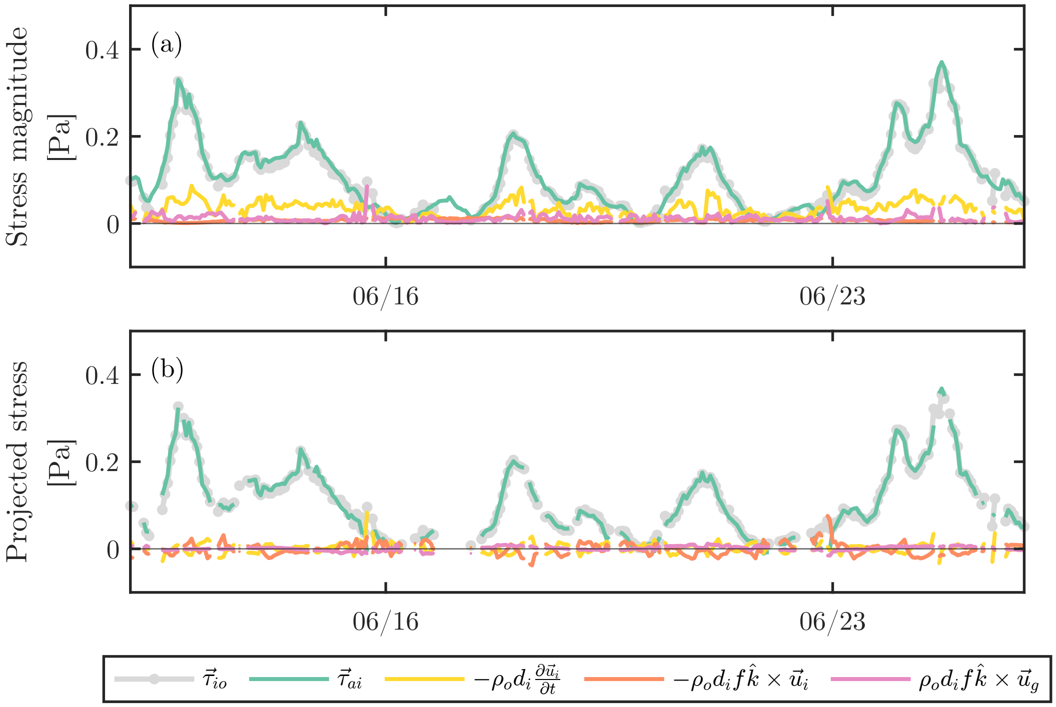

Figure 4.14: An example period from two week period in summer at SODA-B showing the size of different terms in the sea ice momentum balance (eq. 4.3): (a) magnitude of each stress component; (b) stress components projected onto the direction of $\boldsymbol{\tau}_{io}$. Missing values of $|\boldsymbol{\tau}_{io}|$ in (a) and of all stress components in (b) are due to the exclusion of $|\boldsymbol{\tau}_{io}|$ values when the wind factor is $< 2\%$.

Appendix 4.C Sensitivity of results: atmosphere-ice drag coefficient

As the ice-ocean stress in free-drift conditions is largely set by the atmosphere-ice stress (table 4.4 and fig. 4.14), the values of $\boldsymbol{\tau}_{io}$ and consequently C_{io} will be sensitive to the atmosphere-ice stress. The atmospheric stress available from the ERA5 re-analysis product represents the total effective stress $\boldsymbol{\tau}_{atm}$, which is the ice-concentration weighted average of atmosphere-ice and atmosphere-ocean stresses (reproduced from eq. 4.5b):

$$\boldsymbol{\tau}_{atm} = A\boldsymbol{\tau}_{ai} + (1 - A)\boldsymbol{\tau}_{ao}.$$

Thus, the re-analysis stress is not appropriate for predicting sea ice motion, which responds to the atmosphere-ice stress, $\boldsymbol{\tau}_{ai}$ (see eq. 4.2). Instead, the atmosphere-ice stress in this study is determined using the quadratic drag law (eq. 4.4b): $\boldsymbol{\tau}_{ai} = \rho_a C_{ai} \boldsymbol{u}_a \left|\boldsymbol{u}_a\right|$, with an atmosphere-ice drag coefficient C_{ai} (which accounts for the combined effects of both skin and form drag on the ice surface). In past studies of ice-ocean drag using a force balance approach, C_{ai} has been taken as a constant (*Kim et al.*, 2017; *Dewey*, 2019), or may be an additional predicted result (which requires additional modelling; e.g., *Heorton et al.*, 2019). The atmosphere-ice drag coefficient is expected to vary with bulk sea ice surface roughness similarly to the ice-ocean drag coefficient (*Andreas*, 2011; *Lüpkes et al.*, 2012); however, a number of studies have described observed variations as functions of sea ice concentration, A (e.g., *Andreas et al.*, 2010a,b; *Lüpkes et al.*, 2012).

Here, we consider the sensitivity of the calculated ice-ocean drag values to the choice of parameterization of the atmosphere-ice drag coefficient, and describe the choice used in the main body of the study. Three schemes are considered: (1) the formulation from the European Centre for Medium-Range Weather Forecasts (ECMWF) model; (2) a constant drag coefficient; and (3) following a version of the parameterization by *Lüpkes et al.* (2012).

The ECMWF model (scheme 1) parameterizes the ice surface roughness as a function of ice concentration, A as (*ECMWF*, 2019a):

$$z_{0M} = 10^{-3} \times \max\left\{1, \quad 0.93(1 - A) + 6.05\exp[-17(A - 0.5)^2]\right\}, \qquad (4.16)$$

which accounts for the combined effects of sea ice skin roughness and form drag. Then, the neutral drag coefficient $C_{ai} = [\kappa/\ln(z_{ref}/z_{0M})]^2$, with $z_{ref} = 10\,\mathrm{m}$.

The constant drag coefficient (scheme 2) is taken as $C_{ai} = 1.47 \times 10^{-3}$, based on a constant roughness length $z_{0M} = 2.3 \times 10^{-4}\,\mathrm{m}$ (appropriate for winter Arctic conditions; *Andreas et al.*, 2010b).

The parameterization by *Lüpkes et al.* (2012) (scheme 3) forms the basis for the ice-ocean drag parameterization by *Tsamados et al.* (2014) and is based on ice geometry characteristics (similar to section 4.2.1); however, the authors provide a hierarchy of simplifications to the model based on empirical relationships found between ice morphology and concentration (also see *Lüpkes et al.*, 2013). To construct C_{ai} only as a function of A based on *Lüpkes et al.* (2012) for the purpose of sensitivity testing, we use their eqs. 2 and 53–54 with h_f given by their eq. 25 and ignore the effects of melt ponds (consistent with *Elvidge et al.*, 2016). Note that *Lüpkes et al.* (2012) parameterize a total equivalent neutral atmospheric drag coefficient as $C_{atm} = AC_{d,i} + (1 - A)C_{ao} + C_{d,f}$, where $C_{d,i}$ is the skin drag on the ice surface and $C_{d,f}$ is the form drag (C_{ao} is the atmosphere-ocean drag). Since the form drag, $C_{d,f}$, acts only on the ice-covered area, the total atmosphere-ice drag coefficient (accounting for both skin and form drag) from the *Lüpkes et al.* (2012) formulations becomes $C_{ai} = C_{d,i} + C_{d,f}/A$.

The effective total atmospheric drag coefficient, C_{atm} (found as $C_{atm} = AC_{ai} + (1 - A)C_{ao}$, where C_{ai} includes both skin as form drag contributions), has a similar character for both the ECMWF scheme and the scheme by *Lüpkes et al.* (2012) (fig. 4.15a) while the constant drag scheme doesn't include the local maximum at intermediate sea ice concentrations (for fig. 4.15a, C_{ao} is set to a fixed value of 1.1×10^{-3} as an example, following *Elvidge et al.*, 2016). However, these test cases give different forms of the atmosphere-ice drag coefficient, C_{ai}. The three schemes have somewhat similar values of C_{ai} at 100% ice concentration (values vary from 1.47×10^{-3}–1.98×10^{-3}); however, at low concentrations, the value of C_{ai} can more than double depending on the choice of parametrization scheme (values vary from 1.47×10^{-3}–3.91×10^{-3}; fig. 4.15b).

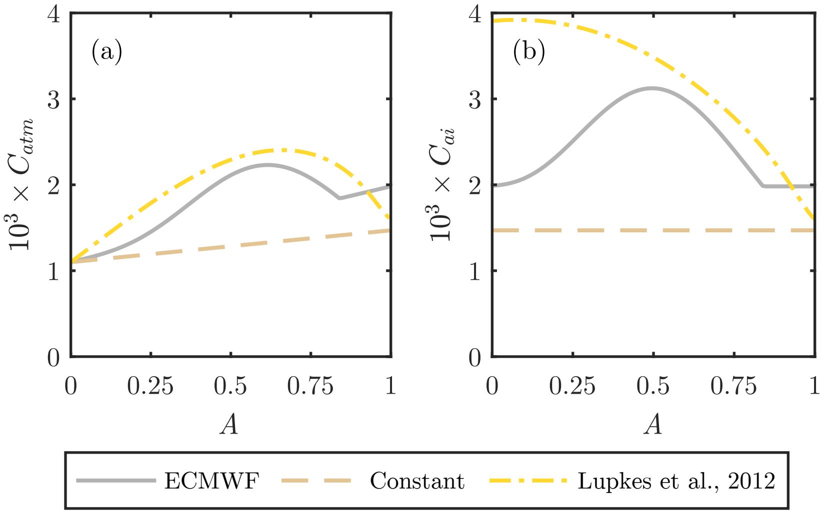

Figure 4.15: Parameterized drag coefficients as a function of sea ice concentration, A: (a) total effective atmospheric drag coefficient, C_{atm}; (b) atmosphere-ice drag coefficient, C_{ai}.

Despite the much higher C_{ai} during the fall season when using the *Lüpkes et al.* (2012) parameterization (compared to ECMWF; fig. 4.16a), the observed seasonal variations in the ice-ocean drag coefficient exist regardless of the C_{ai} scheme used (fig. 4.16b). The differences between the fall minimum and winter maximum C_{io} are slightly muted when using the *Lüpkes et al.* (2012) scheme for C_{ai}, but enhanced when using a constant atmosphere-ice drag coefficient (due to lower values of C_{ai} during the fall). While the seasonal patterns of C_{io} are robust across different C_{ai} parameterization schemes, the values of C_{io} are impacted by the choice of scheme for C_{ai}. Annual average values of C_{io} taken across all three moorings are 4.6×10^{-3} when using the ECMWF parameterization for C_{ai} (fig. 4.10), 4.1×10^{-3} for the *Lüpkes et al.* (2012) parameterization, and 3.3×10^{-3} for constant C_{ai}; these values directly reflect the proportional changes between C_{ai} calculated using the different parameterization schemes.

For the purpose of the main body of the text, $\boldsymbol{\tau}_{ai}$ is calculated with the quadratic drag law (eq. 4.4b), and uses the *ECMWF* (2019a) method of atmosphere-ice drag calculation

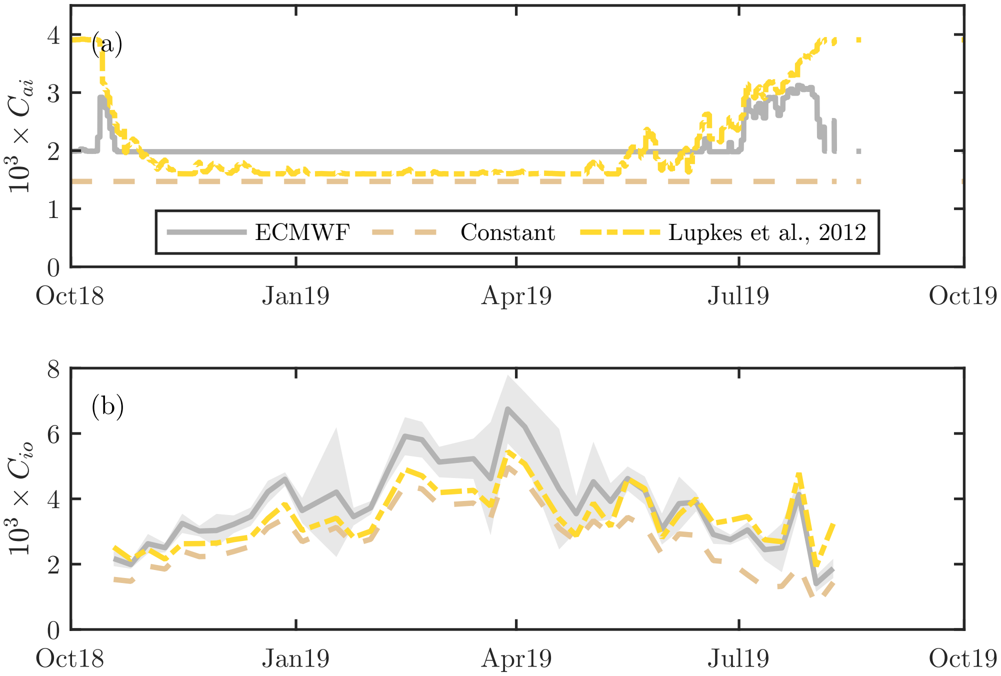

Figure 4.16: Timeseries at SODA-B of (a) atmosphere-ice drag coefficients, C_{ai}, calculated using different parameterization schemes, and (b) corresponding ice-ocean drag coefficients, C_{io}. The grey-shaded region in (b) shows the 95% uncertainty range associated with regression procedure to determine C_{io} when C_{ai} is calculated with the ECMWF scheme.

(C_{ai}), with a surface roughness given by eq. (4.16) that accounts for the effects of both skin and form drag together. Thus, the chosen scheme is consistent with the ERA5 re-analysis product that is used for wind speed.

Chapter 5

WIND-DRIVEN MOTIONS OF SEA ICE AND THE OCEAN SURFACE MIXED LAYER IN THE WESTERN ARCTIC

5.1 *Introduction*

Throughout the ice-covered polar oceans, the transfer of momentum from the wind into the ocean is mediated by the presence of sea ice. Sea ice itself is highly dynamic, moving in response to both winds and ocean currents. A portion of the momentum and energy that would be transferred into the ocean is instead borne by internal stresses in the ice, which result in ice deformation and fracturing. Consequently, the total surface stress into the ocean depends on the mechanics and dynamics of the sea ice, which in turn depend on the ocean currents in a highly coupled system. This complexity has lead to challenges in understanding the extent to which the sea ice might suppress momentum transfer. In the Arctic Ocean, other lines of evidence, such as low interior mixing rates (*D'Asaro and Morison*, 1992; *Rainville and Winsor*, 2008; *Fer*, 2009; *Dosser et al.*, 2021), provide ancillary support for the notion that the ice there is an effective barrier to wind-driven motions. Other factors like the strong halocline might also be important in setting those differences (*Guthrie and Morison*, 2021). The degree to which ice impacts ocean surface stress is still unclear.

Wind is one of the primary drivers of ocean circulation, and by mediating this process sea ice impacts circulation across a range of spatio-temporal scales. The Beaufort Gyre – the dominant mean ocean circulation pattern in the Western Arctic – is controlled by a balance of Ekman pumping, from large-scale gradients in wind-driven Ekman transport, and ice-ocean stress (e.g., *Dewey et al.*, 2018; *Doddridge et al.*, 2019; *Armitage et al.*, 2020; *Meneghello et al.*, 2020a), with important contributions from lateral eddy fluxes (e.g., Manucharyan and Spall, 2016). Low internal wave energy in the Arctic interior relative to lower latitudes (D'Asaro and Morehead, 1991; Levine et al., 1985, 1987) may be a result of the presence of sea ice impacting surface stress transfer (e.g., Rainville and Woodgate, 2009; Martini et al., 2014; Kawaguchi et al., 2019). Shear-driven mixing at the base of the surface mixed layer (ML) arising from wind-forced ocean surface currents (including inertial oscillations; e.g., Lenn et al., 2011; Fer, 2014) can entrain warmer subsurface water (e.g., Meyer et al., 2017; Peterson et al., 2017) and to lead to sea ice melt (Jackson et al., 2012; Peterson et al., 2017; Smith et al., 2018; Graham et al., 2019b). Efforts to predict or interpret any of these dynamics rely on accurate understanding and descriptions of the transfer of momentum and energy through the atmosphere-ice-ocean system.

Inertial oscillations, which are rotational motions that are a natural resonant response to wind forcing, are useful for understanding the role of sea ice in local atmosphere-ocean momentum flux. Both the sea ice and the ocean ML exhibit inertial oscillatory motions with strong seasonal cycles: oscillations are weak in the winter during pack ice cover and stronger in marginal ice and open water (Plueddemann et al., 1998; Rainville and Woodgate, 2009; Martini et al., 2014; Dosser and Rainville, 2016; Kawaguchi et al., 2019). Sea ice inertial oscillations have been studied by ice dynamacists to better understand sea ice mechanical strength and deformation (Colony and Thorndike, 1980; Geiger and Perovich, 2008; Gimbert et al., 2012a; Hutchings and Rigor, 2012). In the ocean, the seasonality of inertial oscillations is taken as an indicator that sea ice suppresses wind-driven currents (e.g., Rainville and Woodgate, 2009; Martini et al., 2014). Due to their fairly simple physics (e.g., Pollard and Millard, 1970; D'Asaro, 1985), ML inertial oscillations provide an ideal test case for the potential of sea ice to impede the transfer of momentum and energy from the wind. Though, as the oscillations of sea ice and the upper ocean are strongly coupled (McPhee, 1978, 1980), it is important to consider both systems together when investigating the implications for momentum and energy transfer.

Arctic sea ice loss in recent decades adds an additional layer of uncertainty to atmosphere-ocean momentum flux. As sea ice in some Arctic regions shifts to a more dominantly seasonal regime (*Thomson et al.*, 2016b; *Onarheim et al.*, 2018), the greater extent of open water will allow direct connection between the wind and the ocean. It is thought that this may lead to a change in the dominant physical processes in the upper ocean, and a shift to an increasingly wind-forced regime (*Rainville et al.*, 2011). While some focus has been placed on the impacts of changing ice concentration (*Guthrie et al.*, 2013; *Dosser et al.*, 2021), associated decreases in thick, multi-year ice (e.g., *Kwok*, 2018) might also lead to mechanical weakening of the sea ice pack. This is supported by studies showing increasing sea ice deformation and drift speeds (e.g., *Rampal et al.*, 2009) and changes in the scale of sea ice inertial oscillations (*Gimbert et al.*, 2012a). Furthermore, the shift to younger sea ice may also be associated with a decrease in sea ice surface roughness, impacting ice-ocean coupling (*Cole et al.*, 2017; *Brenner et al.*, 2021). A weaker and less rough ice pack could have an influence on the efficiency of atmosphere-ocean momentum transfer, even during winter sea ice cover.

In this study we seek to better characterize and understand the impact of sea ice on wind-driven motions in the ocean surface ML.

5.2 *Observations and data*

5.2.1 *Field measurements*

This study is based on *in situ* measurements from a set of three subsurface moorings installed across the Beaufort Sea as part of the Stratified Ocean Dynamics of the Arctic (SODA) experiment (*Lee et al.*, 2016; *Brenner et al.*, 2021). The moorings recorded data over one full annual cycle from fall of 2018 to fall 2019. They were roughly aligned along the axis of the Canadian Basin of the Beaufort Sea, and spanned different sea ice regimes and different parts of the Beaufort Gyre. The southern moorings, designated SODA-A and SODA-B, were both located in the seasonal ice zone with SODA-B being near the September minimum sea ice edge during the deployment season, while the northern mooring, SODA-C, was located in perennial sea ice (fig. 5.1a).

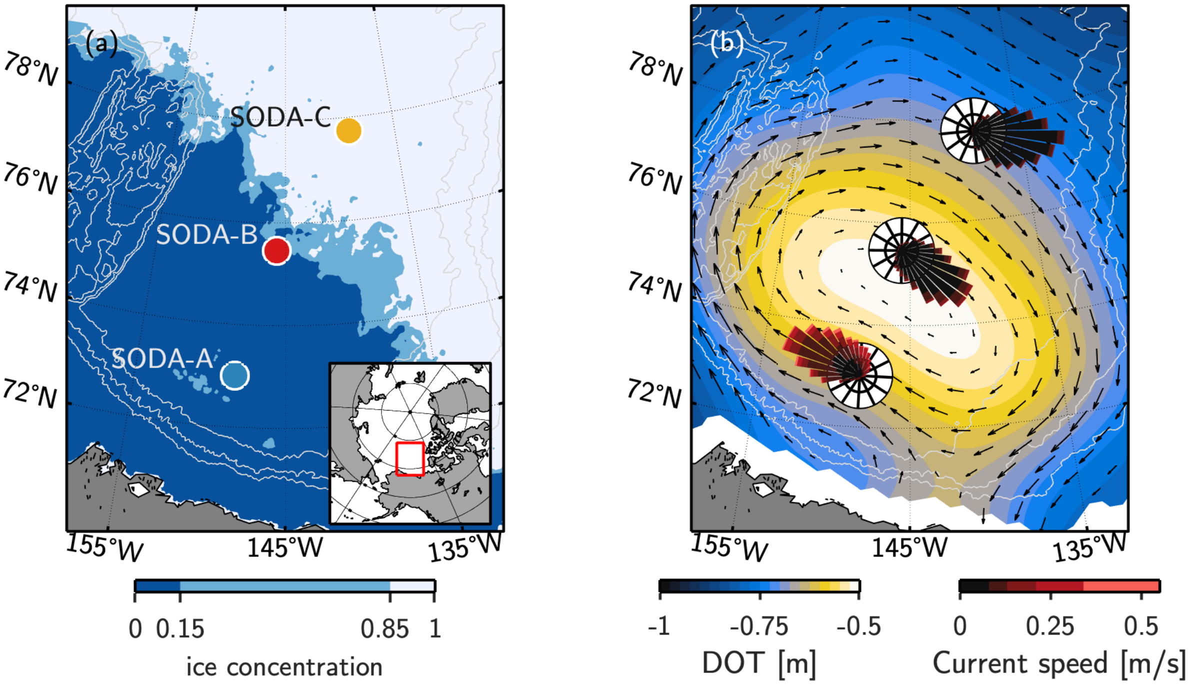

Figure 5.1: Maps showing the locations of the moorings in the context of (a) the sea ice concentration from September 18, 2018 (the 2018 sea ice minimum), with the inset showing the map location; and (b) the Sept. 2018–Oct. 2019 mean Beaufort Gyre circulation from smoothed Dynamic Ocean Topography (DOT; colour) with corresponding geostrophic velocity (black arrows), and from the mooring measured average ML current velocities (current roses). Grey contours show 1000-m isobaths.

This study applies sea ice and ocean velocity measurements, as well as measurements of the sea ice draft made by upward looking acoustic Doppler current profilers (ADCPs) installed on the moorings. Additionally, we use timeseries of ML depth at each mooring derived from a combination of ADCP backscatter and near-inertial velocity shear (chapter 3). *Brenner et al.* (2021, and chapter 3) previously reported data from these moorings and describe data processing and sampling schemes in more detail.

When describing velocities in the "near-inertial" range we consider a frequency band from $0.9f$–$1.1f$, where f is the Coriolis frequency, and selected only the component rotating clockwise (CW) in time. Timeseries of the "slowly-varying" magnitude and phase of the CW inertial signal are extracted using complex demodulation: velocities are frequency-shifted by a factor f (by multiplying the complex velocities by e^{if}) and then low-pass filtered using a fourth-order Butterworth filter with a cutoff of $0.1f$.

5.2.2 *Atmospheric forcing*

As the moorings had no surface expression, re-analysis data were used for atmospheric measurements. For consistency with *Brenner et al.* (2021), we used the European Center for Medium-Range Weather Forecasts (ECMWF) Reanalysis version 5 (ERA5; *Hersbach et al.*, 2020), which provides hourly measurements at a $0.25° \times 0.25°$ grid resolution.

The use of re-analysis wind forcing for this study provides some challenges. Re-analysis wind has been shown to under-represent energy in the super-inertial frequency band (*Fine et al.*, 2020). Furthermore, re-analysis can miss events in the marginal ice zone (*Brenner et al.*, 2020). However, *Cooper et al.* (2022, *submitted manuscript)* show that inferred wind speeds using wave measurements from these moorings and others (following *Thomson et al.*, 2013; *Voermans et al.*, 2020) provide a reasonable match with re-analysis, including for fetch-limited waves in the marginal ice zone (those authors compare with a different re-analysis product, but repeating their analysis for ERA5 produces similar statistical matches). *Brenner et al.* (2021) also showed high correlations between ERA5 wind speeds and observed sea ice drift speeds from the SODA moorings. These results give some confidence that the re-analysis data can be cautiously used for evaluating near-inertial and sub-inertial signals here.

5.2.3 *Sea ice concentration*

While there are a variety of sea ice concentration products available, we use the ice concentration that is included as part of the ERA5 re-analysis. As the atmosphere-ice drag coefficient in ERA5 (and also used here and in *Brenner et al.*, 2021) is parameterized as a function of ice concentration (see section 5.35.3.1), this choice is then self-consistent with the wind forcing used. Sea ice concentration in ERA5 is based on the Operational Sea Surface Temperature and Sea Ice Analysis (OSTIA) data product (*Donlon et al.*, 2012), re-sampled to the re-analysis model grid, effectively spatially smoothing the satellite estimates (*ECMWF*, 2019b). The OSTIA product uses SSM/I passive microwave satellite measurements of ice concentration from the Ocean and Sea Ice Satellite Applications Facility (OSI-SAF; *Breivik et al.*, 2001). Ice concentration data are provided with a daily resolution.

Throughout this study, the marginal ice zone (MIZ) is defined as having fractional ice concentration from 0.15–0.85, concentrations lower than 0.15 are defined as open water, and higher than 0.85 as pack ice (values of both 0.8 and 0.85 have been used as an upper bound concentration on the MIZ in previous literature; e.g., *Strong and Rigor*, 2013; *Heorton et al.*, 2019). While a variety of different metrics exist for defining the MIZ (e.g., *Horvat*, 2021), a transition between marginal ice and pack ice at $A \sim 0.8$–0.85 is reflective of a dynamical shift in the sea ice internal stress, and is evident in our observations.

5.3 ***Modelling framework***

To interpret the observations, we used a one-dimensional, linearly-damped, coupled sea ice-ocean slab model. The damped ocean slab model (from *Pollard and Millard*, 1970) has been used extensively for investigations of ML inertial oscillations in the open ocean (e.g., *D'Asaro*, 1985; *Alford*, 2003). It models the response of the ML velocity to surface wind stress; specifically capturing inertial oscillations and Ekman transport. To account explicitly for the presence of sea ice, we include the sea ice momentum equation and couple the two through ice-ocean stress (similar to *Gimbert et al.*, 2012a).

We adopt the notation for velocity and stress from *D'Asaro* (1985): Z and T represent, respectively, horizontal velocities and (kinematic) stresses expressed in complex form: $Z = u + iv$, $T = (\tau_x + i\tau_y)/\rho_o$, with ρ_o the ocean density. Then the evolution of the wind-forced sea ice and ML-averaged momentum, Z_i and Z_o, are modelled as:

$$\text{Sea ice:} \qquad \frac{dZ_i}{dt} + ifZ_i = \frac{T_{ai} - T_{io}}{d} - r_i Z_i, \tag{5.1a}$$

$$\text{ML:} \qquad \frac{dZ_o}{dt} + ifZ_o = \frac{T_S}{D} - r_o Z_o, \tag{5.1b}$$

where f is the Coriolis parameter; d is the sea ice draft (and the sea ice is assumed to be in hydrostatic balance); D is the ML thickness: $D = H - d$ with H the ML depth; and r_o, r_i are linear damping coefficients (subscripts $[\cdot]_o$ and $[\cdot]_i$ correspond to the ocean and ice respectively). The ocean velocity Z_o is depth-averaged from the underside of the ice to the base of the ML ($Z_o = \frac{1}{D}\int_{-H}^{-d}[u + iv]dz$). The velocities Z_i and Z_o can be thought of as being relative to an underlying geostrophic velocity, Z_g (where a term $-\frac{dZ_g}{dt}$ has been omitted from eq. 5.1a on the basis that Z_g is slowly varying relative to wind forcing; see eq. 7 from *Leppäranta et al.*, 2012). The use of time-variable H in the eq. (5.1b) further assumes that the ML depth is also slowly-varying (i.e., terms with $\frac{dH}{dt}$ are omitted).

The total surface stress acting on the ocean ML, T_S in eq. (5.1b), is taken as the ice-concentration-weighted sum of the direct stress transfer from the atmosphere into the ocean (T_{ao}), and the stress transferred from the sea ice (T_{io}):

$$T_S = AT_{io} + (1 - A)T_{ao}(1 - \beta), \tag{5.2}$$

where A is the fractional sea ice concentration, and the parameter β accounts for the flux of momentum into surface gravity wave generation in open water. The ice-concentration-weighted sum is commonly used to account for the combined impact of sea ice and open water on surface stress (e.g., *Yang*, 2006; *Martin et al.*, 2014; *Meneghello et al.*, 2017; *Dewey et al.*, 2018; *Brenner et al.*, 2021, and others), but is an approximation that likely breaks down at some scales. The effect of surface waves (i.e., the inclusion of β) is not often included, but appears in *Steele et al.* (1989). The atmosphere-ice stress, T_{ai} in eq. (5.1a), and atmosphere-ocean stress, T_{ao} in eq. (5.2), are both represented through a quadratic drag law in terms of wind velocity:

$$T_{a\square} = \left(\frac{\rho_a}{\rho_o}\right) C_{a\square} Z_a |Z_a|, \tag{5.3}$$

where ρ_a is the air density, $C_{a\square}$ is the corresponding atmosphere-ice (C_{ai}) or atmosphere-ocean (C_{ao}) drag coefficient, and Z_a is the complex 10-m wind velocity. The ice-ocean stress, which acts as the coupling between eqs. (5.1a) and (5.1b), is written in a similar quadratic form based on ice-ocean relative velocity (with ice-ocean drag coefficient C_{io}):

$$T_{io} = C_{io}(Z_i - Z_o)|Z_i - Z_o|. \tag{5.4}$$

Implicit in eq. (5.4) are assumptions about the ice-ocean boundary layer structure. In this work, eq. (5.4) represents the momentum flux through a quickly adjusting, shallow, and highly sheared "inner boundary layer" near the ice. As such, it is not necessary to include a turning angle (which would be needed when considering Z_g as a reference velocity, as described by *McPhee*, 2012). The use of Z_o in defining the ice-ocean relative velocity in eq. (5.4) then implies minimal shear in the remainder of the ML (the "outer boundary layer").

That assumption seems to generally hold for velocities in the inertial frequency band (and is part of the basis for ML depth identification in chapter 3). Example profiles show that the average inertial response has a "slab-like" structure (fig. 5.2a) consistent with the model description. Though, upper ocean shear is observed outside of the inertial band (figs. 5.2b and c).

Linear damping terms model stress at the ML base ($r_o Z_o$) and internal stress in the sea ice ($r_i Z_i$). The use of linear damping for both of these effects is a significant simplification

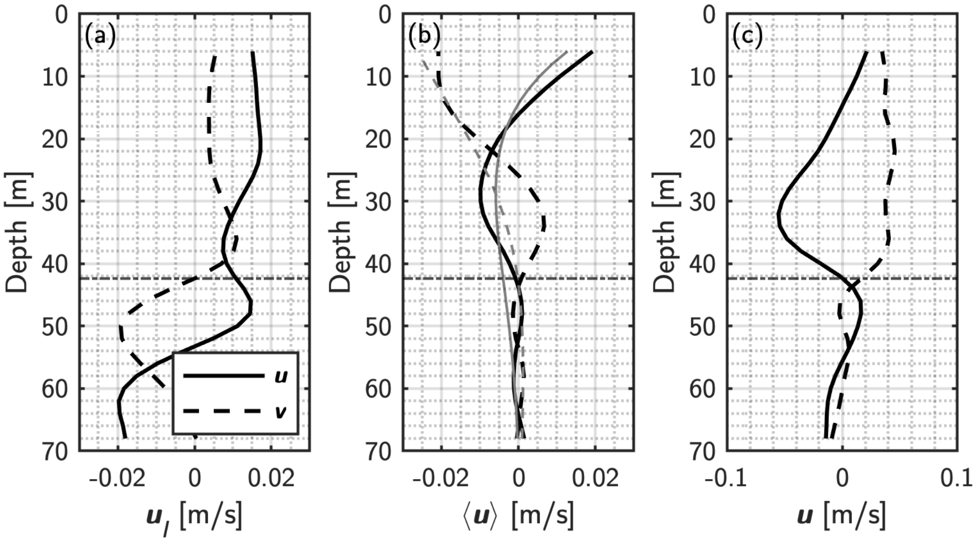

Figure 5.2: Profiles of upper ocean velocity: (a) 3-day average of inertially-filtered velocities after rotation into the frame of reference of sea ice motion. (b) 3-day average of broad-banded velocities after rotation into the frame of reference of sea ice motion, relative to the velocity level at the ML depth. Thick black lines are observations, thin grey lines are a theoretical Ekman spiral fit (following Cole *et al.*, 2017). (c) Example of an instantaneous velocity profile. Averages in (a) and (b) are taken from 10-Feb-2019 – 13-Feb-2019 at SODA-C, and the profile in (c) is from 11-Feb-2019. Horizontal dash-dotted lines in each panel show the averaged ML depth during this timeframe.

of the true physical processes, providing a crude but useful tool for investigating their respective roles in the momentum balance. These terms are discussed in more detail in section 5.35.3.2.

This model is closely related to the damped ice-ocean coupled slab model used by *Gimbert et al.* (2012a). While our approach and goals differ somewhat from those authors (particularly by our explicit inclusion and evaluation of measured ocean ML velocities and depth), their previous use of a similar model provides precedent for our application here.

5.3.1 *Implementation*

The sea ice and ML velocities, Z_i and Z_o were found by integrating eqs. (5.1a) and (5.1b) forward numerically. For numerical stability of the coupled equations, integration was performed with a time-step of 2 min (all model inputs/parameters were interpolated to this resolution). Additionally, for $A > 0$, a minimum sea ice draft d of 0.10 m was permitted to avoid model blow-up (i.e., all $d < 0.10$ m were set to the value of 0.10 m). The modelled near-inertial components of the velocities $(Z_i)_I$ and $(Z_o)_I$ were determined through complex demodulation of the broad-banded results (see section 5.25.2.1; hereafter, subscript $[]_I$ corresponds to inertial-filtered motions). Note that this is distinct from the version of the ocean slab model by *D'Asaro* (1985), which models the ML inertial motions directly.

The drag coefficients in the surface stresses for each of the interfaces (eqns. 5.3–5.4) all vary in time. The atmosphere-ice drag coefficient, C_{ai} was parameterized as a function of sea ice concentration, A, following *ECMWF* (2019a), and varied between $\sim 2 \times 10^{-3}$–3×10^{-3} (also see the supporting information for *Brenner et al.*, 2021). The atmosphere-ocean drag coefficient, C_{ao} was parameterized as a function of wind speed, Z_a following *Large and Yeager* (2004), with an average value of $\sim 1.3 \times 10^{-3}$. We used the ice-ocean drag coefficients C_{io} determined by *Brenner et al.* (2021) for these mooring data, which and varied between $\sim 1 \times 10^{-3}$–12×10^{-3} in response to seasonal changes in sea ice geometry (*Tsamados et al.*, 2014; *Lu et al.*, 2011). In calculating C_{io}, *Brenner et al.* (2021) used the same definitions and parameterizations of C_{ai} and C_{ao} as we used here, so the values are all self-consistent.

The factor β in eq. (5.2) relates to surface gravity wave growth: $\beta = T_{waves}/T_{ao}$, where T_{waves} is the momentum flux from the wind into the waves. *Steele et al.* (1989) use a constant value of $\beta \sim 0.14$. As the moorings measured the surface gravity wave spectra (*Cooper et al.*, 2022, *submitted manuscript)*, we calculate T_{waves} following *Zippel et al.* (2022) (adapted for scalar spectra). In our measurements, β values were always ≤ 0.06, with the highest values during strong wind events in open water.

5.3.2 *Linear damping parameters*

Momentum is removed from the system through the sea ice and ML linear damping terms: $r_i Z_i$ and $r_o Z_o$. The damping coefficients r_i and r_o are the only tunable parameters for fitting the model to observations. These coefficients can alternatively be discussed in terms of their damping timescales: $\mathcal{T}_\square = r_\square^{-1}$.

The damping coefficient for the ML, r_o, has been the subject of a number of previous studies in the open ocean, in which it nominally represents the radiation of near-inertial internal waves from the ML (e.g., *Alford*, 2001, 2003; *Park et al.*, 2009). In practice, shear-driven mixing and entrainment at the ML base also results in the loss of energy from ML inertial oscillations (*Plueddemann and Farrar*, 2006; *Johnston et al.*, 2016; *Alford*, 2020) and mesoscale/submesoscale activity can influence the ML inertial oscillations through a variety of mechanisms (*Johnston et al.*, 2016). As such, it would be expected that r_o has both spatial and temporal variability that might depend on physical properties such as stratification or ML depth. Nonetheless, it is common to take either r_o or $r_o f^{-1}$ as a fixed value. For example, *Voelker et al.* (2020) finds that a damping timescale of $\mathcal{T}_o \sim 5\,\mathrm{d}$ is a good fit to observations across the North Atlantic, while *Alford* (2001) use $r_o \sim 0.15 f$

across the global ocean (which *Martini et al.* 2014 also adopts in a study of under-ice inertial oscillations on the Beaufort continental slope). We take r_o as temporally fixed, but allow it to vary between moorings.

As the sea ice damping term ($r_i Z_i$) parameterizes internal ice stresses, we follow *Gimbert et al.* (2012a) in interpreting the damping coefficient r_i as a proxy for sea ice mechanical strength. At a bulk scale, sea ice strength is known to vary with both ice thickness and concentration, and this is reflected in the damping coefficient values *Gimbert et al.* (2012a) found across a number of ice conditions. A common representation of the thickness and concentration dependence in sea ice rheological models is through an ice strength formulation of the form: $P = P^* d e^{-20(1-A)}$, where P^* is a tunable strength parameter (*Hibler*, 1979). While the usage of P in sea ice models is much more complicated than the linear damping parameterization used here, we adopt this ice strength formulation and make the damping coefficient $r_i = r_i^* d e^{-20(1-A)}$, where a time-invariant parameter r_i^* is based on model fitting. This r_i rapidly decays as ice concentration decreases and results in a free-drift conditions for concentration below $\sim 85\%$, which is consistent with expectations of sea ice behaviour and with our observations.

We chose the tuning parameters r_o and r_i^* to maximize model fit separately for each mooring. While the procedure used by *Alford* (2001) for finding r_o can be adapted to eq. (5.1) by maximizing the model-observation correlation coefficient (R) in a two-dimensional parameter space in r_o and r_i^*, we found this produced unsatisfactory results. Specifically, highly damped sea ice (large r_i^*) combined with a minimally damped ML (low r_o) resulted in a step-like seasonal variation in inertial oscillations. Due to the strong seasonality of the observed inertial oscillation strength, this step-like result produced high correlations with the observations despite not faithfully reflecting any individual peaks in the signal. Instead, we chose r_o and r_i^* based on the criteria of minimizing the least-squares error between the modelled and observed inertial oscillation strength (accomplished with MATLAB's *lsqcurvefit* function). The fits found with the least-squares approach had comparable correlation coefficients as the maximization technique (both

Table 5.1: Damping parameter values and fit statistics for the slab model. Linear damping coefficients are shown in terms of their equivalent damping timescales (values of $\mathcal{T}_i$ are for $d = 1\,\mathrm{m}$ and $A = 1$). Correlation coefficient values (R) and root-mean-square errors (RMSE) for inertial oscillation magnitudes are shown separately for the ocean ML (subscript $[\cdot]_o$) and for sea ice (subscript $[\cdot]_i$).

Mooring	Parameter values		Fit statistics			
	$\mathcal{T}_o$ [days]	$\mathcal{T}_i$ [min]	R_o	R_i	RMSE_o $[\mathrm{m\,s^{-1}}]$	RMSE_i $[\mathrm{m\,s^{-1}}]$
SODA-A	2.3	84	0.63	0.83	0.025	0.015
SODA-B	4.3	39	0.80	0.82	0.018	0.013
SODA-C	3.3	25	0.84	0.80	0.017	0.020

statistical measures are related), but produced results that more reasonably matched during individual storm events as well as throughout the year. Resulting fitting parameter values and statistics are shown in table 5.1.

5.4 *Annual patterns of wind-driven motion*

5.4.1 *Observed patterns of sea ice and upper ocean velocities*

The moorings measured a background flow that is consistent with the large-scale Beaufort Gyre circulation as determined by satellite altimetry (*Armitage et al.*, 2016, 2017). This is shown by the current-roses in fig. 5.1b, and lines in fig. 5.3. The annual DOT-derived geostrophic velocities were 69%, 62% and 125% of the annually-averaged ML velocities at SODA-A to -C, respectively, and were directed at angles $< 30^\circ$ offset from the *in situ* observations.

Superimposed on the gyre circulation, the measured velocities of both sea ice and upper ocean show considerable seasonal modulation, particularly in the magnitude of near-inertial frequency motions (fig. 5.3). At all three moorings, inertial ice drift and current speeds were enhanced in periods of marginal ice and open water ($A \leq 85\%$), and relatively quiescent under pack ice. This seasonality is consistent with prior studies (e.g., *Plueddemann et al.*, 1998; *Rainville and Woodgate*, 2009; *Dosser and Rainville*, 2016; *Kawaguchi et al.*, 2019; *Polyakov et al.*, 2020a).

Across the moorings, the near-inertial sea ice and ML-averaged velocities are nearly identical during the pack-ice covered period (c.f. figs. 5.3a to 5.3c with figs. 5.3d to 5.3f), clearly demonstrating that inertial oscillations of the sea ice and ocean ML are highly coupled throughout the year. This matches with past studies (*McPhee*, 1978; *Lepparanta and Omstedt*, 1990). In our observations, this strong coupling is generally maintained through the marginal ice period, though there are some noticeable discrepancies. In particular, there is a strong peak in the ML inertial oscillations during the marginal ice-covered period at SODA-B (∼Jul. 21, 2019) that is not matched by the sea ice. This decoupling during this event isn't predicted by the model (see sections 5.45.4.2,5.4.3), suggesting the possibility of a separate surface velocity layer shallower than resolvable by the ADCPs (e.g., such as the shallow layers seen by *Cole et al.*, 2017).

Aggregating the measurements from the three moorings reinforces that the seasonality of ML inertial oscillations is linked to sea ice concentration. ML inertial oscillation strength, binned by ice concentration, shows a significant decrease in average momentum for pack-ice-covered conditions (fig. 5.4a). This is also reflected in the near-inertial ML horizontal kinetic energy (HKE) per unit area ($HKE_I = \frac{1}{2}\rho_o \int_{-H}^{-d} (\boldsymbol{u}_I \cdot \boldsymbol{u}_I) dz$). There is roughly an order-of-magnitude difference in the average HKE_I for concentrations above and below $A = 0.85$ (fig. 5.4c).

In contrast to the patterns of inertial oscillation, there was no strong seasonal modulation of the calculated net Ekman transport: $M_{Ek} = T_S(if)^{-1}$ (where the ice-ocean stress, T_{io} in T_S was calculated using observed sea ice and ocean ML velocities). There was no ice concentration dependence on bin-averaged Ekman transport magnitudes, $|M_{Ek}|$ (fig. 5.4e). Stratification can compress the Ekman spiral into shallow MLs (e.g., *Price et al.*, 1987; *Schudlich and Price*, 1998; *Randelhoff et al.*, 2014; *Chaudhuri et al.*, 2021). Averaging

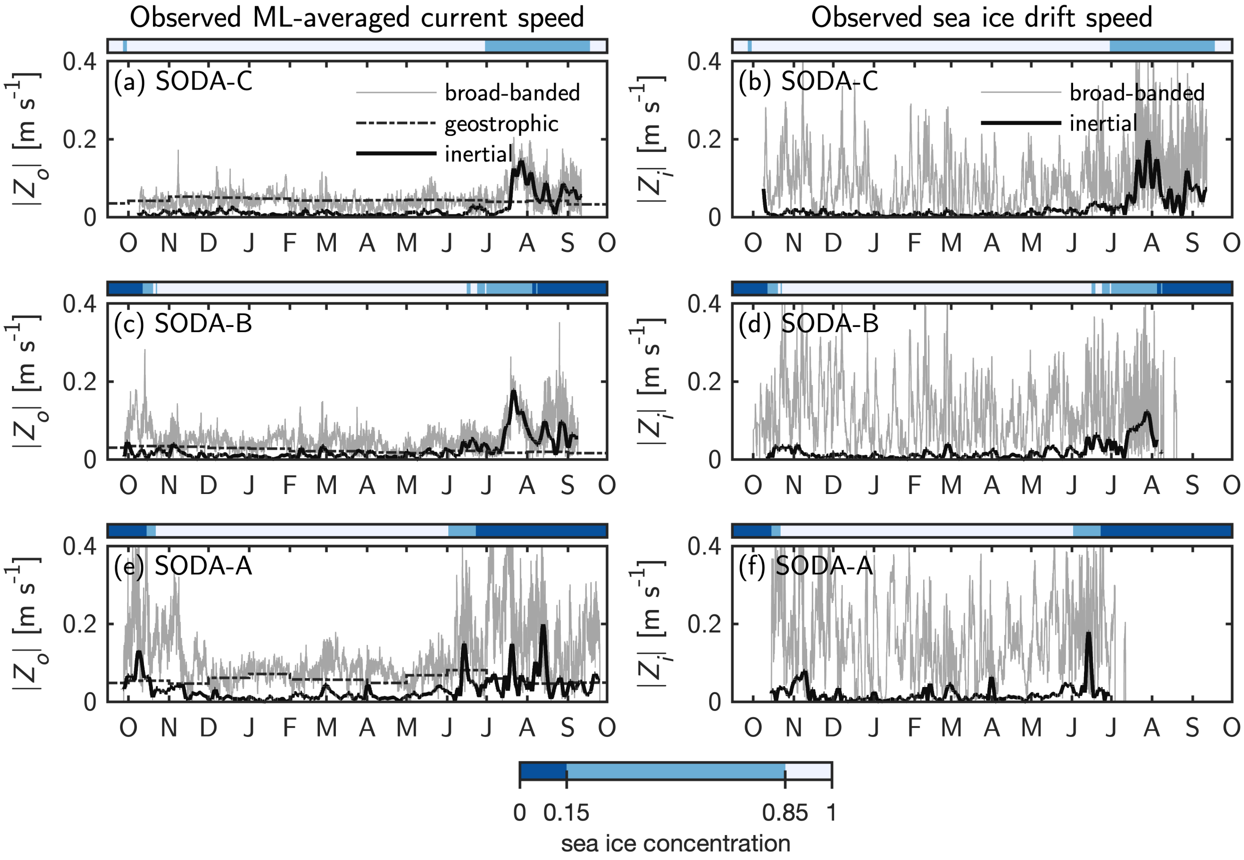

Figure 5.3: Timeseries of (a,c,e) observed ML-averaged current speeds, $|Z_o|$, and (b,d,f) observed sea ice drift speeds, $|Z_i|$, from each of the moorings: (a,b) SODA-C; (c,d) SODA-B; and (e,f) SODA-A. Lighter coloured, thin lines in all panels show the broad-banded speeds while thicker darker lines show the inertially-filtered signals ($|Z_o|_I$, $|Z_i|_I$). Dash-dotted lines in (a,c,e) show the gyre-scale geostrophic current speed from dynamic ocean topography (see fig. 5.1). Coloured bars along the top of each panel show the sea ice concentration.

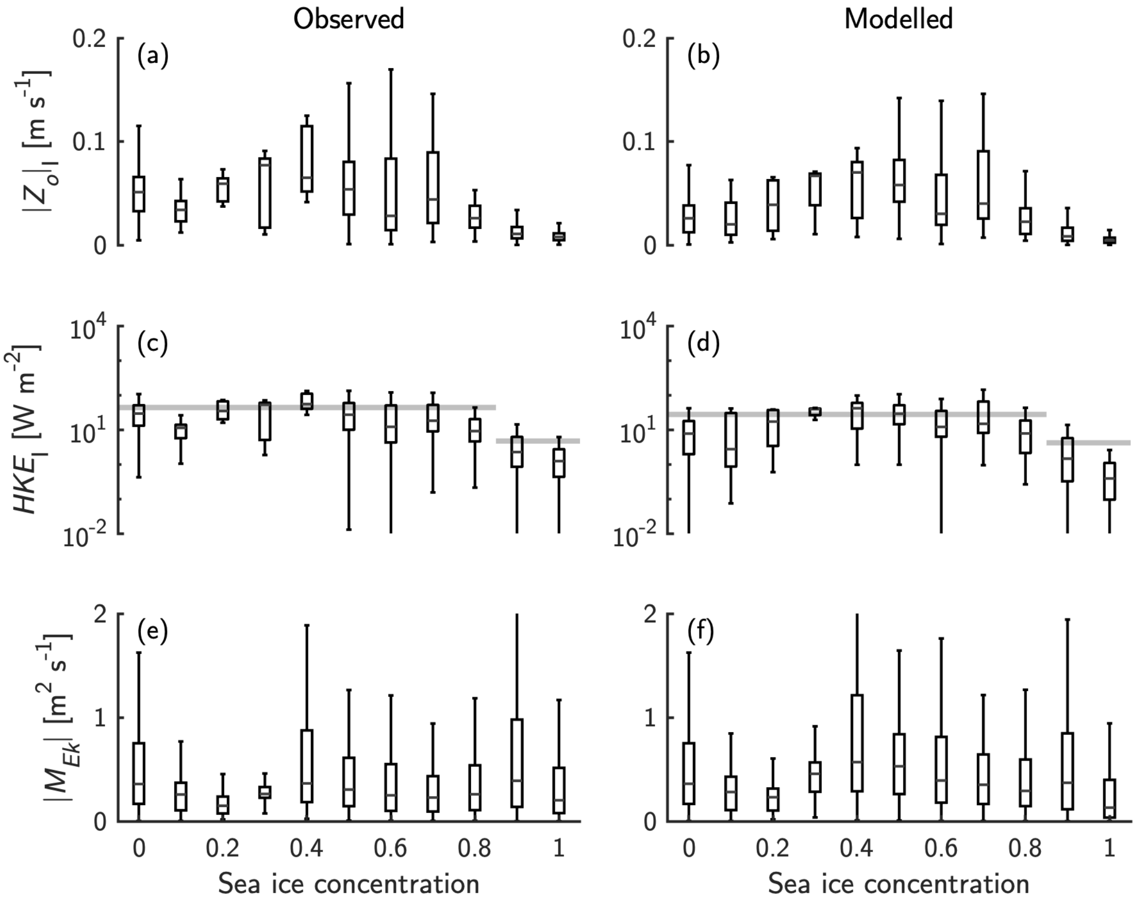

Figure 5.4: (a,b) ML inertial oscillation strength, $|Z_o|_I$, (c,d) inertial horizontal kinetic energy, HKE_I, and (e,f) Ekman transport magnitude, $|M_{Ek}|$ all bin-averaged by sea ice concentration. Column correspond to (a,c,e) observed values and (b,d,f) modelled values. Horizontal grey lines in (c,d) show the mean HKE_I for fractional sea ice concentrations above/below 0.85.

velocity profiles in a rotated frame of reference aligned with the sea ice velocity show similar Ekman spirals constrained within the ML (fig. 5.2b). So the ML average velocity associated with the Ekman transport $Z_{Ek} = M_{Ek}D^{-1}$ will have seasonality associated with ML depth and makes up some of the broad-banded velocity signal seen in fig. 5.3.

Rotary spectra of sea ice and ML velocities reveal additional features of the broad-banded response. Spectra of the complex sea ice and ML velocities (Z_i and Z_o) were created with Welch's method (*Welch*, 1967), using 512-point ($\sim 21.3\,\mathrm{d}$) Hamming windows overlapped by 50%, for a total of ~32 degrees of freedom. For additional context, similar spectra are also created for the wind velocity (Z_a). Observed spectra of both the sea ice and ML velocities show a "red" spectral shape and a strong peak in the clockwise rotating signal at the inertial frequency (figs. 5.5d to 5.5i). The observed spectra of the sea ice velocity are similar across the three moorings (figs. 5.5d to 5.5f), while those of the ocean ML velocity have differing shapes at low frequencies (figs. 5.5g to 5.5i). At SODA-A and -B there is a roughly constant power-law slope of the observed spectra for $\sigma \lesssim 0.4f$ (figs. 5.5g to 5.5h), while at SODA-C the spectral slope rolls off for low frequencies (fig. 5.5i) and is similar in shape to the wind and sea ice spectra.

5.4.2 *Modelled near-inertial and broad-banded response*

The model broadly captures the observed seasonal variations of sea ice and ocean ML inertial oscillation strength (fig. 5.6). The oscillations were small during the pack-ice covered period and increased as the moorings shifted into marginal ice and open water (also fig. 5.4b). Many of the peaks in oscillation strength associated with storm events are faithfully represented both during pack ice covered and marginal ice/open water periods. While some peaks in oscillation strength were weaker in the model than in the observations (including the strong peak in the MIZ at SODA-B when observed ML and sea ice inertial oscillations diverge), the model-observation correlations are high (table 5.1). When aggregated, the ML inertial current speed and HKE_I have ice-

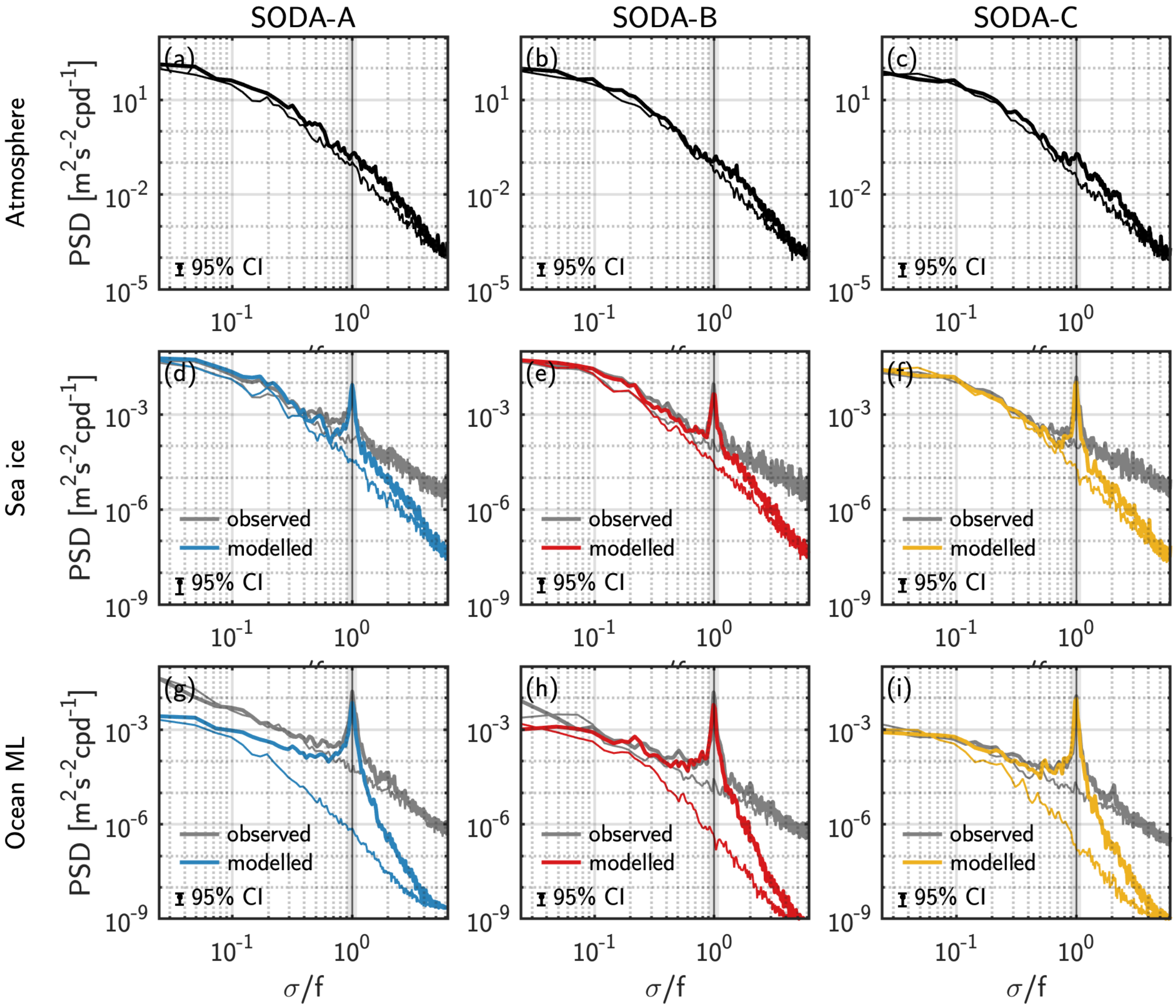

Figure 5.5: Rotary spectra of (a–c) re-analysis wind velocity; (d–f) sea ice velocity; and (g–i) ML velocity. Columns correspond to the different moorings: (a,d,g) SODA-A; (b,e,h) SODA-B; and (c,f,i) SODA-C. In all panels, thick lines are clockwise (CW) rotating velocities and thin lines are counter-clockwise (CCW) rotating velocities. Error-bars in the corner of each panel show the 95% confidence interval (CI).

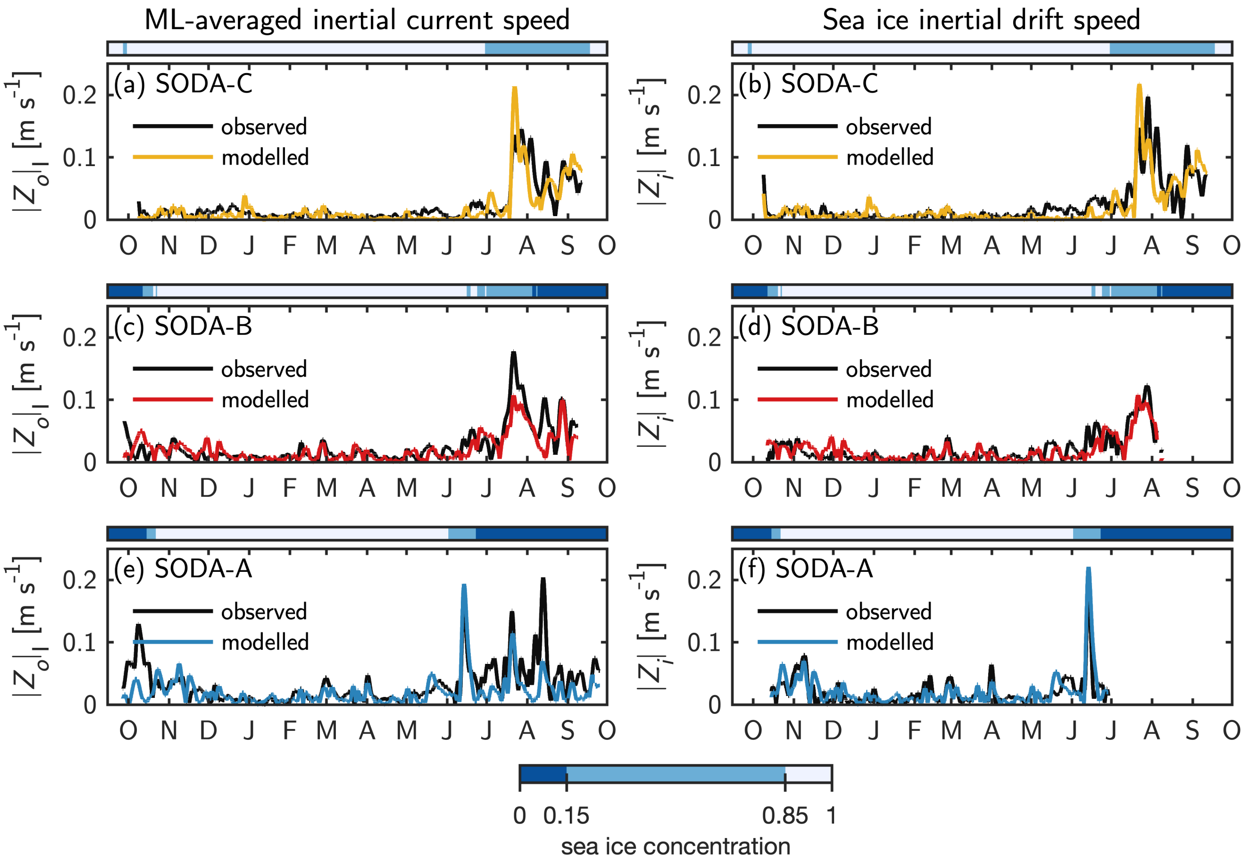

Figure 5.6: Comparison of observed and modelled inertial oscillation strength for each of the moorings (as labelled), for the ML (a,c,e) and sea ice (b,d,f). Grey lines show observations and coloured lines show modelled results. Coloured bars along the top of each panel show the sea ice classification.

concentration dependence that match observations (compare figs. 5.4b and d to figs. 5.4a and c). As such, we deem the model sufficient for further investigating the dynamics associated with inertial oscillations.

The model has mixed success in representing the variability outside of the inertial response, as seen by a comparison of model and observed rotary spectra (fig. 5.5). For sea ice, the model reproduces the CW inertial and sub-inertial spectra at all moorings. For the ML, the match differs between the moorings. At SODA-C, the model reproduces the observed spectra in the sub-inertial range, while at the other two moorings there is more sub-inertial energy and a different spectral shape in the observations than in the model (particularly at SODA-A). The mismatch at high frequencies for both sea ice and the ML is not surprising given the under-representation of super-inertial wind forcing in reanalyses, and the simplifications inherent in the model (i.e., the slab nature of the ML and the representation of internal stress).

Spectral matches/mismatches between the model and the observations at sub-inertial frequencies suggest other details of the sea ice and ocean dynamics. Low frequency sea ice motions are primarily wind-driven and, to a good approximation, can be described as moving at a fixed percentage of the wind speed (*Brunette et al.*, 2022). This explains the similar spectral shape of low frequency wind and sea ice velocity spectra (which both roll off below $\sigma \lesssim 0.4f$ at all locations; c.f., figs. 5.5a to 5.5c with figs. 5.5d to 5.5f), and the good match between observed and sea ice velocity spectra (figs. 5.5d to 5.5f). A similar low-frequency roll off and model-observation spectral match is seen in the low-frequency range of the ML spectra at SODA-C (fig. 5.5h). This suggests that low-frequency ML motions at that mooring are primarily wind driven Ekman transport (which is the only sub-inertial response predicted by the model). In contrast, the steeper spectral shapes and model-observation mismatch at low frequencies at the southern moorings (figs. 5.5g to 5.5h) suggest an increase in non-local ML motions. These could be due to non-local wind forcing (e.g., *Lee and Eriksen*, 1996), or a more energetic mesoscale/submesoscale eddy field in seasonally ice-covered waters. This would be consistent with theories and observations suggesting that sea ice modulates the Arctic surface eddy field and that those motions would be more energetic in seasonally ice-covered regions (e.g., *Meneghello et al.*, 2020b). Indeed, observations have shown surface mesoscale and submesoscale motions are prevalent in open water and the marginal ice zone of the Beaufort Sea (e.g., *Mensa and Timmermans*, 2017; *Kozlov et al.*, 2019; *Brenner et al.*, 2020; *Crews et al.*, 2022).

As with the observations, the Ekman transport (M_{Ek}) is roughly independent of sea ice concentration (fig. 5.4f), with only a small decrease in the median transport in the bin centred at $A = 1$ that is more pronounced than the observations. While the difference may not be statistically significant, it does hint that the linear damping term used for internal ice stress may not faithfully reflect all aspects of the stress transfer (which is not surprising given its simplicity).

5.4.3 *Ice-ocean inertial coupling*

A feature of both the present study and of past observations (*McPhee*, 1978; *Lepparanta and Omstedt*, 1990) is the strong coupling between sea ice and ocean ML inertial oscillations: both mediums oscillate in unison. *McPhee* (1978) explains this coupling with a model of the total vertically-integrated momentum transport, M, of both the sea ice and the ocean boundary layer together (roughly equivalent to $M = \rho_o d Z_i + \rho_o D Z_o$). In his formulation, there is no stress at the base of the boundary layer so momentum is only removed from the system by sea ice internal stress, which he also models as a linear damping term (with a slightly different form than used here).

An alternative approach is to consider an evolution equation for the ice-ocean relative velocity, $Z_{rel} = Z_i - Z_o$. Subtracting eq. (5.1b) from eq. (5.1a), and substituting eqs. (5.2) and (5.4) gives:

$$\frac{dZ_{rel}}{dt} + ifZ_{rel} = \mathcal{F} - \frac{C_{io}}{d_{\text{eff}}} Z_{rel}|Z_{rel}|, \tag{5.5}$$

where $d_{\text{eff}}^{-1} = d^{-1} + AD^{-1}$, and $\mathcal{F}$ is the sum of external forcing terms ($\mathcal{F} = T_{ai}/d - (1 - A)T_{ao}/D + T_{ii} - T_{oo}$, with the linear damping terms replaced with a more generalized internal ice stress, T_{ii}, and stress at the base of the ML T_{oo}). The quadratic form of ice-ocean stress (eq. 5.4) leads to quadratic damping of the relative ice-ocean velocity.

The response to the equivalent initial value problem after some forcing shut-off ($\mathcal{F} = 0$, $Z_{rel}(t = 0) = (Z_{rel})_0$) has an analytical solution:

$$Z_{rel} = \frac{(Z_{rel})_0 \, e^{ift}}{t/\mathcal{T}_{io} + 1}, \quad \text{for} \quad \mathcal{T}_{io} = \frac{d_{\text{eff}}}{C_{io} \, |(Z_{rel})_0|}. \tag{5.6}$$

This solution has a characteristic damping timescale $\mathcal{T}_{io}$ that is $\mathcal{O}(1\,\text{hour})$ for typical values of those parameters. Note that the timescale $\mathcal{T}_{io}$ is (up to a factor of d/D) the "timescale of ice inertia" defined by *Leppäranta et al.* (2012). That the damping timescale is much faster than the inertial period indicates that the behaviour of Z_{rel} is analogous to an over-damped harmonic oscillator: oscillations in Z_{rel} will only persist if they are continually externally forced. Since Z_{rel} is thus not oscillatory, the inertial oscillations of Z_i and Z_o will be coupled.

Using observations that showed in-phase oscillations of sea ice and the ocean surface, *McPhee* (1978) arrived at the same conclusion by comparing the sea ice velocity associated with transport M to observed sea ice oscillatory motion, and contrasted that with a case where the ocean is passive by keeping its velocity set to zero. While those results provided insight into the importance of oceanic inertia on the scale of the oscillations, the choice of fixing the ocean velocity to a constant (zero) value provides a strong constraint on the sea ice velocity due to the damping in eq. (5.5), and should not be considered to represent a "passive" ocean. Similarly, modelling the ocean boundary layer with a fixed sea ice velocity (such as in *Morison et al.*, 1985, and others) may lead to excess dissipation in the ice-ocean boundary layer relative to ice that is allowed to move; though, such a scenario may be reflective of the role of internal stress within the sea ice and therefore somewhat realistic.

A corollary of the of the non-linear damping in eq. (5.5) is that inertial oscillations under sea ice decay more quickly for a constant non-zero sea ice velocity (i.e, the low-frequency wind driven sea ice motion) than when the ice is stationary. As such, only weak internal ice stress is necessary to "stiffen" the ice sufficiently to dissipate the ML inertial oscillations.

5.4.4 *Drivers of inertial current seasonality*

The model provides insight into the observed seasonal cycle of sea ice and ML inertial oscillations. This seasonal cycle provides some evidence that sea ice partly inhibits momentum transfer from the atmosphere into the ocean (fig. 5.4), as has been previously suggested. Though, as seen in the model equations (eqs. (5.1–4)), there are a variety of parameters and inputs that have temporal variations and could contribute to a seasonal response. Of particular note are the significant seasonal variations in the ML depth at each mooring (chapter 3). As the input forcing is distributed over the ML (eq. 5.1b), it is expected that ML velocities will scale directly with ML depth.

Model parameter tests can be used to further investigate the drivers of inertial seasonality. To perform these tests, we considered a number of candidate model parameters and inputs that each have underlying seasonal variations which could contribute to the overall seasonal cycle of the inertial oscillations. For each of those variables, the model was re-run while setting the selected variable to a set of different constant values (and leaving all other variables as seasonally-varying). A comparison of the model runs with both the observations and with a reference model provides information about each variables' relative importance in controlling the seasonal cycle. Candidate variables that we tested were:

- the ice-ocean drag coefficient, C_{io};
- the atmosphere-ice drag coefficient, C_{ai};
- the ML depth, H;
- and the sea ice damping coefficient (sea ice strength parameter), r_i.

For each of these variables, tests set the input values to the 0.01, 0.1, 0.25, 0.5, 0.75, 0.9, 0.99 percentiles of their full range at each of the moorings.

To evaluate the degree of seasonality present in each of the model tests we consider the ratio of the average HKE_I under pack ice ($A > 0.85$) compared to under marginal ice and open water ($A < 0.85$) aggregated over all moorings:

$$\mathcal{R}_{HKE} = \frac{\langle HKE_I \rangle^{A>0.85}}{\langle HKE_I \rangle^{A<0.85}}, \tag{5.7}$$

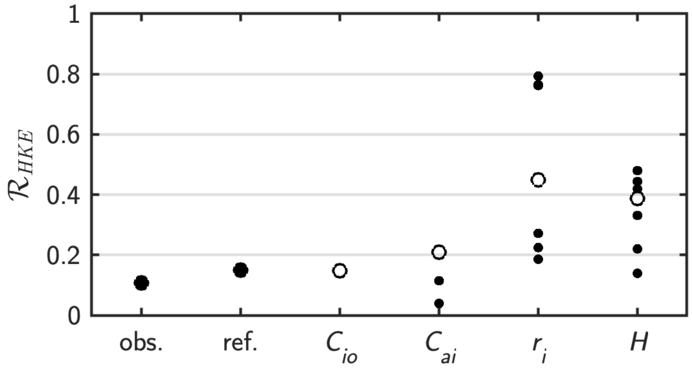

Figure 5.7: Horizontal kinetic energy ratios, $\mathcal{R}_{HKE}$, for parameter tests; "obs." shows the aggregated $\mathcal{R}_{HKE}$ from all mooring observations and "ref." shows the same for the reference model (where all parameters varied temporally). For each parameter listed, points show the range of $\mathcal{R}_{HKE}$ when that parameter is held at different constant values, with the open point corresponding to the annual median value (for each parameter, 7 constant values were tested and are shown but in some cases points overlap).

(angled brackets, $\langle \cdot \rangle$, represent the mean over the given ice concentration range). In both the observations and the reference model there was a distinct separation in the HKE_I for ice concentration above or below 0.85 (figs. 5.4b and c); in both, $\mathcal{R}_{HKE} \sim 0.1 - 0.15$ (fig. 5.7). Tests with values of $\mathcal{R}_{HKE} \gtrsim 0.15$ thus indicate a muted seasonality.

As expected, tests showed that the ML depth and the sea ice internal strength (as represented by the damping coefficient, r_i) both have important contributions to the seasonality of the inertial oscillations. For both of these parameters, tests in which values are held constant have $\mathcal{R}_{HKE}$ values that differed significantly from the observations and reference model (fig. 5.7). Further, the wide range of $\mathcal{R}_{HKE}$ for different constant values of either r_i or H indicate a high degree of sensitivity of the model to those values. While these results affirm prior understanding about the role of sea ice rigidity (internal stress) in preventing strong wintertime oscillatory motion (e.g., *Rainville et al.*, 2011), they also highlight that variability in the ocean structure also plays an important role, despite less frequent discussion in the literature.

The tests further show different degrees of sensitivity of the ice-ocean and atmosphere-ice drag coefficients: C_{io} and C_{ai}, respectively. Removing variability in C_{ai} did impact the seasonality of the inertial response ($\mathcal{R}_{HKE}$ deviating from observations; fig. 5.7), but was less important than r_i or H. Alternatively, the inertial oscillations were largely independent of C_{io} (values of $\mathcal{R}_{HKE}$ were essentially unchanged for different constant values of C_{io}; fig. 5.7).

The lack of sensitivity to C_{io} in the inertial frequency band is reflective of the highly coupled nature of the sea ice and ML oscillations. If the sea ice velocity were fixed (e.g., in a model forced by observed ice motion), then increasing the drag coefficient also increases the stress transfer into the ocean because $T_{io} \propto C_{io}$ (eq. 5.4). But because the ice and ocean are coupled, changes to C_{io} can also be compensated by changes to the sea ice velocity, Z_i, with a minimal change to T_{io} (because of the ice-ocean relative velocity in eq. 5.4). This adjustment is reflected by the damping of ice-ocean relative velocity in section 5.45.4.3. For any physically reasonable values of C_{io} that would match past observations, the damping timescale for ice-ocean relative velocity will be less than the inertial timescale (section 5.45.4.3), and so sea ice and ocean velocities react to changing C_{io} and they oscillate together.

While this study shows a minimal role of C_{io} in setting the strength of inertial oscillations, *Cole et al.* (2018) found that elevated sea ice roughness (represented by high C_{io}) was linked to more energetic near-inertial wave generation within pack ice covered areas. This contrast does not represent a discrepancy between our results and those of *Cole et al.* (2018); instead it highlights that near-inertial internal wave generation is multifaceted. While ML inertial oscillations are a starting point for understanding sea ice impacts on near-inertial wave generation in the Arctic (e.g., *Martini et al.*, 2014; *Kawaguchi et al.*, 2019), there may be other ways that ice affects wave generation. For example, *Jutras* (2016) identifies that in high ice concentrations, differential internal ice stresses can lead to sea ice convergence/divergence that drives inertial pumping and wave generation. Furthermore, the drag coefficients in *Cole et al.* (2017, which are used in *Cole et al.*, 2018) are derived from drifting point measurements of Reynold's stress and capture intermittent, short timescale, highly localized variability, while those used here (from *Brenner et al.*, 2021) are from data fits over week-long periods and reflect larger scale averages that could be used in models (such as in the present context). These differences in definitions of C_{io} may relate to the generation mechanism for internal waves (i.e., if they are predominantly associated only with the largest roughness elements). In any case, the mechanisms by which sea if roughness may separately impact inertial oscillations and internal wave generation provides an opportunity for further study.

5.5 *The role of sea ice in atmosphere-ocean energy and momentum transfer*

5.5.1 *The net impact of sea ice on ML inertial velocity*

The modelling framework used here allows us to investigate idealized scenarios, namely a complete absence of ice ($A = d = 0$ in eq. 5.1b and eq. 5.2), or the presence of ice without internal strength ($r_i = 0$). In both cases, the term involving surface waves (β) is set to zero to avoid introducing seasonal biases.

Differences between these two cases arise because there are a number of ways that sea ice impacts momentum transfer from the wind. While internal stress can act as a sink for momentum, increased surface roughness over sea ice relative to open water ($C_{ai} > C_{ao}$) results in more momentum flux out of the atmosphere for the same wind speed, and amplification of ocean surface stress (e.g., *Martin et al.*, 2014; *Brenner et al.*, 2021). Further, sea ice acceleration/deceleration may lead to phase mismatches between wind stress and inertial oscillations, impacting the resonant response.

To evaluate these two hypothetical scenarios, we consider the ratio of the inertial oscillations strength in the full reference model (with sea ice intact) to the oscillations in the "no ice" scenario or "no stress" test cases:

$$\mathcal{R}_{Z_o} = \frac{|Z_o|_I^{\text{ref}}}{|Z_o|_I^{\text{test}}}. \tag{5.8}$$

As the only source of momentum in the model is the wind, values of $\mathcal{R}_{Z_o}$ that are less than one indicate that sea ice acts to reduce the overall effectiveness of wind-momentum

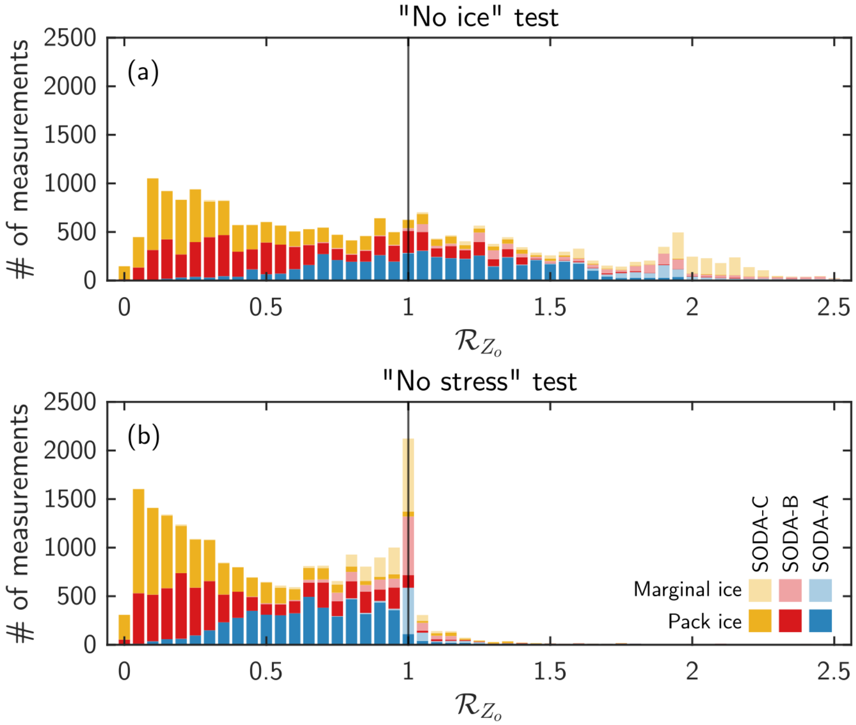

Figure 5.8: Stacked histograms of the ratio of the ML inertial oscillation strength in the full reference model to (a) the "no ice" test, and (b) the "no stress" test. Colours correspond to the different moorings, with bolder colours being measurements in pack ice conditions ($A > 0.85$) and faded colours being marginal ice ($0.15 < A < 0.85$).

transfer relative to the respective test case, while if $\mathcal{R}_{Z_o}$ is greater than one than sea ice causes amplification.

Figure 5.8 shows histograms of $\mathcal{R}_{Z_o}$ for the two test cases, separated for each of the three moorings. Not surprisingly, sea ice tends to reduce the magnitude of inertial oscillations (seen by the high occurrence of measurements with $\mathcal{R}_{Z_o} < 1$), with instructive distinctions between the two tests, and between the different moorings.

Despite the broad range of $\mathcal{R}_{Z_o}$, in the "no ice" test, values are generally ≤ 1 in pack ice conditions (solid coloured bars in fig. 5.8a), but in the 1.5–2.5 range in the marginal ice conditions (faded bars in fig. 5.8a), showing that marginal ice causes a strong amplification of inertial oscillations relative to open-ocean conditions with equivalent wind speeds. The amount of values with $\mathcal{R}_{Z_o} < 1$ varied between moorings, with the northern moorings having a higher proportion of values indicating that sea ice reduces oscillation strength.

In the "no stress" test, $\mathcal{R}_{Z_o}$ in pack ice covered conditions were all < 1 (fig. 5.8b). At the northern moorings (SODA-B and SODA-C; red and yellow) peaks in the histograms for low values of $\mathcal{R}_{Z_o}$ (0.05–0.20) indicate strong damping by sea ice internal stress. In contrast, at the southernmost mooring (SODA-A), a broad peak in the histogram from $\mathcal{R}_{Z_o}$ of 0.5–1 suggest that internal stress plays a much smaller role at that mooring. This is consistent with the expected weakening of sea ice as it shifts to a thinner, younger ice pack.

5.5.2 *Surface kinetic energy flux*

The kinetic energy flux from the wind into the surface of the ocean (the "wind work" per unit area) has often been calculated as (*Wunsch*, 1998):

$$\Pi^{ao} = \boldsymbol{\tau}_{ao} \cdot \boldsymbol{u}_o, \tag{5.9}$$

where $\boldsymbol{\tau}_{ao}$ is the surface wind stress and $\boldsymbol{u}_o$ is a characteristic ocean surface velocity. In the open ocean, surface gravity waves act as roughness elements on the boundary layer, so wave phase speed c_p is also used in place of $\boldsymbol{u}_o$ to calculate Π^{ao} (*Gemmrich et al.*, 1994). Moreover, boundary layer turbulent kinetic energy (TKE) production and dissipation associated with the waves reduces the proportion of wind work that can be used to drive surface currents (*Rascle et al.*, 2008; *Zippel et al.*, 2022). Wind work into ML inertial oscillations, Π_I^{ao}, is strongly impacted by boundary layer turbulence (*Plueddemann and Farrar*, 2006; *Alford*, 2020).

In sea ice cover, where the ice itself provides the roughness elements, ice-ocean boundary layer turbulence impacts the efficiency of kinetic energy transfer from the wind into the ocean. It has been further cited as a source of dissipation for internal waves (*Morison et al.*, 1987; *Pinkel*, 2005; *Fer*, 2014). Here, we show that an estimate for inner boundary layer TKE production can be constructed from bulk parameters by comparing the separate sea ice-ocean kinetic energy flux terms (Π^{io}) from the *HKE* evolution equations from sea ice (Π^{io}_{ice}) and ocean surface layer (Π^{io}_{ocn}):

$$\Pi^{io}_{\text{ice}} = \boldsymbol{\tau}_{io} \cdot \boldsymbol{u}_i, \tag{5.10a}$$

$$\Pi^{io}_{\text{ocn}} = \boldsymbol{\tau}_{io} \cdot \boldsymbol{u}_o, \tag{5.10b}$$

where $\boldsymbol{\tau}_{io}$ is the ice-ocean stress and $\boldsymbol{u}_i$ is the sea ice velocity. Assuming that the inner boundary layer represents a constant stress layer consistent with the "law-of-the-wall" as a first-order approximation, the vertically-integrated turbulent shear production is $\int \mathcal{P} dz = \boldsymbol{\tau}_{io} \cdot (\boldsymbol{u}_i - \boldsymbol{u}_o)$, which is exactly equal to the difference $\Pi^{io}_{\text{ice}} - \Pi^{io}_{\text{ocn}}$. Substituting the quadratic drag law for ice-ocean stress (eq. 5.4) gives the estimate $\int \mathcal{P} dz = \rho_o C_{io} |\boldsymbol{u}_i - \boldsymbol{u}_o|^3$.

The partitioning of ice-ocean kinetic energy flux during pack ice cover ($A \geq 0.85$) in the mooring record was evaluated with eqs. (5.10a–b) using the shallowest resolvable velocity measurement for $\boldsymbol{u}_o$ (at ~6 m depth). Both the peak and modal magnitudes of the kinetic energy flux out of the ice, Π^{io}_{ice}, were roughly an order of magnitude greater than the energy flux into the ML, Π^{io}_{ocn}, and the surface turbulent production, $\int \mathcal{P} dz$, largely balanced Π^{io}_{ice} (figs. 5.9a to 5.9c). This balance shows that the majority of *HKE* flux out of the ice goes to TKE production in the inner boundary layer. As this analysis only considers the kinetic energy transfer associated with the sea ice, it may miss details in the marginal ice zone, where there is also direct atmosphere-ocean interaction. *Smith and Thomson* (2019) considered surface boundary layer dissipation in marginal ice, and found different regimes of behaviour depending on the wave conditions. Their work highlights additional variability and dependencies that would not be captured with the bulk descriptions that we use here. Of note, *Smith and Thomson* (2019) found that in the "ice-transferred marginal ice zone", the integrated surface turbulent dissipation was $\int \varepsilon dz = \boldsymbol{\tau}_{io} \cdot (\boldsymbol{u}_i - \boldsymbol{u}_o)$. Assuming that turbulent production and dissipation balance, this is consistent with our definition.

Notwithstanding challenges in determining the energy flux into the inertial oscillations

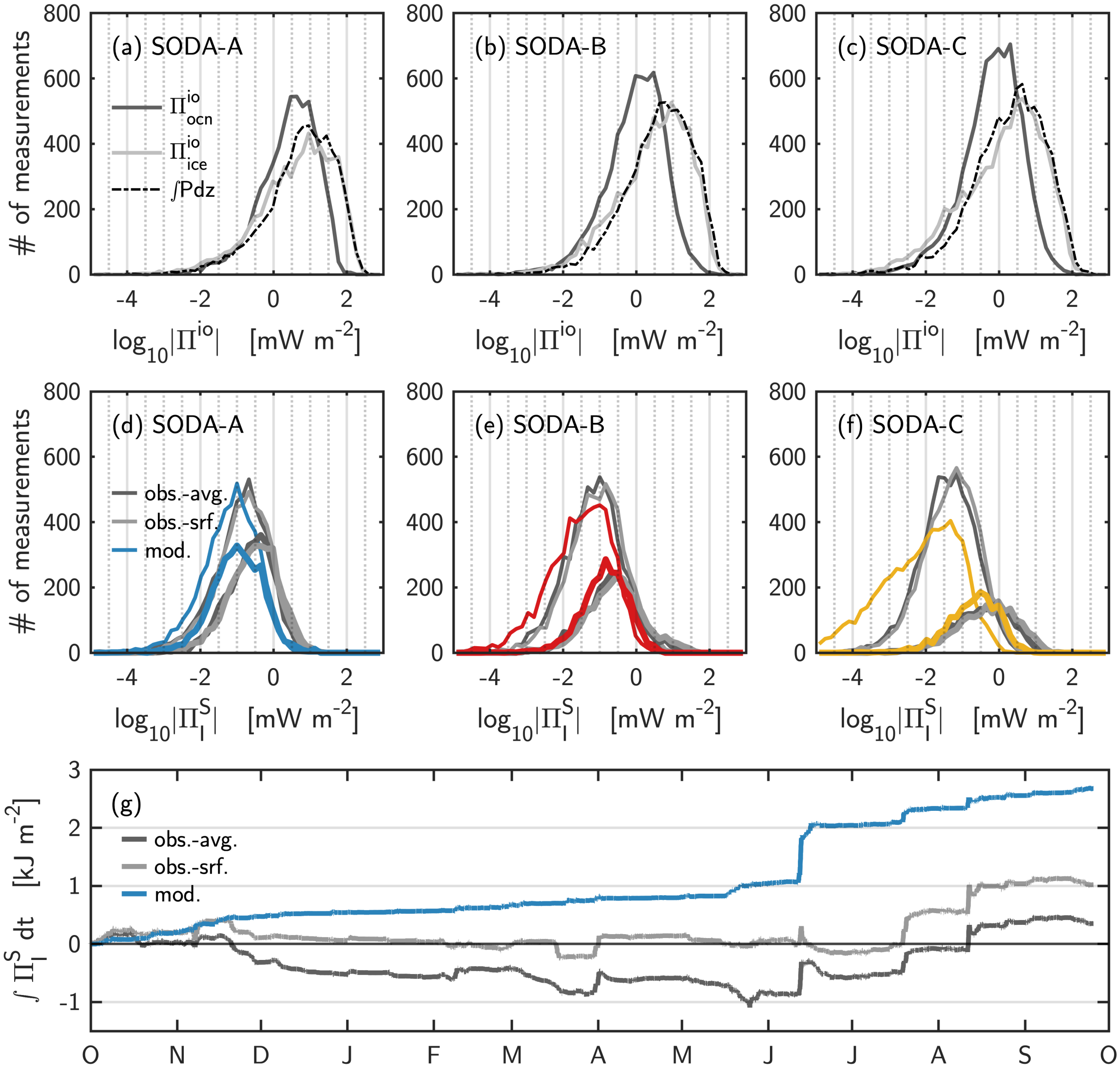

Figure 5.9: Surface kinetic energy fluxes: (a–c) histograms of the ice-ocean kinetic energy flux during pack ice cover ($A \geq 0.85$), *out* of the sea ice (Π^{io}_{ice}; light grey) and *into* the ML (Π^{io}_{ocn}; dark grey), and histograms of TKE production ($\int \mathcal{P}dz$; black dashed lines). Panels corresponds to different moorings (as labelled). (d–f) histograms of the total surface kinetic energy flux into ML inertial oscillations (Π^S_I) for each mooring. Thick lines correspond to marginal ice and open water periods ($A < 0.85$) and thin lines correspond to pack ice covered periods ($A > 0.85$). Different lines colours reflect calculations of eq. (5.11) using different choices of $(Z_o)_I$: dark grey are using ML-averaged $(Z_o)_I$ ("obs.-avg."); light grey are using near-surface $(Z_o)_I$ ("obs.-srf."); and coloured lines use modelled $(Z_o)_I$ ("mod."). (g) Timeseries of cumulative energy transfer $\int \Pi^S_I dt$ for SODA-A; lines colours correspond to the different choices of $(Z_o)_I$ as in (d).

that may arise from turbulent production in the water column, it is still instructive to calculate the flux using traditional methods as a point of comparison to past studies. *Kawaguchi et al.* (2019) previously calculated Π_I^{io} in the sea ice-covered Northwind Abyssal Plain using Z_o determined using a similar slab-model (they calculated surface stress using eq. 5.4, with their observed sea ice velocity used for Z_i). Their results show some seasonality in the kinetic energy flux, with larger values of Π_I^{io} during periods of lower ice concentration, but non-zero values throughout the full ice-covered part of the year; however, their analysis does not account for differences in surface stress associated with mixed sea ice and open water conditions. *Martini et al.* (2014) also use the slab-ocean model (without sea ice representation) to effectively calculate Π_I^{ao}. Differences between observed *HKE* and their modelled Π_I^{ao} were used to infer details about the impact of ice on inertial motions, with the result that ice concentrations above 90% resulted in significant damping of inertial motions.

For each of the moorings, we calculate the per-unit-area kinetic energy input to ML inertial oscillations across both open water and ice-covered periods as (adapted from *D'Asaro*, 1985):

$$\Pi_I^S = \rho_o D \,\mathrm{Re}\left[\frac{(Z_o)_I^*}{(r_o + if)}\frac{d}{dt}\left(\frac{T_S}{D}\right)\right], \tag{5.11}$$

where $(Z_o)_I^*$ is the complex conjugate of $(Z_o)_I$, the near-inertial ocean velocity, and T_S is the total ocean surface stress from eq. (5.2). The slab model framework assumes minimal vertical shear associated with the inertial currents, which is why the ML averaged velocity $(Z_o)_I$ is appropriate for use in eq. (5.11). If eq. (5.11) were re-derived in a system that allowed ML shear, then the calculation of Π_I^S would use the surface inertial velocity instead.

Calculations of Π_I^S (eq. 5.11) where highly sensitive to the choice of $(Z_o)_I$ used: whether modelled, observed ML averaged, or observed near-surface values. For all of the moorings, broad seasonal patterns of Π_I^S are similar when calculated with different choices of $(Z_o)_I$: in all cases, higher values of Π_I^S occurred in marginal ice and open water periods (figs. 5.9d to 5.9f). Compared with the observations, Π_I^S determined with model inputs had slightly lower peak values and were more heavily skewed towards lower values. Peak summer values of Π_I^S were $\mathcal{O}(10\,\mathrm{mW\,m^{-2}})$ – comparable to those found by *Kawaguchi et al.* (2019), though an order of magnitude lower than Π_I^{ao} calculated by *Martini et al.* (2014). Statistics of the magnitudes of Π_I^S were nearly identical when calculated with either the observed depth-averaged inertial velocities or the observed near-surface velocities (taken as the velocity in the shallowest ADCP depth bin at $\sim 6\,\mathrm{m}$), which is indicative of the small vertical shear in the inertial currents. However, slight differences between the velocities (especially phase differences) contributed to different relative balances of positive and negative fluxes. As the rotation of inertial currents results in both positive and negative Π_I^S over an inertial period, it is common to consider the time integrated flux, $\int \Pi_I^S dt$, to evaluate the net tendency for energy input (e.g., *D'Asaro*, 1985). Despite the similarity in values of Π_I^S for different choices of $(Z_0)_I$, $\int \Pi_I^S dt$ diverged significantly (fig. 5.9g).

We highlight that because of uncertainties associated both with boundary layer turbulence and with calculation sensitivity, it is difficult to make conclusive statements about kinetic energy flux into inertial motions.

5.6 *Summary and conclusions*

In this study we investigated wind-driven sea ice and surface ML velocities, with a particular focus on the inertial-frequency response. Using a simplified one-dimensional ice-ocean coupled model to interpret observations across the Beaufort Sea, we identified drivers of the seasonality in sea ice and ocean ML inertial velocities. The results also provides insight in the role of sea ice in mediating momentum and energy transfer across the atmosphere-ice-ocean system. Our main findings are summarized as follows:

1. Observed and modelled seasonality in the ML inertial signal is linked to sea ice concentration, with a marked difference in inertial horizontal kinetic energy, HKE_I

above and below an ice concentration of $A \sim 0.85$. In contrast, the calculated Ekman transport, M_{Ek}, had no significant variation with ice concentration.

2. The broad-banded ML velocities included a mixture of local and non-local signals (including signatures of the large-scale gyre circulation). At the northernmost mooring (SODA-C), low-frequency wind driven motions were primarily due to local Ekman transport, but at the southern moorings (SODA-A and -B), there was an increased level of low-frequency energy that could not be explained by local wind forcing.

3. The model shows that the seasonality in the inertial oscillations is driven by a combination of both internal mechanical strength of the sea ice, and by seasonal variations of the ML depth. The degree to which sea ice strength dampens the oscillations varies between moorings; at the southern mooring internal stress plays a modest role. Nonetheless, the strong seasonal differences is ML depth imply that even in the absence of internal ice stress, seasonal differences in inertial oscillation strength will persist. Sea ice roughness (expressed by the ice-ocean drag coefficient) had no impact on the seasonality of inertial oscillation strength.

4. Under pack ice, bulk metrics suggest that the majority of kinetic energy flux out of the sea ice is dissipated in the ice-ocean boundary layer, but characterizing the net surface flux of energy into ML inertial motions is highly sensitive to calculation details.

Importantly, we show that the paradigm that sea ice reduces the transfer of momentum in to the ocean surface layer is more nuanced than has been previously discussed. Sea ice internal stresses acted as a momentum sink that decreased inertial oscillation strength in pack ice, but the net Ekman transport, M_{Ek}, had no ice concentration dependence. This suggests that in the Beaufort Sea, sea ice may act as a filter, reducing higher frequency motions while transmitting momentum at low (sub-inertial) frequencies. Though, differences in the sub-inertial rotary spectra between moorings does support that sea ice stresses play a role in damping non-local motions.

Finally, because of the strong coupling between sea ice and ocean ML velocities (especially in the inertial frequency band), observed trends of sea ice inertial motion (e.g., *Gimbert et al.*, 2012a,b) should not be taken a reflective of changes in sea ice strength without also accounting for trends in ML depth (e.g., *Peralta-Ferriz and Woodgate*, 2015).

APPENDICES

Appendix 5.A Case studies: individual storm events

Additional insight can be gained by examining the upper ocean response in more detail during individual wind events. We investigate four similarly energetic events spanning across a range of sea ice conditions and ML depths at the southernmost mooring (SODA-A), labeled A1–A4, respectively. Table 5.2 provides a summary of the dates and conditions during the chosen events, and fig. 5.10 shows a variety of measurements during a 7-d window centered on each event. For each event, we also compare the ML-averaged velocity to that predicted by the slab model using the same results as shown in previous sections (i.e., the model applied over the full annual cycle, and not run/tuned individually for each wind event).

5.A.1 Event A1 – Dec. 26, 2018

As wind speeds increased at the onset of event A1, the sea ice initially remained motionless (figs. 5.10a and e), suggesting that internal stress may have opposed the wind (typical adjustment timescales in free drift are less than one hour; *Lepparanta and Omstedt*, 1990). Once the ice started moving, there was a velocity response in the upper ocean (figs. 5.10i and m) with an evident deepening of the wind-forced velocity layer over the course of roughly 2 d, until reaching the previously defined ML depth (seen in figs. 5.10m and q).

Development of this velocity signal highlights differences between different surface layer definitions and dynamics. The mix*ed* layer used in the modelling framework (the black line infigs. 5.10i, m, and q) is the approximately homogeneous surface layer (where there is no barrier to vertical turbulence), while the velocity signal represents the mix*ing* layer, which is the depth of penetration of active turbulence (e.g., *Brainerd and Gregg*, 1995).

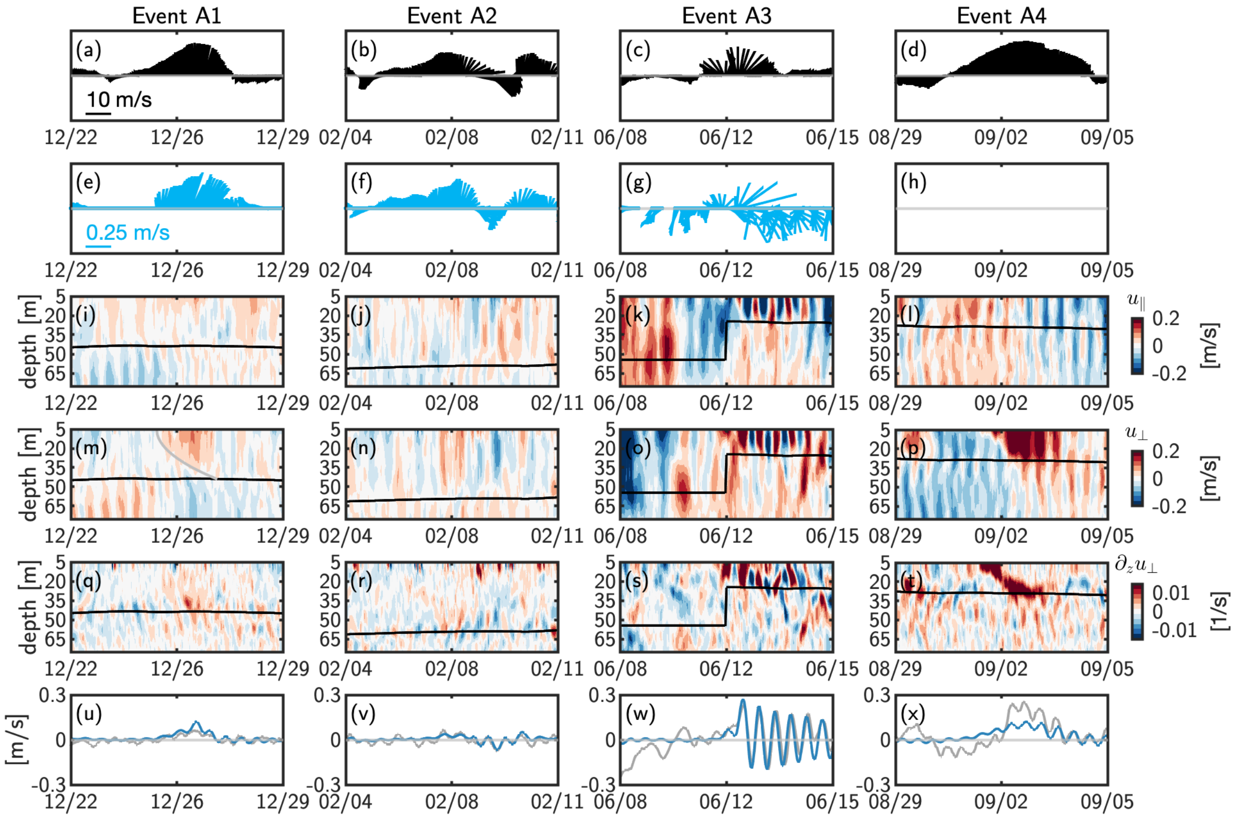

Figure 5.10: Observations during individual event case studies. Each column of panels corresponds to an event (as labelled). Rows of panels show: (a–d) vector plots of wind speed, rotated for clarity so that the peak wind speed is pointed upwards; this rotation defines a local coordinate system used for all other panels for each event; (e–h) vector plots of sea ice velocity in the rotated coordinate system; (i–l) upper ocean velocity in the direction parallel to the peak wind speed direction, $u_{||}$; (m–p) upper ocean velocity in the direction perpendicular to the peak wind speed direction, $u_\perp$ (positive $u_\perp$ corresponds with the direction of Ekman tranpsort, i.e., to the right of the peak wind direction); (q–t) vertical shear of the perpendicular velocity. (u–x) observed (grey lines) and modelled (blue lines) ML-averaged perpendicular velocity. Black lines in (e–t) show the ML depth.

Table 5.2: Summary of dates and conditions for event case studies. Multiple values of H for event A3 reflect the ML depth before and after the onset of shallow "summer" stratification (fig. 5.10).

Event	Date	A	d [m]	H [m]	Peak $\lvert Z_a \rvert$ [$\mathrm{m\,s^{-1}}$]
A1	Dec. 26, 2018	0.99	0.64	44.0	14.2
A2	Feb. 08, 2019	1.00	1.19	59.7	14.0
A3	Jun. 12, 2019	0.60	1.02	54.6, 25.3	12.6
A4	Sep. 02, 2019	0.00	n/a	29.1	15.2

As the ice was initially immobile, and thus provided no pathway for local wind stress to be transferred to the ocean, this event provides a relatively clean signal of the deepening of the mixing layer. This signal can be interpreted by adopting an diffusive framework for ocean stress below the base of some shallow surface layer: $\boldsymbol{\tau} = \nu_E \frac{\partial \boldsymbol{u}}{\partial z}$ for ν_E the eddy viscosity. Then, scaling of the horizontal momentum equation suggests that the depth of the mixing layer should grow as $\sqrt{\nu_E t}$, thus $\nu_E \sim H^2/\mathcal{T}_H$ where $\mathcal{T}_H$ is the timescale for the mix*ing* layer and the mix*ed* layer to converge. To first order, this appears to describe the mixing-layer development in these observations when using an eddy viscosity of $\nu_E \sim 0.01\,\mathrm{m^2\,s^{-1}}$ (see grey line in fig. 5.10m). This value of ν_E is roughly consistent with past measurements in this region (e.g., *Cole et al.*, 2014).

A background of relatively weak inertial oscillations were also present throughout the event, as were near-inertial waves. The waves were visible below the ML as slanted bands visible in vertical shear (fig. 5.10q); with upward energy propagation (downward phase propogation; *Leaman and Sanford*, 1975). The slab model (blue line in fig. 5.10u) captures the depth-averaged low frequency velocity and some of the small inertial oscillating signal following the peak of the event, but doesn't fully replicate the strength of the inertial oscillations through the full period of interest. The model has no explicit representation of the near-inertial waves, and so would not capture the wave energy fluxed into the ML.

5.A.2 *Event A2 – Feb. 08, 2019*

Event A2 occurred under similar conditions to A1, with full ice cover and a deep ML. This event had much more variable wind speed direction including clockwise turning, especially following the peak wind speed on Feb. 08 (fig. 5.10b). The variability of wind velocity translated into variable sea ice motion, which largely followed the wind (fig. 5.10f). It is likely that this variability in surface forcing drove inertial oscillations; while still relatively weak, the inertial oscillations during event A2 were comparable to or greater than those during A1 (c.f., figs. 5.10u and v) despite similar wind speed and a ML that was ∼36% deeper (table 5.2). These oscillations are captured by the model in the latter part of the event, but missed before Feb. 08 (fig. 5.10v). Beneath the ML, the vertical shear reveals near-inertial waves radiating energy downwards (fig. 5.10r).

The distinction between the ML and the base of the mixing layer was less apparent during this event as ice movement allowed surface momentum transfer throughout the lead up to the event (in contrast to A1 where the ice was initially immobile). Throughout the event, ML inertial oscillations were vertically coherent through the full ML depth.

5.A.3 *Event A3 – Jun. 12, 2019*

Event A3 corresponds to the most energetic peak of inertial oscillations throughout the full mooring record. During this event, highly rotational wind acted on a quickly decaying marginal ice pack, energizing both sea ice and ML inertial oscillations. The peak of the wind speed during the event also coincides with the shift from the deeper winter ML to the shallow summer ML. The summer ML forms from the shear-driven downward mixing of surface freshwater input from sea ice melt (e.g., *Peralta-Ferriz and Woodgate*, 2015). Although we don't have measurements of this surface freshwater layer, this effect is evident in the strong peak in shear that deepens from Jun. 12–14 (fig. 5.10s). During this period, the velocity signal was entirely comprised of inertial oscillations (fig. 5.10w) which were responsible for upper ocean mixing in the MIZ.

Despite the rapidly changing ML depth, this strong inertial ML-averaged velocity was captured fairly well by the slab model (fig. 5.10w).

5.A.4 Event A4 – Sep. 02, 2019

Event A4 provides an open-water comparison. This event was characterized by strong, sustained direction winds and a core of upper ocean sub-inertial velocity directed perpendicular to the wind (figs. 5.10d and p). This velocity signal surface constrained intially, and deepend over 1–2 d timescale until the full ML was moving together.

During this event, an autonomous Seaglider was sampling upper ocean temperature and salinity in the vicinity of SODA-A (chapter 3), and provides additional context for the oceanic response. The Seaglider measurements show a shallow, and relatively cool and fresh surface layer coincident with the low-frequency velocity signal (fig. 5.11). The strong shear in fig. 5.10t shows the wind driven deepening of that layer through the storm. At the time of the storm, there was no sea ice near SODA-A, but the T-S properties of this shallow layer (colder and fresher than the bulk of the ML) imply that it may be modified meltwater. This suggests an advective source, similar to that seen by *Crews et al.* (2022). We further note until this shallow layer was mixed downwards, it effectively trapped the wind-driven current and provided a strong decoupling of the surface from the bulk of the ML.

Despite the strong wind and shallow ML, inertial oscillations were only moderate (fig. 5.10x). This may be due to the lack of turning in wind direction, and the dissipative nature of shear-driven ML deepening (*Plueddemann and Farrar*, 2006; *Alford*, 2020).

This event highlights the importance of non-local processes the upper ocean response.

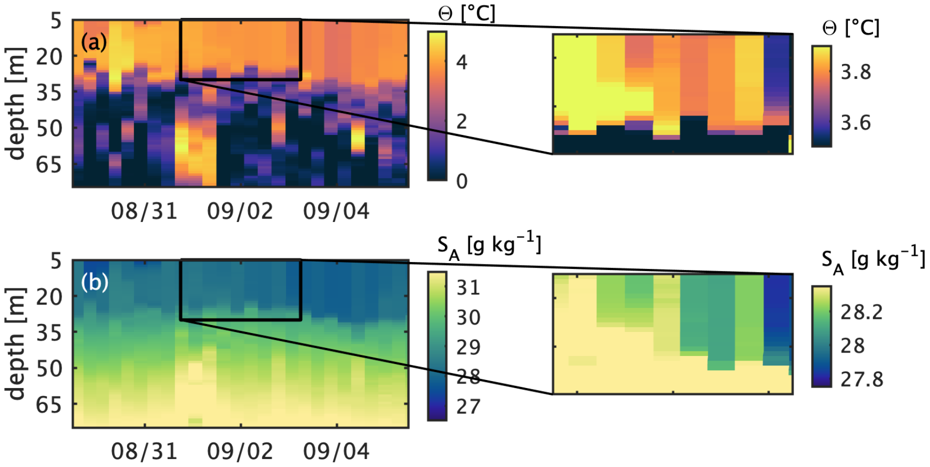

Figure 5.11: Sealglider sections of (a) Conservative Temperature, Θ; and (b) Absolute Salinity, S_A during event A4. Insets zoom in on the time during which there were strong velocity and shear signals (figs. 5.10p and t). Note the saturation of the colourbars in the insets to highlight the shallow fresh layer.

Appendix 5.B Internal ice stress

In this model we've prescribed sea ice mechanical strength as a function of only ice thickness and concentration: $r_i = r_i^* d e^{-C^*(1-A)}$, where $C^* = 20$, and use that in a linear damping parameterization to estimate internal ice stress. This results in a "free-drift" sea ice regime (where internal stress is negligible) below ice concentrations of A ∼0.8–0.85. While this is consistent with empirical concentration-based definitions of the MIZ and free-drift regimes (e.g., *Hunke and Dukowicz*, 2003; *Heorton et al.*, 2019), sea ice stress is complicated with variability across a range of spatiotemporal scales (e.g., *Weiss and Marsan*, 2004). Alternative values of C^*, which could arise due to different ice types, would strongly influence the concentration for free drift conditions (e.g., see *Methods* and *Supplementary material* in *Manucharyan and Thompson*, 2022).

An alternative approach to the presecribed functional form of r_i is to treat r_i as a temporally-varying fitting parameter at each mooring. To do so, we break the model into one-week-long windows and using the least-squares approach described in section 5.3.1 fit values of r_i while keeping r_o fixed (with the same parameter values as used in the main text). For each week-long test window, a 2-day buffer is added both before and after the window to allow for spin-up and for edge effects in the filtering process (so each run is 11 days long, of which only data in the middle 7 days are retained). This process essentially assumes that all unresolved variability in inertial oscillation strength during the ice covered period is attributed to difference in sea ice strength.

Results show the expected seasonality in fitted r_i (expressed in terms of the equivalent damping timescales $\mathcal{T}_i$), with low values of $\mathcal{T}_i$ in winter and an increase in the MIZ, but also show variablity in $\mathcal{T}_i$ that is not present in the prescribe thickness/concentration dependent paramterization (fig. 5.12). A comparison of normalized damping coefficients ($r_i/(r_i^* d)$) shows some ice concentration dependance of the fitted values (fig. 5.13). While there is a clear decrease in r_i as ice concentration decreases and some qualitative agreement with the prescribed concentration dependance ($e^{-C^*(1-A)}$), there is no clear value of critical

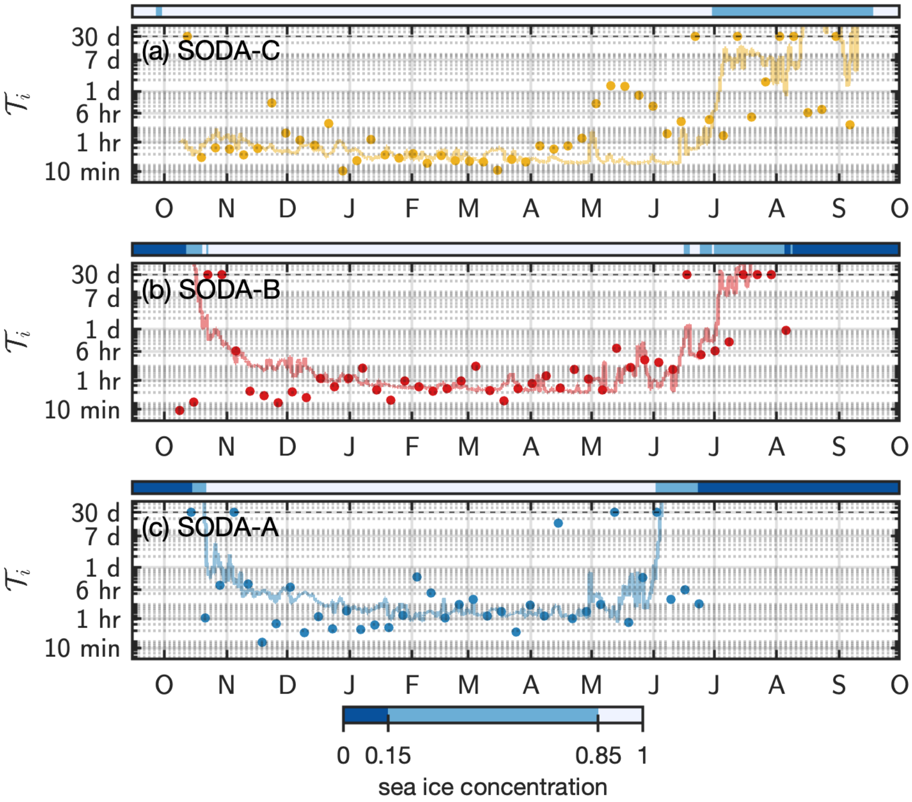

Figure 5.12: Timeseries of ice damping coefficients (expressed in terms of the equivalent damping timescales $\mathcal{T}_i$), from each of the three moorings (a–c, as labelled). Points show weekly-fitted values of $\mathcal{T}_i$ while thin lines show the prescribed values used in the main text of the study. The dashed line at $\mathcal{T}_i = 30\,\mathrm{d}$ reflects the upper-bound $\mathcal{T}_i = 30\,\mathrm{d}$ in the fitting procedure (for those values of $\mathcal{T}_i = 30\,\mathrm{d}$, the ice is essentially undamped). Coloured bars along the top of each panel show the sea ice concentration.

ice concentration that would reflect a transition to free-drift conditions. Further, the wide range of variability even at $A = 1$ shows that there are other factors contributing to the inferred sea ice strength. The fitted values of r_i are weakly correlated with a number of other measured ice geometric parameters (from chapter 4; now shown), but as all of these factors are highly seasonal, such correlations are expected and not individually instructive.

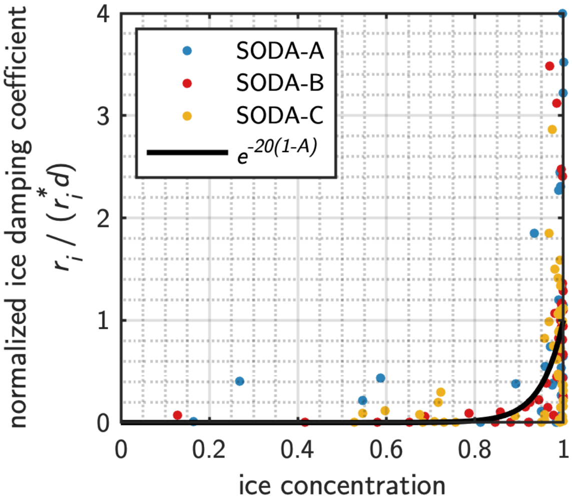

Figure 5.13: Fitted sea ice damping coefficients from all moorings, normalized by $r_i * d$, as a function of ice concentration averaged over each week-long fitting window.

Chapter 6

EVOLUTION OF A SHALLOW FRONT IN THE ARCTIC MARGINAL ICE ZONE

6.1 Introduction

Arctic sea ice is rapidly changing, with summer sea ice extent and thickness declining more quickly than winter (*Perovich et al.*, 2018). These changes are particularly pronounced in the Chukchi and Beaufort seas of the Western Arctic which have increased open-water in the summer while maintaining winter ice cover, and thus have much higher seasonal ice variability than in the past (*Thomson et al.*, 2016a; *Stroeve and Notz*, 2018; *Peng et al.*, 2018). Accompanying these changes is an increase in width of the summer marginal ice zone (MIZ; *Strong and Rigor*, 2013): the band of low concentration, highly dynamic ice that separates the open ocean from the ice pack. This increase has led to a renewed interest in understanding the dynamic processes at play in the Beaufort Sea MIZ, with an emphasis on ice-ocean-atmosphere coupling and feedbacks (*Lee et al.*, 2012).

Strong lateral buoyancy gradients in the upper ocean of the MIZ have been identified as having a potentially important role in the heat transport in the ice-ocean-atmosphere system as a result of ice edge upwelling (e.g., *Niebauer*, 1982; *Røed and O'Brien*, 1983; *Häkkinen*, 1986) or eddy generation (e.g., *Lu et al.*, 2015). Historically, many of the observational studies of MIZ fronts have taken place in the shallow regions of the Bering Sea (*Niebauer*, 1982) or the energetic Fram Strait (*Johannessen et al.*, 1983, 1987; *Smith IV and Bird*, 1991) where topographic effects may have a significant influence on ocean currents. As the marginal ice zone shifts north into the deeper basins of the Arctic Ocean, these fronts may begin to resemble open-ocean frontal systems. The lateral gradients in upper ocean density observed across the MIZ can have horizontal length scales on the order of

1–10 km (e.g. *Buckley et al.*, 1979). At these scales, submesoscale processes with Rossby and Richardson numbers of order one may dominate the momentum balance (*Thomas et al.*, 2008).

The role of submesoscale dynamics in the MIZ is a subject of recent and active research. Numerical simulations of idealized MIZ have shown spontaneous generation of mixed-layer eddy fields due to submesoscale baroclinic instabilities (SBI) energized by either an existing frontal structure (*Manucharyan and Thompson*, 2017), or by freshwater input from ice melt (*Horvat et al.*, 2016). Observations and simulations of a submesoscale meltwater front in the Chukchi Sea suggest similar SBI (*Lu et al.*, 2015). These simulations are corroborated by satellite observations showing that MIZ eddy fields are common at scales consistent with SBI (e.g., *Bondevik*, 2011; *Kozlov et al.*, 2019), and a drifter study has provided in-situ evidence for MIZ submesoscale lateral dispersion (which would be associated with mixed layer eddies (MLE); *Mensa et al.*, 2018). In contrast, high-resolution observations of a submesoscale filament in the Fram Strait instead suggest an alternative instability mechanism as the dominant submesoscale process. *Timmermans et al.* (2012) suggests that the presence of ice-ocean friction may act to modify typical submesoscale processes. Few direct oceanographic measurements of the evolution of MIZ submesoscale fronts have yet been collected, so how the dynamics and forcing are impacted by presence of ice is unclear. Furthermore, while slumping and re-stratification of Arctic submesoscale fronts have been suggested (*Timmermans et al.*, 2012; *Timmermans and Winsor*, 2013; *Wulff et al.*, 2016), these studies have relied on a limited number of cross-front sections which are unable to resolve any temporal variation.

This paper presents detailed observations of a localized ice-edge front, and addresses its observed evolution in the context of existing submesoscale theory. Following a description of the observations and methods, the evolution of the front is discussed in terms of the dynamical processes that could explain the observed frontogenesis and frontolysis. While these observations with high resolution in both time and space combined with existing submesoscale theory and scaling arguments provide intriguing insight into dynamics of ice-edge fronts, conclusions highlight the need for additional studies.

6.2 *Observations and methods*

6.2.1 *Study location and description*

A ship-based survey took place aboard *Norseman II* along the edge of the MIZ in the Canada Basin of the Beaufort Sea (fig. 6.1a). Data were collected over a ∼3-day period from 01–04 Oct 2014, so the timing of the survey corresponded to the start of the fall ice-growth season, when the ocean was rapidly cooling and sea ice was beginning to form (the 2014 minimum sea ice extent occurred on 17 Sept 2014; NSIDC *Fetterer et al.* 2017). In the vicinity of the study site the basin is approximately 3800 m deep and the nearest shelf break is roughly 200 km away, so topographic influence on the local submesoscale dynamics is unlikely. Shipboard measurements were complemented by a number of short deployments (3 to 6 hours each) of two SWIFT drifting buoys (*Thomson*, 2012). *Zippel and Thomson* (2016) previously presented data collected during part of this survey in a study about MIZ surface wave dynamics. The experiment was part of the larger Office of Naval Research Marginal Ice Zone program (*Lee et al.*, 2012, 2017).

Oceanographic measurements were collected shipboard using a Teledyne Oceanscience underway profiling system with an underway conductivity-temperature-depth (uCTD) sensor operated on a winch from the stern of the ship (e.g., *Rudnick and Klinke*, 2007). The uCTD was operated in "yo-yo" mode while the ship was underway (without recovery between casts), thus multiple profiles were executed between instrument recoveries (when probes were swapped and data downloaded). This approach allows for increased temporal and spatial resolution compared to traditional CTD operations; with the ship travelling at 4 kn ($\sim 2\,\mathrm{m\,s^{-1}}$), profiles collected with a $\sim$ 4-min period extend to depths of 120–150 m and have $\sim$ 380 m along-track spacing. The temperature and conductivity sensors both react to variability in the signal on different time frames, so the delay between

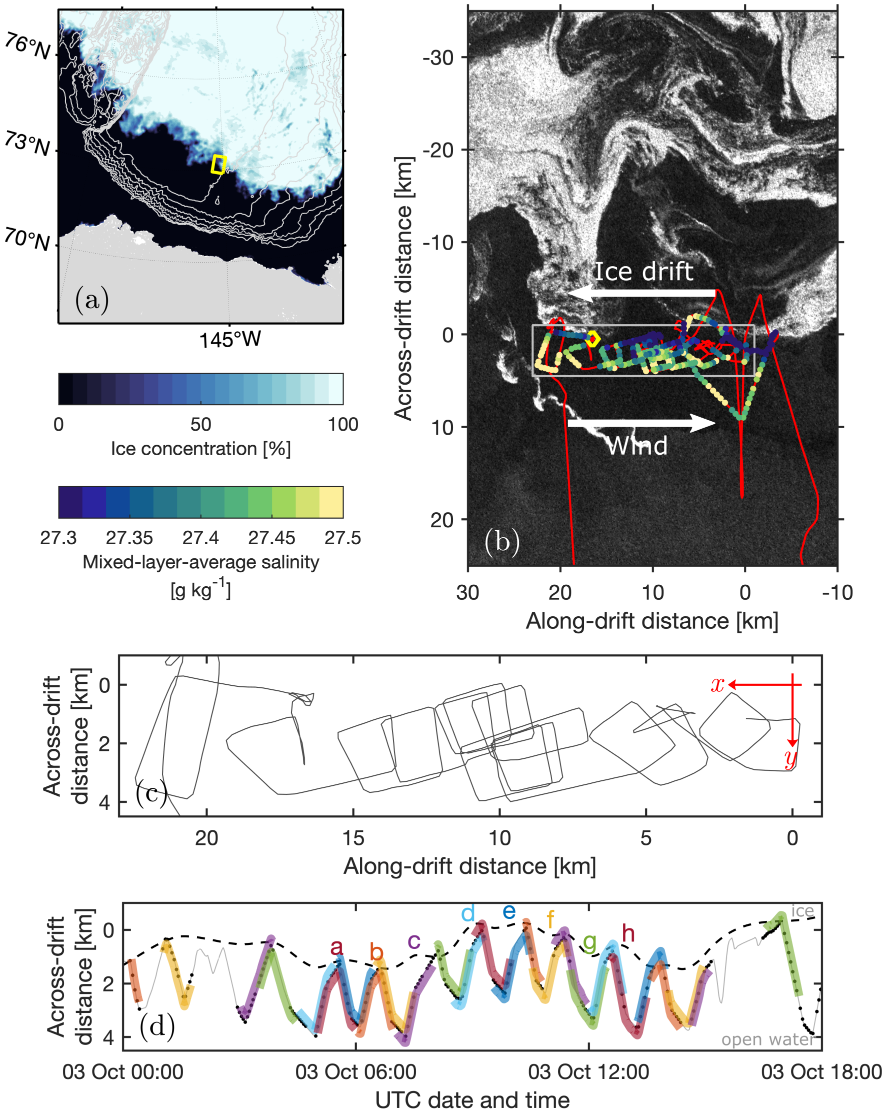

Figure 6.1: (a) The western Arctic Ocean with ice concentration from 03 Oct, 2014. Bathymetry is shown by grey contour lines (contours are 500-m isobaths). The yellow rectangle marks the location of the MIZ survey. (b) The study area rotated to the local coordinate system, showing the ship track (red line) and mixed-layer-averaged salinity (colour points) overlaid on a SAR RADARSAT-2 image of the MIZ. The average ice drift and wind directions are shown schematically (arrows). The yellow diamond shows the ship location at the time of the SAR image. The grey box corresponds to the domain of (c). (c) A zoomed-in view of the ship track in the local coordinate system, showing the definition of the $x - y$ axis. (d) The ship track shown in across-drift distance versus time. Black dots show the locations of uCTD casts. Coloured lines denote the range of measurement area used in creating across-drift sections. Coloured letters, a-h, show which tracks correspond to the panels in fig. 6.5. The dashed black line shows the approximate excursion of the drifting ice feature (inferred from ship motion). RADARSAT-2 Data and Products are from MDA Geospatial Services Inc., provided via the National Ice Center.

these becomes a function of fall speed. We corrected for non-uniform fall speed using a technique similar to *Ullman and Hebert* (2014) and binned the results onto a regular 1-m depth grid. The profile locations were obtained from the navigation files, interpolated to the start time of each cast. Additional post-process quality control was done manually to remove profiles that showed contamination from icing or salinity spiking. The top 4 m of each profile were discarded due to potential ship contamination (the ship has a 4-m draft); however, the strong bulk lateral gradients observed here exist at scales that would be influenced minimally by ship contamination.

Profiles taken with the uCTD showed a strong two-layer structure in the upper ocean (fig. 6.2). In the open water, a relatively warm and fresh surface layer ($T \sim 1.5\,^{\circ}\mathrm{C}$, $S_A \sim 27.5\,\mathrm{g\,kg^{-1}}$) extended to a depth of 20–25 m, where a sharp pycnocline separated it from colder saltier water below ($T \sim -1.5\,^{\circ}\mathrm{C}$, $S_A \sim 30\,\mathrm{g\,kg^{-1}}$). Transects showed a distinct front of cold and even more fresh water ($T \sim -1.5\,^{\circ}\mathrm{C}$, $S_A \sim 26.5\,\mathrm{g\,kg^{-1}}$) located at the ice edge (fig. 6.2). Within the front, water temperature approached the in-situ temperature of freezing based on measured salinity, suggesting that the front may be residual meltwater from the sea ice melt season. In the temperature-salinity range observed here, density is driven by changes in salinity (the haline contraction coefficient $\beta \sim 7.8 \times 10^{-4}\,\mathrm{kg\,g^{-1}}$, while the thermal expansion coefficient $\alpha \sim 3 \times 10^{-5}\,\mathrm{K^{-1}}$), so the density structure mimics salinity. Adopting a definition of the mixed layer as the density threshold of $0.25\,\mathrm{kg\,m^{-3}}$ compared to the shallowest observation (e.g., *Cole et al.*, 2017), the mixed-layer depth was consistent with the surface layer depth (which we define by the $22.15\sigma_{\Theta}$ isopycnal) in open water, while near the ice the mixed layer is shallower due to the presence of the front. While we consider the separate definitions for the surface layer and the mixed layer here, in studies of submesoscale dynamics, descriptions of the "mixed layer" may be based on the locations of the pycnocline and thus would be more consistent with what we refer to as the surface layer (e.g., *Fox-Kemper et al.*, 2008).

The MIZ in the survey area consisted of loose brash ice floes (up to approximately 1 m in diameter) interspersed with small first year floes (up to approximately 5 m in

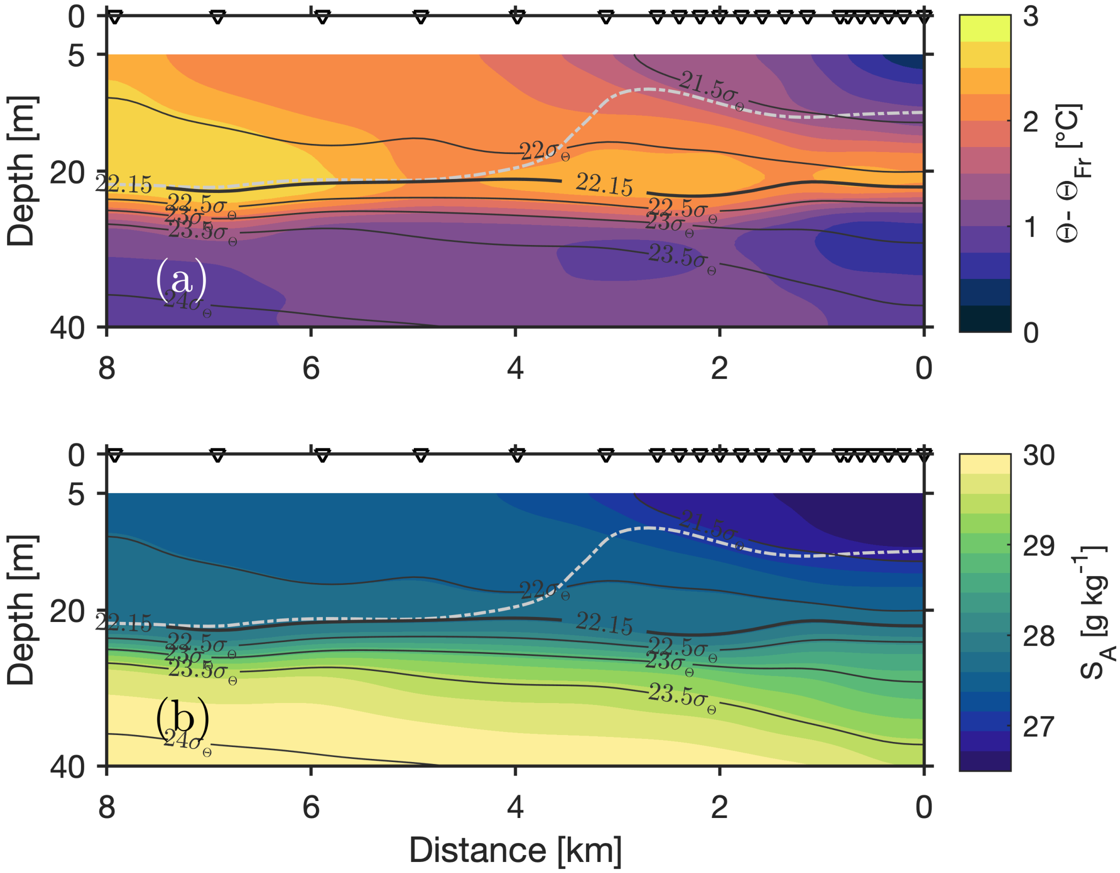

Figure 6.2: Across-drift section of (a) conservative temperature (Θ) relative to in-situ freezing (Θ_{Fr}), and (b) absolute salinity (S_A) taken on 01 Oct, 2014. Contours show potential density anomaly (σ_Θ), with the thicker 21.15σ_Θ contour representing the defined base of the surface layer. The light grey dashed-dotted line shows the base of the mixed-layer. Triangles at the surface show the locations of the uCTD casts. Distance in the across-drift direction is relative to the start of the section (with 0 being nearest to the ice, and moving towards open water as distance increases).

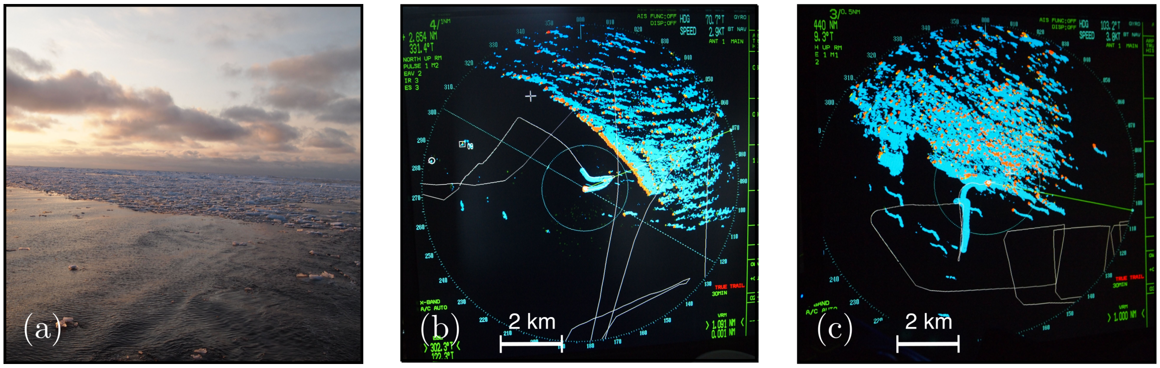

Figure 6.3: Photographs taken during the survey of (a) the ice edge of the MIZ and (b,c) the ship's radar from near the beginning and near the end of the survey (at approximately 02 Oct 19:00Z and 03 Oct 15:40Z, respectively). Approximate scale bars are provided in (b,c) for reference; however, these are uncalibrated and do not account for distortion introduced by the photograph.

diameter; fig. 6.3a). Upon arriving in the survey area, a coherent ice edge feature was visually identified on the ship's navigation radar (figs. 6.3b and c) and the ship followed that feature as the MIZ deformed and drifted; the ship maintained this feature on the radar during the sampling period. For a roughly 12-hour period on 03 Oct, *Norseman II* performed short looping patterns while maintaining a relatively constant speed of $4\,\mathrm{kn}$ ($\sim 2\,\mathrm{m\,s^{-1}}$) and following the moving ice (figs. 6.1b to 6.1d). *Norseman II* is not an ice-capable vessel so for most of the survey the ship only approached the MIZ edge without travelling into the ice; the oceanographic features described here likely extend farther into the MIZ.

The observed MIZ drift pattern was used to identify a local coordinate system with along- and across-drift directions. An origin point was chosen close to the start of the drift. Based on uCTD measurements, this coordinate system is also aligned with the bulk horizontal gradients of temperature and salinity (fig. 6.1b). The along-drift coordinate axis is approximately parallel with the larger-scale ice edge. Figure 6.1b shows the path of ship while it was in the survey area, rotated to the local reference frame, and overlaid on a synthetic aperture radar (SAR) image taken by RADARSAT-2 (from MDA Geospatial

Services Inc., provided via the U.S. National Ice Center), which shows the ice cover. The angle of the coordinate system was chosen based on approximately matching the direction of the ship track and the bulk gradients of salinity and temperature in the mixed-layer; the results are not sensitive to this angle. The coordinate system is used to define a right-handed x-y axis (fig. 6.1c), with x aligned in the along-drift (and therefore along-front) direction, and y aligned across-drift/front (so a positive horizontal velocity u is "down-front", in the direction of a geostrophic frontal jet).

While the movement of regional large-scale ice pack over the survey period was small ($\sim 0.05\,\mathrm{m\,s^{-1}}$) and generally eastward (NSIDC: Polar Pathfinder; *Tschudi et al.* 2019), ice in the MIZ was observed to drift to the west and slightly north (indicated by the arrow on fig. 6.1b). The ice feature being tracked was moving at approximately $0.3\,\mathrm{m\,s^{-1}}$ (inferred from the mean along-drift translation of the ship during the looping track). During two deployments bookending this period, both the SWIFT buoys drifted with a speeds ranging from 0.25–$0.4\,\mathrm{m\,s^{-1}}$ towards a mean compass direction of 315°. This drift opposed the local wind direction which originated from 270–300° (Figures 6.1b and 6.4b). The observed ice and surface drift direction is consistent with the expected direction of a geostrophic frontal jet formed across the meltwater front. Assuming a level-of-no-motion at the base of the surface layer ($z = -h_{sl}$, defined as the $21.15\sigma_\Theta$ isopycnal, where the strong halocline may decouple surface motions from below), the thermal wind balance ($u(0) = f^{-1}\int_{-h_{sl}}^{0} -b_y dz$, for buoyancy $b = -g\sigma/\rho_0$, and f the Coriolis parameter) predicts a velocity of $0.25\,\mathrm{m\,s^{-1}}$ within the front for the profile shown in fig. 6.2. This velocity is roughly consistent with the measured drift velocities from the SWIFTs and inferred velocity from the ship track.

Profiles taken with the uCTD during the looping path were separated into a series of across-drift sections showing temporal evolution of the front in a reference frame following the identified MIZ ice feature (figs. 6.1c and d). Each section was composed of all casts taken within a 1-hour window, interpolated onto a regular grid in y and z (the across-drift distance and depth), and smoothed with a 2-dimensional Gaussian kernel.

The windows overlapped by 30 minutes, so some individual casts may be shared across two different sections; in this way, the sections form a type of moving average and do not map directly to individual "loops" from the path (fig. 6.1d). Sections containing fewer than 5 casts or spanning a range of less than 1.8 km in the across-drift direction were discarded. We assume that the reference frame following the ice feature provides a good approximation for a Lagrangian frame of the front as a necessary step in describing temporal evolution. Differential ice-ocean velocities and upper-ocean shear may impact this assumption; these effects are discussed later.

An acoustic doppler current profiler (ADCP) was mounted in a well on the ship to measure the ocean currents. The ADCP reported measurements in 1-m bins with a sampling period of 30 seconds. The first bin was a depth of 7.3 m below the water surface, so details of velocity within the front were not fully resolved. A VmDas data acquisition system was used to remove ship motion; however, examination of the resulting velocity profiles suggests that some ship contamination was still present in the velocity signal, obscuring small cross-front horizontal velocity gradients. Despite these limitations, we recovered some additional contextual information from the ADCP system during the looping survey (when the ship was moving relatively slowly) through additional processing. We created smoothed, across-drift velocity sections using a method identical to that used for for creating uCTD sections. Because these sections often average over times when the ship was travelling in different directions (fig. 6.1c), the ship contamination was largely removed by this process.

We characterized temporal evolution of the front by considering a number of section-averaged quantities averaged within the surface layer, which we define by the $22.15\sigma_\Theta$ isopycnal. We denote these averages by $\langle\cdot\rangle_{sl}$, which represent 2-dimensional averages in y-z. This isopycnal choice for the surface layer depth is slightly shallower than the pycnocline separating the surface layer from the water below, which ensures that the sharp gradients within the pycnocline are not skewing averaged quantities. The overall results are not overly sensitive to the choice of isopycnal to describe surface layer depth provided that pycnocline is sufficiently excluded from averages. Additionally, we calculated the bulk frontal slope for each section in two ways. (1) A linear fit was made of some characteristic isopyncals within the front; we contrast results from choosing either the $21.65\sigma_\Theta$ and $21.85\sigma_\Theta$ isopyncals. (2) A ratio of the values of the lateral buoyancy gradient ($M^2 = -b_y$) to the vertical buoyancy gradient ($N^2 = b_z$) averaged within the mixed layer for each section also provides an approximation of isopyncal slope: $\langle M^2 \rangle_{sl} [\langle N^2 \rangle_{sl}]^{-1} \sim \Delta z [\Delta y]^{-1}$.

6.2.2 *Atmospheric measurements*

Atmospheric variables were measured locally by meteorological packages aboard *Norseman II* and on one of the two SWIFTs. On *Norseman II*, these variables included air temperature, relative humidity, barometric pressure, and wind speed and direction. *Norseman II* additionally carried a sonic anemometer mounted on the mast at a height of 10.3 m above the mean water level. The sonic anemometer recorded 3-component relative wind speeds and virtual temperature at 10 Hz sampling rate. These data were processed in 10-minute intervals using the inertial dissipation method described by *Yelland et al.* (1994) and developed by *Large and Pond* (1981) in order to calculate the wind stress. Within each 10-minute interval data were de-spiked using the phase-space method of *Goring and Nikora* (2002), and wind velocity spectra were constructed with 512 point 75% overlapping windows. A $-5/3$ frequency-power slope was fit within the inertial subrange (identified as 0.6–2 Hz) of each spectra. When wind was from the ship's stern, erroneous measurements were recorded due to contamination from the ship's exhaust, so these data were discarded. This matches the procedure used by *Zippel and Thomson* (2016) for the same measurement data.

We compared measured quantities with atmospheric re-analysis. In an evaluation of different re-analysis products, *Lindsay et al.* (2014) show that Modern-Era Retrospective analysis for Research and Applications (MERRA) produces the most consistent results with independent observations. Based on those results, we chose to use the updated "version 2" of the MERRA product (MERRA-2; *Global Modeling and Assimilation Office (GMAO)*, 2015; *Gelaro et al.*, 2017), which provides hourly data at 0.5° × 0.625° degree resolution. We compared the on-site measurements with the average of two grid points that fall within the survey area (located at [73°N, 145.62°W] and [73°N, 146.25°W]). Additional comparison was done with two other re-analysis products: the National Center for Climate Prediction and Department of Energy re-analysis version 2 (NCEP-2; *Kanamitsu et al.*, 2002), and the European Centre for Medium-Range Weather Forecasts (ECMWF) interim re-analysis (ERA-Interim; *Dee et al.*, 2011). There was good agreement between the three different re-analysis products during the region and time-frame of record (not shown).

Wind speeds measured aboard *Norseman II* were generally low, and varied from $0\,\mathrm{m\,s^{-1}}$ to a maximum of $10.0\,\mathrm{m\,s^{-1}}$ with a mean of $4.3\,\mathrm{m\,s^{-1}}$ (fig. 6.4a) from a compass direction ranging between ∼260–300° (westerly to northwesterly; fig. 6.4b). MERRA-2 re-analysis agrees in a bulk sense, showing similar westerly to northwesterly winds with means wind speeds of $3.5\,\mathrm{m\,s^{-1}}$, but displays much less variability than locally measured wind. Through most of the survey, the wind direction was approximately aligned with the front, in the "up-front" direction (compare the wind direction in fig. 6.4 with the approximate frontal orientation indicated by the dashed lines). Shipboard wind measurements show a number of events lasting ∼ 4–6 hours in which the local wind speeds significantly exceeded those reported by re-analysis products, with discrepancies of up to 100% (fig. 6.4a; peaks at 01 Oct 12:00Z, 02 Oct 13:00Z, 03 Oct 10:00Z, and 03 Oct 20:45Z). The timing of these high-wind events does not correspond to day-night transitions or changes in ship operation (heading or speed, etc.). One of these events occurred while the ship was performing the looping patterns described above and collecting high resolution oceanographic data (denoted by the shaded grey area in fig. 6.4).

The COARE bulk algorithms (v3.5; *Fairall et al.*, 2003; *Edson et al.*, 2013) were used to estimate both surface heat fluxes and wind stress using the shipboard measured atmospheric variables. Downward radiative fluxes (long- and short-wave) were not measured,

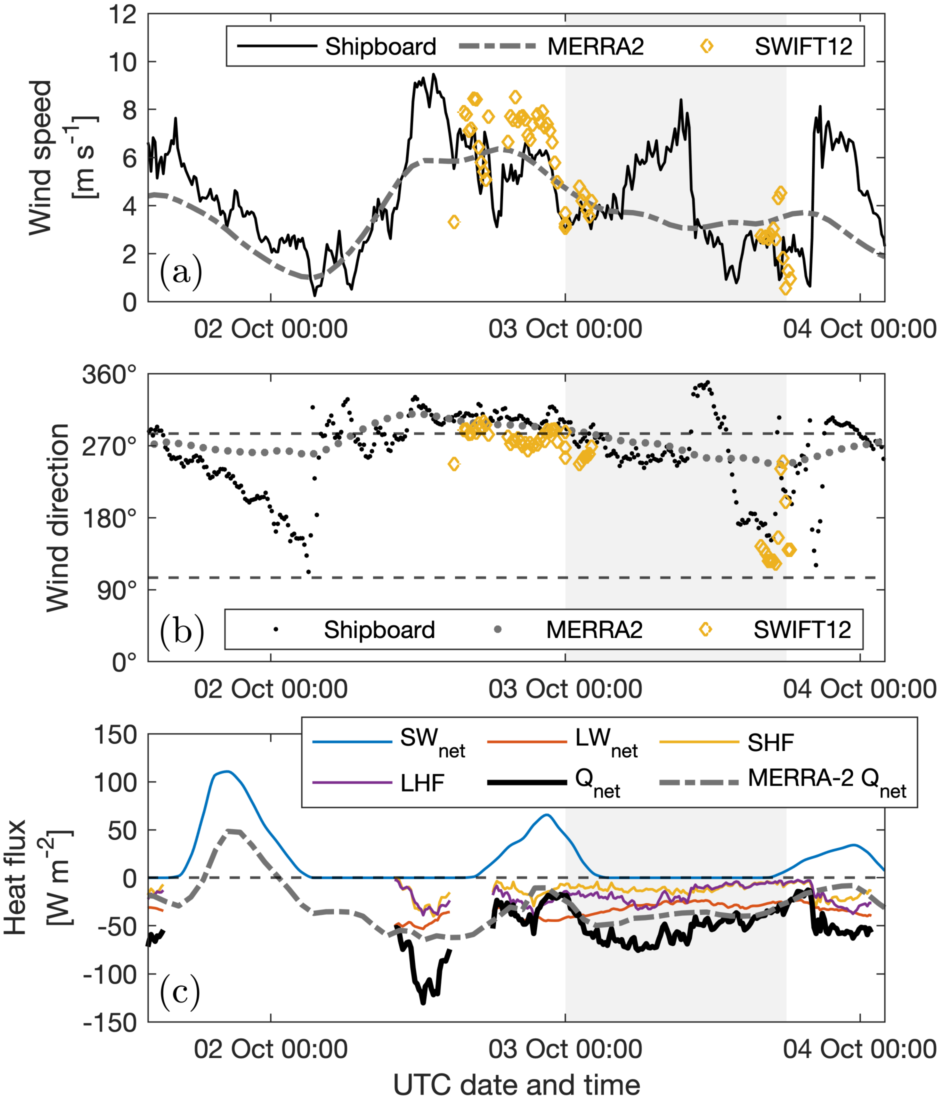

Figure 6.4: Time series of measured and re-analysis (a) wind speed, and (b) direction, and (c) surface heat flux: net short-wave (SW), net long-wave (LW), latent heat flux (LHF), sensible heat flux (SHF), and total net surface heat flux (Q_{net}) determined from the COARE algorithms and MERRA-2 re-analysis; for all components, negative heat flux represents heat out of the ocean. Horizontal dashed lines at 105° and 285° in (b) show the approximate orientation of the front. The shaded grey band shows the time that the ship was performing high resolution oceanographic measurements described in the text.

so the COARE algorithms were run using MERRA-2 re-analysis values as inputs for those variables. Despite the differences between re-analysis data and observations present in the wind (fig. 6.4a), the choice to use re-analysis values for calculating the heat flux is justified by the lower variability and smaller error associated with downwelling radiative fluxes over a variety of re-analysis products compared to other atmospheric variables (*Chaudhuri et al.*, 2014). Sea surface temperature input for the heat flux calculations was taken as the uppermost retained bin of the uCTD casts (at 5-m depth) interpolated onto the time series of atmospheric measurements, so heat fluxes are only available during times when uCTD casts were being taken. This approach provides a "bulk" sea surface temperature. Precipitation was not measured so it was not included in the heat flux estimate. Version 3.5 of the COARE algorithms also includes parametrization to account for sea state using the significant wave height, H_s, and phase speed, c_p, of the waves. We computed heat fluxes using the averages of surface wave properties measured by the two SWIFTs ($H_s = 0.38\,\mathrm{m}$, and $c_p = 5.8\,\mathrm{m\,s^{-1}}$ based on deep-water waves with a measured average peak period of $T_p = 3.7\,\mathrm{s}$). Given the influence of the MIZ on sea state (e.g., *Zippel and Thomson*, 2016), whether if these are indicative values for the use in the parametrization is unclear; however, in this case the results of application of the COARE routines to the shipboard meteorological data showed limited sensitivity to the inclusion of wave information (heat flux calculated with and without the inclusion of the sea state differed by $< 1\,\mathrm{W^2\,m^{-1}}$). The COARE-derived wind stress estimates matched very closely with those measured using the inertial dissipation method.

As expected, there was net ocean cooling throughout the record consistent with the period of ice advance (fig. 6.4c). Weak incoming short-wave radiation (peaks of $\sim 50\,\mathrm{W\,m^{-2}}$) on both 03 and 04 Oct was insufficient to reverse the heat flux direction during daylight hours, although MERRA-2 shows a brief period of heating ($\sim 6\,\mathrm{h}$) during daylight on 01 Oct. The net heat flux given by MERRA-2 re-analysis significantly underestimated that calculated by the COARE algorithms during times that the wind speed differed between observations and re-analysis. Differences between the two measures are largely a result of differences in the sensible and latent heat flux components which are both sensitive to wind speed.

6.3 Results

Strong gradients across the MIZ suggest that sea-ice-atmosphere interactions drive the processes in these regions. Here, the frontal adjustment appears to be linked to the atmospheric forcing, but dynamics differ from traditional descriptions associated with submesoscale frontal evolution. A number of details of this behaviour are still unresolved.

6.3.1 Observed frontal evolution

Across-drift sections show that the front rapidly evolved over an approximately 12- to 18-hour period on 03 Oct (figs. 6.5a to 6.5h). The front steepened over a time period of a few hours with the slope reaching a maximum at approximately 10:00Z on 03 Oct, then subsequently collapsed over a period of roughly 4 h. The qualitative pattern of steepening and collapse is robust across a broad range of isopycnals, as demonstrated by the $21.65\sigma_\Theta$ and $21.85\sigma_\Theta$ isopycnal slopes (fig. 6.5i); however, the magnitude of the change in slope depends on the specific choice of isopycnal. The bulk estimate of slope (based on the ratio of lateral and vertical buoyancy gradients) generally agrees with the slope of 21.65σ isopycnal. The initial steepening and subsequent collapse of isopyncal slope is reflected in the horizontal buoyancy gradient, $\left\langle M^2 \right\rangle_{sl}$ (fig. 6.6a), so the evolution can be divided into a frontogenic phase followed by a frontolytic phase. The depth of the mixed layer, as defined by a density difference threshold compared to the shallowest density measurement, does not show similar evolution (figs. 6.5a to 6.5h, grey dashed-dotted line).

While the vertical buoyancy gradient, $\left\langle N^2 \right\rangle_{sl}$, evolved over a similar time-frame, its behaviour was more oscillatory with a maximum that appears later and a less pronounced peak compared with $\left\langle M^2 \right\rangle_{sl}$ (fig. 6.6b). The overall change in isopycnal slope (fig. 6.5i)

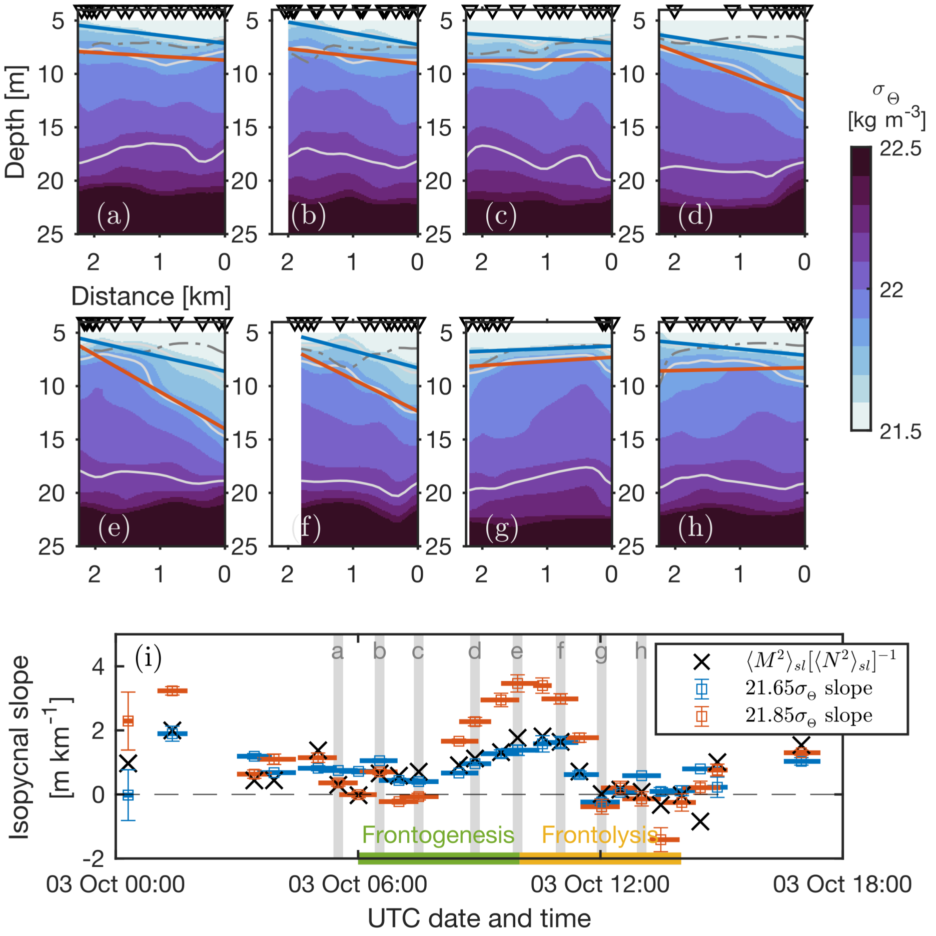

Figure 6.5: (a-h) Example density sections. Grey contours show the $21.65\sigma_\Theta$, $21.85\sigma_\Theta$, and $22.85\sigma_\Theta$ isopycnals, and linear fits to the first two isopycnals are shown by the blue and orange lines, respectively. The darker grey dashed-dotted line shows the depth of the mixed layer based on a $0.25\sigma_\Theta$ threshold. Triangles at the top of each section show the locations of the uCTD casts. Distance is the across-drift distance relative to the start of each section (with 0 being nearest to the ice, and moving towards open water as distance increases). (i) Time series of the bulk isopycnal slope ($\langle M^2\rangle_{sl}\,[\langle N^2\rangle_{sl}]^{-1}$) and slopes of the linear fits of 21.65σ and 21.85σ isopycnals for all sections. Vertical error bars on the 21.65σ and 21.65σ slope measures show the 95% uncertainty (using a two-tailed t-test) associated for each fit (*Bendat and Piersol*, 1971). Horizontal bars show the range of time over which uCTD casts corresponding with each section were taken. Vertical grey bands indicate which sections are shown in (a-h), as labelled. Green and yellow bands along the bottom of the figure demarcate the frontogenic and frontolyic phases of evolution discussed in the text.

was driven primarily by changes in $\left\langle M^2 \right\rangle_{sl}$ which has a high variability, while $\left\langle N^2 \right\rangle_{sl}$ only deviates slightly from its time-mean ($\left\langle M^2 \right\rangle_{sl}$ ranges from $\sim -0.3 \times 10^{-6}$–$1 \times 10^{-6}\,\mathrm{s}^{-2}$; $\left\langle N^2 \right\rangle_{sl}$ ranges from $\sim 4 \times 10^{-4}$–$5.6 \times 10^{-4}\,\mathrm{s}^{-2}$; figs. 6.6a and b).

During the evolution, the along- and across-front velocities in the surface layer ($\langle u \rangle_{sl}$, $\langle v \rangle_{sl}$ respectively) also both showed an oscillatory character with a timescale close to the inertial period (figs. 6.6d and e), and seem to have varied in quadrature. In contrast, the section-averaged vertical shears in the surface layer ($\langle u_z \rangle_{sl}$, $\langle v_z \rangle_{sl}$) do not have apparent oscillatory motion, and instead vary together. Through the record, the along-front shear $\langle u_z \rangle_{sl}$ appears to be in approximate balance with $\left\langle M^2 \right\rangle_{sl} (f^{-1})$, consistent with an along-front thermal wind balance (fig. 6.6f).

Differential advection by sheared inertial oscillations can lead to oscillations of the stratification $\left\langle N^2 \right\rangle_{sl}$ (*Thomas et al.*, 2016). While the observed stratification does appear to exhibit such a response (sinusoidal curve fit in fig. 6.6b), these oscillations would theoretically arise from a stratification budget $(\left\langle N^2 \right\rangle_{sl})_t \sim \langle v_z \rangle_{sl} \left\langle M^2 \right\rangle_{sl}$ with constant $\left\langle M^2 \right\rangle_{sl}$ and oscillatory $\langle v_z \rangle_{sl}$ (e.g., see figure 5 in *Thomas et al.*, 2016). We tested if sheared inertial oscillations are setting the stratification by integrating the budget forward with the observed $\langle v_z \rangle_{sl}$ and $\left\langle M^2 \right\rangle_{sl}$. Because $\langle v_z \rangle_{sl}$ and $\left\langle M^2 \right\rangle_{sl}$ typically have the same sign (fig. 6.6f), the budget leads only to increases in stratification and cannot reproduce the observed oscillatory motion (fig. 6.6b, blue line). Sheared inertial oscillations are related to the geostrophic adjustment described by *Tandon and Garrett* (1994), in which an inviscid system that has been disturbed from thermal wind balance (by passing storms, for example) will oscillate around its balanced state. In contrast, our observations show that the front roughly maintains thermal wind balance throughout the adjustment (fig. 6.6f), suggesting that whatever mechanism is forcing the along-front shear $\langle u_z \rangle_{sl}$ may also be simultaneous forcing the cross-front buoyancy gradient $\left\langle M^2 \right\rangle_{sl}$.

The observed oscillations of the average velocity fields can be characterized with an estimate of the horizontal momentum equations (i.e., a simple slab model):

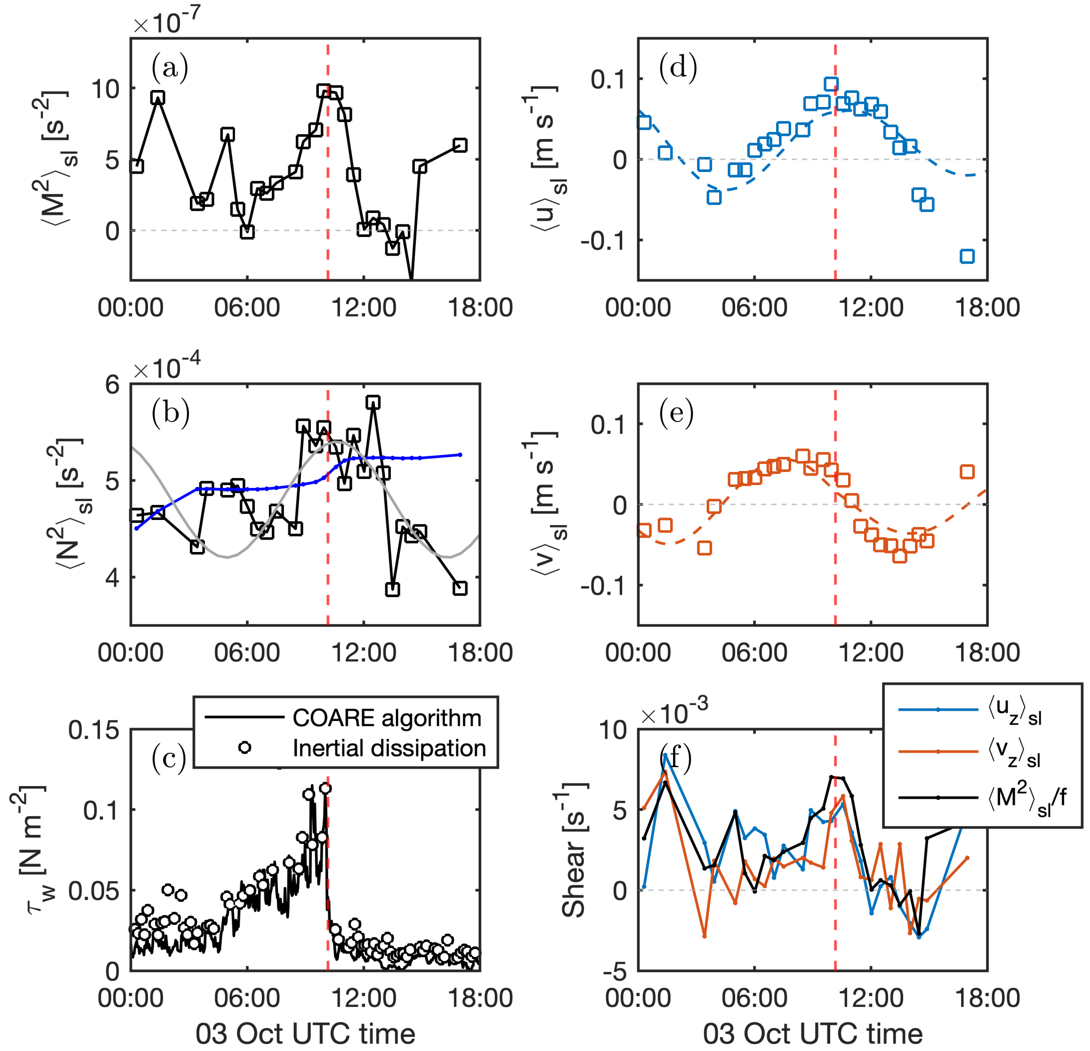

Figure 6.6: Time series of (a) averaged across-front buoyancy gradient $\langle M^2 \rangle_{sl}$; (b) averaged vertical buoyancy gradient $\langle N^2 \rangle_{sl}$ (solid lines with squares), along with a sinusoidal fit (grey line), and the result of the integrated stratification budget (blue line); (c) wind stress magnitude measured with the inertial dissipation method (circles) and estimated with the COARE algorithms (solid line); (d,e) averaged along-front (u) and across-front (v) velocity, respectively (squares), and the results of the slab model (dashed lines); (f) averaged vertical shear along-front and across-front, and shear predicted by the thermal wind balance ($\langle M^2 \rangle_{sl}$). Vertical red dashed line in all panels shows the time when the wind stopped (for reference).

$$\frac{\partial U}{\partial t} = (f+\zeta)V + \frac{\tau_w^x}{\rho_0 h}$$
$$\frac{\partial V}{\partial t} = -fU + \frac{\tau_w^y}{\rho_0 h},$$

where U, V are the surface layer-average ageostrophic velocities ($U = \langle u \rangle_{sl} - u_{bg}$ with a background [e.g., geostrophic] flow u_{bg}, and $V = \langle v \rangle_{sl}$)), and ζ the background vertical vorticity (where we assume no along-front gradients so $\zeta = -u_y$), and h is the depth over which wind stress acts (e.g., the mixed-layer or surface layer depth). Numerically integrating these equations with the observed wind (over a fixed surface layer depth $h = 25\,\mathrm{m}$), and using u_{bg} and ζ as fitting parameters produces good estimates for the observed velocities (figs. 6.6d and e) with $u_{bg} = 0.02\,\mathrm{m\,s^{-1}}$ and $\zeta = 0.16f$ if non-zero initial conditions are used for U, V. However, here the non-zero initial conditions necessary to fit the observed response result in the wind forcing terms being of negligible size, so the velocities vary almost exactly as sinusoids with frequency $f_{\mathrm{eff}} = \sqrt{f(f+\zeta)}$ (a period of $2\pi/f_{\mathrm{eff}} \sim 11.1\,\mathrm{h}$). Alternatively, taking the velocity as initially at rest and integrating forward with wind from the beginning of the record (on 01 Oct; fig. 6.4a) does not capture the phase of the observed oscillations, but can produce oscillations with comparable magnitude ($\sim$0.05 $\mathrm{m\,s^{-1}}$). Choosing smaller values of h (e.g, the mixed-layer depth as opposed to the surface layer depth) increases the strength of the wind forcing term and produces less desirable fits to the observed velocity.

In describing the frontal evolution, we have assumed that measurements are made in a Lagrangian reference frame following the front. The oscillatory nature of many of the measured fields (fig. 6.6) suggest the possibility that this is not the case. If instead the front was moving independently from the sampling scheme, then the frontogenic/frontolytic behaviour may be simply a result of advection by an underlying spatially homogeneous inertial velocity field, such as is described by the slab model. Such independent movement would further explain the fact that variations in vertical velocity shear match the variation in lateral buoyancy (fig. 6.6f). However, because the ice drift opposes the wind direction (fig. 6.1b), it is likely moving with ocean surface currents. Given the speed of the ice drift, this scenario would require significant decoupling and shear between the near-surface currents and the bulk of the surface layer. Additionally, an explanation would be needed for what was driving those surface currents. Inertial advection of the front past a non-Lagrangian measurement platform does not directly explain the link between the wind stress increase and the increase in lateral buoyancy gradient (see "*Frontogenesis*" section, below). Furthermore, the development of an eddy field visible in the ice (see "*Frontolysis*" section, below) suggests that currents driving the ice motion extend beyond a shallow surface layer. While we cannot rule out the possibility that our observations result from simple advection of a steady front, we proceed with the assumption that the primary driver of the observations is unsteady frontal evolution.

6.3.2 *Atmosphere-ocean feedbacks*

Throughout the looping survey, none of the atmospheric variables measured aboard *Norseman II* (e.g., air temperature, wind stress) showed any measurable cross-front variation, indicating that the front does not drive changes in the atmosphere on $\mathcal{O}(1\,\mathrm{km})$ scales. Nevertheless, we did observe a cross-front variation in the surface heat flux on the order of roughly $10\,\mathrm{W\,m^{-2}}$ (fig. 6.7a) based on composites of the surface heat flux anomaly as a function of across-drift distance (calculated as the heat flux minus the section-averaged heat flux and averaged in 250-m across-drift bins). This variation is driven by the cross-front variation in bulk sea surface temperature ($\sim 0.5\,^{\circ}\mathrm{C}$ change; fig. 6.7b). The ocean is losing heat faster away from the ice edge, where the difference between water and air temperature is greater. As the front adjusts, it will mediate the location and magnitude of horizontal gradients in the surface heat flux.

The mean wind speed ($\sim 5\,\mathrm{m\,s^{-1}}$) and duration ($\sim 5\,\mathrm{h}$) of the higher-wind events (when the observed wind deviates from the re-analysis) correspond to an advective length scale of $\sim 90\,\mathrm{km}$ (i.e., the length scale if the wind events represent passing storms). Such a

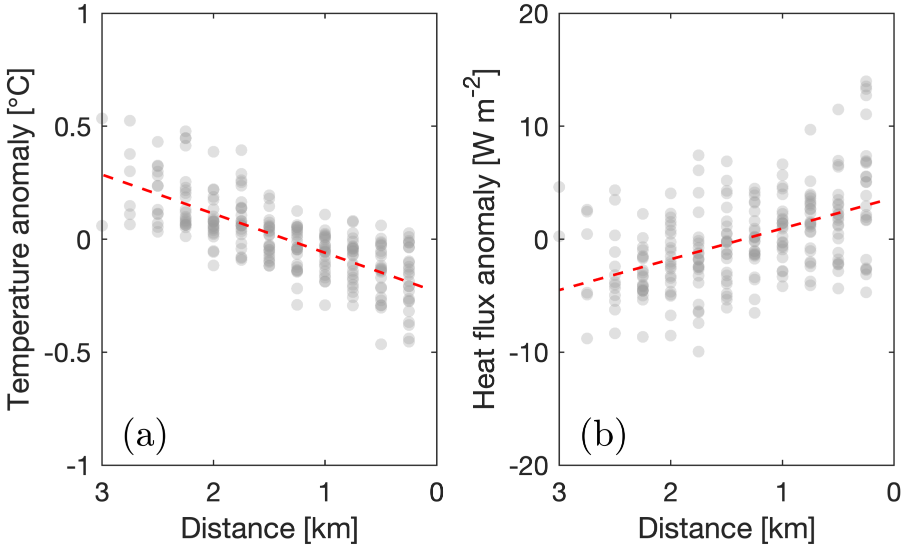

Figure 6.7: Across-drift (a) near-surface (bulk) water temperature anomaly and (b) net surface heat flux anomaly. Grey dots show values binned at 250 m and are anomalies relative to a section average. Distance is relative to the start of each section (with a distance of 0 being nearest to the ice and moving towards open water as distance increases). Dashed red lines show linear fits to binned values.

scale would only be minimally resolvable by re-analysis products suggesting that these are localized events. Furthermore, this scale is of roughly the same order as the MIZ width, which may indicate that they are laterally constrained by atmospheric heterogeneity across the MIZ. Localized MIZ atmospheric variations associated with the temperature and boundary layer differences across ice-edge have been documented previously (e.g., *Grønas and Skeie*, 1999; *Inoue and Hori*, 2011; *Guest et al.*, 2018). Furthermore, *Wenta and Herman* (2018) found that air circulation within the atmospheric boundary layer is sensitive to ice floe properties on scales typically unresolved by mesoscale weather models.

6.3.3 Frontogenesis

The submesoscale MLE in the MIZ predicted by models (*Lu et al.*, 2015; *Horvat et al.*, 2016; *Manucharyan and Thompson*, 2017) have a frontolytic tendency and alone are unable to explain the observed frontal steepening. The frontogenesis is exactly coincident with wind stress increase (compare fig. 6.6a and fig. 6.6c), so steepening is driven in some way by surface forcing: either wind stress directly, or associated changes in surface heat flux that accompany the wind. Because the density is set primarily by salinity in this temperature-salinity range, heat flux alone is not expected to have a significant direct affect on the front; however, heat loss from the polar ocean has the secondary impact of causing ice growth which itself is associated with convection.

Convective and shear-driven deepening

Some frontal studies evaluate the interaction of surface forcing with MLE by comparing either parametrized magnitudes of the vertical buoyancy flux, $\langle w'b' \rangle$, associated with each of the drivers of stratification (*Mahadevan et al.*, 2012) or comparing the strength of overturning stream functions (*Mahadevan et al.*, 2010). In this framework, the observed wind stress is unable to lead to isopyncal steepening as the associated buoyancy flux relies on Ekman dynamics (*Thomas and Lee*, 2005; *Mahadevan et al.*, 2010) which are characterized by subinertial time frames that are longer than the observations. Furthermore, the direction of the wind ("up-front") would also have a frontolytic sense if it persisted long enough for the Ekman dynamics to manifest.

Convection could lead to frontal steepening by mixing waters at the heal of the front. *Mahadevan et al.* (2010) considers convection only due to surface cooling, which is parametrized by $\langle w'b' \rangle_Q = -\alpha Q g (\rho c_p)^{-1}$ for c_p the heat capacity of water, α the coefficient of thermal expansion, Q and the rate of surface heating/cooling (heat flux out of the ocean is negative). In polar regions, additional convection is possible due to brine rejection during sea ice formation (*McPhee*, 2008); an associated vertical buoyancy flux, analogous to $\langle w'b' \rangle_Q$ can be constructed for surface salinity input as: $\langle w'b' \rangle_S = g\beta\rho_i(\rho_0)^{-1}\Delta S(C_i h_i)_t$, where β is the haline contraction coefficient, $(C_i h_i)$ the "effective ice thickness" (C_i is ice concentration and h_i is the ice thickness), ρ_i the ice density, and ΔS the difference in salinity between the ocean and the sea ice. Using reasonable values for sea ice properties ($\rho_i = 938\,\mathrm{kg\,m^{-3}}$, $S_i = 6\,\mathrm{g\,kg^{-1}}$, from the Beaufort Sea MIZ in Oct 2015; *Smith et al.*, 2018), and assuming that approximately 5 cm of ice grew during the course of the survey in a 15% ice concentration zone (by visual observation while on site), the total convective buoyancy flux is $\langle w'b' \rangle_Q + \langle w'b' \rangle_S \sim 8.6 \times 10^{-9}\,\mathrm{m^2\,s^{-3}}$. This value is an order of magnitude below the mean vertical buoyancy gradient associated with MLE: $\langle w'b' \rangle_{MLE} = 0.06 h_{sl}^2 M^4 f^{-1} \sim 9 \times 10^{-8}\,\mathrm{m^2\,s^{-3}}$ (*Fox-Kemper et al.*, 2008), suggesting that convection cannot explain the observed steepening.

Other studies (*Dewey et al.*, 2017; *Smith et al.*, 2018) show that one-dimensional mixing processes often dominate upper ocean physics in the MIZ. We test this with the use of a one-dimensional mixing model: the Price-Weller-Pinkel model (PWP; *Price et al.*, 1986). This model accounts for the combined effects of both wind-driven mixing (due to shear) and convective mixing (due to surface cooling). We ran the model using the surface heat fluxes and wind stresses from the COARE algorithm as forcing for two different vertical profiles. The profiles were separated by a distance of roughly 2 km, so one was located within the front while the other was near the edge of the front. The model applied wind stress over the mixed-layer depth (as defined by a $0.25\,\mathrm{kg\,m^{-3}}$ density threshold compared to the shallowest density measurement; as above), so the initial mixed-layer depths were roughly 8 m and 14 m for the two profiles, which is consistent with the depth of the front. In the model, momentum-driven deepening of the mixed layer (due to entrainment) is based on shear between the mixed-layer base and an underlying transition layer (based on Richardson number criteria). The model predicted no appreciable change to the depth of the front for either starting profile (not shown), so the inclusion of shear-driven-mixing (in combination with convection) is still unable to account for the observed frontogenesis. Running the model with different mixed-layer depth definitions (e.g., based on different σ_Θ thresholds, or based on thresholds of $\Delta\sigma_\Theta/\Delta z$) may have resulted in slightly different initial mixed-layer depths, but produced no difference in the qualitative behaviour of the model (i.e., no mixed-layer deepening). To recreate deepening of the front comparable to observations in the model required multiplying the wind stress by a factor of 5.

Strain-induced frontogenesis and wind stress heterogeneity

Frontogenesis is classically explained as a result of horizontal strain fields on a front (*Hoskins*, 1982, and references therein). In the ocean, mesoscale eddy fields have been shown to provide frontogenic strain fields (e.g., *Capet et al.*, 2008). SAR imagery shows an apparently active eddy field (see *Frontolysis* section, below), so that there was likely sufficient energy at the mesoscale to provide such a strain field, although our measurements do not allow further resolution of those features. However, if the frontogenic behaviour is a response to a non-local mesoscale strain, then its modulation by the local wind field over short time-scales is unlikely. Instead, we consider processes by which the wind field would induce a strain on the front.

Ignoring mixing and non-conservative terms (justified by the results from the convective/shear-driven deepening experiments), and assuming that along-front fields are uniform (so ∂_x terms are zero), the evolution of lateral buoyancy can be written as

$$D_t(M^2) = -v_y M^2 + w_y N^2,$$

where D_t represents the material derivative ($D_t = \partial_t + v\partial_y + w\partial_z$). If advective terms are sufficiently small (which may or may not be a reasonable assumption, as discussed above), changes in $\langle M^2 \rangle_{sl}$ are driven by cross-front variations in the ageostrophic velocity fields. Spatially heterogeneous surface stress may drive cross-front variations in the velocity, and thus provide a mechanism by which the front directly responds to the temporally increasing wind stress.

The presence of ice modifies the stress transfer from the atmosphere to the ocean and can lead to heterogeneity in the surface stress input to the ocean. While careful representation of stress transfer across the ice-ocean-atmosphere system requires accounting separately for wind-ice and ice-ocean stresses (e.g., *Steele et al.*, 1989; *McPhee*, 2008; *Cole et al.*, 2014, 2017), some studies in the MIZ (e.g., *Fennel and Johannessen*, 1998) consider a single bulk wind stress, with a drag coefficient modulated by the ice. Surface stress measurements complementing that approach show heterogeneity moving from the ocean to the ice, with a local maximum of surface stress in the MIZ even for a spatially homogeneous wind field (this heterogeneity is represented by a spatially varying drag coefficient), where the increase in stress is due to the increased surface roughness elements in the MIZ (*Guest et al.*, 1995; *Birnbaum and Lüpkes*, 2002; *Andreas et al.*, 2010a). Our observations do not show measurable cross-front variations in either wind speed or wind stress over $\mathcal{O}(1\,\mathrm{km})$ scales, but the existence of surface stress variations over the MIZ scale of ($\mathcal{O}(10\,\mathrm{km})$ is probable.

Furthermore, the ice may have an impact on the depth to which wind forcing penetrates through modification of the surface turbulent boundary layer. In the slab model presented above we assumed a fixed depth $h \sim 25\,\mathrm{m}$ over which the wind stress is applied based on the approximate open-ocean surface layer depth. However, studies of under-ice boundary layers have shown that the Ekman layer depth (the steady state depth of wind stress penetration) is less than the mixed-layer depth (*McPhee*, 2008; *Cole* *et al.*, 2014, 2017; *Randelhoff et al.*, 2014, and others); for example, measurements from an ice-tethered-profiler in the Beaufort Sea MIZ in Oct 2014 showed an average Ekman layer depth of approximately 10 m in Oct, compared to a mixed-layer depth of 30–40 m (see Figure 10 in *Cole et al.*, 2017).

In previous studies, non-uniform surface stress across the MIZ is associated with ice-edge upwelling/downwelling (e.g., *Niebauer*, 1982; *Fennel and Johannessen*, 1998), and eddy generation and shedding (*Häkkinen*, 1986). However, these studies consider longer subinertial timescales, so that Ekman dynamics can be set up (upwelling/downwelling at the ice edge is associated with convergence/divergence in the Ekman layer, and eddy shedding is a non-linear interaction with Ekman velocity). If the along-front wind stress was maintained, the system may evolve towards one of those states; however, we see highly dynamic transient behaviour that was not discussed in those studies.

6.3.4 Frontolysis

Following relaxation of the wind, the front rapidly collapsed (fig. 6.5). Submesoscale frontolysis is driven by instabilities such as SBI, which lead to the development of eddies in the mixed layer and re-stratification. A comparison of SAR images prior to the survey and at the end of the survey show a change in character of the ice edge (fig. 6.8). Prior to the survey (29 Sept; fig. 6.8a), the ice edge was generally compact, while over the course of the survey there was considerable deformation of the ice edge. A SAR image from late on 03 Oct (fig. 6.8b) shows that this deformation resulted in a number of coherent filaments and vortical structures over a wide range of scales. Within the MIZ, sea ice is particularly mobile (*Lund et al.*, 2018) and can act as tracer for surface ocean currents (e.g., *Johannessen et al.*, 1987; *Manucharyan and Thompson*, 2017), so this deformation is indicative of an underlying ocean eddy field.

The appearance of these eddies may be due to the development of an eddy field over this time frame (i.e., the growth of MLE; *Manucharyan and Thompson*, 2017). Linear stability

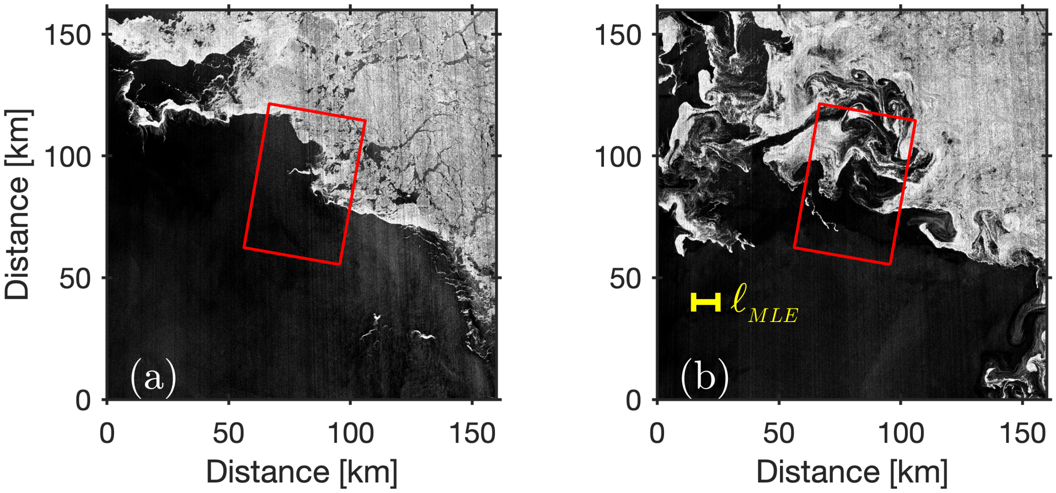

Figure 6.8: SAR RADARSAT-2 image of the MIZ in the vicinity of the survey on (a) 29 Sept 16:37Z, and (b) 03 Oct 16:20Z. The red rectangle represents the the boundaries of fig. 6.1b. The yellow line shows the length of the 10-km eddy scale predicted for the MLE field. RADARSAT-2 Data and Products are from MDA Geospatial Services Inc., provided via the National Ice Center.

analysis (*Stone*, 1966) gives that the fastest growing SBI mode has a wavelength of $\ell_{MLE} = 2\pi\mathcal{U}(f^{-1})[(2/5)(\mathrm{Ri}+1)]^{1/2}$, where $\mathcal{U}$ is a characteristic velocity, and $\mathrm{Ri} = N^2(u_z^2 + v_z^2)^{-1}$ is the Richardson number (which is $\mathcal{O}(1)$ in submesoscale flows). The linear model is valid during the initial stages of instability, before the inverse cascade transfers energy to longer wavelengths (*Fox-Kemper et al.*, 2008). Median values for Ri in the mixed layer for the different sections were $\mathcal{O}(1)$ (section medians varied approximately from 0.3 to 1.2, although spatially varying values varied over several orders of magnitude). Using $\mathrm{Ri} = 1$, and the surface velocity as a characteristic velocity scale, $\mathcal{U} \sim 0.25\,\mathrm{m\,s^{-1}}$, gives the wavelength of the most unstable SBI mode as $\ell_{MLE} \sim 10\,\mathrm{km}$. This scale is consistent with many of the observed eddies within the SAR image (fig. 6.8b) suggesting the possibility that MLE and associated processes are present here. This presents evidence for MLE-driven frontolysis; however, such frontolysis is also associated with restratification (*Fox-Kemper et al.*, 2008). The apparent oscillatory behaviour of $\langle N^2 \rangle_{sl}$ (fig. 6.6b) does not present strong evidence for MLE restratification. Furthermore, the speed of frontolysis may be faster than would be associated with MLE re-stratification (which might evolve over several days *Fox-Kemper et al.*, 2008).

Alternatively, frontolysis may be separate from the eddy activity. Instead of developing over the course of the survey, an ocean eddy field may have already been active but decoupled from the sea ice (for example, due to the influence of wind). Figure 6.8b shows the MIZ at a time when the wind had been effectively stopped for a period of hours (fig. 6.4a; at 16:20Z on 03 Oct), so it is possible that the ocean currents arranged the ice into the visible eddy field over that time. For example, *Kozlov et al.* (2019) observed eddies in the satellite record within the MIZ that may be associated with gyre processes. From the onset of the survey, however, the observed ice drift opposed the direction of local winds, suggesting that it was already moving along with the upper ocean. *Cole et al.* (2017) have suggested at these low ice concentrations, the transfer of momentum from wind to ice is relatively inefficient.

6.4 *Conclusions*

The primary contribution of this study is a set of high resolution observations of an ice-edge located front taken over a period of days, which allowed us to investigate its temporal evolution. These observations show a dynamic adjustment of the front over fast timescales that has not been described previously in the literature. The front appears to respond to a wind event that drives a frontogenic behaviour; following relaxation of the wind, the front rapidly relaxes. While important metrics are derived (e.g., fig. 6.6), our measurements are insufficient to fully explain what is driving this behaviour. We hypothesize that the presence of sea in the MIZ may be important factor by driving spatial heterogeneity in the surface stress and momentum transfer from the atmosphere to the ocean. Furthermore, the wind event driving the frontal adjustment may be a localized event that itself is impacted by the MIZ.

Drag from differential ice-ocean velocity and variations in surface roughness in the presence of ice have both been shown to modify wind stress transfer to the ocean (*McPhee*, 2008). In considering wind-ice and ice-ocean stresses separately, *Cole et al.* (2017) indicated that at low ice concentrations the transfer of momentum from the wind to the ice is inefficient, but also suggested that ice-ocean momentum transfer might be highest in low ice concentrations. Atmospheric measurements show an increase in surface stress moving from the open ocean to the MIZ (*Guest et al.*, 1995; *Birnbaum and Lüpkes*, 2002; *Andreas et al.*, 2010a). In mixed ice and open water conditions (e.g., in the MIZ), estimates of bulk drag coefficients have been constructed based on open-ocean and ice-based coefficients weighted by ice concentration (*Zippel and Thomson*, 2016). However, in low-concentration MIZs, observations of the total atmosphere-ice-ocean momentum transfer are sparse, and do not yet give a full picture of all processes. For example, recent work suggests that in an energetic sea state the damping of short waves by ice in the MIZ may decrease the effective transfer velocity from wind to ocean (*Smith and Thomson*, 2019). Overlaid on the complicated picture of wind stress transfer to the ocean in MIZs are localized weather patterns, such as low-level jets, which may result from the transitions of atmospheric properties across the MIZ (e.g., *Guest et al.*, 2018; *Liu and Schweiger*, 2019).

The use of the COARE algorithms has been shown previously as insufficient for predicting surface fluxes in the MIZ (*Yu et al.*, 2017); however, in this case the strong match between the wind stress estimated with COARE versus that calculated using the inertial dissipation method (fig. 6.6c) suggests that the COARE results here are valid. The validity of the COARE algorithms here is likely because the ship track was generally travelling only on the open-water side of the ice edge. Travel into the ice may have necessitated a different approach for calculating surface fluxes (e.g., with alternative parameterizations for turbulent transfer coefficients from *Andreas et al.*, 2010a). We used the COARE-derived wind stress and heat fluxes as forcing for the PWP model. Previous application of PWP to the MIZ has used a hybrid approach where surface fluxes were derived from a three-dimensional Arctic model in order to account for ice growth/melt, and impacts from ice on surface forcing (*Dewey et al.*, 2017). However, that study examined much longer trends (annual variations) where melt/growth processes may have been significant. For the short model runs we performed (evolving over hours), we do not expect the sea ice to modify our application of the PWP model significantly, with the exception of its role in modifying surface stress. We can test the effect of sea ice on the PWP model results through application of some scaling factor on the surface stress. For example, *Guest et al.* (2018) predicted a factor 2.5 times greater drag coefficient in the MIZ compared to open water. However, in our simulations a factor of 5 increase was required for any appreciable deepening of the front that would be comparable to the observations.

Lateral buoyancy fluxes due to MLE have been theorized to be a potential driving process for setting the upper ocean structure in the MIZ (*Lu et al.*, 2015; *Horvat et al.*, 2016; *Manucharyan and Thompson*, 2017). SAR imagery shows an active eddy field at the study location (fig. 6.8b) with a number of features with scales consistent with the fastest growing mode from linear instability theory (*Stone*, 1966). The lack of direct observations of horizontal density and velocity structure, however, whether MLE processes are dominant here is not yet clear. The interaction of surface forcing (and in particular wind stress) with MLE restratification has not yet been investigated for the MIZ. In the open ocean, wind aligned in an "up-front" direction leads to frontolytic behaviour (*Thomas and Lee*, 2005), as opposed to the frontogenesis observed here. However, that effect is driven by Ekman buoyancy flux, which is driven necessarily by Ekman dynamics that need a longer time-scale to develop. For open-ocean fronts the competing effects of re-stratification from MLE and de-stratification from convection has been investigated previously based on the relative strength of parametrized vertical buoyancy flux $\langle w'b' \rangle$ associated with MLE and surface cooling. We have extended that approach by developing an equivalent convective $\langle w'b' \rangle$ to account for brine rejection during surface cooling.

The apparent response of an ice-edge meltwater front to variations in localized wind forcing emphasizes the need to study the combined ice-ocean-atmosphere system rather than considering these components individually. This study highlights the challenges inherent to studying these processes in the MIZ. Shipboard sampling of these meltwater fronts is particularly difficult due to the relatively small horizontal and vertical spatial scales. Sampling near-surface stratification and velocity from ships with large drafts relative to the depth of the upper ocean mixed layer is particularly challenging. *Wulff et al.* (2016) have demonstrated that autonomous underwater vehicle platforms are capable of capturing near-surface profiles within a meltwater front with a high enough horizontal resolution to properly characterize a number of frontal properties and without the inherent problems associated with ship wake contamination. However, whether such vehicles can sample with an appropriate temporal resolution to capture the type of dynamic adjustment we have observed here is not clear. Furthermore, these platforms are unable to measure local wind patterns and thus must rely on re-analysis products, which we have shown to miss local ice-edge variations.

Episodic ice melt during the fall ice-growth season due to strong winds has been observed previously in the MIZ due to one-dimensional mixing processes (*Smith et al.*, 2018). However, the impact of wind on mixing is strongly mediated by underlying oceanographic conditions; as we have seen here, one-dimensional mixing may not be valid in the presence of a strong frontal structure in the MIZ. Modelling studies indicate that sea ice may be particularly sensitive to vertical and lateral heat fluxes associated with MLE (*Fox-Kemper et al.*, 2011; *Horvat et al.*, 2016), though the present study is unable to answer questions about the impact of MIZ frontal processes on ice growth/melt.

While the specifics of the frontal steepening are not fully resolved, the described contrast with open-ocean conditions indicates that different frontogenic mechanisms may be of importance in the MIZ and provides a first step in understanding the forced dynamics of submesoscale fronts in polar regions. As the sea ice edge retreats farther north over the deep basin of the Beaufort Sea during the summer ice minimum, these processes may become increasingly important in controlling the heat fluxes during the fall freeze-up period.

Chapter 7

CONCLUSION

7.1 *Summary*

This dissertation provides both technological (part I) and scientific (part II) advancements for understanding atmosphere-sea ice-ocean interaction processes in the Arctic.

Chapters 2 and 3 (part I) described methods used in processing the data collected by uplooking moored Acoustic Doppler Current Profilers (ADCPs) that were deployed as part of the Stratified Ocean Dynamics of the Arctic (SODA) experiment (*Lee et al.*, 2016) and used in subsequent chapters. In addition to outlining some of the unique data processing challenges involved with these instruments, chapter 2 also described a novel method for consistent post-deployment compass calibrations of multiple instruments based on overlapping measurements. Chapter 3 presented methods for using data from these instruments to remotely infer both the depth and temperature of the ocean's surface mixed layer (ML), which are critical parameters for understanding the connections between the ocean surface and deeper waters. These methods have the potential to be adapted to a range of different mooring arrays already deployed across the Arctic, thereby allowing for additional data recovery and expanding the utility of those observations.

In part II, chapter 4 (reproduced from *Brenner et al.*, 2021) investigated how sea ice properties impact ice-ocean momentum transfer. Specifically, it considered annual variability of the ice-ocean drag coefficient, C_{io}, using both a force-balance technique and ice-morphology-based parameterization schemes. These measurements both validated and invalidated different components of the parameterizations, and showed that existing mismatches between observed and modelled drag coefficients are due to misrepresentations of the sea ice geometry. The results showed that the order-of-magnitude differences in C_{io} across the year were primarily driven by the seasonal cycle of growth and melt of sea ice keels.

Building on those results, chapter 5 sought to better characterize and understand the impact of sea ice on wind-driven motions in the ocean surface ML, with a particular focus on the inertial-frequency response. A simplified one-dimensional ice-ocean coupled model provided an interpretation of the mooring observations of sea ice and ML velocities, and insight into the drivers of seasonal variation. The model showed that, against expectations, sea ice roughness (as represented by C_{io}) had minimal impacts on inertial oscillations – this due to the highly coupled nature sea ice and ocean velocities. The frequently seen seasonal decreases in inertial oscillation strength during the winter (e.g., *Plueddemann et al.*, 1998; *Rainville et al.*, 2011; *Polyakov et al.*, 2020a) were explained by the model as resulting from a combination of sea ice internal strength and seasonally varying ML depth. While the dependence on internal stress agreed with previous intuition (*Rainville et al.*, 2011), the importance of ML depth on inertial oscillation strength is less frequency discussed in the literature.

The analyses in both chapters 4 and 5 needed to make some account for unresolved internal stresses within the sea ice pack. The methods used to do so necessarily simplify the complex processes associated with sea ice rheology. Despite the simplicity, the different methods used to account for ice stress in each chapter (a filtering method combined robust fitting in chapter 4, and a linear damping model in chapter 5) both provide the same broad conclusion: that internal stresses varied between moorings. In each chapter, the northernmost mooring (located in perennial sea ice) was most impacted by internal stress, while the southernmost mooring (within the seasonal ice zone) may be minimally impacted by those stresses even during the winter ice pack. As sea ice internal stress is the primary way that sea ice regulates the overall atmosphere-ocean momentum transfer, this result conforms to anticipated trends of increasing atmosphere-ocean coupling in the Arctic (*Rainville et al.*, 2011). Additionally, both chapters separately provide evidence that wind-ocean momentum transfer may be maximized at some intermediate sea ice concentration (in agreement with *Martin et al.*, 2014).

Using shipboard observations from the Marginal Ice Zone Project (*Lee et al.*, 2012, 2017), chapter 6 (reproduced from *Brenner et al.*, 2020) moved beyond the one-dimensional viewpoint of the previous chapters to describe the evolution of a well-defined density front located along the ice edge. Over the ∼3-d survey period, underway measurements of upper ocean temperature-salinity structure showed a frontal adjustment that was temporally correlated with a localized wind event. Concurrent synthetic aperture radar (SAR) imagery showed evolution of the sea ice and the emergence of active oceanic eddy field that may have been indicative of submesoscale motions. The observations were insufficient to fully resolve the dynamics of the adjustment process, but the heterogeneity of the surface momentum flux due to the presence of sea ice was suspected as a contributor to the response.

7.2 *Impacts and future trends*

There is a downwards trend of sea ice concentration at each of the moorings in the SODA mooring array, along with considerable interannual variability (fig. 7.1). Conditions during the SODA experiment (2018–2019) were approximately representative of the recent past. Differences in momentum transfer between the moorings (chapters 4 and 5), which span from thin sea ice in the seasonal ice zone to thicker perennial ice, are indicative of future changes in the ice-ocean system. The results of this dissertation show that ice-ocean drag coefficients are likely to become more seasonal due to the growth/melt of sea ice keels in the seasonal ice zone, and will have an overall decreasing trend as maximum keel sizes shrink. The shift to thinner, more seasonal sea ice will also lead to mechanical weakening of the ice pack and a decrease in internal sea ice stresses.

Ongoing trends in ice-ocean drag coefficients and sea ice internal stresses will have different impacts on both sea ice motion and the net atmosphere-ice-ocean momentum transfer. These differences are demonstrated by separately considering the equations for ice-ocean stress, $\boldsymbol{\tau}_{io}$, from the quadratic drag law (eq. 4.4a) and from re-arranging the sea

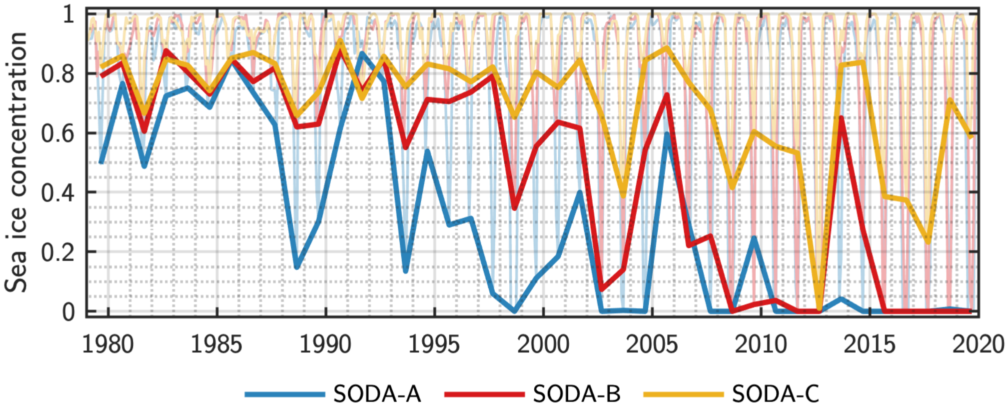

Figure 7.1: Sea ice concentration at each of the SODA moorings from 1979 to 2020 (the end of the SODA deployment). Faded colours show monthly-average concentration values, while bold lines highlight the trends in annual minimum values. Monthly ice concentration values are from the National Snow and Ice Data Center (NSIDC) Sea Ice Index, Version 3 (*Fetterer et al.*, 2017), interpolated to the locations of the moorings.

ice momentum equation (similar to what was done in eq. 4.6):

$$\boldsymbol{\tau}_{io} = \rho_o C_{io} \left(\boldsymbol{u}_i - \boldsymbol{u}_o\right) \|\boldsymbol{u}_i - \boldsymbol{u}_o\|, \tag{7.1}$$

$$\boldsymbol{\tau}_{io} = \boldsymbol{\tau}_{ai} + \sum \boldsymbol{F}_{ice}. \tag{7.2}$$

From eq. (7.1), it would initially appear that decreasing the ice-ocean drag coefficient would lead to a decreasing ice-ocean stress because $\boldsymbol{\tau}_{io} \propto C_{io}$. This is not necessarily the case though. Instead, chapter 5 showed that in this coupled system, sea ice drift speeds can instead adjust, so changes in C_{io} in eq. (7.1) can be compensated by changes in the relative ice-ocean velocity, $\boldsymbol{u}_i - \boldsymbol{u}_o$, without directly impacting $\boldsymbol{\tau}_{io}$. This is further evidenced by eq. (7.2), in which $\boldsymbol{\tau}_{io}$ is independent of C_{io}. Equation (7.2) shows that momentum flux into the ocean is controlled by a balance of the momentum flux out of the atmosphere with the other forces on the sea ice ($\sum \boldsymbol{F}_{ice}$, which primarily take the form of internal stress; see appendix 4.B and *Steele et al.*, 1997). Decreasing internal ice stress then results in a higher proportion of the wind stress reaching the ocean.

Together, these changes suggest that the direct impacts of changing ice-ocean drag and internal stresses will be both an increase in sea ice drift speeds and an increase in the efficiency of momentum transfer from the wind into the ocean, even in the presence of sea ice. Due to the complex nature of the sea ice rheological terms (governing the internal stress), the changing ice drift speed may lead to additional indirect impacts and potential feedbacks as ice deformation rates could be affected, but these are challenging to predict.

7.3 *Outlook*

7.3.1 *Open questions*

These results expand our knowledge of role of sea ice in mediating atmosphere-ocean momentum transfer, but also highlight a variety of unresolved questions.

The fate of stored upper ocean heat and its viability for enhancing sea ice melt depends on a balance of momentum input (which can drive vertical mixing) and stratification (which can suppress turbulence and sequester deeper waters). Observations of shoaling ML depths across much of the Arctic (*Peralta-Ferriz and Woodgate*, 2015) indicate that trends in stratification are currently outpacing any potential trends in changing surface stress, but predictions of future conditions remain challenging. *Martin et al.* (2016) showed that trends in modelled total ocean surface stress were sensitive to how ice-ocean drag was parameterized. As chapter 4 shows differences between modelled and observed drag coefficient seasonality (due to mismatches in parameterized ice geometry), the reality of those trends is still unknown. Increased atmosphere-ocean coupling due to the mechanical weakening of of sea ice may be resulting in an increasing trend of surface stress, but this has not been quantified with any *in situ* observations.

In addition to uncertainties in long term trends, there are a range of ice-ocean interaction dynamics that are not yet understood. Chapter 5 showed that sea ice roughness had minimal impact on driving ML velocity and inertial oscillation strength in the bulk sense (section 5.4.4), but past work has shown that it is an important factor for near-inertial wave (NIW) generation (*Cole et al.*, 2018). *Dosser et al.* (2021) further suggests that wintertime reductions of NIW-related turbulent dissipation may be due to changes in ice surface roughness. This mismatch of sensitivity of inertial oscillations and NIW generation to the sea ice roughness suggests that there are a variety of ways in which sea ice might impact NIW generation. More work is needed to understand these links.

Limitations in the current theoretical framework for the ice-ocean boundary layer (section 1.2.3) present challenges in the scaling up of in situ point measurements of Reynold's stresses (and derived drag coefficients) to floe-scale or regional-scale representative values. Differences in the range of drag coefficient values found from force-balance approaches and from localized Reynold's stress measurements (chapter 4) might indicate either (a) a systematic error in the force balance approach; or (b) that point measurements of turbulence are not representative of floe-integrated results. While the former option cannot be ruled out, the previously observed sensitivity of turbulent measurements to the presence of ice keel wakes (*Fer and Sundfjord*, 2007; *Shaw et al.*, 2008; *Randelhoff et al.*, 2014) suggests the latter option is a major factor. Spatial heterogeneity of implied drag coefficients within a turbulent wake would lead to challenges in the interpretation of point measurements.

The interaction of submesoscale motions with sea ice and the associated feedback mechanisms remains an active area of research. Even since the initial publication of chapter 6, significant advancements have been made in this realm (e.g., *Shrestha and Manucharyan*, 2021; *Manucharyan and Thompson*, 2022). Nonetheless, *in situ* measurements of these processes are challenging to make.

7.3.2 *Potential future work*

There are a number of avenues that potential future work could proceed, including both continued analysis of the SODA mooring data as well as expansion to other data sources.

Here, some projects and research needs are identified within a range of frameworks and themes that would address some of the open questions above.

Observations

The use of upward looking ADCPs for identifying the ML depth in chapter 3 may allow for an expanded ability to measure Arctic MLs, but these methods would benefit from further testing and validation, especially during the onset of ice melt and the shift to shallow summer stratification. Coordinated measurements from an autonomous Seaglider in the vicinity of one of the SODA moorings provided significant value in validating the method during the period where the Seaglider was active. Additional Seaglider deployments from ongoing observational campaigns (such as the "Arctic Mobile Observing System") coincident with moored ADCP measurements would be useful for further validation.

Long term trends

The SODA moorings have provided an opportunity to analyse sea ice and upper ocean processes over their year-long deployment, but it would be valuable to understand how those processes are changing. Many similar measurements are also made with moorings from the Beaufort Exploration Project (BGEP), which have been in place since 2003 (`https://www2.whoi.edu/site/beaufortgyre/data/mooring-data/`). For a number of those years, these measurements have included sea ice velocities, upper ocean velocities (*Armitage et al.*, 2016), and upward looking sonar (*Krishfield et al.*, 2014). As such, some of the analysis performed in chapter 4 and chapter 5 could be also done with those data, facilitating the evaluation of longer term trends. By repeating different stages of the analysis in chapter 4 using BGEP data, it would be possible to investigate trends of:

- sea ice geometry statistics;
- ice ocean drag coefficients, C_{io};

- ice-ocean stress, $\boldsymbol{\tau}_{io}$; and
- total ocean surface stress, $\boldsymbol{\tau}_{s}$.

Knowing whether trends of these quantities are increasing or decreasing would help understanding and predicting ongoing environmental change. Additionally, with a more complete data set of C_{io} derived from both ice geometry and the force-balance ice drift model (chapter 4), better optimization of the parameterization scheme could be performed.

Measurements from Ice Tethered Profilers (ITPs; `https://www2.whoi.edu/site/itp/`, and *Krishfield et al.*, 2008; *Toole et al.*, 2010) could also be used in the context of chapter 5 and the study by *Gimbert et al.* (2012a) to infer changes and trends in sea ice mechanical strength in the Beaufort Sea. While *Gimbert et al.* (2012a) applied their analysis to drifting buoy data to consider shifts in sea ice strength, they lacked details about the ocean ML depth (which then became one of their fitting parameters) and only made broad comparisons between short, discrete data sets. Analysis with ITP data could follow appendix 5.B, to generate timeseries of the damping parameter r_i. Then seasonal and inter-annual variations in r_i could be investigated. In contrast to the work done by *Gimbert et al.* (2012a), data from ITPs would have the advantage that the ML depth would generally be known, thereby reducing some uncertainty in the model.

Dynamical understanding

The controls on NIW generation under sea ice were not fully addressed in this work. While understanding ML inertial oscillations (chapter 5) provides a starting point for understanding this process (*Martini et al.*, 2014; *Kawaguchi et al.*, 2019), it appears that there are other factors involved as well. As NIW propagation is visible in the SODA mooring record (figs. 5.10q to 5.10t), these measurements may be useful for resolving and understanding generation processes. Timeseries of downward NIW kinetic energy flux (calculated following *Halle and Pinkel*, 2003) could be compared to measurements of sea ice drift and geometric properties, or to surface inertial kinetic energy input (Π_I^S; provided caution was taken to consider associated sensitivity to vertical shear and ML turbulence; section 5.5.2) to better ascertain controlling factors.

The case studies presented in appendix 5.A provided additional insight and context for understanding the upper ocean response to surface forcing. In this dissertation, these events were only briefly considered but they could be analysed in much greater depth. In particular, remote sensing measurements (especially SAR imagery, which is available at the mooring locations for the full deployment period) would potentially allow for better evaluation of both the coherence of sea ice motion, and sea ice deformation processes (i.e., lead opening). Cursory investigation of those data suggests that wintertime ice drift is coherent over a wide area ($\mathcal{O}(10\text{–}100\,\text{km})$), while in the MIZ sea ice motion was more spatially variable. Observed oceanic responses during these events could be linked to larger contexts (e.g., the SAR imagery described above, or regional weather systems), and to local conditions (e.g., sea ice geometric properties, such as keel sizes).

The SAR imagery and other remote sensing products might also be useful for expanding on the role of sea ice rheology in atmosphere-ice-ocean coupling. Remote sensing images can be used to construct spatial fields of sea ice motion in the vicinity of the moorings using correlation techniques between adjacent sets of images. While a variety of products exist based on these techniques, typically on daily-to-weekly temporal resolutions, the availability of multiple-source SAR imagery (from both Sentinel-1 and RadarSAT) at the mooring locations potentially allows for construction of those fields from images with short temporal offsets (hours). Such data could be used to quantify sea ice deformation fields and calculate internal stress at the mooring locations based on viscoplastic rheological laws. Similar techniques applied in the marginal ice zone may allow for quantification of under-ice eddy motions.

Differences in strength and character of sub-inertial ML motions between the SODA moorings (chapter 5) may relate to differences in the strength of surface mesoscale and submesoscale motions. This is consistent with theoretical considerations suggesting that ice-ocean friction damps out these motions (*Meneghello et al.*, 2020b; *Shrestha and Manucharyan*, 2021; *Manucharyan and Thompson*, 2022). It may be instructive to use the SODA mooring data to investigate if mesoscale motions are associated with increased surface dissipation in order to better quantify and verify this effect. As the moorings provide point measurements it is not necessarily straightforward to separate mesoscale/submesoscale velocities from other motions (e.g., wind-driven velocity), but as a first step the non-local components can be diagnosed as residual sub-inertial ML motions after subtracting modelled Ekman transport (using the slab model approach from chapter 5). Then, it would be possible to evaluate if these non-local velocities are associated with different patterns of bulk estimated surface turbulent kinetic energy production ($\int \mathcal{P} dz$) or negative ice-ocean work (Π^{io}_{ocn}) following section 5.5.2.

Modelling and parameterization

While chapter 4 has validated a portion of the existing parameterization scheme for ice-ocean drag (*Tsamados et al.*, 2014), it also highlights that the parameterization of sea ice geometry used in that scheme is lacking and leads to model-observation mismatches. Direct modelling schemes of both floe size distributions and ice keels are being developed and implemented in sea ice models (*Roach et al.*, 2018; *Roberts et al.*, 2019, respectively), but simpler empirical schemes (i.e., similar to those proposed by *Lüpkes et al.*, 2012) may still be useful. Ice concentration based models are used in the atmospheric community (e.g., *Andreas et al.*, 2010a, and others), but observed variability in C_{io} indicates that additional factors should also be considered. As a baseline, keel height parameterization might be based on the level sea ice draft (e.g., based on its square root, as in *Martin*, 2007). Any ongoing work in parameterizing the ice-ocean drag coefficient should also consider the impacts of non-neutral buoyancy.

Modelling could be used to better understand differences between drag coefficients determined from Reynold's stress estimates and from force-balance approaches, and the role of boundary layer heterogeneity in impacting the interpretation of observations. Using modelling frameworks similar to *Skyllingstad* (2003) or *Zu et al.* (2021), the impact of wake effects on floe-integrated stress and drag coefficients could be compared to simulated point measurements. Results could be used to develop statistical fits that might allow for a better "scaling up" of current observations.

7.4 *Final thoughts*

This dissertation set out to address two primary research questions (section 1.3.1), summarized briefly as: (1) how do sea ice properties impact ice-ocean momentum transfer? and, (2) how does the upper ocean respond to the net surface stress in ice covered regions? The results of the studies presented here show that the answers to these questions are linked to the ice itself. It is the internal stress within the sea ice that impacts its ability to transmit stress from the wind, and also changes how it reacts to stresses imparted by ocean currents – impacting the degree to which it may dissipate ML kinetic energy. As both the sea ice and the upper ocean move in response to these stresses, studying each independently effectively imposes constraints on the ice-ocean system that might not be representative of its true evolution. Above all else, this work highlights the importance of considering the ice-ocean system in a coupled framework when asking questions about momentum and energy transfer.

BIBLIOGRAPHY

Alford, M. H., Internal Swell Generation: The Spatial Distribution of Energy Flux from the Wind to Mixed Layer Near-Inertial Motions, *Journal of Physical Oceanography*, *31*(8), 2359–2368, doi:10.1175/1520-0485(2001)031<2359:ISGTSD>2.0.CO;2, 2001.

Alford, M. H., Improved global maps and 54-year history of wind-work on ocean inertial motions, *Geophysical Research Letters*, *30*(8), doi:10.1029/2002GL016614, 2003.

Alford, M. H., Revisiting Near-Inertial Wind Work: Slab Models, Relative Stress, and Mixed Layer Deepening, *J. Phys. Oceanogr.*, *50*(11), 3141–3156, doi:10.1175/JPO-D-20-0105.1, 2020.

Andreas, E. L., A relationship between the aerodynamic and physical roughness of winter sea ice, *Q.J.R. Meteorol. Soc.*, *137*(659), 1581–1588, doi:10.1002/qj.842, 2011.

Andreas, E. L., T. W. Horst, A. A. Grachev, P. O. G. Persson, C. W. Fairall, P. S. Guest, and R. E. Jordan, Parametrizing turbulent exchange over summer sea ice and the marginal ice zone, *Q.J.R. Meteorol. Soc.*, *136*(649), 927–943, doi:10.1002/qj.618, 2010a.

Andreas, E. L., P. O. G. Persson, A. A. Grachev, R. E. Jordan, T. W. Horst, P. S. Guest, and C. W. Fairall, Parameterizing Turbulent Exchange over Sea Ice in Winter, *J. Hydrometeor.*, *11*(1), 87–104, doi:10.1175/2009JHM1102.1, 2010b.

Ardyna, M., M. Babin, M. Gosselin, E. Devred, L. Rainville, and J.-É. Tremblay, Recent arctic ocean sea ice loss triggers novel fall phytoplankton blooms, *Geophys. Res. Lett.*, *41*(17), 6207–6212, doi:10.1002/2014GL061047, 2014.

Armitage, T. W. K., S. Bacon, A. L. Ridout, S. F. Thomas, Y. Aksenov, and D. J. Wingham, Arctic sea surface height variability and change from satellite radar altimetry and GRACE, 2003–2014, *Journal of Geophysical Research: Oceans*, *121*(6), 4303–4322, doi:10.1002/2015JC011579, 2016.

Armitage, T. W. K., S. Bacon, A. L. Ridout, A. A. Petty, S. Wolbach, and M. Tsamados, Arctic Ocean surface geostrophic circulation 2003-2014, *Cryosphere*, *11*(4), 1767–1780, doi:10.5194/tc-11-1767-2017, 2017.

Armitage, T. W. K., G. E. Manucharyan, A. A. Petty, R. Kwok, and A. F. Thompson, Enhanced eddy activity in the Beaufort Gyre in response to sea ice loss, *Nat. Commun.*, *11*(1), 761, doi:10.1038/s41467-020-14449-z, 2020.

Årthun, M., I. H. Onarheim, J. Dörr, and T. Eldevik, The Seasonal and Regional Transition to an Ice-Free Arctic, *Geophysical Research Letters*, *48*(1), e2020GL090,825, doi:10.1029/2020GL090825, 2021.

Arya, S. P. S., A drag partition theory for determining the large-scale roughness parameter and wind stress on the Arctic pack ice, *J. Geophys. Res.*, *80*(24), 3447–3454, doi:10.1029/JC080i024p03447, 1975.

Barton, B. I., Y.-D. Lenn, and C. Lique, Observed Atlantification of the Barents Sea Causes the Polar Front to Limit the Expansion of Winter Sea Ice, *Journal of Physical Oceanography*, *48*(8), 1849–1866, doi:10.1175/JPO-D-18-0003.1, 2018.

Belliveau, D. J., G. L. Bugden, and S. G. K. Melrose, Measurement of sea ice motion using bottom mounted Acoustic Doppler Current Profilers, *Sea Technology*, *30*, 1989.

Bendat, J. S., and A. G. Piersol, *Random Data: Analysis and Measurement Procedures*, Wiley-Interscience, New York, 1971.

Birnbaum, G., and C. Lüpkes, A new parameterization of surface drag in the marginal sea ice zone, *Tellus A: Dynamic Meteorology and Oceanography*, *54*(1), 107–123, doi:10.3402/tellusa.v54i1.12121, 2002.

Blackadar, A. K., and H. Tennekes, Asymptotic similarity in the neutral barotropic planetary boundary layer, *J. Atmos. Sci.*, *25*(6), 1015–1020, doi:10.1175/1520-0469(1968)025<1015:ASINBP>2.0.CO;2, 1968.

Bondevik, E., Studies of eddies in the marginal ice zone along the east Greenland current using spaceborne synthetic aperture radar (SAR), Ph.D. thesis, University of Bergen, 2011.

Brainerd, K. E., and M. C. Gregg, Surface mixed and mixing layer depths, *Deep Sea Research Part I: Oceanographic Research Papers*, *42*(9), 1521–1543, doi:10.1016/0967-0637(95)00068-H, 1995.

Breivik, L.-A., S. Eastwood, Ø. Godøy, H. Schyberg, S. Andersen, and R. Tonboe, Sea Ice Products for EUMETSAT Satellite Application Facility, *Canadian Journal of Remote Sensing*, *27*(5), 403–410, doi:10.1080/07038992.2001.10854883, 2001.

Brenner, S., L. Rainville, J. Thomson, and C. Lee, The evolution of a shallow front in the Arctic marginal ice zone, *Elem. Sci. Anth.*, *8*(17), 17, doi:10.1525/elementa.413, 2020.

Brenner, S., L. Rainville, J. Thomson, S. Cole, and C. Lee, Comparing observations and parameterizations of ice-ocean drag through an annual cycle across the Beaufort Sea, *Journal of Geophysical Research: Oceans*, *126*(4), 29, doi:10.1029/2020JC016977, 2021.

Brunette, C., L. B. Tremblay, and R. Newton, A new state-dependent parameterization for the free drift of sea ice, *The Cryosphere*, *16*(2), 533–557, doi:10.5194/tc-16-533-2022, 2022.

Buckley, J. R., T. Gammelsrød, J. A. Johannessen, O. M. Johannessen, and L. P. Røed, Upwelling: Oceanic structure at the edge of the arctic ice pack in winter, *Science, New Series*, *203*(4376), 165–167, 1979.

Capet, X., J. C. McWilliams, M. J. Molemaker, and A. F. Shchepetkin, Mesoscale to submesoscale transition in the California current system. Part II: Frontal processes, *J. Phys. Oceanogr.*, *38*(1), 44–64, doi:10.1175/2007JPO3672.1, 2008.

Carmack, E., et al., Toward quantifying the increasing role of oceanic heat in sea ice loss in the new Arctic, *Bull. Amer. Meteor. Soc.*, *96*(12), 2079–2105, doi:10.1175/BAMS-D-13-00177.1, 2015.

Carmack, E. C., The alpha/beta ocean distinction: A perspective on freshwater fluxes, convection, nutrients and productivity in high-latitude seas, *Deep Sea Research Part II: Topical Studies in Oceanography*, *54*(23), 2578–2598, doi:10.1016/j.dsr2.2007.08.018, 2007.

Carmack, E. C., et al., Freshwater and its role in the Arctic Marine System: Sources, disposition, storage, export, and physical and biogeochemical consequences in the Arctic and global oceans, *Journal of Geophysical Research: Biogeosciences*, *121*(3), 675–717, doi:10.1002/2015JG003140, 2016.

Castellani, G., C. Lüpkes, S. Hendricks, and R. Gerdes, Variability of Arctic sea-ice topography and its impact on the atmospheric surface drag, *J. Geophys. Res. Oceans*, *119*(10), 6743–6762, doi:10.1002/2013JC009712, 2014.

Castellani, G., R. Gerdes, M. Losch, and C. Lüpkes, Impact of Sea-Ice Bottom Topography on the Ekman Pumping, in *Towards an Interdisciplinary Approach in Earth System Science: Advances of a Helmholtz Graduate Research School*, edited by G. Lohmann, H. Meggers, V. Unnithan, D. Wolf-Gladrow, J. Notholt, and A. Bracher, Springer Earth System Sciences, pp. 139–148, Springer International Publishing, Cham, doi:10.1007/978-3-319-13865-7_16, 2015.

Castellani, G., M. Losch, M. Ungermann, and R. Gerdes, Sea-ice drag as a function of deformation and ice cover: Effects on simulated sea ice and ocean circulation in the Arctic, *Ocean Model.*, *128*, 48–66, doi:10.1016/j.ocemod.2018.06.002, 2018.

Castro, S. L., G. A. Wick, and M. Steele, Validation of satellite sea surface temperature analyses in the Beaufort Sea using UpTempO buoys, *Remote Sensing of Environment*, *187*, 458–475, doi:10.1016/j.rse.2016.10.035, 2016.

Charnock, H., Wind stress on a water surface, *Quarterly Journal of the Royal Meteorological Society*, *81*(350), 639–640, doi:10.1002/qj.49708135027, 1955.

Chaudhuri, A. H., R. M. Ponte, and A. T. Nguyen, A comparison of atmospheric reanalysis products for the Arctic Ocean and implications for uncertainties in air–sea fluxes, *J. Climate*, *27*(14), 5411–5421, doi:10.1175/JCLI-D-13-00424.1, 2014.

Chaudhuri, D., D. Sengupta, E. D'Asaro, and S. Shivaprasad, Trapping of Wind Momentum in a Salinity-Stratified Ocean, *Journal of Geophysical Research: Oceans*, *126*(12), e2021JC017,770, doi:10.1029/2021JC017770, 2021.

Claussen, M., Estimation of areally-averaged surface fluxes, *Boundary-Layer Meteorol*, *54*(4), 387–410, doi:10.1007/BF00118868, 1991.

Claussen, M., Flux aggregation at large scales: On the limits of validity of the concept of blending height, *Journal of Hydrology*, *166*(3), 371–382, doi:10.1016/0022-1694(94)05098-I, 1995.

Cole, S. T., and J. Stadler, Deepening of the Winter Mixed Layer in the Canada Basin, Arctic Ocean Over 2006–2017, *Journal of Geophysical Research: Oceans*, *124*(7), 4618–4630, doi:10.1029/2019JC014940, 2019.

Cole, S. T., M.-L. Timmermans, J. M. Toole, R. A. Krishfield, and F. T. Thwaites, Ekman Veering, Internal Waves, and Turbulence Observed under Arctic Sea Ice, *J. Phys. Oceanogr.*, *44*(5), 1306–1328, doi:10.1175/JPO-D-12-0191.1, 2014.

Cole, S. T., J. M. Toole, L. Rainville, and C. M. Lee, Internal waves in the Arctic: Influence of ice concentration, ice roughness, and surface layer stratification, *J. Geophys. Res. Oceans*, *123*(8), 5571–5586, doi:10.1029/2018JC014096, 2018.

Cole, S. T., et al., Ice and ocean velocity in the Arctic marginal ice zone: Ice roughness and momentum transfer, *Elem. Sci. Anth.*, *5*, 55, doi:10.1525/elementa.241, 2017.

Colony, R., and A. S. Thorndike, The Horizontal Coherency of the Motion of Summer Arctic Sea Ice, *Journal of Physical Oceanography*, *10*(8), 1281–1289, doi:10.1175/1520-0485(1980)010<1281:THCOTM>2.0.CO;2, 1980.

Connolley, W. M., J. M. Gregory, E. C. Hunke, and A. J. Mclaren, On the consistent scaling of terms in the sea-ice dynamics equation, *J. Phys. Oceanogr.*, *34*, 5, 2004.

Cooper, V., L. Roach, C. Bitz, S. Brenner, and J. Thomson, Towards Validating Wave-Ice Interactions in Climate Models Using In Situ Observations, doi:10.1002/essoar.10505914.2, 2021.

Cooper, V. T., L. A. Roach, J. Thomson, S. D. Brenner, M. M. Smith, M. H. Meylan, and C. M. Bitz, Wind waves in sea ice of the western Arctic and a global coupled wave-ice model, [Manuscript submitted for publication], 2022.

Crews, L., C. M. Lee, L. Rainville, and J. Thomson, Direct Observations of the Role of Lateral Advection of Sea Ice Meltwater in the Onset of Autumn Freeze Up, *Journal of Geophysical Research: Oceans*, *127*(2), e2021JC017,775, doi:10.1029/2021JC017775, 2022.

D'Asaro, E. A., The energy flux from the wind to near-inertial motions in the surface mixed layer, *J. Phys. Oceanogr.*, *15*(8), 1043–1059, doi:10.1175/1520-0485(1985)015<1043:TEFFTW>2.0.CO;2, 1985.

D'Asaro, E. A., and M. D. Morehead, Internal waves and velocity fine structure in the Arctic Ocean, *Journal of Geophysical Research: Oceans*, *96*(C7), 12,725–12,738, doi:10.1029/91JC01071, 1991.

D'Asaro, E. A., and J. H. Morison, Internal waves and mixing in the Arctic Ocean, *Deep Sea Research Part A. Oceanographic Research Papers*, *39*(2, Part 1), S459–S484, doi:10.1016/S0198-0149(06)80016-6, 1992.

Davis, N. R., and P. Wadhams, A statistical analysis of Arctic pressure ridge morphology, *J. Geophys. Res.*, *100*(C6), 10,915, doi:10.1029/95JC00007, 1995.

Davis, P. E. D., C. Lique, H. L. Johnson, and J. D. Guthrie, Competing effects of elevated vertical mixing and increased freshwater input on the stratification and sea ice cover in a changing Arctic Ocean, *J. Phys. Oceanogr.*, *46*(5), 1531–1553, doi:10.1175/JPO-D-15-0174.1, 2016.

Dee, D. P., et al., The ERA-Interim reanalysis: Configuration and performance of the data assimilation system, *Quarterly Journal of the Royal Meteorological Society*, *137*(656), 553–597, doi:10.1002/qj.828, 2011.

Deines, K., Backscatter estimation using Broadband acoustic Doppler current profilers, in *Proceedings of the IEEE Sixth Working Conference on Current Measurement (Cat. No.99CH36331)*, pp. 249–253, doi:10.1109/CCM.1999.755249, 1999.

Dewey, S., Evolving ice-ocean dynamics of the western Arctic, Ph.D. thesis, University of Washington, 2019.

Dewey, S., J. Morison, R. Kwok, S. Dickinson, D. Morison, and R. Andersen, Arctic ice-ocean coupling and gyre equilibration observed with remote sensing, *Geophys. Res. Lett.*, *45*(3), 1499–1508, doi:10.1002/2017GL076229, 2018.

Dewey, S. R., J. H. Morison, and J. Zhang, An edge-referenced surface fresh layer in the Beaufort Sea seasonal ice zone, *J. Phys. Oceanogr.*, *47*(5), 1125–1144, doi:10.1175/JPO-D-16-0158.1, 2017.

Dmitrenko, I. A., et al., Sea-ice and water dynamics and moonlight impact the acoustic backscatter diurnal signal over the eastern Beaufort Sea continental slope, *Ocean Sci.*, *16*(5), 1261–1283, doi:10.5194/os-16-1261-2020, 2020.

Dmitrenko, I. A., et al., Coastal polynya disrupts the acoustic backscatter diurnal signal over the eastern Laptev Sea shelf, *Frontiers in Marine Science*, *8*, 1935, doi:10.3389/fmars.2021.791096, 2021.

Doddridge, E. W., G. Meneghello, J. Marshall, J. Scott, and C. Lique, A Three-Way Balance in the Beaufort Gyre: The Ice-Ocean Governor, Wind Stress, and Eddy Diffusivity, *J. Geophys. Res. Oceans*, *124*(5), 3107–3124, doi:10.1029/2018JC014897, 2019.

Donlon, C. J., M. Martin, J. Stark, J. Roberts-Jones, E. Fiedler, and W. Wimmer, The Operational Sea Surface Temperature and Sea Ice Analysis (OSTIA) system, *Remote Sensing of Environment*, *116*, 140–158, doi:10.1016/j.rse.2010.10.017, 2012.

Dosser, H. V., and L. Rainville, Dynamics of the Changing Near-Inertial Internal Wave Field in the Arctic Ocean, *J. Phys. Oceanogr.*, *46*(2), 395–415, doi:10.1175/JPO-D-15-0056.1, 2016.

Dosser, H. V., L. Rainville, and J. M. Toole, Near-Inertial Internal Wave Field in the Canada Basin from Ice-Tethered Profilers, *J. Phys. Oceanogr.*, *44*(2), 413–426, doi:10.1175/JPO-D-13-0117.1, 2014.

Dosser, H. V., M. Chanona, S. Waterman, N. C. Shibley, and M.-L. Timmermans, Changes in Internal Wave-Driven Mixing Across the Arctic Ocean: Finescale Estimates From an 18-Year Pan-Arctic Record, *Geophysical Research Letters*, *48*(8), e2020GL091,747, doi:10.1029/2020GL091747, 2021.

ECMWF, Part IV: Physical Processes, in *IFS Documentation CY46R1*, IFS Documentation, ECMWF, 2019a.

ECMWF, Part II: Data Assimilation, in *IFS Documentation CY46R1*, IFS Documentation, ECMWF, 2019b.

Edson, J. B., et al., On the Exchange of Momentum over the Open Ocean, *J. Phys. Oceanogr.*, *43*(8), 1589–1610, doi:10.1175/JPO-D-12-0173.1, 2013.

Ekman, V. W., On the influence of the earth's rotation on ocean-currents., *Arkiv Mat. Astr., Fys.*, *2*(11), 52, 1905.

Ekman, V. W., Beiträge zur theorie der meeresströmungen, *Ann. Hydrogr.*, *34*, 1906.

Ekman, V. W., Eddy-viscosity and skin friction in the dynamics of winds and ocean currents, *Mem. R. met. Soc.*, *2*(20), 161–172, 1928.

Elvidge, A. D., I. A. Renfrew, A. I. Weiss, I. M. Brooks, T. A. Lachlan-Cope, and J. C. King, Observations of surface momentum exchange over the marginal ice zone and recommendations for its parametrisation, *Atmos. Chem. Phys.*, *16*(3), 1545–1563, doi:10.5194/acp-16-1545-2016, 2016.

Fairall, C. W., E. F. Bradley, J. E. Hare, A. A. Grachev, and J. B. Edson, Bulk Parameterization of Air–Sea Fluxes: Updates and Verification for the COARE Algorithm, *J. Climate*, *16*(4), 571–591, doi:10.1175/1520-0442(2003)016<0571:BPOASF>2.0.CO;2, 2003.

Feltham, D. L., Sea Ice Rheology, *Annu. Rev. Fluid Mech.*, *40*(1), 91–112, doi:10.1146/annurev.fluid.40.111406.102151, 2008.

Fennel, W., and O. M. Johannessen, Wind forced oceanic responses near ice edges revisited, *Journal of Marine Systems*, *14*(1-2), 57–79, doi:10.1016/S0924-7963(97)00018-3, 1998.

Fer, I., Weak Vertical Diffusion Allows Maintenance of Cold Halocline in the Central Arctic, *Atmospheric and Oceanic Science Letters*, *2*(3), 148–152, doi:10.1080/16742834.2009.11446789, 2009.

Fer, I., Near-Inertial Mixing in the Central Arctic Ocean, *Journal of Physical Oceanography*, *44*(8), 2031–2049, doi:10.1175/JPO-D-13-0133.1, 2014.

Fer, I., and A. Sundfjord, Observations of upper ocean boundary layer dynamics in the marginal ice zone, *Journal of Geophysical Research: Oceans*, *112*(C4), doi:10.1029/2005JC003428, 2007.

Fer, I., M. G. McPhee, and A. Sirevaag, Conditional statistics of the Reynolds stress in the under-ice boundary layer, *Geophysical Research Letters*, *31*(15), doi:10.1029/2004GL020475, 2004.

Fetterer, F., K. Knowle, W. Meier, M. Savoie, and A. Windnagel, Sea Ice Index, Version 3, doi:10.7265/N5K072F8, [accessed May 26, 2022], 2017.

Fine, E. C., and S. T. Cole, Decadal Observations of Internal Wave Energy, Shear, and Mixing in the Western Arctic Ocean, *Journal of Geophysical Research: Oceans*, *127*(5), e2021JC018,056, doi:10.1029/2021JC018056, 2022.

Fine, E. C., M. H. Alford, J. A. MacKinnon, and J. B. Mickett, Microstructure Mixing Observations and Finescale Parameterizations in the Beaufort Sea, *Journal of Physical Oceanography*, *51*(1), 19–35, doi:10.1175/JPO-D-19-0233.1, 2020.

Fox-Kemper, B., R. Ferrari, and R. Hallberg, Parameterization of mixed layer eddies. Part I: Theory and diagnosis, *J. Phys. Oceanogr.*, *38*(6), 1145–1165, doi:10.1175/2007JPO3792.1, 2008.

Fox-Kemper, B., G. Danabasoglu, R. Ferrari, S. Griffies, R. Hallberg, M. Holland, M. Maltrud, S. Peacock, and B. Samuels, Parameterization of mixed layer eddies. III: Implementation and impact in global ocean climate simulations, *Ocean Modelling*, *39*(1-2), 61–78, doi:10.1016/j.ocemod.2010.09.002, 2011.

Francois, R. E., and G. R. Garrison, Sound absorption based on ocean measurements. Part II: Boric acid contribution and equation for total absorption, *The Journal of the Acoustical Society of America*, *72*(6), 1879–1890, doi:10.1121/1.388673, 1982.

Gallaher, S. G., The importance of capturing late melt season sea ice conditions for modeling the western Arctic ocean boundary layer, *Elementa: Science of the Anthropocene*, *7*(53), doi:10.1525/elementa.391, 2019.

Gallaher, S. G., T. P. Stanton, W. J. Shaw, S. T. Cole, J. M. Toole, J. P. Wilkinson, T. Maksym, and B. Hwang, Evolution of a Canada Basin ice-ocean boundary layer and mixed layer across a developing thermodynamically forced marginal ice zone: IOBL-OML Evolution of Thermodynamic MIZ, *J. Geophys. Res. Oceans*, *121*(8), 6223–6250, doi:10.1002/2016JC011778, 2016.

Garbrecht, T., C. Lüpkes, J. Hartmann, and M. Wolff, Atmospheric drag coefficients over sea ice–validation of a parameterisation concept, *Tellus A*, *54*(2), 205–219, doi:10.3402/tellusa.v54i2.12129, 2002.

Geiger, C. A., and D. K. Perovich, Springtime ice motion in the western Antarctic Peninsula region, *Deep Sea Research Part II: Topical Studies in Oceanography*, *55*(3), 338–350, doi:10.1016/j.dsr2.2007.11.008, 2008.

Gelaro, R., et al., The modern-era retrospective analysis for research and applications, version 2 (MERRA-2), *J. Climate*, *30*(14), 5419–5454, doi:10.1175/JCLI-D-16-0758.1, 2017.

Gemmrich, J. R., T. D. Mudge, and V. D. Polonichko, On the Energy Input from Wind to Surface Waves, *Journal of Physical Oceanography*, *24*(11), 2413–2417, doi:10.1175/1520-0485(1994)024<2413:OTEIFW>2.0.CO;2, 1994.

Giles, K. A., S. W. Laxon, A. L. Ridout, D. J. Wingham, and S. Bacon, Western Arctic Ocean freshwater storage increased by wind-driven spin-up of the Beaufort Gyre, *Nature Geoscience*, *5*(3), 194–197, doi:10.1038/ngeo1379, 2012.

Gimbert, F., N. C. Jourdain, D. Marsan, J. Weiss, and B. Barnier, Recent mechanical weakening of the Arctic sea ice cover as revealed from larger inertial oscillations, *Journal of Geophysical Research: Oceans*, *117*(C11), doi:10.1029/2011JC007633, 2012a.

Gimbert, F., D. Marsan, J. Weiss, N. C. Jourdain, and B. Barnier, Sea ice inertial oscillations in the Arctic Basin, *The Cryosphere*, *6*(5), 1187–1201, doi:10.5194/tc-6-1187-2012, 2012b.

Global Modeling and Assimilation Office (GMAO), GES DISC Dataset: MERRA-2 tavg1_2d_rad_Nx: 2d,1-Hourly,Time-Averaged,Single-Level,Assimilation,Radiation Diagnostics V5.12.4 (M2T1NXRAD 5.12.4), https://disc.gsfc.nasa.gov/datasets/M2T1NXRAD_5.12.4/summary, 2015.

Gordon, L., Signature 55 Long Range Current Profiler Data from a Short Deployment, *Technical Note*, Doppler Ltd., 2015.

Goring, D. G., and V. I. Nikora, Despiking Acoustic Doppler Velocimeter Data, *Journal of Hydraulic Engineering*, *128*(1), 117–126, doi:10.1061/(ASCE)0733-9429(2002)128:1(117), 2002.

Gostiaux, L., and H. van Haren, Extracting meaningful information from uncalibrated backscattered echo intensity data, *J. Atmos. Oceanic Technol.*, *27*(5), 943–949, doi:10.1175/2009JTECHO704.1, 2010.

Grachev, A. A., E. L. Andreas, C. W. Fairall, P. S. Guest, and P. O. G. Persson, SHEBA flux–profile relationships in the stable atmospheric boundary layer, *Boundary-Layer Meteorol*, *124*(3), 315–333, doi:10.1007/s10546-007-9177-6, 2007.

Graham, R. M., L. Cohen, N. Ritzhaupt, B. Segger, R. G. Graversen, A. Rinke, V. P. Walden, M. A. Granskog, and S. R. Hudson, Evaluation of Six Atmospheric Reanalyses over Arctic Sea Ice from Winter to Early Summer, *J. Climate*, *32*(14), 4121–4143, doi:10.1175/JCLI-D-18-0643.1, 2019a.

Graham, R. M., et al., Winter storms accelerate the demise of sea ice in the Atlantic sector of the Arctic Ocean, *Scientific Reports*, *9*(1), 9222, doi:10.1038/s41598-019-45574-5, 2019b.

Grønas, S., and P. Skeie, A case study of strong winds at an Arctic front, *Tellus A*, *51*(5), 15, 1999.

Guest, P., P. O. G. Persson, S. Wang, M. Jordan, Y. Jin, B. Blomquist, and C. Fairall, Low-level baroclinic jets over the new Arctic Ocean, *J. Geophys. Res. Oceans*, *123*(6), 4074–4091, doi:10.1002/2018JC013778, 2018.

Guest, P. S., and K. L. Davidson, The effect of observed ice conditions on the drag coefficient in the summer East Greenland Sea Marginal Ice Zone, *J. Geophys. Res.*, *92*(C7), 6943, doi:10.1029/JC092iC07p06943, 1987.

Guest, P. S., J. W. Glendening, and K. L. Davidson, An observational and numerical study of wind stress variations within marginal ice zones, *J. Geophys. Res.*, *100*(C6), 10,887, doi:10.1029/94JC03391, 1995.

Guthrie, J. D., and J. H. Morison, Not Just Sea Ice: Other Factors Important to Near-inertial Wave Generation in the Arctic Ocean, *Geophysical Research Letters*, *48*(3), e2020GL090,508, doi:10.1029/2020GL090508, 2021.

Guthrie, J. D., J. H. Morison, and I. Fer, Revisiting internal waves and mixing in the Arctic Ocean, *Journal of Geophysical Research: Oceans*, *118*(8), 3966–3977, doi:10.1002/jgrc.20294, 2013.

Häkkinen, S., Coupled ice-ocean dynamics in the marginal ice zones: Upwelling/downwelling and eddy generation, *J. Geophys. Res.*, *91*(C1), 819, doi:10.1029/JC091iC01p00819, 1986.

Halle, C., and R. Pinkel, Internal wave variability in the Beaufort Sea during the winter of 1993/1994, *Journal of Geophysical Research: Oceans*, *108*(C7), doi:10.1029/2000JC000703, 2003.

Harding, S., L. Kilcher, and J. Thomson, Turbulence Measurements from Compliant Moorings. Part I: Motion Characterization, *J. Atmos. Oceanic Technol.*, *34*(6), 1235–1247, doi:10.1175/JTECH-D-16-0189.1, 2017.

Heorton, H. D. B. S., D. L. Feltham, and J. C. R. Hunt, The response of the sea ice edge to atmospheric and oceanic jet formation, *J. Phys. Oceanogr.*, *44*(9), 2292–2316, doi:10.1175/JPO-D-13-0184.1, 2014.

Heorton, H. D. B. S., M. Tsamados, S. T. Cole, A. M. G. Ferreira, A. Berbellini, M. Fox, and T. W. K. Armitage, Retrieving sea ice drag coefficients and turning angles from in situ and satellite observations using an inverse modeling framework, *J. Geophys. Res. Oceans*, *124*(8), 6388–6413, doi:10.1029/2018JC014881, 2019.

Hersbach, H., et al., The ERA5 global reanalysis, *Q.J.R. Meteorol. Soc.*, *146*(730), 1999–2049, doi:10.1002/qj.3803, 2020.

Hibler, W. D., A Dynamic Thermodynamic Sea Ice Model, *Journal of Physical Oceanography*, *9*(4), 815–846, doi:10.1175/1520-0485(1979)009<0815:ADTSIM>2.0.CO;2, 1979.

Hibler, W. D., W. F. Weeks, and S. J. Mock, Statistical aspects of sea-ice ridge distributions, *J. Geophys. Res.*, *77*(30), 5954–5970, doi:10.1029/JC077i030p05954, 1972.

Holbrook, W. S., and I. Fer, Ocean internal wave spectra inferred from seismic reflection transects, *Geophysical Research Letters*, *32*(15), doi:10.1029/2005GL023733, 2005.

Holton, J. R., *An Introduction to Dynamic Meteorology*, no. v. 88 in International Geophysics Series, 4th ed ed., Elsevier Academic Press, Burlington, MA, 2004.

Hordoir, R., et al., Changes in Arctic Stratification and Mixed Layer Depth Cycle: A Modeling Analysis, *Journal of Geophysical Research: Oceans*, *n/a*(n/a), e2021JC017,270, doi:10.1029/2021JC017270, 2022.

Horvat, C., Marginal ice zone fraction benchmarks sea ice and climate model skill, *Nature Communications*, *12*(1), 2221, doi:10.1038/s41467-021-22004-7, 2021.

Horvat, C., and E. Tziperman, The evolution of scaling laws in the sea ice floe size distribution, *J. Geophys. Res. Oceans*, *122*(9), 7630–7650, doi:10.1002/2016JC012573, 2017.

Horvat, C., E. Tziperman, and J.-M. Campin, Interaction of sea ice floe size, ocean eddies, and sea ice melting, *Geophys. Res. Lett.*, *43*(15), 8083–8090, doi:10.1002/2016GL069742, 2016.

Hoskins, B. J., The mathematical theory of frontogenesis, *Annu. Rev. Fluid Mech.*, *14*(1), 131–151, doi:10.1146/annurev.fl.14.010182.001023, 1982.

Huber, P. J., *Robust Statistics*, John Wiley & Sons, 1981.

Hunke, E. C., Thickness sensitivities in the CICE sea ice model, *Ocean Model.*, *34*(3), 137–149, doi:10.1016/j.ocemod.2010.05.004, 2010.

Hunke, E. C., and J. K. Dukowicz, The sea ice momentum equation in the free drift regime, *Tech. Rep. LA-UR-03-2219*, Los Alamos National Laboratory, Los Alamos, New Mexico, US, 2003.

Hunke, E. C., et al., CICE-Consortium/CICE: CICE Version 6.1.2, Zenodo, doi:10.5281/zenodo.3888653, 2020.

Hunkins, K., Ekman drift currents in the Arctic Ocean, *Deep-Sea Res. Oceanogr. Abstr.*, *13*(4), 607–620, doi:10.1016/0011-7471(66)90592-4, 1966.

Hutchings, J. K., and I. G. Rigor, Role of ice dynamics in anomalous ice conditions in the Beaufort Sea during 2006 and 2007, *J. Geophys. Res. Oceans*, *117*(C8), doi:10.1029/2011JC007182, 2012.

Inoue, J., and M. E. Hori, Arctic cyclogenesis at the marginal ice zone: A contributory mechanism for the temperature amplification, *Geophys. Res. Lett.*, *38*(12), n/a–n/a, doi:10.1029/2011GL047696, 2011.

IOC, SCOR, and IAPSO, The international thermodynamic equation of seawater – 2010: Calculation and use of thermodynamic properties, *Tech. Rep. Intergovernmental Oceanographic Commission, Manuals and Guides No. 56*, UNESCO, 2010.

IPCC, Summary for Policymakers, in *IPCC Special Report on the Ocean and Cryosphere in a Changing Climate*, 2019.

Ivanov, V., V. Alexeev, N. V. Koldunov, I. Repina, A. B. Sandø, L. H. Smedsrud, and A. Smirnov, Arctic Ocean Heat Impact on Regional Ice Decay: A Suggested Positive Feedback, *J. Phys. Oceanogr.*, *46*(5), 1437–1456, doi:10.1175/JPO-D-15-0144.1, 2016.

Jackson, J. M., S. E. Allen, F. A. McLaughlin, R. A. Woodgate, and E. C. Carmack, Changes to the near-surface waters in the Canada Basin, Arctic Ocean from 1993–2009: A basin in transition, *J. Geophys. Res. Oceans*, *116*(C10), doi:10.1029/2011JC007069, 2011.

Jackson, J. M., W. J. Williams, and E. C. Carmack, Winter sea-ice melt in the Canada Basin, Arctic Ocean, *Geophysical Research Letters*, *39*(3), doi:10.1029/2011GL050219, 2012.

Johannessen, J. A., et al., Mesoscale eddies in the Fram Strait marginal ice zone during the 1983 and 1984 Marginal Ice Zone Experiments, *J. Geophys. Res.*, *92*(C7), 6754, doi:10.1029/JC092iC07p06754, 1987.

Johannessen, O. M., Note on some vertical profiles below ice floes in the Gulf of St. Lawrence and near the North Pole, *J. Geophys. Res.*, *75*(15), 2857–2861, doi:10.1029/JC075i015p02857, 1970.

Johannessen, O. M., J. A. Johannessen, J. Morison, B. A. Farrelly, and E. A. S. Svendsen, Oceanographic conditions in the marginal ice zone north of Svalbard in early fall 1979 with an emphasis on mesoscale processes, *J. Geophys. Res.*, *88*(C5), 2755, doi:10.1029/JC088iC05p02755, 1983.

Johnston, S., D. Chaudhuri, M. Mathur, D. Rudnick, D. Sengupta, H. Simmons, A. Tandon, and R. Venkatesan, Decay Mechanisms of Near-Inertial Mixed Layer Oscillations in the Bay of Bengal, *Oceanog*, *29*(2), 180–191, doi:10.5670/oceanog.2016.50, 2016.

Jutras, M., Energy transfers in the ice and surface Arctic Ocean at near inertial frequencies, Ph.D. thesis, McGill University, 2016.

Kanamitsu, M., W. Ebisuzaki, J. Woollen, S.-K. Yang, J. J. Hnilo, M. Fiorino, and G. L. Potter, NCEP–DOE AMIP-II Reanalysis (R-2), *Bulletin of the American Meteorological Society*, *83*(11), 1631–1644, doi:10.1175/BAMS-83-11-1631, 2002.

Kawaguchi, Y., M. Itoh, Y. Fukamachi, E. Moriya, J. Onodera, T. Kikuchi, and N. Harada, Year-round observations of sea-ice drift and near-inertial internal waves in the Northwind Abyssal Plain, Arctic Ocean, *Polar Science*, *21*, 212–223, doi:10.1016/j.polar.2019.01.004, 2019.

Kim, J. G., E. C. Hunke, and W. H. Lipscomb, Sensitivity analysis and parameter tuning scheme for global sea-ice modeling, *Ocean Model.*, *14*(1), 61–80, doi:10.1016/j.ocemod.2006.03.003, 2006.

Kim, T. W., H. K. Ha, A. K. Wåhlin, S. H. Lee, C. S. Kim, J. H. Lee, and Y. K. Cho, Is Ekman pumping responsible for the seasonal variation of warm circumpolar deep water in the Amundsen Sea?, *Cont. Shelf Res.*, *132*, 38–48, doi:10.1016/j.csr.2016.09.005, 2017.

Kirillov, S., D. Babb, I. Dmitrenko, J. Landy, J. Lukovich, J. Ehn, K. Sydor, D. Barber, and J. Stroeve, Atmospheric forcing drives the winter sea ice thickness asymmetry of Hudson Bay, *J. Geophys. Res. Oceans*, *125*(2), doi:10.1029/2019JC015756, 2020.

Kobayashi, S., et al., The JRA-55 Reanalysis: General Specifications and Basic Characteristics, *Journal of the Meteorological Society of Japan. Ser. II*, *93*(1), 5–48, doi:10.2151/jmsj.2015-001, 2015.

Köberle, C., and R. Gerdes, Mechanisms Determining the Variability of Arctic Sea Ice Conditions and Export, *J. Climate*, *16*(17), 2843–2858, doi:10.1175/1520-0442(2003)016<2843:MDTVOA>2.0.CO;2, 2003.

Kozlov, I. E., A. V. Artamonova, G. E. Manucharyan, and A. A. Kubryakov, Eddies in the western Arctic Ocean from spaceborne SAR observations over open ocean and marginal ice zones, *J. Geophys. Res. Oceans*, *124*(9), 6601–6616, doi:10.1029/2019JC015113, 2019.

Krishfield, R., J. Toole, A. Proshutinsky, and M.-L. Timmermans, Automated Ice-Tethered Profilers for Seawater Observations under Pack Ice in All Seasons, *Journal of Atmospheric and Oceanic Technology*, *25*(11), 2091–2105, doi:10.1175/2008JTECHO587.1, 2008.

Krishfield, R. A., A. Proshutinsky, K. Tateyama, W. J. Williams, E. C. Carmack, F. A. McLaughlin, and M.-L. Timmermans, Deterioration of perennial sea ice in the Beaufort Gyre from 2003 to 2012 and its impact on the oceanic freshwater cycle, *J. Geophys. Res. Oceans*, *119*(2), 1271–1305, doi:10.1002/2013JC008999, 2014.

Kwok, R., Arctic sea ice thickness, volume, and multiyear ice coverage: Losses and coupled variability (1958–2018), *Environ. Res. Lett.*, *13*(10), 105,005, doi:10.1088/1748-9326/aae3ec, 2018.

Kwok, R., G. Spreen, and S. Pang, Arctic sea ice circulation and drift speed: Decadal trends and ocean currents, *J. Geophys. Res. Oceans*, *118*(5), 2408–2425, doi:10.1002/jgrc.20191, 2013.

Large, W. G., and S. Pond, Open Ocean Momentum Flux Measurements in Moderate to Strong Winds, *Journal of Physical Oceanography*, *11*(3), 324–336, doi:10.1175/1520-0485(1981)011<0324:OOMFMI>2.0.CO;2, 1981.

Large, W. G., and S. G. Yeager, Diurnal to decadal global forcing for ocean and sea-ice models: The data sets and flux climatologies, *Technical Note NCAR/TN-460+STR*, National Center for Atmospheric Research, Boulder Colorado, 2004.

Leaman, K. D., and T. B. Sanford, Vertical energy propagation of inertial waves: A vector spectral analysis of velocity profiles, *Journal of Geophysical Research (1896-1977)*, *80*(15), 1975–1978, doi:10.1029/JC080i015p01975, 1975.

Lee, C., J. Thomson, T. M. I. Z. Team, and T. A. S. S. Team, An Autonomous Approach to Observing the Seasonal Ice Zone in the Western Arctic, *Oceanog.*, *30*(2), 56–68, doi:10.5670/oceanog.2017.222, 2017.

Lee, C., et al., Marginal Ice Zone (MIZ) Program: Science and Experiment Plan, *Technical Report APL-UW 1201*, Applied Physics Laboratory, University of Washington, Seattle, Washington, 2012.

Lee, C. M., and C. C. Eriksen, The Subinertial Momentum Balance of the North Atlantic Subtropical Convergence Zone, *Journal of Physical Oceanography*, *26*(9), 1690–1704, doi:10.1175/1520-0485(1996)026<1690:TSMBOT>2.0.CO;2, 1996.

Lee, C. M., et al., Stratified Ocean Dynamics of the Arctic: Science and Experiment Plan, *Technical Report APL-UW-1601*, Applied Physics Laboratory, University of Washington, Seattle, Washington, 2016.

Lemke, P., and T. O. Manley, The seasonal variation of the mixed layer and the pycnocline under polar sea ice, *Journal of Geophysical Research: Oceans*, *89*(C4), 6494–6504, doi:10.1029/JC089iC04p06494, 1984.

Lenn, Y.-D., T. P. Rippeth, C. P. Old, S. Bacon, I. Polyakov, V. Ivanov, and J. Hölemann, Intermittent Intense Turbulent Mixing under Ice in the Laptev Sea Continental Shelf, *J. Phys. Oceanogr.*, *41*(3), 531–547, doi:10.1175/2010JPO4425.1, 2011.

Leppäranta, M., *The Drift of Sea Ice*, Springer Praxis Books, Springer, Berlin, Heidelberg, doi:10.1007/978-3-642-04683-4_2, 2011.

Lepparanta, M., and A. Omstedt, Dynamic coupling of sea ice and water for an ice field with free boundaries, *Tellus A*, *42*(4), 482–495, doi:10.1034/j.1600-0870.1990.t01-2-00007.x, 1990.

Leppäranta, M., A. Oikkonen, K. Shirasawa, and Y. Fukamachi, A treatise on frequency spectrum of drift ice velocity, *Cold Regions Science and Technology*, *76–77*, 83–91, doi:10.1016/j.coldregions.2011.12.005, 2012.

Levine, M. D., C. A. Paulson, and J. H. Morison, Internal Waves in the Arctic Ocean: Comparison with Lower-Latitude Observations, *Journal of Physical Oceanography*, *15*(6), 800–809, doi:10.1175/1520-0485(1985)015<0800:IWITAO>2.0.CO;2, 1985.

Levine, M. D., C. A. Paulson, and J. H. Morison, Observations of internal gravity waves under the Arctic pack ice, *Journal of Geophysical Research: Oceans*, *92*(C1), 779–782, doi:10.1029/JC092iC01p00779, 1987.

Lin, P., R. S. Pickart, G. W. K. Moore, M. A. Spall, and J. Hu, Characteristics and dynamics of wind-driven upwelling in the Alaskan Beaufort Sea based on six years of mooring data, *Deep Sea Research Part II: Topical Studies in Oceanography*, *162*, 79–92, doi:10.1016/j.dsr2.2018.01.002, 2019.

Lindsay, R., M. Wensnahan, A. Schweiger, and J. Zhang, Evaluation of seven different atmospheric reanalysis products in the Arctic, *J. Climate*, *27*(7), 2588–2606, doi:10.1175/JCLI-D-13-00014.1, 2014.

Liu, Q., A. V. Babanin, S. Zieger, I. R. Young, and C. Guan, Wind and wave climate in the Arctic Ocean as observed by altimeters, *J. Climate*, *29*(22), 7957–7975, doi:10.1175/JCLI-D-16-0219.1, 2016.

Liu, Z., and A. Schweiger, Low-level and surface wind jets near sea ice edge in the Beaufort Sea in late autumn, *J. Geophys. Res. Atmos.*, p. 2018JD029770, doi:10.1029/2018JD029770, 2019.

Losch, M., D. Menemenlis, J.-M. Campin, P. Heimbach, and C. Hill, On the formulation of sea-ice models. Part 1: Effects of different solver implementations and parameterizations, *Ocean Model.*, *33*(1-2), 129–144, doi:10.1016/j.ocemod.2009.12.008, 2010.

Lu, K., T. Weingartner, S. Danielson, P. Winsor, E. Dobbins, K. Martini, and H. Statscewich, Lateral mixing across ice meltwater fronts of the Chukchi Sea shelf, *Geophys. Res. Lett.*, *42*(16), 6754–6761, doi:10.1002/2015GL064967, 2015.

Lu, P., Z. Li, B. Cheng, and M. Leppäranta, A parameterization of the ice-ocean drag coefficient, *J. Geophys. Res.*, *116*(C7), C07,019, doi:10.1029/2010JC006878, 2011.

Lund, B., H. C. Graber, P. O. G. Persson, M. Smith, M. Doble, J. Thomson, and P. Wadhams, Arctic sea ice drift measured by shipboard marine radar, *J. Geophys. Res. Oceans*, *123*(6), 4298–4321, doi:10.1029/2018JC013769, 2018.

Lüpkes, C., and G. Birnbaum, Surface drag in the Arctic marginal sea-ice zone: A comparison of different parameterisation concepts, *Bound.-Lay. Meteorol.*, *117*(2), 179–211, doi:10.1007/s10546-005-1445-8, 2005.

Lüpkes, C., and V. M. Gryanik, A stability-dependent parametrization of transfer coefficients for momentum and heat over polar sea ice to be used in climate models, *J. Geophys. Res. Atmos.*, *120*(2), 552–581, doi:10.1002/2014JD022418, 2015.

Lüpkes, C., V. M. Gryanik, J. Hartmann, and E. L. Andreas, A parametrization, based on sea ice morphology, of the neutral atmospheric drag coefficients for weather prediction and climate models, *J. Geophys. Res. Atmos.*, *117*(D13), n/a–n/a, doi:10.1029/2012JD017630, 2012.

Lüpkes, C., V. M. Gryanik, A. Rösel, G. Birnbaum, and L. Kaleschke, Effect of sea ice morphology during Arctic summer on atmospheric drag coefficients used in climate models, *Geophys. Res. Lett.*, *40*(2), 446–451, doi:10.1002/grl.50081, 2013.

Macrander, A., R. H. Käse, U. Send, H. Valdimarsson, and S. Jónsson, Spatial and temporal structure of the Denmark Strait Overflow revealed by acoustic observations, *Ocean Dynamics*, *57*(2), 75–89, doi:10.1007/s10236-007-0101-x, 2007.

Madsen, O. S., and M. S. Bruno, A Methodology for the Determination of Drag Coefficients for Ice Floes, *Journal of Offshore Mechanics and Arctic Engineering*, *109*(4), 381–387, doi:10.1115/1.3257035, 1987.

Maeda, K., N. Kimura, and H. Yamaguchi, Temporal and spatial change in the relationship between sea-ice motion and wind in the Arctic, *Polar Research*, doi:10.33265/polar.v39.3370, 2020.

Magnell, B., L. Ivanov, and E. Siegel, Measurements of ice parameters in the Beaufort Sea using the Nortek AWAC acoustic Doppler current profiler, in *OCEANS 2010 MTS/IEEE SEATTLE*, pp. 1–8, doi:10.1109/OCEANS.2010.5664016, 2010.

Mahadevan, A., A. Tandon, and R. Ferrari, Rapid changes in mixed layer stratification driven by submesoscale instabilities and winds, *J. Geophys. Res.*, *115*(C3), C03,017, doi:10.1029/2008JC005203, 2010.

Mahadevan, A., E. D'Asaro, C. Lee, and M. J. Perry, Eddy-driven stratification initiates North Atlantic spring phytoplankton blooms, *Science*, *337*(6090), 54–58, doi:10.1126/science.1218740, 2012.

Manucharyan, G. E., and M. A. Spall, Wind-driven freshwater buildup and release in the Beaufort Gyre constrained by mesoscale eddies, *Geophys. Res. Lett.*, *43*(1), 273–282, doi:10.1002/2015GL065957, 2016.

Manucharyan, G. E., and A. F. Thompson, Submesoscale sea ice-ocean interactions in marginal ice zones, *J. Geophys. Res. Oceans*, *122*(12), 9455–9475, doi:10.1002/2017JC012895, 2017.

Manucharyan, G. E., and A. F. Thompson, Heavy footprints of upper-ocean eddies on weakened Arctic sea ice in marginal ice zones, *Nat Commun*, *13*(1), 2147, doi:10.1038/s41467-022-29663-0, 2022.

Martin, T., Arctic sea ice dynamics: Drift and ridging in numerical models and observations, Ph.D. thesis, University of Bremen, 2007.

Martin, T., M. Steele, and J. Zhang, Seasonality and long-term trend of Arctic Ocean surface stress in a model, *J. Geophys. Res. Oceans*, *119*(3), 1723–1738, doi:10.1002/2013JC009425, 2014.

Martin, T., M. Tsamados, D. Schroeder, and D. L. Feltham, The impact of variable sea ice roughness on changes in Arctic Ocean surface stress: A model study, *J. Geophys. Res. Oceans*, *121*(3), 1931–1952, doi:10.1002/2015JC011186, 2016.

Martini, K. I., H. L. Simmons, C. A. Stoudt, and J. K. Hutchings, Near-inertial internal waves and sea ice in the Beaufort Sea, *J. Phys. Oceanogr.*, *44*(8), 2212–2234, doi:10.1175/JPO-D-13-0160.1, 2014.

Maslanik, J., J. Stroeve, C. Fowler, and W. Emery, Distribution and trends in Arctic sea ice age through spring 2011, *Geophysical Research Letters*, *38*(13), doi:10.1029/2011GL047735, 2011.

Maykut, G. A., and N. Untersteiner, Some results from a time-dependent thermodynamic model of sea ice, *J. Geophys. Res.*, *76*(6), 1550–1575, doi:10.1029/JC076i006p01550, 1971.

McPhee, M. G., A simulation of inertial oscillation in drifting pack ice, *Dynamics of Atmospheres and Oceans*, *2*(2), 107–122, doi:10.1016/0377-0265(78)90005-2, 1978.

McPhee, M. G., The Effect of the Oceanic Boundary Layer on the Mean Drift of Pack Ice: Application of a Simple Model, *J. Phys. Oceanogr.*, *9*(2), 388–400, doi:10.1175/1520-0485(1979)009<0388:TEOTOB>2.0.CO;2, 1979.

McPhee, M. G., An analysis of pack ice drift in summer, *Sea ice processes and models*, pp. 62–75, 1980.

McPhee, M. G., Sea ice drag laws and simple boundary layer concepts, including application to rapid melting, *Tech. rep.*, U.S. Army Cold Regions Research and Engineering Laboratory, 1982.

McPhee, M. G., Small scale processes, in *Polar Oceanography*, edited by W. Smith, pp. 287–334, Academic Press, San Diego, CA, USA, 1990.

Mcphee, M. G., On the Turbulent Mixing Length in the Oceanic Boundary Layer, *Journal of Physical Oceanography*, *24*(9), 2014–2031, doi:10.1175/1520-0485(1994)024<2014:OTTMLI>2.0.CO;2, 1994.

McPhee, M. G., Parameterization of mixing in the ocean boundary layer, *Journal of Marine Systems*, *21*(1), 55–65, doi:10.1016/S0924-7963(99)00005-6, 1999.

McPhee, M. G., Turbulent stress at the ice/ocean interface and bottom surface hydraulic roughness during the SHEBA drift, *J. Geophys. Res.*, *107*(C10), 8037, doi:10.1029/2000JC000633, 2002.

McPhee, M. G., *Air-Ice-Ocean Interaction: Turbulent Ocean Boundary Layer Exchange Processes*, Springer-Verlag, New York, doi:10.1007/978-0-387-78335-2, 2008.

McPhee, M. G., Advances in understanding ice–ocean stress during and since AIDJEX, *Cold Reg. Sci. Technol.*, *76–77*, 24–36, doi:10.1016/j.coldregions.2011.05.001, 2012.

McPhee, M. G., and L. H. Kantha, Generation of internal waves by sea ice, *J. Geophys. Res.*, *94*(C3), 3287, doi:10.1029/JC094iC03p03287, 1989.

McPhee, M. G., and J. D. Smith, Measurements of the Turbulent Boundary Layer under Pack Ice, *Journal of Physical Oceanography*, *6*(5), 696–711, doi:10.1175/1520-0485(1976)006<0696:MOTTBL>2.0.CO;2, 1976.

McPhee, M. G., C. Kottmeier, and J. H. Morison, Ocean Heat Flux in the Central Weddell Sea during Winter, *J. Phys. Oceanogr.*, *29*(6), 1166–1179, doi:10.1175/1520-0485(1999)029<1166:OHFITC>2.0.CO;2, 1999.

Meier, W., and J. Stroeve, An Updated Assessment of the Changing Arctic Sea Ice Cover, *Oceanog*, doi:10.5670/oceanog.2022.114, 2022.

Meinen, C. S., and D. R. Watts, Calibrating Inverted Echo Sounders Equipped with Pressure Sensors, *Journal of Atmospheric and Oceanic Technology*, *15*(6), 1339–1345, doi:10.1175/1520-0426(1998)015<1339:CIESEW>2.0.CO;2, 1998.

Meneghello, G., J. Marshall, S. T. Cole, and M.-L. Timmermans, Observational Inferences of Lateral Eddy Diffusivity in the Halocline of the Beaufort Gyre, *Geophysical Research Letters*, *44*(24), 12,331–12,338, doi:10.1002/2017GL075126, 2017.

Meneghello, G., J. Marshall, J.-M. Campin, E. Doddridge, and M.-L. Timmermans, The Ice-Ocean Governor: Ice-Ocean Stress Feedback Limits Beaufort Gyre Spin-Up, *Geophys. Res. Lett.*, *45*(20), 11,293–11,299, doi:10.1029/2018GL080171, 2018a.

Meneghello, G., J. Marshall, M.-L. Timmermans, and J. Scott, Observations of Seasonal Upwelling and Downwelling in the Beaufort Sea Mediated by Sea Ice, *J. Phys. Oceanogr.*, *48*(4), 795–805, doi:10.1175/JPO-D-17-0188.1, 2018b.

Meneghello, G., E. Doddridge, J. Marshall, J. Scott, and J.-M. Campin, Exploring the Role of the "Ice–Ocean Governor" and Mesoscale Eddies in the Equilibration of the Beaufort Gyre: Lessons from Observations, *Journal of Physical Oceanography*, *50*(1), 269–277, doi:10.1175/JPO-D-18-0223.1, 2020a.

Meneghello, G., J. Marshall, C. Lique, P. E. Isachsen, E. Doddridge, J.-M. Campin, H. Regan, and C. Talandier, Genesis and Decay of Mesoscale Baroclinic Eddies in the Seasonally Ice-Covered Interior Arctic Ocean, *Journal of Physical Oceanography*, *51*(1), 115–129, doi:10.1175/JPO-D-20-0054.1, 2020b.

Menn, M. L., A. Lusven, E. Bongiovanni, P. L. Dû, D. Rouxel, S. Lucas, and L. Pacaud, Current profilers and current meters: Compass and tilt sensors errors and calibration, *Meas. Sci. Technol.*, *25*(8), 085,801, doi:10.1088/0957-0233/25/8/085801, 2014.

Mensa, J. A., and M.-L. Timmermans, Characterizing the seasonal cycle of upper-ocean flows under multi-year sea ice, *Ocean Modelling*, *113*, 115–130, doi:10.1016/j.ocemod.2017.03.009, 2017.

Mensa, J. A., M.-L. Timmermans, I. E. Kozlov, W. J. Williams, and T. M. Özgökmen, Surface Drifter Observations From the Arctic Ocean's Beaufort Sea: Evidence for Submesoscale Dynamics, *Journal of Geophysical Research: Oceans*, *123*(4), 2635–2645, doi:10.1002/2017JC013728, 2018.

Meyer, A., I. Fer, A. Sundfjord, and A. K. Peterson, Mixing rates and vertical heat fluxes north of Svalbard from Arctic winter to spring, *Journal of Geophysical Research: Oceans*, *122*(6), 4569–4586, doi:10.1002/2016JC012441, 2017.

Minnett, P. J., et al., Half a century of satellite remote sensing of sea-surface temperature, *Remote Sensing of Environment*, *233*, 111,366, doi:10.1016/j.rse.2019.111366, 2019.

Monin, A. S., and A. M. Obukhov, Basic laws of turbulent mixing in the surface layer of the atmosphere, *Trudy Geofiz. Inst. Akad. Nauk SSSR*, *24*(151), 163–187, 1954.

Morison, J. H., C. E. Long, and M. D. Levine, Internal wave dissipation under sea ice, *Journal of Geophysical Research: Oceans*, *90*(C6), 11,959–11,966, doi:10.1029/JC090iC06p11959, 1985.

Morison, J. H., M. G. McPhee, and G. A. Maykut, Boundary layer, upper ocean, and ice observations in the Greenland Sea Marginal Ice Zone, *J. Geophys. Res. Oceans*, *92*(C7), 6987–7011, doi:10.1029/JC092iC07p06987, 1987.

Niebauer, H., Wind and melt driven circulation in a marginal sea ice edge frontal system: A numerical model, *Continental Shelf Research*, *1*(1), 49–98, doi:10.1016/0278-4343(82)90032-2, 1982.

Notz, D., and J. Stroeve, Observed Arctic sea-ice loss directly follows anthropogenic CO2 emission, *Science*, *354*(6313), 747–750, doi:10.1126/science.aag2345, 2016.

Onarheim, I. H., T. Eldevik, L. H. Smedsrud, and J. C. Stroeve, Seasonal and Regional Manifestation of Arctic Sea Ice Loss, *Journal of Climate*, *31*(12), 4917–4932, doi:10.1175/JCLI-D-17-0427.1, 2018.

Overland, J. E., Atmospheric boundary layer structure and drag coefficients over sea ice, *Journal of Geophysical Research: Oceans*, *90*(C5), 9029–9049, doi:10.1029/JC090iC05p09029, 1985.

Park, H.-S., and A. L. Stewart, An analytical model for wind-driven Arctic summer sea ice drift, *Cryosphere*, *10*(1), 227–244, doi:10.5194/tc-10-227-2016, 2016.

Park, J. J., K. Kim, and R. W. Schmitt, Global distribution of the decay timescale of mixed layer inertial motions observed by satellite-tracked drifters, *Journal of Geophysical Research: Oceans*, *114*(C11), doi:10.1029/2008JC005216, 2009.

Peng, G., M. Steele, A. Bliss, W. Meier, and S. Dickinson, Temporal means and variability of Arctic sea ice melt and freeze season climate indicators using a satellite climate data record, *Remote Sensing*, *10*(9), 1328, doi:10.3390/rs10091328, 2018.

Penrose, J., and T. Beer, Acoustic reflection from estuarine pycnoclines, *Estuarine, Coastal and Shelf Science*, *12*(3), 237–249, doi:10.1016/S0302-3524(81)80122-3, 1981.

Peralta-Ferriz, C., and R. A. Woodgate, Seasonal and interannual variability of pan-Arctic surface mixed layer properties from 1979 to 2012 from hydrographic data, and the dominance of stratification for multiyear mixed layer depth shoaling, *Progress in Oceanography*, *134*, 19–53, doi:10.1016/j.pocean.2014.12.005, 2015.

Perovich, D., et al., Arctic Report Card 2018: Sea Ice, doi:10.25923/N170-9H57, 2018.

Perovich, D. K., B. Light, H. Eicken, K. F. Jones, K. Runciman, and S. V. Nghiem, Increasing solar heating of the Arctic Ocean and adjacent seas, 1979–2005: Attribution and role in the ice-albedo feedback, *Geophysical Research Letters*, *34*(19), doi:10.1029/2007GL031480, 2007.

Perrie, W., and Y. Hu, Air–ice–ocean momentum exchange. Part II: Ice drift, *J. Phys. Oceanogr.*, *27*, 21, 1997.

Peterson, A. K., I. Fer, M. G. McPhee, and A. Randelhoff, Turbulent heat and momentum fluxes in the upper ocean under Arctic sea ice, *J. Geophys. Res. Oceans*, *122*(2), 1439–1456, doi:10.1002/2016JC012283, 2017.

Petty, A. A., M. C. Tsamados, and N. T. Kurtz, Atmospheric form drag coefficients over Arctic sea ice using remotely sensed ice topography data, spring 2009-2015, *J. Geophys. Res. Earth Surf.*, *122*(8), 1472–1490, doi:10.1002/2017JF004209, 2017.

Phillips, O. M., Spectral and statistical properties of the equilibrium range in wind-generated gravity waves, *J. Fluid Mech.*, *156*(-1), 505, doi:10.1017/S0022112085002221, 1985.

Pinkel, R., Near-Inertial Wave Propagation in the Western Arctic, *Journal of Physical Oceanography*, *35*(5), 645–665, doi:10.1175/JPO2715.1, 2005.

Pite, H. D., D. R. Topham, and B. J. van Hardenberg, Laboratory measurements of the drag force on a family of two-dimensional ice keel models in a two-layer flow, *J. Phys. Oceanogr.*, *25*(12), 3008–3031, doi:10.1175/1520-0485(1995)025<3008:LMOTDF>2.0.CO;2, 1995.

Plueddemann, A. J., and J. T. Farrar, Observations and models of the energy flux from the wind to mixed-layer inertial currents, *Deep Sea Research Part II: Topical Studies in Oceanography*, *53*(1), 5–30, doi:10.1016/j.dsr2.2005.10.017, 2006.

Plueddemann, A. J., R. Krishfield, T. Takizawa, K. Hatakeyama, and S. Honjo, Upper ocean velocities in the Beaufort Gyre, *Geophys. Res. Lett.*, *25*(2), 183–186, doi:10.1029/97GL53638, 1998.

Pollard, R., and R. Millard, Comparison between observed and simulated wind-generated inertial oscillations, *Deep Sea Research and Oceanographic Abstracts*, *17*(4), 813–821, doi:10.1016/0011-7471(70)90043-4, 1970.

Pollard, R. T., P. B. Rhines, and R. O. R. Y. Thompson, The deepening of the wind-Mixed layer, *Geophysical Fluid Dynamics*, *4*(4), 381–404, doi:10.1080/03091927208236105, 1973.

Polyakov, I. V., et al., Greater role for Atlantic inflows on sea-ice loss in the Eurasian Basin of the Arctic Ocean, *Science*, *356*(6335), 285–291, doi:10.1126/science.aai8204, 2017.

Polyakov, I. V., et al., Intensification of Near-Surface Currents and Shear in the Eastern Arctic Ocean, *Geophys. Res. Lett.*, *47*(16), e2020GL089,469, doi:10.1029/2020GL089469, 2020a.

Polyakov, I. V., et al., Weakening of Cold Halocline Layer Exposes Sea Ice to Oceanic Heat in the Eastern Arctic Ocean, *J. Climate*, *33*(18), 8107–8123, doi:10.1175/JCLI-D-19-0976.1, 2020b.

Price, J. F., R. A. Weller, and R. Pinkel, Diurnal cycling: Observations and models of the upper ocean response to diurnal heating, cooling, and wind mixing, *Journal of Geophysical Research: Oceans*, *91*(C7), 8411–8427, doi:10.1029/JC091iC07p08411, 1986.

Price, J. F., R. A. Weller, and R. R. Schudlich, Wind-Driven Ocean Currents and Ekman Transport, *Science*, *238*(4833), 1534–1538, doi:10.1126/science.238.4833.1534, 1987.

Proshutinsky, A., et al., Analysis of the Beaufort Gyre Freshwater Content in 2003–2018, *Journal of Geophysical Research: Oceans*, *124*(12), 9658–9689, doi:10.1029/2019JC015281, 2019.

Rainville, L., and P. Winsor, Mixing across the Arctic Ocean: Microstructure observations during the Beringia 2005 Expedition, *Geophys. Res. Lett.*, *35*(8), L08,606, doi:10.1029/2008GL033532, 2008.

Rainville, L., and R. A. Woodgate, Observations of internal wave generation in the seasonally ice-free Arctic, *Geophys. Res. Lett.*, *36*(23), L23,604, doi:10.1029/2009GL041291, 2009.

Rainville, L., C. Lee, and R. A. Woodgate, Impact of wind-driven mixing in the Arctic Ocean, *Oceanography*, *24*(3), 136–145, 2011.

Rampal, P., J. Weiss, and D. Marsan, Positive trend in the mean speed and deformation rate of Arctic sea ice, 1979–2007, *J. Geophys. Res.*, *114*(C5), C05,013, doi:10.1029/2008JC005066, 2009.

Rampal, P., S. Bouillon, E. Ólason, and M. Morlighem, NeXtSIM: A new Lagrangian sea ice model, *Cryosphere*, *10*(3), 1055–1073, doi:10.5194/tc-10-1055-2016, 2016.

Randelhoff, A., A. Sundfjord, and A. H. H. Renner, Effects of a shallow pycnocline and surface meltwater on sea ice–ocean drag and turbulent heat flux, *J. Phys. Oceanogr.*, *44*(8), 2176–2190, doi:10.1175/JPO-D-13-0231.1, 2014.

Rascle, N., F. Ardhuin, P. Queffeulou, and D. Croizé-Fillon, A global wave parameter database for geophysical applications. Part 1: Wave-current–turbulence interaction parameters for the open ocean based on traditional parameterizations, *Ocean Modelling*, *25*(3), 154–171, doi:10.1016/j.ocemod.2008.07.006, 2008.

Regan, H. C., C. Lique, and T. W. K. Armitage, The Beaufort Gyre Extent, Shape, and Location Between 2003 and 2014 From Satellite Observations, *Journal of Geophysical Research: Oceans*, *124*(2), 844–862, doi:10.1029/2018JC014379, 2019.

Roach, L. A., C. Horvat, S. M. Dean, and C. M. Bitz, An Emergent Sea Ice Floe Size Distribution in a Global Coupled Ocean-Sea Ice Model, *J. Geophys. Res. Oceans*, *123*(6), 4322–4337, doi:10.1029/2017JC013692, 2018.

Roberts, A. F., E. C. Hunke, S. M. Kamal, W. H. Lipscomb, C. Horvat, and W. Maslowski, A variational method for sea ice ridging in earth system models, *J. Adv. Model. Earth Syst.*, *11*(3), 771–805, doi:10.1029/2018MS001395, 2019.

Røed, L. P., and J. J. O'Brien, A coupled ice-ocean model of upwelling in the marginal ice zone, *J. Geophys. Res.*, *88*(C5), 2863, doi:10.1029/JC088iC05p02863, 1983.

Rogers, W. E., J. Thomson, H. H. Shen, M. J. Doble, P. Wadhams, and S. Cheng, Dissipation of wind waves by pancake and frazil ice in the autumn Beaufort Sea: WAVE DAMPING BY ICE IN THE BEAUFORT SEA, *J. Geophys. Res. Oceans*, *121*(11), 7991–8007, doi:10.1002/2016JC012251, 2016.

Rolph, R. J., D. L. Feltham, and D. Schröder, Changes of the Arctic marginal ice zone during the satellite era, *The Cryosphere*, *14*(6), 1971–1984, doi:10.5194/tc-14-1971-2020, 2020.

Ross, T., and A. C. Lavery, Acoustic scattering from density and sound speed gradients: Modeling of oceanic pycnoclines, *The Journal of the Acoustical Society of America*, *131*(1), EL54–EL60, doi:10.1121/1.3669394, 2012.

Rossby, C.-G., and R. B. Montgomery, The layer of frictional influence in wind and ocean currents, *Papers Phys. Oceanogr. Meteor.*, *3*(3), 1935.

Rothrock, D. A., and A. S. Thorndike, Geometric properties of the underside of sea ice, *Journal of Geophysical Research: Oceans*, *85*(C7), 3955–3963, doi:10.1029/JC085iC07p03955, 1980.

Rousset, C., et al., The Louvain-La-Neuve sea ice model LIM3.6: Global and regional capabilities, *Geosci. Model Dev.*, *8*, 2991–3005, doi:10.5194/gmd-8-2991-2015, 2015.

Rudnick, D. L., and J. Klinke, The underway conductivity–temperature–depth instrument, *J. Atmos. Oceanic Technol.*, *24*(11), 1910–1923, doi:10.1175/JTECH2100.1, 2007.

Sanchez, R., F. Straneo, and M. Andres, Using Acoustic Travel Time to Monitor the Heat Variability of Glacial Fjords, *Journal of Atmospheric and Oceanic Technology*, *38*(9), doi:10.1175/JTECH-D-20-0176.1, 2021.

Scheifele, B., S. Waterman, and J. R. Carpenter, Turbulence and Mixing in the Arctic Ocean's Amundsen Gulf, *Journal of Physical Oceanography*, *-1*(aop), doi:10.1175/JPO-D-20-0057.1, 2020.

Schudlich, R. R., and J. F. Price, Observations of Seasonal Variation in the Ekman Layer, *Journal of Physical Oceanography*, *28*(6), 1187–1204, doi:10.1175/1520-0485(1998)028<1187:OOSVIT>2.0.CO;2, 1998.

Shaw, W. J., and T. P. Stanton, Vertical diffusivity of the Western Arctic Ocean halocline, *Journal of Geophysical Research: Oceans*, *119*(8), 5017–5038, doi:10.1002/2013JC009598, 2014.

Shaw, W. J., T. P. Stanton, M. G. McPhee, and T. Kikuchi, Estimates of surface roughness length in heterogeneous under-ice boundary layers, *J. Geophys. Res.*, *113*(C8), C08,030, doi:10.1029/2007JC004550, 2008.

Shcherbina, A., E. A. D'Asaro, B. Light, J. W. Deming, and E. Rehm, Maiden Voyage of the Under-Ice Float, poster prresented at Ocean Sciences Meeting 2016, 2016.

Shibley, N. C., M.-L. Timmermans, and C. Stranne, Analysis of Acoustic Observations of Double-Diffusive Finestructure in the Arctic Ocean, *Geophysical Research Letters*, *47*(18), e2020GL089,845, doi:10.1029/2020GL089845, 2020.

Shirasawa, K., and R. G. Ingram, Characteristics of the turbulent oceanic boundary layer under sea ice. Part 1: A review of the ice-ocean boundary layer, *J. Marine Sys.*, *2*(1), 153–160, doi:10.1016/0924-7963(91)90021-L, 1991.

Shirasawa, K., and R. G. Ingram, Currents and turbulent fluxes under the first-year sea ice in Resolute Passage, Northwest Territories, Canada, *J. Marine Sys.*, *11*(1-2), 21–32, doi:10.1016/S0924-7963(96)00024-3, 1997.

Shirasawa, K., R. G. Ingram, and M. Aota, Measurements in the boundary layer under landfast ice in the southeast Hudson Bay, Canada, *Low Temp. Sci.*, *A*(47), 213–221, 1989.

Shrestha, K., and G. E. Manucharyan, Parameterization of submesoscale mixed layer restratification under sea ice, *Journal of Physical Oceanography*, *-1*(aop), doi:10.1175/JPO-D-21-0024.1, 2021.

Skyllingstad, E. D., Effects of keels on ice bottom turbulence exchange, *J. Geophys. Res.*, *108*(C12), 3372, doi:10.1029/2002JC001488, 2003.

Smith, M., and J. Thomson, Ocean surface turbulence in newly formed marginal ice zones, *J. Geophys. Res. Oceans*, *124*(3), 1382–1398, doi:10.1029/2018JC014405, 2019.

Smith, M., S. Stammerjohn, O. Persson, L. Rainville, G. Liu, W. Perrie, R. Robertson, J. Jackson, and J. Thomson, Episodic reversal of autumn ice advance caused by release of ocean heat in the Beaufort Sea, *J. Geophys. Res. Oceans*, *123*(5), 3164–3185, doi:10.1002/2018JC013764, 2018.

Smith IV, D. C., and A. A. Bird, The interaction of an ocean eddy with an ice edge ocean jet in a marginal ice zone, *Journal of Geophysical Research: Oceans*, *96*(C3), 4675–4689, doi:10.1029/90JC02262, 1991.

Spreen, G., L. Kaleschke, and G. Heygster, Sea ice remote sensing using AMSR-E 89-GHz channels, *J. Geophys. Res. Oceans*, *113*(C2), doi:10.1029/2005JC003384, 2008.

Spreen, G., R. Kwok, and D. Menemenlis, Trends in Arctic sea ice drift and role of wind forcing: 1992-2009, *Geophys. Res. Lett.*, *38*(19), n/a–n/a, doi:10.1029/2011GL048970, 2011.

Steele, M., J. H. Morison, and N. Untersteiner, The partition of air-ice-ocean momentum exchange as a function of ice concentration, floe size, and draft, *J. Geophys. Res.*, *94*(C9), 12,739, doi:10.1029/JC094iC09p12739, 1989.

Steele, M., J. Zhang, D. Rothrock, and H. Stern, The force balance of sea ice in a numerical model of the Arctic Ocean, *J. Geophys. Res. Oceans*, *102*(C9), 21,061–21,079, doi:10.1029/97JC01454, 1997.

Steiner, N., Introduction of variable drag coefficients into sea-ice models, *Ann. Glaciol.*, *33*, 181–186, doi:10.3189/172756401781818149, 2001.

Stern, H. L., A. J. Schweiger, J. Zhang, and M. Steele, On reconciling disparate studies of the sea-ice floe size distribution, *Elem. Sci. Anth.*, *6*(1), 49, doi:10.1525/elementa.304, 2018.

Stone, P. H., On Non-Geostrophic Baroclinic Stability, *Journal of the Atmospheric Sciences*, *23*(4), 390–400, doi:10.1175/1520-0469(1966)023<0390:ONGBS>2.0.CO;2, 1966.

Stranne, C., L. Mayer, T. C. Weber, B. R. Ruddick, M. Jakobsson, K. Jerram, E. Weidner, J. Nilsson, and K. Gårdfeldt, Acoustic Mapping of Thermohaline Staircases in the Arctic Ocean, *Sci Rep*, *7*(1), 15,192, doi:10.1038/s41598-017-15486-3, 2017.

Stranne, C., et al., Acoustic mapping of mixed layer depth, *Ocean Science*, *14*(3), 503–514, doi:10.5194/os-14-503-2018, 2018.

Stroeve, J., and D. Notz, Insights on past and future sea-ice evolution from combining observations and models, *Global and Planetary Change*, *135*, 119–132, doi:10.1016/j.gloplacha.2015.10.011, 2015.

Stroeve, J., and D. Notz, Changing state of Arctic sea ice across all seasons, *Environ. Res. Lett.*, *13*(10), 103,001, doi:10.1088/1748-9326/aade56, 2018.

Strong, C., and I. G. Rigor, Arctic marginal ice zone trending wider in summer and narrower in winter, *Geophys. Res. Lett.*, *40*(18), 4864–4868, doi:10.1002/grl.50928, 2013.

Svensson, U., and A. Omstedt, A Mathematical Model of the Ocean Boundary Layer under Drifting Melting ice, *Journal of Physical Oceanography*, *20*(2), 161–171, doi:10.1175/1520-0485(1990)020<0161:AMMOTO>2.0.CO;2, 1990.

Tandon, A., and C. Garrett, Mixed Layer Restratification Due to a Horizontal Density Gradient, *Journal of Physical Oceanography*, *24*(6), 1419–1424, doi:10.1175/1520-0485(1994)024<1419:MLRDTA>2.0.CO;2, 1994.

Thomas, L. N., and C. M. Lee, Intensification of ocean fronts by down-front winds, *J. Phys. Oceanogr.*, *35*(6), 1086–1102, doi:10.1175/JPO2737.1, 2005.

Thomas, L. N., A. Tandon, and A. Mahadevan, Submesoscale processes and dynamics, in *Geophysical Monograph Series*, vol. 177, edited by M. W. Hecht and H. Hasumi, pp. 17–38, American Geophysical Union, Washington, D. C., doi:10.1029/177GM04, 2008.

Thomas, L. N., J. R. Taylor, E. A. D'Asaro, C. M. Lee, J. M. Klymak, and A. Shcherbina, Symmetric instability, inertial oscillations, and turbulence at the gulf stream front, *J. Phys. Oceanogr.*, *46*(1), 197–217, doi:10.1175/JPO-D-15-0008.1, 2016.

Thomson, J., Wave Breaking Dissipation Observed with “SWIFT” Drifters, *J. Atmos. Oceanic Technol.*, *29*(12), 1866–1882, doi:10.1175/JTECH-D-12-00018.1, 2012.

Thomson, J., Long-term measurements of ocean waves and sea ice draft in the central Beaufort Sea, 2020.

Thomson, J., and W. E. Rogers, Swell and sea in the emerging Arctic Ocean, *Geophysical Research Letters*, *41*(9), 3136–3140, doi:10.1002/2014GL059983, 2014.

Thomson, J., E. A. D'Asaro, M. F. Cronin, W. E. Rogers, R. R. Harcourt, and A. Shcherbina, Waves and the equilibrium range at Ocean Weather Station P, *J. Geophys. Res. Oceans*, *118*(11), 5951–5962, doi:10.1002/2013JC008837, 2013.

Thomson, J., M. S. Schwendeman, S. F. Zippel, S. Moghimi, J. Gemmrich, and W. E. Rogers, Wave-Breaking Turbulence in the Ocean Surface Layer, *J. Phys. Oceanogr.*, *46*(6), 1857–1870, doi:10.1175/JPO-D-15-0130.1, 2016a.

Thomson, J., B. Lund, J. Hargrove, M. M. Smith, J. Horstmann, and J. A. MacKinnon, Wave-driven flow along a compact marginal ice zone, *Geophys. Res. Lett.*, doi:10.1029/2020GL090735, 2021.

Thomson, J., et al., Emerging trends in the sea state of the Beaufort and Chukchi seas, *Ocean Modelling*, *105*, 1–12, doi:10.1016/j.ocemod.2016.02.009, 2016b.

Thorpe, S. A., *An Introduction to Ocean Turbulence*, Cambridge University Press, Cambridge, doi:10.1017/CBO9780511801198, 2007.

Timco, G., and R. Burden, An analysis of the shapes of sea ice ridges, *Cold Reg. Sci. Technol.*, *25*(1), 65–77, doi:10.1016/S0165-232X(96)00017-1, 1997.

Timmermann, R., S. Danilov, J. Schröter, C. Böning, D. Sidorenko, and K. Rollenhagen, Ocean circulation and sea ice distribution in a finite element global sea ice–ocean model, *Ocean Model.*, *27*(3-4), 114–129, doi:10.1016/j.ocemod.2008.10.009, 2009.

Timmermans, M.-L., and J. Marshall, Understanding Arctic Ocean Circulation: A Review of Ocean Dynamics in a Changing Climate, *Journal of Geophysical Research: Oceans*, *125*(4), e2018JC014,378, doi:10.1029/2018JC014378, 2020.

Timmermans, M.-L., and P. Winsor, Scales of horizontal density structure in the Chukchi Sea surface layer, *Continental Shelf Research*, *52*, 39–45, doi:10.1016/j.csr.2012.10.015, 2013.

Timmermans, M.-L., S. Cole, and J. Toole, Horizontal density structure and restratification of the arctic ocean surface layer, *J. Phys. Oceanogr.*, *42*(4), 659–668, doi:10.1175/JPO-D-11-0125.1, 2012.

Timmermans, M.-L., J. Toole, and R. Krishfield, Warming of the interior Arctic Ocean linked to sea ice losses at the basin margins, *Sci. Adv.*, *4*(8), eaat6773, doi:10.1126/sciadv.aat6773, 2018.

Toole, J. M., M.-L. Timmermans, D. K. Perovich, R. A. Krishfield, A. Proshutinsky, and J. A. Richter-Menge, Influences of the ocean surface mixed layer and thermohaline stratification on Arctic Sea ice in the central Canada Basin, *Journal of Geophysical Research: Oceans*, *115*(C10), doi:10.1029/2009JC005660, 2010.

Tsamados, M., D. L. Feltham, D. Schroeder, D. Flocco, S. L. Farrell, N. Kurtz, S. W. Laxon, and S. Bacon, Impact of variable atmospheric and oceanic form drag on simulations of Arctic sea ice, *J. Phys. Oceanogr.*, *44*(5), 1329–1353, doi:10.1175/JPO-D-13-0215.1, 2014.

Tschudi, M., W. Meier, J. Stewart, and C. Fowler, Polar Pathfinder Daily 25 km EASE-Grid Sea Ice Motion Vectors, doi:10.5067/INAWUWO7QH7B, 2019.

Ullman, D. S., and D. Hebert, Processing of underway CTD data, *J. Atmos. Oceanic Technol.*, *31*(4), 984–998, doi:10.1175/JTECH-D-13-00200.1, 2014.

Velasco, D. W., S. Nylund, and T. Pettersen, Combined Current Profiling and Biological Echosounding Results from a Single ADCP, in *2018 OCEANS - MTS/IEEE Kobe Techno-Oceans (OTO)*, pp. 1–5, doi:10.1109/OCEANSKOBE.2018.8559356, 2018.

Voelker, G. S., D. Olbers, M. Walter, C. Mertens, and P. G. Myers, Estimates of wind power and radiative near-inertial internal wave flux, *Ocean Dynamics*, *70*(11), 1357–1376, doi:10.1007/s10236-020-01388-y, 2020.

Voermans, J. J., P. B. Smit, T. T. Janssen, and A. V. Babanin, Estimating Wind Speed and Direction Using Wave Spectra, *Journal of Geophysical Research: Oceans*, *125*(2), e2019JC015,717, doi:10.1029/2019JC015717, 2020.

Wadhams, P., and T. Davy, On the spacing and draft distributions for pressure ridge keels, *J. Geophys. Res.*, *91*(C9), 10,697, doi:10.1029/JC091iC09p10697, 1986.

Wadhams, P., and R. J. Horne, An Analysis Of Ice Profiles Obtained By Submarine Sonar In The Beaufort Sea, *J. Glaciol.*, *25*(93), 401–424, doi:10.3189/S0022143000015264, 1980.

Wadhams, P., and N. Toberg, Changing characteristics of arctic pressure ridges, *Polar Science*, *6*(1), 71–77, doi:10.1016/j.polar.2012.03.002, 2012.

Watts, D. R., and H. T. Rossby, Measuring Dynamic Heights with Inverted Echo Sounders: Results from MODE, *Journal of Physical Oceanography*, *7*(3), 345–358, doi:10.1175/1520-0485(1977)007<0345:MDHWIE>2.0.CO;2, 1977.

Weiss, J., and D. Marsan, Scale properties of sea ice deformation and fracturing, *C. R. Physique*, *5*(7), 735–751, doi:10.1016/j.crhy.2004.09.005, 2004.

Welch, P., The use of fast Fourier transform for the estimation of power spectra: A method based on time averaging over short, modified periodograms, *IEEE Transactions on Audio and Electroacoustics*, *15*(2), 70–73, doi:10.1109/TAU.1967.1161901, 1967.

Wenta, M., and A. Herman, The influence of the spatial distribution of leads and ice floes on the atmospheric boundary layer over fragmented sea ice, *Ann. Glaciol.*, *59*(76pt2), 213–230, doi:10.1017/aog.2018.15, 2018.

Williams, E., C. Swithinbank, and G. d. Q. Robin, A submarine sonar study of Arctic pack ice, *J. Glaciol.*, *15*(73), 349–362, doi:10.3189/S002214300003447X, 1975.

Wilson, E. A., S. C. Riser, E. C. Campbell, and A. P. S. Wong, Winter Upper-Ocean Stability and Ice–Ocean Feedbacks in the Sea Ice–Covered Southern Ocean, *J. Phys. Oceanogr.*, *49*(4), 1099–1117, doi:10.1175/JPO-D-18-0184.1, 2019.

Wulff, T., E. Bauerfeind, and W.-J. von Appen, Physical and ecological processes at a moving ice edge in the Fram Strait as observed with an AUV, *Deep Sea Research Part I: Oceanographic Research Papers*, *115*, 253–264, doi:10.1016/j.dsr.2016.07.001, 2016.

Wunsch, C., The Work Done by the Wind on the Oceanic General Circulation, *Journal of Physical Oceanography*, *28*(11), 2332–2340, doi:10.1175/1520-0485(1998)028<2332:TWDBTW>2.0.CO;2, 1998.

Yang, J., The Seasonal Variability of the Arctic Ocean Ekman Transport and Its Role in the Mixed Layer Heat and Salt Fluxes, *Journal of Climate*, *19*(20), 5366–5387, doi:10.1175/JCLI3892.1, 2006.

Yelland, M. J., P. K. Taylor, I. E. Consterdine, and M. H. Smith, The Use of the Inertial Dissipation Technique for Shipboard Wind Stress Determination, *Journal of Atmospheric and Oceanic Technology*, *11*(4), 1093–1108, doi:10.1175/1520-0426(1994)011<1093:TUOTID>2.0.CO;2, 1994.

Yu, L., X. Jin, E. W. Schulz, and S. A. Josey, Air-sea interaction regimes in the sub-Antarctic Southern Ocean and Antarctic marginal ice zone revealed by icebreaker measurements, *J. Geophys. Res. Oceans*, *122*(8), 6547–6564, doi:10.1002/2016JC012281, 2017.

Zippel, S., and J. Thomson, Air-sea interactions in the marginal ice zone, *Elem Sci Anth*, *4*, 000,095, doi:10.12952/journal.elementa.000095, 2016.

Zippel, S. F., J. T. Farrar, C. J. Zappa, and A. J. Plueddemann, Parsing the Kinetic Energy Budget of the Ocean Surface Mixed Layer, *Geophysical Research Letters*, *49*(2), e2021GL095,920, doi:10.1029/2021GL095920, 2022.

Zu, Y., P. Lu, M. Lepparanta, B. Cheng, and Z. Li, On the form drag coefficient under ridged ice: Laboratory experiments and numerical simulations from ideal scaling to real ice conditions, doi:10.1002/essoar.10504763.1, pre-print, 2020.

Zu, Y., P. Lu, M. Leppäranta, B. Cheng, and Z. Li, On the Form Drag Coefficient Under Ridged Ice: Laboratory Experiments and Numerical Simulations From Ideal Scaling to Deep Water, *Journal of Geophysical Research: Oceans*, *126*(8), e2020JC016,976, doi:10.1029/2020JC016976, 2021.